Optimisation of Fabrication Processes for Stable and Scalable Perovskite Solar Cells

Michael Wong-Stringer

Department of Physics and Astronomy
The University of Sheffield

Thesis submitted for the degree of Doctor of Philosophy
(Alternative Format)

September 2018

Acknowledgements

Firstly, I would like to thank my supervisor David Lidzey. He was always ready and able to give guidance, feedback, and advice. I particularly thank him for encouraging me to publish my research!

I would also like to thank the University of Sheffield, Engineering and Physical Sciences Research Council (EPSRC), and the EPSRC Centre for Doctoral Training; New and Sustainable Photovoltaics (CDT-PV) for providing the amazing opportunity that this PhD has been. It has been a privilege to complete research for this thesis submission.

I have also had the luxury of having many great colleagues and friends here in the Electronic and Photonic Molecular Materials group at Sheffield and within CDT-PV. Thank you for the times when you have helped me with understanding experiments and interpreting results and thank you for your friendship. In particular, I thank the collaborating authors on my publications, without this network of incredibly brilliant scientists across fields and universities, I would not have been able to bring together my research.

I am very grateful to Power Roll for involving me in a unique and exciting project that I hope will reach fruition in the near future!

I thank my family for raising me to be inquisitive and for not stifling my unending nerdiness when I was growing up. Thank you for everything you have ever given me, there is not a chance I would have come close to writing a thesis without all the things you taught me.

Finally, and most importantly, I am immensely thankful for my wife; for loving and supporting me during my PhD in little old Sheffield. She gave me strength to work towards my PhD whilst she endured the cold and rainy months and had the patience to be my side when I was silly, stressed, and frustrated with work.

For the Reader’s Attention

This thesis is submitted in an alternative format, as approved by the University of Sheffield Research Services.

Published papers and completed work undergoing peer review are presented as thesis chapters, abiding by the University of Sheffield’s guidelines. To keep pagination and formatting consistent within this thesis, the publications are typeset in word. The papers have not been altered from their peer reviewed versions, however, a brief extended discussion has been added to each paper (as encouraged by the University guidelines in the case of papers being limited in length due rules imposed by journal) to provide further insight and build a better continuity between chapters. The journal name, paper DOI, and citation are provided to allow ease of access to the journals fully typeset PDF version. Collaborating authors consent has been acquired and can be provided upon request.

Pagination is kept throughout all chapters.

Figure and equation numeration are reset for every chapter.

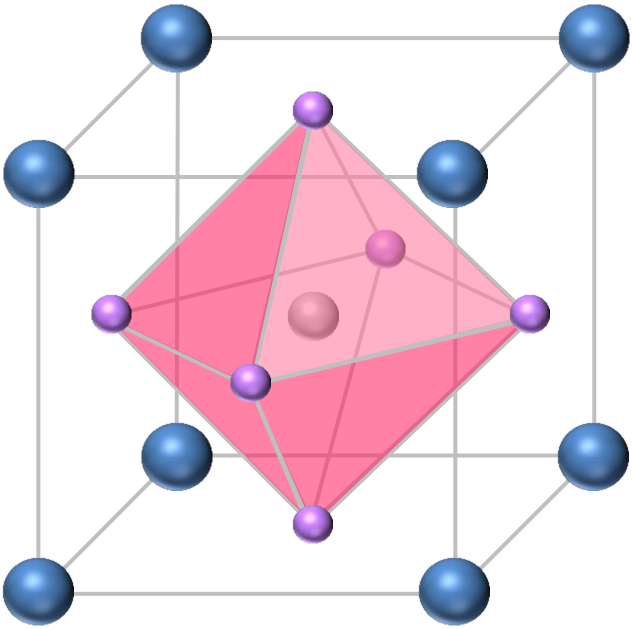

Abstract

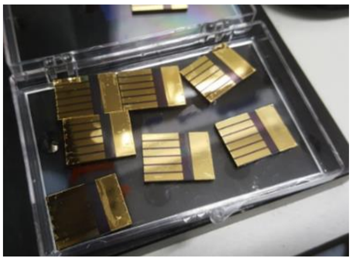

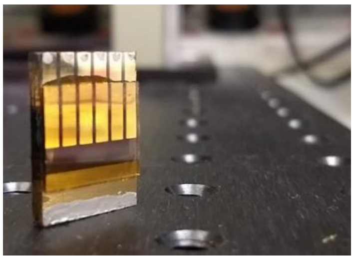

In recent years metal halide perovskites have become a promising photovoltaic (PV) technology, most notable for their high-power conversion efficiencies and potential for cheap, solution-processable, roll-to-roll compatible module production. In this thesis, the materials and fabrication processes that are used to make perovskite photovoltaics are investigated, developing them in such a way to make them cheaper, scalable, and transferable to high throughput manufacturing processes, whilst simultaneously aiming to achieve and maintain efficiency and stability.

A family of carbazole-based conjugated polymers is identified as potential set of materials for hole selective charge transporting materials. A chemically doped polymer poly[N-9'-heptadecanyl-2,7-carbazole-alt-5,5-(4',7'-di-2-thienyl-2',1',3'-benzothiadiazole)] (PCDTBT) hole transport layer is used with multi cation formamidinium lead iodide ($\mathrm{FAPbI_3}$) and methylammonium lead bromide ($\mathrm{MAPbBr_3}$) perovskite $\mathrm{(FAPbI_3)_{0.85}(MAPbBr_3)_{0.15}}$, to achieve standard architecture devices with up to 15.9 % power conversion efficiency, with clear evidence that the chemical doping increases the conductivity and photostability of the PCDTBT.

The stability of perovskite solar cells is a vital issue that must be addressed in further detail if perovskite PV is to become a commercially viable technology. Here, the importance of hydrophobic hole transport layers for perovskite solar cell stability is identified. Facile formation of a moisture free perovskite is achieved by combining the hydrophobic polymer poly(4-butylphenyldiphenylamine) (poly-TPD) with a volatile methylamine bubbled acetonitrile methylammonium lead iodide ($\mathrm{MAPbI_3}$) perovskite solution. A multi-layer encapsulation system, comprised of a protective polyvinylpyrrolidone (PVP) interlayer and a UV-curable epoxy, is used to stabilise perovskite solar cells containing these materials, leading to $\mathrm{MAPbI_3}$ based inverted architecture devices with lifetimes over 1000 hours.

It is also found that solvent-annealed $MAPbI_3$ devices (which generate higher photocurrent) have reduced stability and undergo enhanced burn-in. This result demonstrates that initially enhanced device power conversion efficiency does not necessarily translate to a device having long-term stability. Triple cation $CsI_{0.05}((FAPbI_3)_{0.83}(MAPbBr_3)_{0.17})_{0.95}$ based standard architecture perovskite solar cells are also shown to have impressive stability when encapsulated with a multi-layer encapsulation system that comprises of a protective aluminium oxide (Al_2O_3) interlayer and a UV-curable epoxy.

To pursue low-cost, scalable fabrication of perovskite solar cells, inorganic metal oxide charge transport layers have been explored. Here, the materials nickel oxide (NiO) and titanium dioxide (TiO_2) have been deposited through reactive electron-beam evaporation. NiO and TiO_2 are then utilised to create devices with champion power conversion efficiencies up to 15.8 % and 13.9 % respectively. Both materials are compatible with $MAPbI_3$ and $CsI_{0.05}((FAPbI_3)_{0.83}(MAPbBr_3)_{0.17})_{0.95}$ perovskite active layers. Critically, it is found that such metal oxides can be deposited at high speed (nm/s), and do not require a high-temperature anneal step after deposition, making reactive electron-beam evaporation compatible with roll-to-roll processing on sensitive flexible polymeric substrates.

Finally, a new type of back-contact perovskite PV architecture is explored, solar micro-grooves. Here, such embossed polymeric micro-grooves are directionally coated with evaporable p- or n- type electrodes on to opposing groove walls, and then filled with the highly volatile acetonitrile solution processed $MAPbI_3$ perovskite. These flexible, rare-metal-free, back-contact perovskite solar grooves make use of the p-type reactive electron-beam deposited NiO, and are fabricated without thermal annealing. Individual grooves act as photovoltaic devices, which achieve power conversion efficiencies of up to 7.3 %. It is demonstrated that horizontally-spaced series connected grooves act as mini-modules, which were found to build up to 15 V open circuit voltage. Crucially, these back-contact mini-modules are fully functional without the use of electrode patterning techniques such as electrodeposition, laser ablation, mechanical etching, or photoresist templating.

Publications

As Chapter (4)

1. **Michael Wong-Stringer**, James E. Bishop, Joel A. Smith, David K. Mohamad, Andrew J. Parnell, Vikas Kumar, Cornelia Rodenburg and David G. Lidzey, *Efficient perovskite photovoltaic devices using chemically doped PCDTBT as a hole-transport material*, J. Mater. Chem. A, **2017**, 5, 15714–15723 DOI: 10.1039/c7ta03103c

As Chapter (5)

2. **Michael Wong-Stringer**, Onkar S. Game, Joel A. Smith, Thomas J. Routledge, Bakhet A. Alqurashy, Benjamin G. Freestone, Andrew J. Parnell, Vikas Kumar, Majed O. A. Alawad, Ahmed Iraqi, Cornelia Rodenburg and David G. Lidzey, *High performance multi-layer encapsulation for perovskite photovoltaics Completed*, Advanced Energy Materials, **2018**, 8, 24, 1801234 DOI: 10.1002/aenm.201801234

As Chapter (6)

3. **Michael Wong-Stringer, Thomas J. Routledge,** Onkar S. Game, Joel A. Smith, James E. Bishop, Naoum Vaenas, Benjamin G. Freestone, David M. Coles, Trevor McArdle, Alastair R. Buckley, and David G. Lidzey, *Low-temperature, high-speed reactive deposition of metal oxides for perovskite solar cells*, Journal of Materials Chemistry A, **2019**, Advance Article. DOI: 10.1039/C8TA10827G

As Chapter (7)

4. **Michael Wong-Stringer, Thomas J. Routledge,** Trevor McArdle, Christopher Wood, Onkar S. Game, Joel A. Smith, James E. Bishop, Naoum Vaenas, David M. Coles, Alastair R. Buckley, and David G. Lidzey, *A flexible back-contact perovskite solar micro-module,* **2019**, Submitted for Review.

5. Davide Moia, Ilario Gelmetti, Phil Calado, William Fisher, **Michael Wong-Stringer**, Onkar S. Game, Yinghong Hu, Pablo Docampo, David G, Lidzey, Emilio Palomares, Jenny Nelson, Piers R. F. Barnes, Ionic-to-electronic current amplification in hybrid perovskite solar cells: ionically gated transistor-interface circuit model explains hysteresis and impedance of mixed conducting devices, **2019**, Submitted for Review.

6. James E. Bishop, David K. Mohamad, **Michael Wong-Stringer**, Joel A. Smith and David G. Lidzey, *Spray-cast multilayer perovskite solar cells with an active-area of 1.5 cm^2*, Sci. Rep, **2017**, 7, 7962.

7. Vikas Kumar, Whitney L. Schmidt, Giorgio Schileo, Robert C. Masters, **Michael Wong-Stringer**, Derek C. Sinclair, Ian. M. Reaney, David Lidzey and Cornelia Rodenburg, *Nano-scale mapping of bromide segregation on cross-sections of complex hybrid perovskite photovoltaic films using secondary electron hyperspectral imaging in the scanning electron microscope*, ACS Omega, **2017**, 2, 2126–2133.

8. James E. Bishop Joel A. Smith, Claire Greenland, Vikas Kumar, Naoum Vaenas, Onkar S. Game, Thomas J. Routledge, **Michael Wong-Stringer**, Cornelia Rodenburg, and David G. Lidzey, *High Efficiency Spray-Coated Perovskite Solar Cells Utilising Vacuum Assisted Solution Processing*, *ACS Appl. Mater. Interfaces*, **2018**, *10* (46), pp 39428–39434.

Collaborating Author Declarations

This alternative format thesis contains completed collaborative work (with an intension to submit for publication) and publications which involve collaborating authors. These completed/published works are presented as chapters within this thesis. In all cases the first author or the joint first author is myself, Michael Wong-Stringer. Other publications which I have been a listed author, but not first author, are not used as complete chapters within this thesis.

All the other collaborative authors (listed below) have read and agreed to the following. Contacted via email, their agreement is provided upon request.

I, a collaborating author on publication(s) used in this thesis, agree that the experimental work and/or the analysis and interpretation of work and/or the text within these publication(s) is primarily completed by Michael Wong-Stringer and suitable for use in his thesis.

Majed O. A. Alawad,
Bakhet A. Alqurashy,
James E. Bishop,
Benjamin G. Freestone,
Dr Onkar Game,
Dr Ahmed Iraqi.
Dr Vikas Kumar,
Prof David G. Lidzey,
Dr Trevor Mcardle,
Dr David K. Mohamad,
Dr Andrew J. Parnell,
Dr Cornelia Rodenburg,
Thomas J. Routledge,
Joel A. Smith,
Dr Naoum Vaenas,
Dr Christopher Wood.
Dr Alastair R. Buckley
Dr David M. Coles
Dr Alexander J. Topping

Conference Presentations

Oral presentation

Michael Wong-Stringer, Onkar Game, Ben Freestone, James E. Bishop, Joel A. Smith, Tom Routledge, Andrew J. Parnell, Vikas Kumar, Conny Rodenburg and D. G. Lidzey, *A Polymeric Interlayer and UV-vis Curable Epoxy for the Encapsulation of Highly Stable Perovskite Solar Cells*, Centre for Doctoral Training - Photovoltaic (CDT-PV) Showcase, **November 2017**.

Oral presentation.

Michael Wong-Stringer, James E. Bishop, Joel A. Smith, David K. Mohamad, Andrew J. Parnell, Vikas Kumar, Conny Rodenburg and David G. Lidzey, *Efficient perovskite photovoltaic devices using doped PCDTBT as a hole-transport material*, UK Semiconductors, **July 2017**.

Poster presentation.

Michael Wong-Stringer and David G. Lidzey, *Performance and Stability of Mixed Cation Perovskite Solar Cells with Alternative Hole Transport Materials*, Perovskite Solar Cells and Optoelectronics (PSCO) International, **July 2017**.

Poster presentation.

Michael Wong-Stringer and David G. Lidzey, *Performance and Stability of Mixed Cation Perovskite Solar Cells with Alternative Hole Transport Materials*, Centre for Doctoral Training - Photovoltaic (CDT-PV) Showcase, **November 2016**.

Poster presentation.

Michael Wong-Stringer, Robert Masters and David G. Lidzey, *Perovskite Precursors for Inverted Structure Photovoltaic Devices*, Centre for Doctoral Training Photovoltaic (CDT-PV) Showcase, **November 2015**.

Table of Contents

Chapter 1

Introduction

The evidence is clear, global warming cannot be ignored or refuted. At the time of writing (2018), temperatures in the United Kingdom soar above 30 degrees Celsius, Portugal has broken through the high 40s, and wildfires have practically incinerated a village in Greece. The established scientific consensus is that this prolonged extreme weather, recently occurring worldwide, is due to climate change, which is exacerbated by human interference.[1,2]

Fossil fuels still provide 80 % of global energy consumption, which includes supplying 65 % of global electricity generation,[3] and have long been identified as the main culprit behind climate change. Whilst the sun can wreak havoc on a 'greenhouse' earth with a polluted atmosphere, it is also the solution to breaking free from fossil fuel reliance. The total potential solar energy available on earth is estimated to be 23,000 terawatts years;[4] this reservoir of solar energy eclipses all other finite and renewable resources. There is an obvious limitation to solar power; solar irradiance is not globally uniform all the time – it is dependent on time of day, shading from local weather, and seasonal variations. However, in combination with other renewables, new advances in energy storage, and a restructuring of national power grids to more localised systems, solar modules easily have the capacity to provide the 20 terawatts years annual global energy consumption.[4]

A societal and political shift away from fossil fuel energy sources towards carbon neutral energy generation has already made headway. However, it does not help that since the turn of the millennia, the vast majority of the $2 billion spent on climate change related lobbying of the U.S Congress was from fossil fuel and transportation corporations, and their associated trade affiliations.[5] Despite this pressure, government policies around the globe have become more favourable towards renewables. Feed-in tariffs have been established in many countries to help encourage investment in solar modules. Unfortunately, it is an balanced economic requirement that most feed-in tariff policies are continually reduced to keep the energy market competitive and fair.[6]

Despite the progressiveness of carbon capture technology, it is a costly mitigator of climate change. Carbon capture does not address the fact that fossil fuels are a rapidly shrinking, finite source of energy. However, carbon capture will still be vital in counteracting the effects of climate change until the consumption of fossil fuels is reduced significantly.[7] It is unclear if the growth of alternative energy sources will include nuclear power, which is unpopular due to termination and waste management costs, and negative cultural opinion - and is not classified as renewable. Ultimately, renewables, by their very definition, are the only long-term available energy source. With the race for clean energy to meet the goals of the Paris Agreement (which now lacks support from the US), there has been a surge in large scale photovoltaic (PV) deployment on rooftops and solar farms in the past ten years. At the end of 2012, total global PV installed exceeded 100 GWp (Giga-watt peak).[8] It has been predicted that close to a third of all newly-installed electrical generation will be PV by 2030.[9] From now until 2040 it is predicted that 72 % of all investments in new power generation capacity will be based on renewables, with investment in solar capacity second only to wind power.[10] Despite fiscal reductions, government feed-in tariffs across Europe have stimulated growth and investment interest in solar energy. But crucially, the tipping point for PV return-on-investment (which is bringing solar energy up to grid cost-parity with other energy sources) resulted from the continuously falling prices of crystalline silicon (c-Si).[11] Remarkably, the average price for 1 watt (capability) of silicon PV has dropped from $ 100 (USD) to approximately $ 0.5 in the last 40 years, and can be as low as $ 0.2 in ‘sunny’ regions. Auctions for obtaining supplies of energy from renewable sources have shown bids for solar energy fall from 250 $/MWh in 2010 to below 50 $/MWh by 2016.[12,13]

Thin-film PV light-absorbing semiconductors are the focal point of a well-established scientific community, aiming to provide a semiconducting material to compete with popular solar module materials that are based on crystalline (c-Si) and amorphous silicon (a-Si). Inorganic alternatives include cadmium telluride (CdTe), copper indium gallium selenide (CIGS), and copper zinc tin sulphide (CZTS).

Thin-film active materials commonly have lower efficiencies, but rely on using less bulk material and cheaper processing techniques to produce a cost-competitive device. CdTe solar cells have managed to fill a small portion of the PV market (1.8 GWp in 2012). However, cadmium is recognised as a toxic material and tellurium is a rare-earth element. Both are factors that may hold back the wider-spread deployment of CdTe. CIGS PV has similar commercial issues, as it contains two rare-earth elements: indium and gallium. Perhaps the only promising emergent inorganic PV technology is CZTS, which only uses earth-abundant elements. However, world-class CZTS solar cells have power conversion efficiency (PCE) of around 10 %, significantly lower than any silicon-based PV.[14] There is still an opportunity for an alternative thin-film PV commercial technology to establish itself as a competitor to silicon PV. Carbon-based organic PV (OPVs), utilising semiconducting conjugated polymers and fullerenes or small molecule acceptors, along with dye-sensitised solar cells (DSSCs), were the first alternative competitors to inorganic thin-film PV. Crucially, these alternative thin-film semiconductors are often processed at low temperatures (<150 °C), and from solution. In practice, this allows them to be coated onto flexible substrates using roll-to-roll techniques (such as slot-die coating, spray coating, or screen printing). Despite lower PCEs than silicon PV, these advantages are regularly used to claim that OPVs and DSSCs would make them cost-competitive enough to reach grid parity.[15–19]

A surprise development in PV community came with the fabrication of the perovskite sensitised solar cells (PSSC). In 2006, a sensitised solar cell (see Chapter 2.5 for details), based on a metal-organic hybrid semiconductor within a nanoporous titanium dioxide (TiO_2) layer, achieved a PCE of 2.2 %.[9,20] The metal-organic used was a $CH_3NH_3PbBr_3$ perovskite; a material with ABX_3 crystal structure containing an ‘A’ site organic methylammonium (MA or CH_3NH_3) cation, a ‘B’ site metal lead (Pb) cation, and a ‘X’ site halide bromide (Br) anion.[21,22] The last decade has seen research on perovskite PV explode. From the advent of the PSSC in 2006, a rapid increase in PCE has led to a world-record perovskite solar cell (PSC) with a PCE of 23.3 %.[23] The increase in world record performance of all solar cell technologies is given in Figure 1, as tracked by the National Renewable Energy Laboratory.[23] It is clear that perovskites are the fastest-developing solar technology to date. By comparison, state-of-the-art single junction organic solar cells, which have been a competitive research field for twice as long, have only recently surpassed 14 % PCE.[24,25]

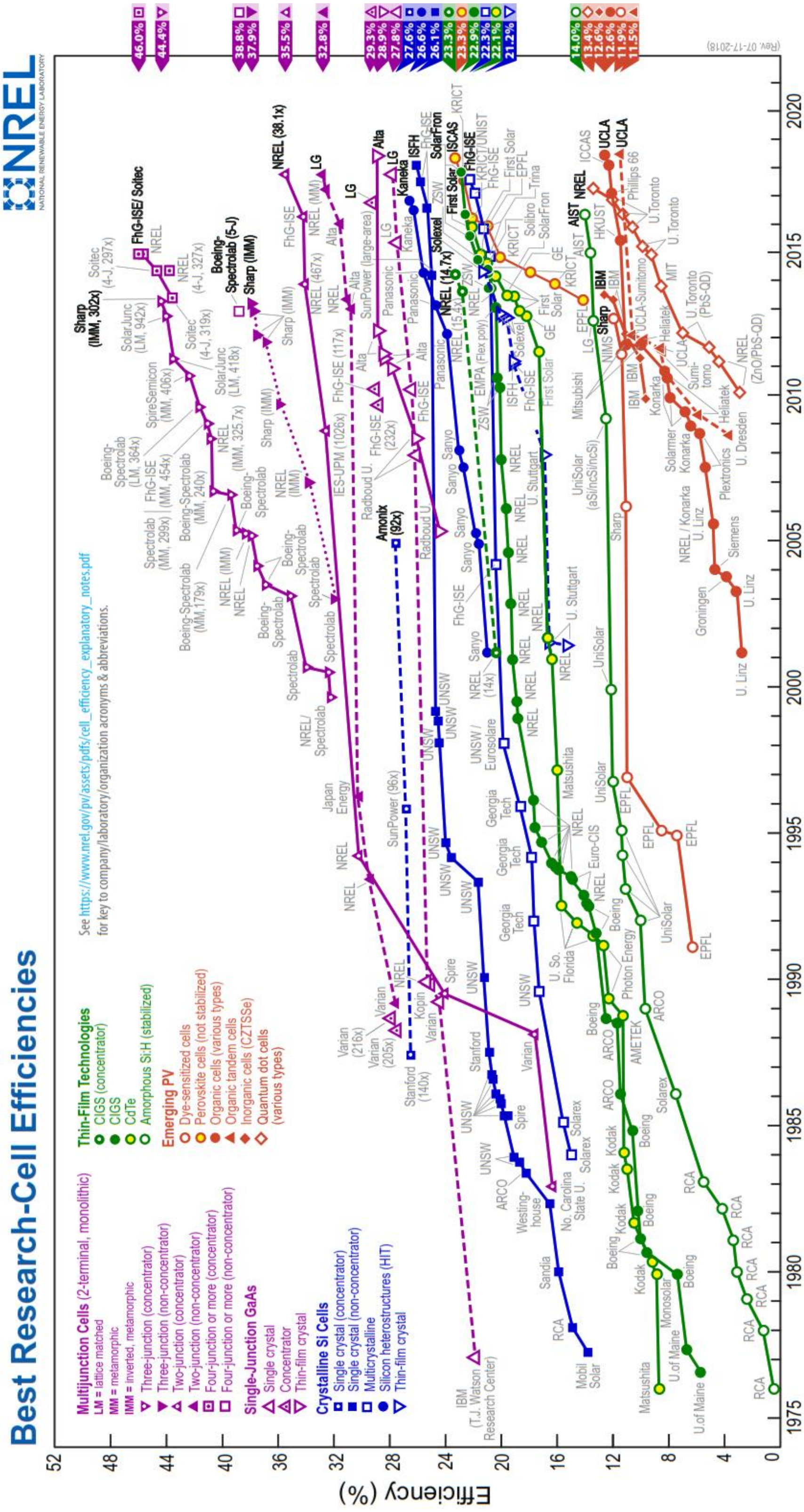

Figure 1: *National Renewable Energy Laboratory (NREL) certified world record solar cell power conversion efficiencies for PV technologies (Accessed August 2018).*[23]

Metal-organic perovskites exhibit such an impressive performance due to their near ideal optoelectronic properties. They have a band gap which can be tuned, depending on the chemical constituents and stoichiometry of the perovskite crystal, which commonly includes MA, formamidinium (FA or $CH(NH_2)_2$), Iodine (I) and Br. With a typical band gap of around 1.5 eV, metal-organic halide perovskites are highly-absorbent materials that convert a significant portion of the solar spectrum into photocurrent.[22] Their large charge-carrier mobilities also make them capable of effectively transporting the resultant photocurrent to charge-selective electrodes. The maximum energy that perovskite active layers extract from incoming photons is exceptional, producing open-circuit voltages with less than 400 meV lost from their bandgap.[21,22] By comparison, this is already lower than established CdTe technologies, which lose approximately 590 meV.[21] Like CdTe, the best PSCs contain a toxic element; lead. There have been many attempts to change the perovskite composition with the goal being improving PCE and incorporating a metal less toxic than Pb with no carcinogenic manufacturing bi-products.[9,26–28] The perovskite community has demonstrated that a catastrophic failure of perovskite solar cell encapsulation would not cause toxic concentrations of lead in the ground. In fact, the quantities of lead involved are considered relatively limited, and failure models indicate it would disperse easily, preventing lead from accumulating in dangerous concentrations. It is likely inclusion of lead will not cause a socio-political barrier preventing PSCs from becoming commercialised.[29–31]

PSCs have had the advantage of immediate integration into the two decades of engineering already completed on their predecessors: DSSC and OPVs. PSCs utilise the similar device architectures to these predecessors, allowing the chemical and electronic understanding of charge transport layers, electrode contacts, transparent conducting oxides (TCOs), and interface physics to be directly applied to PSC development.[9] Both organic and perovskite PV have another significant advantage; by adjusting perovskite formulations, it is possible to tune the perovskite band gap and collect photons that silicon solar cells (with a 1.1 eV band gap) cannot. Therefore, they can be stacked with other solar cells or form tandem solar cells with multiple light-absorbing layers. The company Oxford PV have recently reported a 1cm^2 27.3 % PCE silicon-perovskite tandem solar cell.[32] By comparison, the world-record single junction silicon solar cell has a PCE of 26.7 %. If the cost of fabricating silicon-perovskite tandems can be brought to grid-parity, it would make them a highly competitive PV technology. Dual organic and dual perovskite tandem solar cells have also been demonstrated. A 2-terminal organic tandem with certified 17.3 % PCE has (at the time of writing) just been reported.[33] Additionally, a 4-terminal perovskite-only tandem with a narrow back 1.25 eV and wide front 1.75 eV band gap material has been reported to exceed 23 % PCE.[34] There are other solar cell architectures that can be developed to increase the PCE of thin-film PV. For example, back-contact solar cells have front-facing absorbing layers, with all charge-collecting electrodes located at the rear of cell. This architecture is ideal for maximising the amount of light reaching the active layer. Most typical single junction and tandem flat solar cells discussed earlier utilise substrates and TCOs and charge-transport layers that absorb and waste a portion of the incoming light.[35–37]

Despite all these advantages of perovskite light-absorbing layers, any conversation based around the commercial viability of perovskite PV (as recently as four years ago, and perhaps still today) would have been centred on one topic - stability. Many members of the established PV community were apprehensive of the outstanding performance of perovskite-based solar cells. For many, it was a case of viewing the perovskite as a bad battery or capacitor. There were even doubts about whether the current reportedly produced from perovskite solar cells was exclusively a photocurrent - and if so, there were worries about how long it would last. These suspicions were not unfounded. Perovskite solar cells function when under illumination, yet perovskite active materials and charge-transport layers are often susceptible to degradation caused by UV light.[38] Perovskites are water soluble and they form reversible and irreversible hydrated crystal structures that do not efficiently generate photocurrent in the presence of water.[21,39–41] Perovskites and charge-transporting materials are often more susceptible to light and water in the presence of oxygen. Typical methylammonium lead iodide perovskite active layers also undergo a crystal lattice transition (away from the ideal tetragonal crystal phase at 54 °C), which lies within the typical operating conditions of a solar cell.[39,42–44] Taken together, it is of little surprise that many research laboratories observed instability in both perovskite films and perovskite solar cells.

Fortunately, the development of more complex perovskite compositions involving the temperature-stable cation FA, the combination of multiple organic and inorganic cations, the use of both I and Br, and the introduction of 2D materials into the perovskite active layer have all resulted in ever-increasing stability of PSCs. The most stable PSCs have now shown no loss in performance over 10,000 hours under constant simulated solar illumination.[45]

1.1: Thesis Motivation

To develop a commercialised perovskite solar product, the PV scientific community must develop materials and fabrication processes that maintain both high efficiency and long-term stability. In addition to this, those same materials and processes must be cheap, scalable, and transferable to high-throughput manufacturing techniques. To this end, this thesis focuses on such key requirements. Solar cell fabrication recipes for different device architectures are established, adapting the work of many research groups to produce devices with high power conversion efficiency. An ideal reference perovskite solar cell is fabricated and then altered to investigate several organic and inorganic charge-transport materials. To investigate how altering the fabrication of perovskite solar cells affects their long-term stability, an effective encapsulation system is developed. Finally, a novel, flexible, back-contact, scalable, and cheap perovskite solar module architecture is investigated.

1.2: Thesis Overview

Chapter 2 details background theory covering the operation of a solar cell. The optoelectronic properties of metal-organic hybrid perovskite materials and charge transporting semiconductors that make up a perovskite solar cell are also discussed. To give context to Chapters 4-7, The arrival of the perovskite photovoltaic community is summarised, and a brief review of perovskite fabrication techniques, perovskite stability, and back-contact perovskite solar cells is provided.

Chapter 3 focuses on the fabrication and characterisation techniques that enable the investigation of alternative perovskite active materials, transport layers, encapsulants, and device architecture. The main techniques used to deposit thin-films (spin coating and evaporation) are described in the context of making perovskite solar cells. The majority of work provided in the remaining chapters is reliant on current-voltage measurements of perovskite solar cells, which are described in Chapter 2. Current-voltage responses are used in combination with microscopy, spectroscopy, and profilometry (described in Chapter 3) of individual layers and entire perovskite cells in order to understand their operation and optimise them for maximum PV performance.

Chapter 4 discusses perovskite solar cell optimisation utilising a PCDTBT carbazole-based conjugated polymer as a hole-transport layer. The PCDTBT is doped with the same dopants used in the ubiquitous hole-selective small molecule spiro-OMeTAD. It is found that the p-doping increases the conductivity of PCDTBT by a factor of 10^5 times compared to its undoped conductivity, and improves the photostability of the PCDTBT. Demonstrating the hole transport capabilities of PCDTBT opens an avenue for many similar conjugated polymers to be utilised as PSC charge-transport layers. It is observed that a degradation in transparent conductive oxides is linked to the inclusion of Li-TFSI. This, in combination with perovskite literature, suggests that organic dopants should be avoided, and that it is extremely important to demonstrate perovskite solar cell stability when trying any new alternative transport layers.

Chapter 5 addresses the issue of optimization of perovskite efficiency being a separate goal to optimization perovskite stability. In Chapter 5, perovskite solar cells are encapsulated using a multi-layer technique (where a polyvinylpyrrolidone or alumina interlayer is used between the PSC and UV-curable epoxy), protecting the perovskite from the epoxy before it is fully cured. Long-term stability is achieved, but only for solar cells that are processed in certain ways. It is found that a solvent-anneal step (used to grow large perovskite grains) creates solar cells with good initial performance, but poor operational stability. The polymer poly-TPD is shown to enable high performance of the PSCs used in this study, as its hydrophobic nature prevents moisture-trapping and ingress inside the multi-layer encapsulation.

Chapter 6 explores the use of low-cost metal oxide transport layers in perovskite solar cells. A novel high-speed reactive electron-beam process is used to evaporate neat nickel and titanium pellets, combining them with oxygen to produce nickel oxide and titanium dioxide thin films. This process is compatible with substrates that cannot be exposed to high temperatures. As such, evaporation of metal oxides is presumed to be compatible with roll-to-roll deposition involving flexible polymeric substrates. This process lays the foundation for the final chapter, which focuses on new a perovskite solar cell architecture.

Chapter 7 combines the reactive electron-beam process (demonstrated in **C**hapter 6) with a directional evaporation technique, whereby nickel, nickel oxide, titanium and C_{60} are all directionally-deposited on the walls of ‘V’ shaped polymeric grooves. These grooves (coated with charge selective materials) form the base of horizontally-spaced solar cells. After deposition of a perovskite, these grooves are flexible, free from rare-metals and form back-contact solar cells. In addition to this, the grooves can be patterned to obtain integrated, series interconnected perovskite mini-modules, building voltage across multiple grooves. The entire fabrication of the flexible grooves is scalable and fast, making it an ideal architecture for roll-to-roll production.

The results of this thesis are summarised in **Chapter 8**, along with comments on how this work has inspired other research and suggestions for other future projects. Taken together, this research takes PSCs closer towards commercialisation.

1.3: References

[1] T. F. Stocker, Q. Dahe, G.-K. Plattner, L. V. Alexander, S. K. Allen, N. L. Bindoff, F.-M. Bréon, J. A. Church, U. Cubash, S. Emori, P. Forster, P. Friedlingstein, L. D. Talley, D. G. Vaughan, S.-P. Xie, *Clim. Chang. 2013 Phys. Sci. Basis. Contrib. Work. Gr. I to Fifth Assess. Rep. Intergov. Panel Clim. Chang.* **2013**, 33.

[2] J. Cook, N. Oreskes, P. T. Doran, W. R. L. Anderegg, B. Verheggen, E. W. Maibach, J. S. Carlton, S. Lewandowsky, A. G. Skuce, S. A. Green, D. Nuccitelli, P. Jacobs, M. Richardson, B. Winkler, R. Painting, K. Rice, *Environ. Res. Lett.* **2016**, *11*.

[3] Key World Energy Statistics Agency for Natural Resources and Energy, *IEA Int. Energy Agency* **2016**.

[4] R. Perez, M. Perez, *Int. Energy Agency SHC Program. Sol. Updat.* **2015**, *62*, 4.

[5] R. J. Brulle, *Clim. Change* **2018**, *149*, 289, DOI 10.1007/s10584-018-2241-z.

[6] Y. Karneyeva, R. Wüstenhagen, *Energy Policy* **2017**, *106*, 445.

[7] K. Zweibel, *Energy Policy* **2010**, *38*, 7519.

[8] G. Hodes, *Science,* **2013**, *342*, 317.

[9] M. A. Green, A. Ho-Baillie, H. J. Snaith, *Nat. Photonics* **2014**, *8*, 506.

[10] Bloomberg New Energy Finance, **2017**, 6.

[11] P. Docampo, J. M. Ball, M. Darwich, G. E. Eperon, H. J. Snaith, *Nat. Commun.* **2013**, *4*, 2761.

[12] W. F. Pickard, *Energy Policy* **2017**, *107*, 488.

[13] Renewable Energy Auctions, *International Renewable Energy Association* **2016**.

[14] S. Rao, A. Morankar, H. Verma, P. Goswami, *J. Appl. Chem.* **2016**, *2016*, 1.

[15] F. C. Krebs, *Sol. Energy Mater. Sol. Cells* **2009**, *93*, 394.

[16] B. Azzopardi, C. J. M. Emmott, A. Urbina, F. C. Krebs, J. Mutale, J. Nelson, *Energy Environ. Sci.* **2011**, *4*, 3741.

[17] S. Lizin, S. Van Passel, E. De Schepper, W. Maes, L. Lutsen, J. Manca, D. Vanderzande, *Energy Environ. Sci.* **2013**, *6*, 3136.

[18] N. Espinosa, R. García-Valverde, A. Urbina, F. C. Krebs, *Sol. Energy Mater. Sol. Cells* **2011**, *95*, 1293.

[19] S. Berny, N. Blouin, A. Distler, H. J. Egelhaaf, M. Krompiec, A. Lohr, O. R. Lozman, G. E. Morse, L. Nanson, A. Pron, T. Sauermann, N. Seidler, S. Tierney, P. Tiwana, M. Wagner, H. Wilson, *Adv. Sci.* **2015**, *3*, 1.

[20] A. Kojima, K. Teshima, Y. Shirai, T. Miyasaka, *J. AM. CHEM. SOC*. **2009**, *131*, 6050–6051

[21] H. J. Snaith, *J. Phys. Chem. Lett* **2013**, *4*, 3623–3630.

[22] H. J. Snaith, *Nat. Mater.* **2018**, *17*, 372.

[23] NREL, "NREL Efficiency Chart (Accessed August 2018)", can be found under http://www.nrel.gov/ncpv/images/efficiency_chart.jpg, **2018.**

[24] H. Zhang, H. Yao, J. Hou, J. Zhu, J. Zhang, W. Li, R. Yu, B. Gao, S. Zhang, J. Hou, *Adv. Mater.* **2018**, *1800613*, 1.

[25] Z. Xiao, X. Jia, L. Ding, *Sci. Bull.* **2017**, *62*, 1562.

[26] M. Grätzel, *Nat. Mater.* **2014**, *13*, 838.

[27] P. V. Kamat, J. Bisquert, J. Buriak, *ACS Energy Lett.* **2017**, *2*, 904.

[28] A. Abate, *Joule* **2017**, *1*, 659.

[29] J. Gong, S. B. Darling, F. You, *Energy Environ. Sci.* **2015**, *8*, 1953.

[30] J. M. Kadro, A. Hagfeldt, *Joule* **2017**, *1*, 29.

[31] B. Hailegnaw, S. Kirmayer, E. Edri, G. Hodes, D. Cahen, *J. Phys. Chem. Lett.* **2015**, *6*, 1543.

[32] "Oxford PV sets world record for perovskite solar cell," can be found under https://www.oxfordpv.com/news/oxford-pv-sets-world-record-perovskite-solar-cell, **2018**.

[33] L. Meng, Y. Zhang, X. Wan, C. Li, X. Zhang, Y. Wang, X. Ke, Z. Xiao, L. Ding, R. Xia, H. Yip, Y. Cao, Y. Chen, *Science* **2018**, *2612*, 1.

[34] D. Zhao, C. Wang, Z. Song, Y. Yu, C. Chen, X. Zhao, K. Zhu, Y. Yan, *ACS Energy Lett.* **2018**, *3*, 305.

[35] Z. Hu, G. Kapil, H. Shimazaki, S. S. Pandey, T. Ma, S. Hayase, *J. Phys. Chem. C* **2017**, *121*, 4214.

[36] Q. Hou, D. Bacal, A. N. Jumabekov, W. Li, Z. Wang, X. Lin, S. H. Ng, B. Tan, Q. Bao, A. S. R. Chesman, Y.-B. Cheng, U. Bach, *Nano Energy* **2018**, *50, 710.*

[37] A. Jumabekov, E. Della Gaspera, Z. Xu, A. Chesman, J. van Embden, S. Bonke, Q. Bao, D. Vak, U. Bach, *J. Mater. Chem. C.* **2016**, *4*, 3125.

[38] T. Leijtens, G. E. Eperon, S. Pathak, A. Abate, M. M. Lee, H. J. Snaith, *Nat. Commun.* **2013**, *4*, 2885.

[39] G. Niu, X. Guo, L. Wang, *J. Mater. Chem. A* **2015**, *3*, 8970.

[40] K. Miyano, M. Yanagida, N. Tripathi, Y. Shirai, *Appl. Phys. Lett*. **2015**, *106,* 093903

[41] A. Leguy, Y. Hu, M. Campoy-Quiles, M. I. Alonso, O. J. Weber, P. Azarhoosh, M. van Schilfgaarde, M. T. Weller, T. Bein, J. Nelson, P. Docampo, P. R. F. Barnes, *Chem. Mater.* **2015**, *27,* 3397−3407

[42] K. Wu, A. Bera, C. Ma, Y. Du, Y. Yang, L. Li, T. Wu, *Phys. Chem. Chem. Phys.* **2014**, *16*, 22476.

[43] S. A. Bretschneider, J. Weickert, J. a. Dorman, L. Schmidt-Mende, *APL Mater.* **2014**, *2*, 040701.

[44] A. Poglitsch, D. Weber, *J. Chem. Phys.* **1987**, *87*, 6373.

[45] G. Grancini, C. Rolda´n-Carmona, I. Zimmermann, E. Mosconi, X.Lee, D. Martineau, S. Narbey, F. Oswald, F. De Angelis, M. Grätzel, M. K. Nazeeruddin, *Nat. Coms.* **2017**, *8,* 15684.

Chapter 2

Background Theory

2.0: An Introduction to Photovoltaics

Solar cells, also known as photovoltaics (PV), convert light into electricity. First observed in 1839 by Edmond Becquerel,[1] the photovoltaic effect is a process in which semiconducting materials can generate photocurrent and photovoltage when under illumination. In order to understand the photovoltaic effect, it is important to establish some of the underlying and related physical concepts, some of which will be expanded on throughout this chapter.

2.0.1: A Quick Overview

The photoelectric effect is a similar phenomenon to the photovoltaic effect, whereby light causes the liberation of charge carriers from a material. Such charge carriers are only emitted from the material when the energy (E_γ = hf) of the incoming light exceeds a material dependent value, known as the material's work function (Φ). The photoelectric effect is historically important; it is experimental evidence for the particle like (part of the wave-particle duality) nature of light, but the photoelectric effect causes ejection of free charges and does not make use of photons to generate useable current.[2] Unlike conductors, which have fully delocalised free charges, or insulators, which have very few delocalised free charges, semiconductors have a number of delocalised free charges and electronic properties between that of a conductor and insulator. In solid-state physics these properties are best explained using quantum mechanical electronic band structure, which describes the energetic positions that electrons can take within a solid. Whilst at room temperature intrinsic semiconductors have bands that at any one time are statistically likely to be partially filled with electrons. The outer shell valence elections of a material form a band of the highest filled electron energy levels known as the valence band (VB). The VB is split from a lowest unoccupied energy band, known as a conduction band (CB), by a band gap of unavailable electron energies with size E_G. Incident photons with energies equivalent to or exceeding E_G can excite electrons into or above the CB. Electrons excited above the CB have excess thermal energy and can relax back down to the CB edge through thermalization.[3,4]

Valence and conduction bands are terms typically used to describe the electronic band structure of inorganic semiconductors, where the crystal structure of the semiconductor forms the band structure of the solid material from the overlapping electronic structure of its constituents' atoms.[4] Photovoltaics can also involve the use of organic semiconductors. Organics do not have band structures defined by repetitive crystal structures, but instead have band-like structure defined by the molecular orbital bonding of constituent organic atoms, where highest occupied molecular orbital (HOMO) and lowest unoccupied molecular orbital (LUMO) levels are analogous to the valence and conduction bands of inorganics respectively.[5,6]

In all cases, the photoexcitation process can be described simply as an electron being photoexcited across the band gap, leaving behind the absence of an electron, a quasiparticle known as a hole. This electron hole pair will either remain bound as a quasiparticle known as an exciton, or will quickly disassociate into a free election and hole.[7,8] The excitation and transport of a photogenerated electron through the band structure of inorganic, organic, and hybrid materials is discussed in more detail later in this chapter.

To complete the photovoltaic process and generate a photocurrent with a photovoltage electromotive force (with charges that recombine to do work later), the electron and hole must be dissociated and split apart selectively, exiting the photoactive semiconductor. Free charges will be affected by two different processes: diffusion of charges driven by charge concentration, and the drift of charges caused by an in-built or external electric field.[9] An in-built electric field is generated when a semiconductor with electronic band structure favourable accepting electrons (a p-type acceptor) is brought into contact with a semiconductor that favourably donates electrons (an n-type donor). The resultant p-n junction reaches an energetic equilibrium with a central region known as the space charge region or depletion region, which is drained of intrinsic charge carriers - resulting in a strong electric field.[9] Unhindered charge selective extraction also requires interfaces with semiconductors that have a band structure causing well aligned affinity (relative to the photoactive semiconductor) for one charge (e.g. positive hole) and unaligned affinity for the other charge (e.g. negative electron).[10,11] If the photogenerated charges remain as a strongly bound exciton, then the exciton will diffuse until it recombines or reaches an interface with a material that has a band structure that makes it energetically favourable for the exciton to disassociate across the interface, rather than remain as a bound state. Equation 1 below describes the resultant transported electron or hole current ($J_{n/p}$), where n is electron density, p is hole density, q is the electronic charge, $\mu_{n/p}$ is the electron or hole mobility and $D_{n/p}$ is the electron or hole diffusivity, $\boldsymbol{E}$ is the electric field, and $\frac{dn/p}{dx}$ is the charge density concentration gradient. Diffusivity is also provided below.

$$J_{n/p} = (n/p)\mu_{n/p} q\boldsymbol{E} \pm qD_{n/p}\frac{dn/p}{dx} \qquad D_{n/p} = \mu_{n/p}\frac{K_B T}{q} \qquad (Eq. 1)$$

The former term describes the drift whilst the later described diffusion. Note that functionality of perovskite solar cells (PSCs) is still under investigation. More detail on these processes, particularly in the context of perovskite active layers, is given later in this chapter.

2.0.2: Absorbing Solar Irradiation – The Shockley–Queisser Limit

The formation of a band gap in semiconductors is vital for the absorption of light. However, only some semiconductors have an ideal band gap for PV applications. Above the atmosphere the sun (a blackbody with a temperature of 5870K) irradiates the Earth with an extra-terrestrial spectral irradiance known as the AM0. The solar irradiance we receive on the Earth's surface is not uniform, but a standardised spectral irradiance known as the AM1.5 characterises the amount of average sunlight available at all wavelengths that reach the Earth's surface at mid-latitudes, after some light is attenuated and absorbed by 1.5 thickness of atmosphere (due to an incident angle of sunlight of 48.2° at mid-latitudes). Figure 1 shows these standardised spectral irradiances (as a function of wavelength λ or photon energy E_λ) and includes the AM1.5 Global and AM1.5 Direct, whereby the AM1.5 Direct is useful for concentrator solar cells that make use of diffuse circumsolar light from a solid angle (2.5° half angle) centred around the sun.

For flat solar cells, like those used in the thesis, the AM1.5 global is the best estimation of the spectra of light that the solar cells would receive when under operation. Standard intensity of sunlight on a solar cell is measured in suns, with 1 sun equivalent to 1000 Wm^{-2} of AM1.5 illumination.[12,13] The quality of a solar cell is usefully described by a power conversion efficiency (PCE), which is a percentage based on the ratio of power generated by the solar cell versus the power of incident illumination on the solar cell. PCE is explained in more detail later on in this chapter.

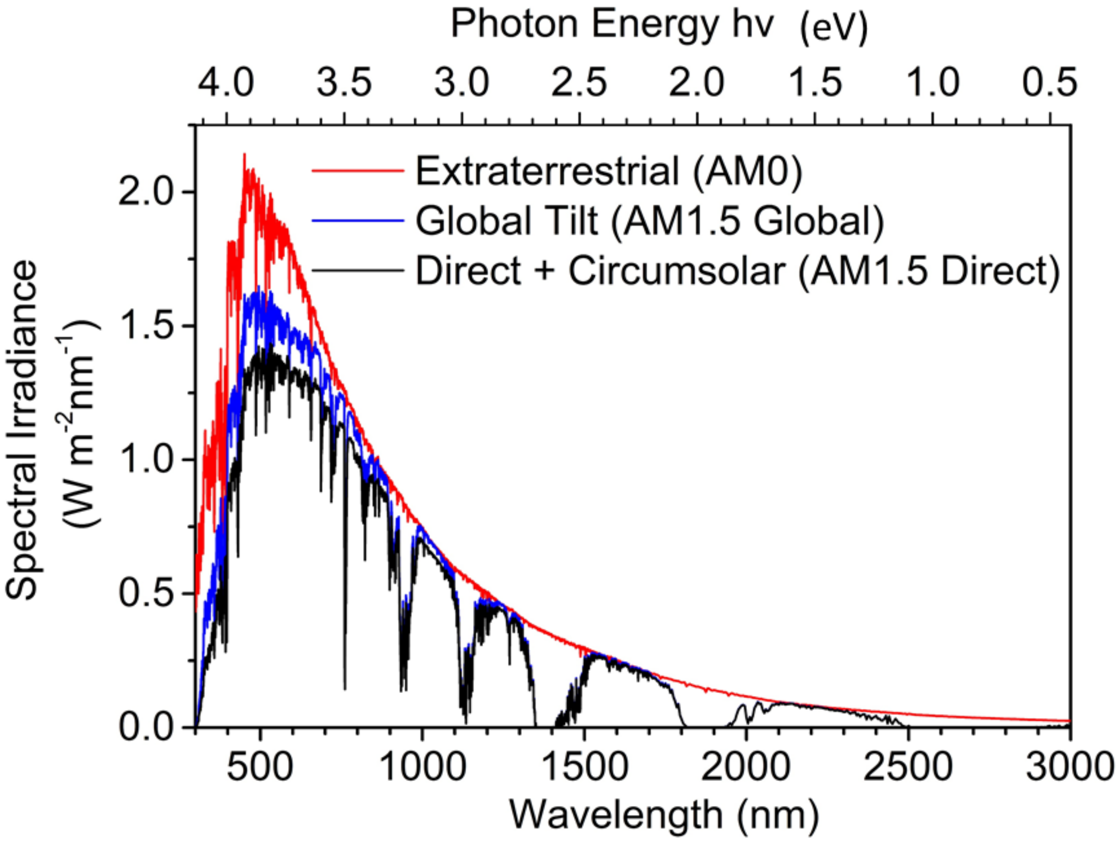

Figure 1: *From NREL.*[13] *Standardised spectral irradiance received outside the Earth's atmosphere (AM0), and on the surface of Earth at mid latitudes, defined by light irradiating at a zenith angle of 48.2°, passing through 1.5 atmosphere thickness, (AM1.5). The AM1.5 spectra is calculated in two ways: AM1.5 Global is used for most flat solar cells and considers the Earth as plane with a horizontally tilted steradian field of view, AM1.5 Direct is commonly used for solar concentrators and considers the direct sunlight incident on a plane normal to the Sun, collecting diffuse circumsolar light from a solid angle (2.5° half angle) centred around the Sun.*

A PV semiconductor with a small band gap would satisfy $E_\gamma \geq E_G$ for a large portion of the AM1.5 spectrum, and therefore would absorb the majority of incoming photons. Conversely, a large band gap would lead to only a small portion of short wavelength, high-energy sunlight being able to excite charges from the valence band. Unfortunately, this is not an indicator that all PV should be based on small band gap semiconductors as photons that exceed the energy of the band gap ($E_\gamma > E_G$) do not directly convert that energy into more free charges, rather they just impart increased kinetic energy on the same number of charges. Charge excitation occurs, but the excess energy is wasted as thermal energy as the highly excited electrons thermalize back down to the conduction band edge. There are ways of harvesting a small portion of the resultant heat, but ultimately the PCE of a solar cell is dependent on this balance between loss of photon energy as heat against absorbing as much of the spectral irradiance as possible. No matter what the band gap of the solar cell, a solar cell under illumination will always radiate heat to reach equilibrium with its environment. This understanding of detailed balance can be combined with a calculation of potential wasteful recombination of photogenerated charges (discussed later), to calculate a theoretical maximum PCE of solar cells as a function of band gap, known as the Shockley–Queisser (S-Q) limit.[14,15] Figure 2 presents the S-Q limit for solar cells with band gaps from 0.5-2 eV. As can be seen the maximum efficiency approaches 34 % for a semiconductor with a 1.34 eV wide band gap.

This thesis focusses on the use of PSCs. It is apt to note that current PSCs with E_g ~1.5 eV already reach 75 % of their estimated maximum possible efficiency; a value higher than all alternative PV materials aside from crystalline silicon (c-Si), gallium arsenide (GaAs), and gallium indium phosphide (GaInP). Ubiquitous perovskite PV materials are not currently located around the ideal 1.34 eV band gap, however, perovskites have band gap tuneable crystal structures that are elaborated upon later in this chapter.[14,15] The S-Q limit is the expected PCE limit for a single junction device (a solar cell or module with only one photoactive semiconductor band gap). Solar cells can also be stacked on top of each other and designed to collect photons of different energies by having multiple semiconductors with different band gaps. Henry Snaith first popularised a major advantage of perovskites – that their tuneable band gap allows them to potentially collect photons with wavelengths of light which the major commercial solar cells such as c-Si (1.1eV) and CIGS do not.[16] Tandem silicon-perovskite and tandem band gap tuned perovskite-perovskite solar cells are both possible ways to break the S-Q limit and achieve higher PCEs.[17,18]

It is estimated that a tandem perovskite/c-Si cell that can limit its parasitic losses will reach 29.6 % PCE.[16] Further studies using an oscillator model based on optical n-k data predicted a similar 29 % PCE for a perovskite/CIGS tandem cell.[19,20] Tandems are often referred to as monolithic 2-terminal devices (with only 2 metal electrodes and all layers touching) and stacked 4-terminal devices, where two solar cells are placed on top of each other and connected via two sets of metal contacts. Oxford-PV have very recently (at the time of writing) fabricated a 27.3 % PCE silicon-perovskite tandem solar cell with a 1 cm^2 active area, but have not disclosed information on the materials involved.[17] A perovskite-only 4-terminal tandem with a $(FASnI_3)_{0.6}(MAPbI_3)_{0.4}$ 1.25 eV narrow-bandgap bottom cell and a $FA_{0.8}Cs_{0.2}Pb(I_{0.7}Br_{0.3})_3$ 1.75 eV wide-bandgap perovskite top cell has also demonstrated 23 % PCE.[18]

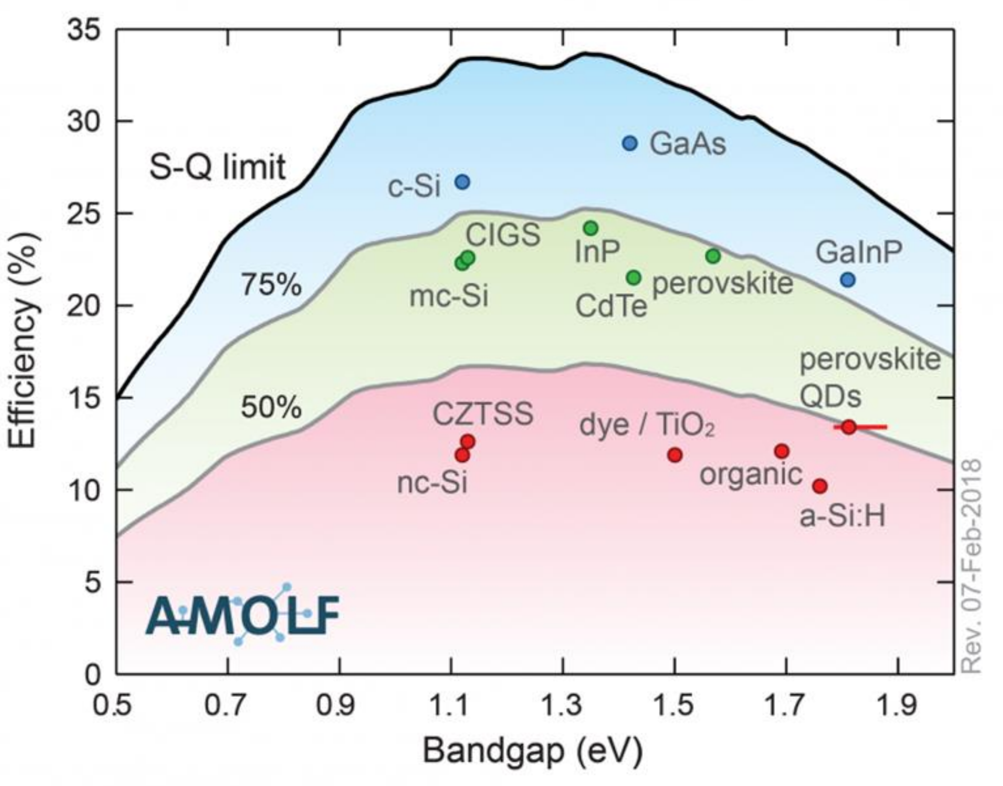

Figure 2: *From Science, A. Polman et al.*[15] *The Shockley-Queisser detailed-balance limit. PSCs are approaching 75% of the Shockley-Queisser limit.*

2.1: Characterising Solar Cells and Building Solar Modules

2.1.1: Equivalent Circuit Model

The nature of a simple PV device is best modelled by the Shockley ideal photodiode equation (Equation 2), and the solar cell equivalent circuit (Figure 3a). Here J_{ph} is the photocurrent provided by the photoactive absorbing layer, the J_D diode current (also known as dark diode current) and J_0 the diode reverse saturation current. As the applied voltage (V) increases, the diode current (which opposes the photocurrent) exponentially increases.[9]

$$J(V) = J_{ph} - J_D = J_{ph} - J_0 \left[\exp\left(\frac{eV}{K_B T}\right) - 1\right] \qquad (Eq. 2)$$

When solar cell parasitic losses and a non-ideal diode are considered, the model transforms into Equation 3. R_S is the series resistance that considers all processes that oppose the photocurrent generation and extraction, R_{SH} is the shunt resistance against all of the parallel circuit pathways that bypass one or more of that layers that generate or select charges, K_B is the Boltzmann constant, and T is the temperature (in kelvin). The ideality factor n is mostly a measure of the type recombination occurring in solar cell. For an ideal diode with $n=1$, all recombination must occur outside the depletion region of the photoactive absorbing layer. For absorbing layers with charge recombination or diodes with energetic barriers (for example poorly aligned metal-semiconductor Schottky diodes, described later in this chapter) the ideality factor can exceed n = 2.

$$J(V) = J_{ph} - J_0 \left[\exp\left(\frac{e(V + JR_S)}{nK_B T}\right) - 1\right] - \frac{V + JR_S}{R_{sh}} \qquad (Eq. 3)$$

It is widely agreed that this simple circuit model is not able to fully characterise a perovskite solar cell (Due to ion migration and charge transport modulations at charge extraction interfaces – see Chapter 2.6). Whilst an accurate model is still debated upon, a soon to be published study by Moia *et al.* "*Ionic-to-electronic current amplification in hybrid perovskite solar cells: ionically gated transistor-interface circuit model explains hysteresis and impedance of mixed conducting devices*" (as listed in my author contributions) will likely be of interest to any reader interested in perovskite PV device functionality and circuit modelling.

In the following section we discuss all the important solar cell metrics that contribute to the final power conversion efficiency of a solar cell.

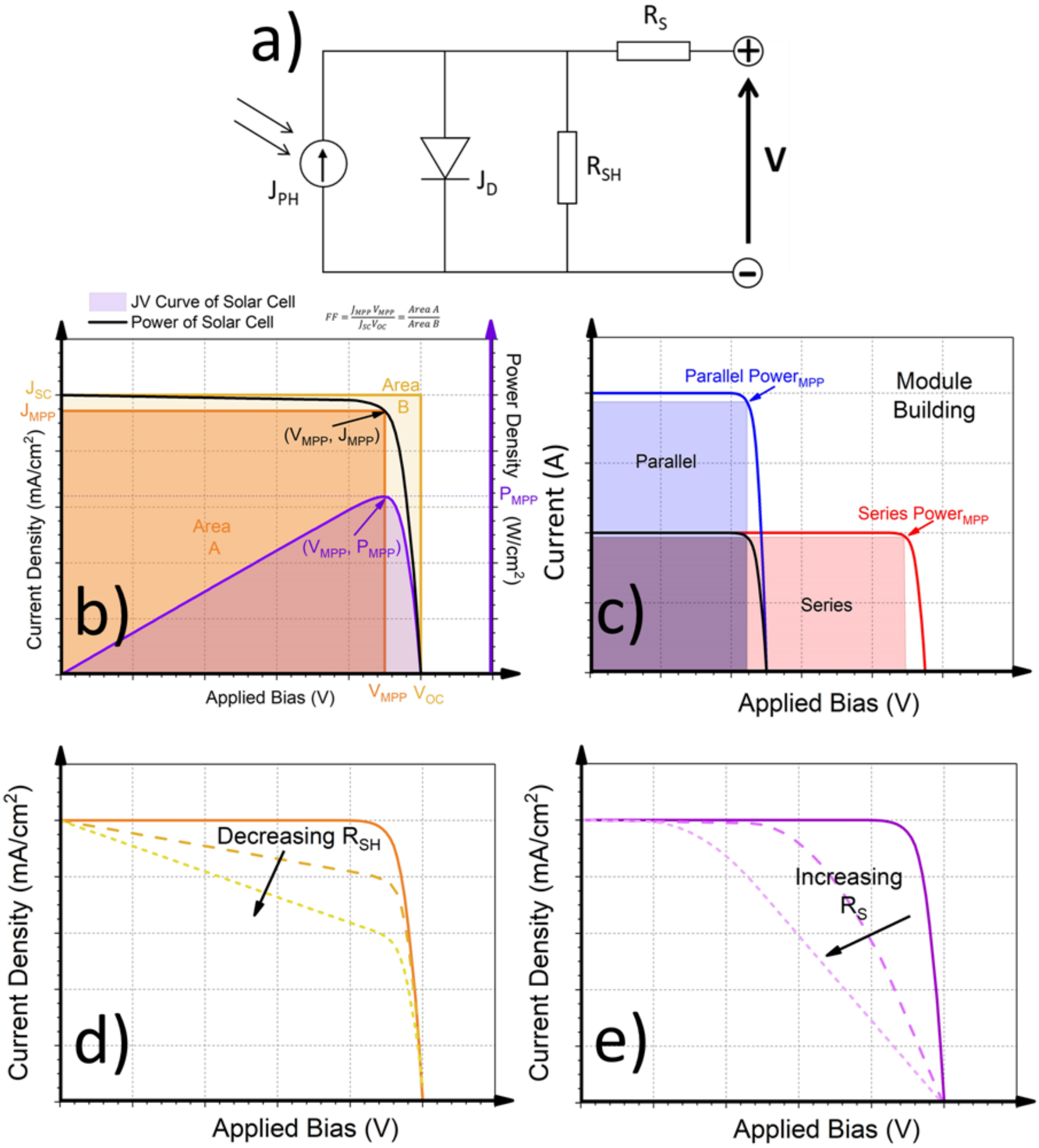

Figure 3: *Solar cell operation and response with, a) solar cell diode circuit generating photovoltage V with J_{PH} photocurrent density, J_D dark diode leakage current, R_{SH} shunt resistance of parallel circuit pathways, and R_S series resistance opposing generated photocurrent. b) JV curve and power density output of a solar cell at applied bias V. The ratio of shaded area A and B can be used to calculate the fill factor of the solar cell, which determines the maximum power point voltage (V_{MPP}) of the maximum power point (P_{MPP}). c) Current-voltage curves of modules made of equivalent solar cells connected in either series or parallel and their associated maximum power points. d) JV curves indicated with dotted curves demonstrate decreasing R_{SH}. e) JV curves indicated with dotted curves demonstrate increasing R_S.*

2.1.2: Current-Voltage Measurements

Current-voltage sweeps are used to determine the device performance metrics of a solar cell. A solar cell with a known active area is connected to a source measure units and the current output is measured at different applied voltage biases. Figure 3b shows a typical current-voltage sweep for a solar cell, where the direction of photocurrent is taken as positive. The current-voltage sweep shows the position of key performance metrics: short circuit current density (J_{SC}) and open circuit voltage (V_{OC}), with other metrics described below.

In the context of perovskite PV, there is a requirement for illumination masks to accurately measure the active area of the of solar cell. There is also a significant sweep dependence on the speed at which the sweep is taken. PSC current-voltage sweeps can be significantly affected by the recent history of a solar cell, including the illumination and voltage biasing conditions of the cell prior to sweep. An effect known as current-voltage sweep hysteresis, where the forward and reverse sweeps of a PSC are not equivalent is reviewed later in this chapter.

As such there is an expectation to characterise PSs with stabilised current measurements, whereby the short term (1-10 minute) current output of the solar cell is recorded whilst holding at a constant voltage or tracking the voltage that provides the maximum power of the solar cell.

There have been several key reviews of checklists for accurate and reliable solar cell testing in PV research. Nature family publications now require authors to provide a checklist form upon submission.[21] An interpretation of these requirements is listed below:[22–26]

- Proper filters and diffusion optics should be used to produce simulated AM1.5 illumination. If light emitting diodes are used, or there is a significant spectral mismatch, it should be clearly stated.
- Illumination sources should be regularly calibrated, calibration reference cell spectral mismatch should be declared. The source optics should be kept aligned and cleaned.
- An illumination mask with a known area should always be used and declared.

- If more than one active area is illuminated on a single substrate then the device must be tested for cross-talk between those areas to make sure that more than one active area is not contributing to photocurrent.
- Divergent and diffuse light should be minimised as light can often be scattered in through the edges of devices. Both the device layout and testing setup should be designed to minimise this.
- Current-voltage sweeps should be consistent across devices which are being compared, and (where possible) performed at different scan speeds and should be cycled several times to investigate the effect of multiple sweeps. All sweeps speeds and direction of sweeps must be declared.
- Any preconditioning based on voltage or illumination and storage should be declared. PSCs have been known to improve under storage or illumination.
- Confirmed PCE and J_{SC} require a stabilised current and power output measurement OR a maximum power tracking measurement.
- The J_{SC} should be double checked with integrated internal or external quantum efficiency measurements when possible (explained in the following sub-section).

Short Circuit Current (J_{SC})

It is important to clarify the difference between current and current density. In most common engineering and PV physics nomenclature, I is ascribed to current, with units A (amps) and J ascribed to current density, with units $mAcm^{-2}$. Although they are often used interchangeably when describing the physics of solar cells, the current density is used for current-voltage sweeps when the illuminated area is accurately measured. Current density is usually more accessible as a device metric to compare between different solar cells.

The J_{SC} is the photocurrent density provided by the solar cell when there is no applied voltage. As photocurrent is proportional to incoming photons, it is often higher for photoactive absorbing layers with a small band gap that can collect photons with a wider range of energies.

Photocurrent is reduced by any unwanted charge recombination during charge generation, diffusion of excitons within the active material (if charges are bound), free charge transport within the active material, and charge transfer and extraction between any interfaces into charge transport layers and metal contacts. Maximising the amount of light absorbed by the photoactive layer is the primary way to increase photocurrent. The thickness of the absorbing layer must be thick enough to absorb as many photons as possible, without losing too many photogenerated charges to recombination during the exciton diffusion or free charge transport process. As will be discussed in more detail, perovskites have remarkable charge mobilities, allowing perovskite active layers to extract charge across micron thick films. It is also becoming increasingly accepted that the J_{SC} obtained in perovskites is enhanced due to photon recycling, where long lived free charges recombine with other free charges and generate a photon that later re-excites the perovskite. This allows perovskite thickness to be large, as recombination will not necessarily reduce the J_{SC}.[27]

The optoelectrical properties that affect the J_{SC} can be significantly different for different perovskite materials. Crucially, J_{SC} is dependent on the quality of the perovskite active layer (for example, large crystal grain sizes and low defect densities), which is highly dependent on the fabrication routine for the perovskite.

Open Circuit Voltage (V_{OC})

The V_{OC} is the voltage provided by the solar cell when there is no current flowing. In a typical solar cell, this is when the electric field of the applied voltage cancels out the built-in potential of the solar cell. Assuming that an electric field is required to sweep current out of the photoactive area, then this point of cancellation leads to photogenerated charges that are no longer extracted from the solar cell. In the context of PSCs there is some subtle contention over the exact requirements for charges to be extracted out of a perovskite active layer. These shall be discussed later in the chapter.

As the maximum potential photovoltage is determined by the band gap of the photoactive absorbing layer, the V_{OC} is decreases when the bandgap decreases. In the context of PSCs (and other alternative thin-film PV technologies), the band structure of the perovskite (or other thin-film photoactive absorbing layers) is not the only factor that influences the V_{OC}. The band structure and work functions of the charge selective semiconductors and metal electrodes that are used to extract photocurrent from the solar cell also influence the V_{OC}. Typically, such layers must have a well aligned charge affinity with the active layer without having a step up in energy landscape (which would make it energetically unfavourable for charges to leave the active layer). These layers must be thick enough to form a complete layer to select charges effectively, but they should not be so thick as to cause a loss in charge extraction. Theoretically, device performance metrics would be reduced if the charge selective layers block or accept both charge types. However, PSCs have exhibited some unusual responses to non-ideal alignment of charge selective layers and have even been shown to retain high V_{OC} in the absence of such layers.[28]

The complex surface chemistry and surface defects mean that V_{OC} loss at these contact interfaces is not well understood. Nevertheless, perovskites solar cells have already been demonstrated to have open circuit voltages with less than 400 meV lost from their band gap.[7,16,29]

Fill Factor (*FF*)

The Fill Factor is a percentage calculated from the ratio of area A to area B, shown in Figure 3b. Area B corresponds to a product of the J_{SC} and V_{OC}, whilst area A corresponds to the maximum power point (P_{MPP}) where the product of voltage and current is maximised. Using the notation of the maximum power point voltage (V_{MPP}) and current (J_{MPP}), FF is determined as shown in Equation 4.

$$FF = \frac{J_{MPP}\,V_{MPP}}{J_{SC}V_{OC}} = \frac{Area\ A}{Area\ B} \qquad (Eq. 4)$$

A good solar cell has a high FF, and this is a performance metric that should always be maximised during fabrication optimisation. Good FFs typically approach 80 %; such high values are entirely reliant on obtaining low series resistance and high shunt resistance which are described blow.[9,30]

Power Conversion Efficiency (PCE)

The power conversion efficiency is a percentage of the power that a solar cell can generate relative to the power that is incident onto the solar cell. PCE is calculated either from that ratio of powers, where the power of the incident light is P_{in} and the P_{MPP} is calculated from the product of the V_{MPP} and current J_{MPP}. This is equivalent to calculating the P_{MPP} from the product of V_{OC}, J_{SC} and FF. This is shown in Equation 5.[9]

$$PCE = \frac{P_{out}}{P_{in}} = \frac{P_{MPP}}{P_{in}} = \frac{V_{MPP}J_{MPP}}{P_{in}} = \frac{V_{OC}J_{SC}FF}{P_{in}} \qquad (Eq.5)$$

As can be seen, the PCE is affected by all the other important device metrics (V_{OC}, J_{SC}, and FF), and the parameters that govern those metrics.

Shunt Resistance (R_{SH})

The shunt resistance of a solar cell is the resistance against current bypassing the photoactive absorbing layer or any charge transport layers employed in the solar cell. The higher the shunt resistance the less current leaks through unwanted pathways. In the context of thin-film solar cells, this is most evident in the uniformity of all layers in the solar cell. For example, incomplete layers caused by the roughness of films or pin-holes caused during film fabrication can lead to currents that bypass those layers, resulting in a loss in R_{SH}. In such cases, the incomplete charge transport layers no longer generate maximum V_{OC}.

The shunt resistance manifests itself as the slope of a current-voltage sweep from the current axis, and can be approximated by taking the inverse of the gradient of the sweep at $V=0$. Figure 3d demonstrates the effect of a reduction in shunt resistance on a solar cell's JV characteristics.

Series Resistance (R_S)

The series resistance of a solar cell encompasses all the processes that oppose the extraction of the charge from the solar cell. Primarily this is caused by recombination of charges during generation, and transfer and transport of charges out of the solar cell. This is caused by several factors that are closely related. Series resistance is high if the photoactive or charge extraction layers of the solar cell have low charge carrier mobilities or are too thick even for charge carriers that can travel a long way before being trapped or recombining. If a solar cell has a large density of defects inside the photoactive material, charge extraction layers, or in the interfaces between any layers; (and hence intra band gap traps for photogenerated charges) then they will act to increase the likelihood of charge recombination and decrease the mobility of photogenerated charges. Any energetic barriers caused by non-ideal charge affinity alignment between layers can also prevent photogenerated charges from leaving the solar cell.

The series resistance manifests itself as the slope of a current-voltage sweep from the voltage axis, and can be approximated by taking the inverse of the gradient of the sweep at $V=V_{OC}$.[31] Figure 3e demonstrates the effect of increased series resistance on a solar cell's *JV* characteristics. Large R_S can also cause a loss in V_{OC}.

2.1.3: Solar Cell Recombination and Quantum Efficiency

Important Charge Recombination Types

PSCs have been demonstrated to have a remarkably low rate of trap-assisted recombination.[32–34] Nevertheless, it is important to summarize charge recombination types that contribute to reduced device performance metrics. Recombination due to traps within the band gap are known as non-radiative Shockley Reed Hall recombination.[35] Traps can either be shallow or deep traps. In the context of perovskite photoactive absorbing layer, it has been reported that most intra band gap traps are caused by iodine species due to their low energy of activation. Perovskite crystal lattice (neutral) lead vacancies, negative iodine interstitial ionic species, and positive iodine vacancies have also been considered as trap sites.[32,33] A recently identified advantage of metal-halide perovskites is that accumulated negative iodide vacancies at the interfaces and crystal grain boundaries are neutral when filled with photogenerated charges. These filled traps cause limited hindrance to the highly mobile holes. Perovskite grain boundaries are sites of increased defect densities, which act as regions rich with charge traps. If compact perovskites with large crystal grains and a low density of grain boundaries can be fabricated, then the influence of traps is greatly diminished.

Trapping sites are also common (and are dominant) at the interfaces between perovskite materials and charge transport layers.[33] Recombination does not have to be trap assisted involving only one charge (monomolecular). Two charges (bimolecular) can also recombine radiatively. If two charges are not split apart by diffusion, electric fields or charge selective interfaces, then they can recombine to form another photon. This radiative recombination can either be germinate, involving the original pair of charges (common in strongly bound excitonic systems that cannot split photogenerated charges apart easily), or non-germinate involving charges from other photogeneration sites. In the context of PSCs non-germinate recombination does not contribute significantly to reduced device performance metrics, as photon recycling can regenerate more photogenerated charges. [27]

Quantum Efficiencies

The external radiative efficiency (ERE) is the percentage of total recombination that ends in the emission of light. Despite ERE being more important for light emitting diodes, it has also been identified as a good indicator of an efficient solar cell. Non-radiative trap-assisted recombination pathways should always be minimised, however radiative recombination can lead to photon recycling. As such, whilst it seems counterintuitive, a bright luminescing solar cell is often a good solar cell. Perovskites typically have EREs of up to 4 %, exceeding common EREs of c-Si solar cells.[29]

The internal quantum efficiency (IQE) is a more traditional indicator of solar cell performance. This is the percentage of the number of photons absorbed by the solar cell relative to the number of photogenerated charges extracted from the solar cell. It characterises all of the processes which supress charge generation, transport and transfer from the photoactive absorbing layer.

The external quantum efficiency (EQE) is a more applicable performance metric to compare solar cells. This is the number of extracted charges relative to the number of incident photons at every specific wavelength. It can be calculated from Equation 6, where $P(\lambda)$ is the incident power of photons as a function of wavelength, hc/λ is the energy of one photon, J is the photocurrent and e is the electronic charge.[9]

$$EQE(\lambda) = \frac{Jhc}{P(\lambda)\lambda e} \qquad (Eq. 6)$$

The EQE takes into account all of the photons that do not reach or are not absorbed by the active layer. In the context of thin-film PV, this loss of incident photons is mostly caused by parasitic absorption and reflection occurring from the front facing encapsulation surface and electrodes. Most thin-film PV devices utilise transparent conductive oxides which, despite their name, still have a photon transmission below 90 %. Alternative back-contact solar cell architectures reduce this loss by having all charge selective electrodes positioned at the rear of the solar cell behind the photoactive absorbing layer.[36]

2.1.3: Solar Module Deployment

Solar modules are made from a number of constituent solar cells. Connecting solar cell in series leads to building higher operational voltages. Connecting solar cells in parallel leads to building higher operational photocurrents. Figure 3c demonstrates the resultant current-voltage for both of these cases. Note that whilst current is built in parallel circuits or remains constant in series circuits, current density remains the same for parallel circuits and is reduced for series circuits.

In PV modules, the reported PCE should also include any wasted space that is not the active area of the constituent solar cells. This geometry corrected PCE will be lower than that of an individual solar cell. In real world deployment, solar modules will have inverters that can find and track the maximum power point of the solar modules, isolate and disconnect solar cells that are no longer working, and convert the variable direct current (DC) to alternating current (AC) suitable for grid redistribution or home usage. Solar modules may also have voltage regulators that help provide suitable voltages for storing photocurrent in batteries or running home appliances.

2.2: Electronic Band Structure of Semiconductors

The origin of the energy band gap, conduction bands, valence bands, highest occupied molecular orbitals, and lowest unoccupied molecular orbitals in inorganic and organic semiconductors comes from the nature of molecular orbital bonding, hybridisation, and band formation in repeating crystal structures and in organic materials. This thesis does not include any research regarding organic PV, however it does utilise organic polymers as charge transporting layers. The nature of crystalline solids is discussed here, whereas atomic orbital hybridisation and the formation of band-like structure of organic polymers are outside the relevant scope of this thesis. As such, such processes are briefly described, with citations indicating where they are discussed with clarity and detail.

2.2.1: Atomic Orbitals and Molecular Orbital Bonding

Atoms have a nucleus surrounded by electrons orbitals of different energies where the positions of electrons can only be described as probably distributions. The shape, occupation and properties of electrical orbitals define the properties of the atom and how it interacts with other atoms. Because of the fundamental uncertainty in the exact position of electrons these orbitals are described as electron density clouds.[4,37,38] Electronic orbitals are described by four quantum numbers. To satisfy the Schrödinger equation, ensure quantisation, and obey conservation of observable quantities, these properties may only take a set of discrete values.[4,38] Pauli's Exclusion Principle states that no two electrons can have the same value for all four quantum numbers.[37]

As two atoms are brought close together, their atomic orbitals will overlap. The occupancy, direction and relative energies of the electronic orbitals defines how an atom will bond with other atoms when forming a bond. As two atoms orbitals overlap, their electron wavefunctions may combine (constructively) in-phase, become a bonding orbital, or (destructively) out of phase, creating an antibonding orbital where the lack of electron density between the atoms causes a reduction in Coulombic shielding, which increases the relative energy of the bond.

Due to Pauli's Exclusions Principle, any available additional electrons will be unable to join the already occupied stable bonding orbital and will instead occupy an antibonding orbital.

2.2.2: Band Formation in Crystals

Crystals are structures of tightly ordered atoms arranged in a periodic pattern. This periodicity can be simplified to a unit cell, an example of such a unit cell is given in Figure 4a.

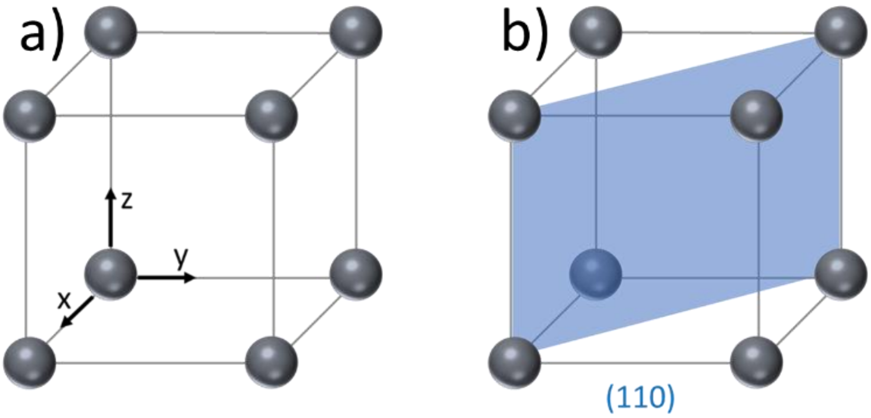

Figure 4: *a) Unit cell for generic simple cubic crystal lattice. b) Unit cell with the [110] plane demonstrated.*

Crystal structures can be identified or 'indexed' by using crystallography to find lattice planes. In Figure 4b a typical lattice plane is shown. Like the crystal itself, this plane passes through the entire solid and periodically interacts with the repeating crystal lattice. Planes are named after their Miller indices, which are the smallest possible ratio of integers of the reciprocal values at the intercepts for the plane at the edge of the unit cell. The lattice plane in Figure 4b has the Miller indices (110).[3]

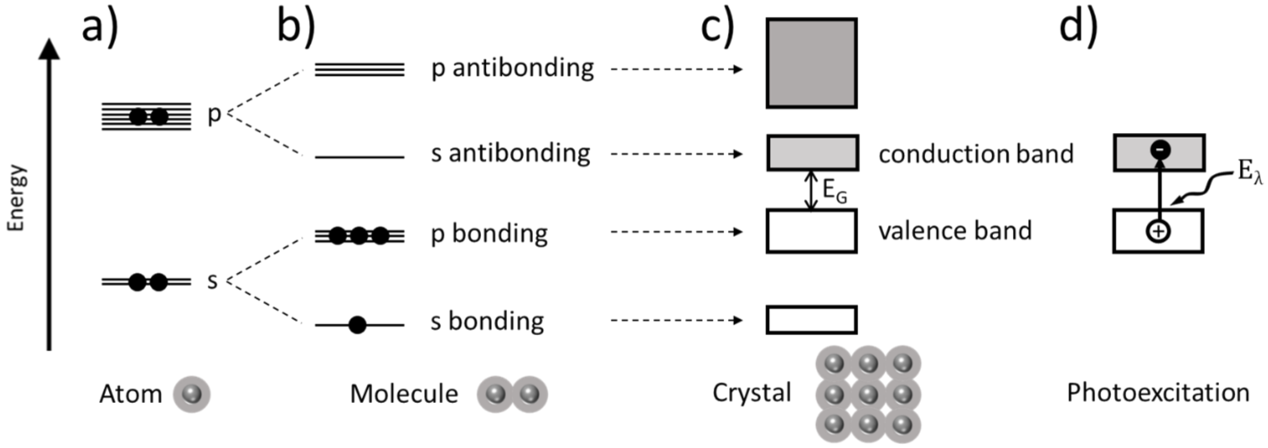

Figure 5: *Adapted from Oxford master series in condensed matter physics, M. Fox.*[39] *From atoms to crystals. a) Relative s and p states of a four-valent atom. b) Relative levels of p and s bonding and antibonding during covalent bonding between these atoms. c) Formation of conduction and valence bands in a crystalline solid made up of many atoms. d) Excitation of a valence electron to the conduction band by a photon where* $E_\lambda > E_G$.

When multiple atoms are brought together to form a molecule, their electronic orbitals overlap. In the process of covalent bonding, hybridisation of *p* and *s* states occurs, allowing more bonds to be formed between adjacent atoms. The resultant bonding and antibonding that occurs leads to multiple allowed bonding and antibonding energy levels, which electrons can occupy. This is demonstrated in Figure 5a, in which a four-valent atom (with four unfilled *p* orbitals) undergoes hybridisation upon covalent bonding, leading to the promotion of an s electron into a molecular *p* bonding orbital, and also leading to the formation of unfilled *s* and *p* antibonding energy levels (both shown in Figure 5b).[39]

Due to Pauli's Exclusion Principle, none of these orbitals can have the same energy, and every resultant orbital forms at a slightly different energy. The larger the number of atoms, the more orbitals are formed, a process that continues until the high density of energy states can be said to form a band of potential energy states.[37] Figure 5c shows how the band structure of a four-valent crystal is formed.

Here, the four valence electrons located in the s and p bonding orbitals, make up the valence band, with the top of the valence band determined by the energy level of the *p* bonding orbitals. The base of the conduction band arises due to the s antibonding orbitals.[39]

The energy of all bands is typically given as an energy value away from vacuum energy. For example, when an energy level of band is given, or a work function value is stated (typically in eV) that is the energy it would take to promote an electron from that level to escape to infinity with no remaining energy. Electron affinity refers to the energy difference between the bottom of a conduction band and infinity (vacuum energy) whilst hole affinity refers to the energy difference between the top of the valence band and vacuum energy.[3]

An incoming photon can excite a valence electron to the conduction band if it satisfies the condition $E_\lambda > E_G$ (see Figure 5d), where such a *p* to *s* transition is known to be electron-dipole allowed.[39]

Theoretical solid-state physics describes these bands through Bloch theory and Brillouin zones, where the Schrödinger equation is solved with wavefunctions of allowed eigenstates for electrons in a periodic lattice. This leads to bands (with index n) that are characterised by their energy, crystal momentum *k* vector and a dispersion relation $E_n(k)$. Since there are a set of bands within a semiconductor, then there are also many available energy levels for any given value of k. Semiconductors will either have direct or indirect band gaps between their conduction and valence bands, where the closest proximity of the band structures will either be aligned or displaced by a *k* vector. Modelling the band structure of a density of states can then lead to semiconductor optoelectronic properties being extracted from band structure.[3] Solving the Schrödinger equation and deriving properties such as charge carrier density from the density of states is outside the scope of this thesis, but is well described elsewhere.[3,40,41]

2.3: Perovskite Crystal and Band Structure

Perovskites are crystalline materials with a chemical structure of the form ABX_3, where A and B cations with X anions form a crystal structure demonstrated in Figure 6.[7,42–44] PSCs typically utilize organic-metal halide hybrid perovskite active layers in which A is a large organic cation MA (CH_3NH_3), FA ($HC(NH_2)_2$), inorganic cesium (Cs), or potassium (K). The B cation atom in most high PCE devices is lead (Pb), but research increasingly focusses on perovskite with tin (Sn) B site cations. The halides iodine (I), chloride (Cl), and bromide (Br) are all implemented individually or as halide blends. Perovskite with blends of various cations and anions are often used for reasons that should become clearer throughout the remainder of this chapter. Perovskite blends that result in high efficiency devices include: $MAPbI_{3-x}Cl_x$,[45,46] $MAPb(I_{1-x}Br_x)_3$,[47] $FAPbI_yBr_{3-y}$,[48] $FAPbI_{3-x}Cl_x$[49], $(FAPbI_3)_{0.85-0.87}(MAPbBr_3)_{0.15-0.13}$,[50] fully inorganic cation perovskites $Cs_{0.925}K_{0.075}PbI_2Br$,[51] with the most recent high PCE PSCs using triple cation compositions $CsI_{0.05}((FAPbI_3)_{0.85-0.83}(MAPbBr_3)_{0.15-0.17})_{0.95}$,[52] sometimes with additional 0-10 %M of potassium.[53]

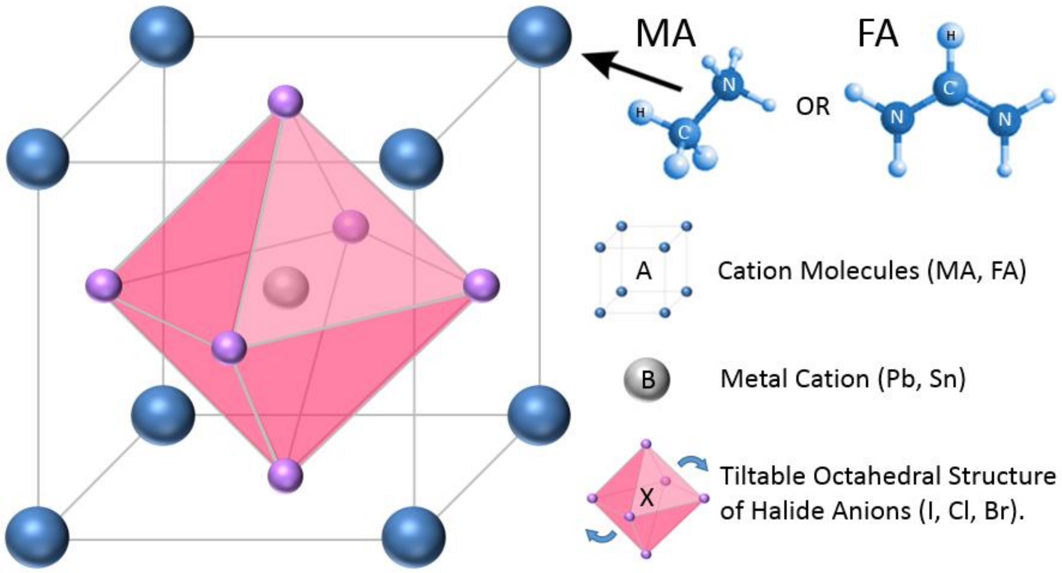

Figure 6: *The crystal structure of a perovskite in a cubic or pseudocubic -phase (α). The positions and chemical structure of common materials for the organic cations A, metal cations B and halide anions X in the* ABX_3 *formula are indicated. Whilst in the cubic phase, the perovskites unit cell may be taken as a repetition of A organic cations (as shown) or as a unit cell of B metal cations. The halides form octahedra which can tilt whilst maintaining the perovskite structure.*

2.3.1: Perovskite Unit Cell

The perovskite unit cell can be represented as a cage of organic A cations enclosing an octahedral structure of halide anions X with the metal cation B in the centre. There are several phases of the extended perovskite crystal structure with differing unit cells. Phase changes are influenced by changes in temperature, pressure and the composition of the perovskite. Modelling of MA+ cations has predicted that they are rotating rapidly at room temperature. Larger organic A site molecules may cause the tilting of the internal octahedra and the shifting of the halide-Pb bond angles.[7,54,55] The stability of a crystal structure can be described with a Goldschmidt tolerance factor (t), calculated from Equation 7 below. This uses the ionic radii R of constituent atoms to determine whether the crystal is stable, distorted, or unstable. In order for the perovskite cubic crystal structure to form, the relative size of the anions and cations must have a Goldschmidt tolerance factor between 0.8 → 1. Lower values of t may result in tetragonal or orthorhombic structures at room temperature. Ionic radii come with a range of reported values, in the case of $MAPbI_3$: $R_A \sim 1.8$ Å for MA, $R_X \sim 2.22$ Å for I and $R_B \sim 1.19$ ˚A for Pb. $MAPbI_3$ has $t = 0.99$. Other important ionic radii include: FA ~ 1.9→2.2 Å , Br ~ 1.96 Å and Cl ~ 1.81 Å.[7,56]

$$t = \frac{R_A + R_X}{\sqrt{2}(R_B + R_x)} \qquad (Eq. 7)$$

2.3.2: Methylammonium Lead Iodide Perovskite Band Structure

Metal-organic methylammonium lead iodide perovskite, $MAPbI_3$, has an electronic band structure that is primarily determined by the electronic bonding orbitals of the lead and iodide. Lead and iodide are Pb^{2+} cations and I^- anions when in the perovskite crystal, and have electronic configurations of $5d^{10}$, $6s^2$, $6p^0$ and $4d^{10}$, $5s^2$, $5p^6$ respectively. The highest energy orbital is therefore the empty 6p Pb^{2+} ion, which forms the conduction band. Hybridisation of the I 5p and Pb 6s states (with such orbitals shielding each other) leads to an antibonding orbital, forming the valence band.[34,57,58]

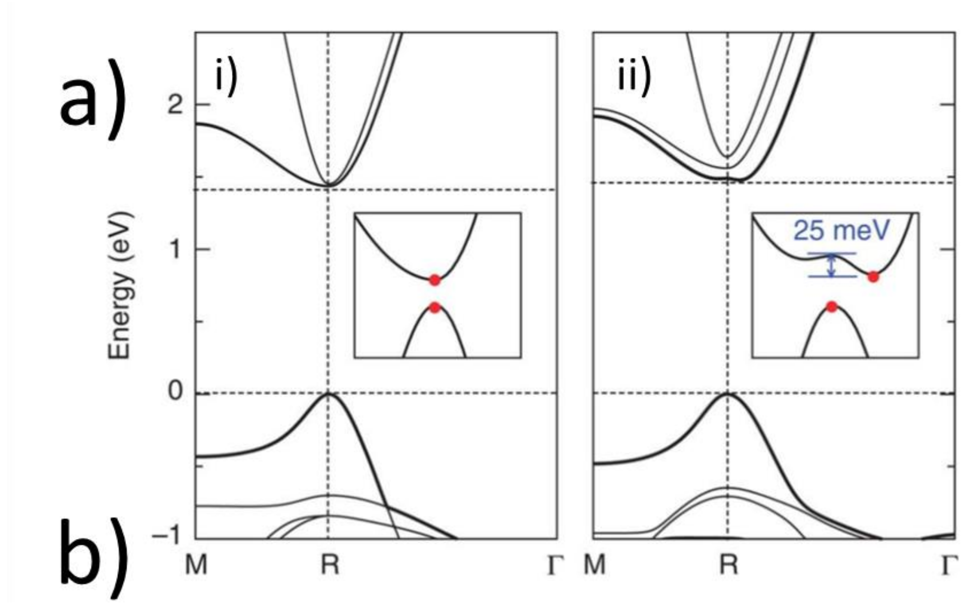

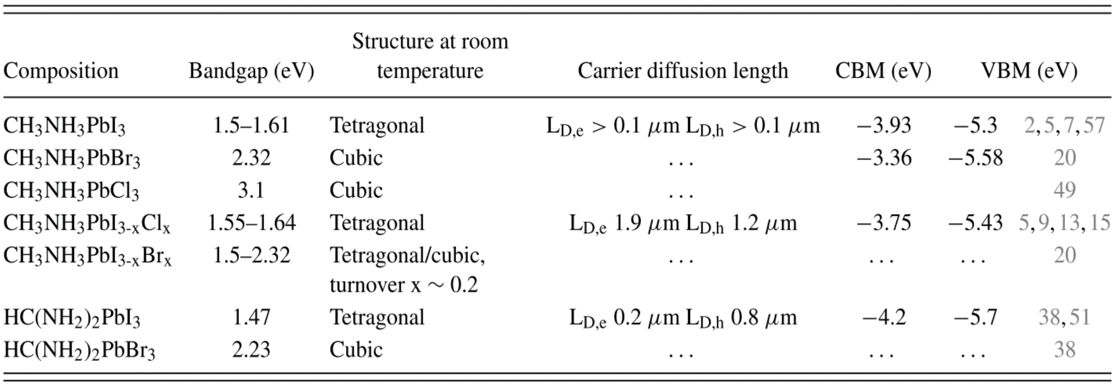

Composition	Bandgap (eV)	Structure at room temperature	Carrier diffusion length	CBM (eV)	VBM (eV)	
$CH_3NH_3PbI_3$	1.5–1.61	Tetragonal	$L_{D,e} > 0.1\ \mu m$ $L_{D,h} > 0.1\ \mu m$	−3.93	−5.3	2, 5, 7, 57
$CH_3NH_3PbBr_3$	2.32	Cubic	...	−3.36	−5.58	20
$CH_3NH_3PbCl_3$	3.1	Cubic	...			49
$CH_3NH_3PbI_{3-x}Cl_x$	1.55–1.64	Tetragonal	$L_{D,e}$ 1.9 μm $L_{D,h}$ 1.2 μm	−3.75	−5.43	5, 9, 13, 15
$CH_3NH_3PbI_{3-x}Br_x$	1.5–2.32	Tetragonal/cubic, turnover x ~ 0.2	...	...	...	20
$HC(NH_2)_2PbI_3$	1.47	Tetragonal	$L_{D,e}$ 0.2 μm $L_{D,h}$ 0.8 μm	−4.2	−5.7	38, 51
$HC(NH_2)_2PbBr_3$	2.23	Cubic	...	...	...	38

Figure 7: *a) From Nature Communications, Motta et al.*[57] *Band structure of MAPbI*$_3$ *CH*$_3$*NH*$_3$*PbI*$_3$ *calculated from density functional theory. With zero energy taken from the top of the valence band, the band gap is found to be (i) direct when the methylammonium cation is oriented along the [111] and (ii) indirect when orientated along the [011] directions. b) From APL Materials, Bretschneider et al.*[58] *Table summarizing perovskite band gap energies (eV), structure at room temperature, carrier diffusion lengths and conduction band minima (CBM) and valence band minima (VBM) with energy levels collated from well cited literature. The common chemicals used in the perovskite active layer are; iodide (I), bromide (Br), chloride (Cl), methylammonium (MA, CH*$_3$*NH*$_3$*), and formamidinium (FA, HC(NH*$_2$*)*$_2$*).*

Density functional theory (DFT) can be used to model the crystal structure and obtain an expected electron band structure. This has been previously calculated by Motta *et al*. and is given in Figure 7a i.[57] This DFT calculation has been used to confirm that the MA^+ cation can contribute to the band gap of the $MAPbI_3$ perovskite. As the orientation of the MA^+ changes it can exert a strain on the PbI_6 octahedra, generating a band edge that is 25 meV lower and offset from the originally band gap (see Figure 7a ii). Such a change is therefore predicted to turn the perovskite from a direct to indirect bandgap semiconductor. Although this change is small, it may allow a room temperature perovskite (with a rapidly rotating MA^+ cation) to absorb light into its direct band gap, whilst retarding radiative recombination as charges thermalize to the bottom of the indirect bandgap before recombining.[57]

2.3.3: Perovskite Crystal Phases

In the case of $MAPbI_3$ composition, the perovskite is in an orthorhombic phase up until temperatures of 162 K, at which point it becomes tetragonal. It will remain tetragonal at room temperature and only enters a cubic phase state at high temperatures above 327 K.[59–61] It is notable that this expected phase state change from tetragonal to cubic occurs within the expected operating temperature of a solar cell (up to $\sim$ 350 K). The use of different cations or cation blends, and halides or halide blends leads to different phase structures of perovskite around room temperature, and different temperatures for phase transitions. Each phase has different electronic and optical properties.[54]

A compendium table detailing the phases at room temperature, band gaps (optical and electrical), conduction band minima (CBM) and valence band minima (VBM) for non-mixed halide $MAPbX_3$ and $FAPbX_3$ films can be found in Figure 7b.[58]

2.3.4: Effect of Changing Constituents

The band structure of perovskite materials is relatively insensitive to the ionic radius of the A site cation, however it can still be used to adjust perovskite band structure.[42,62]

A large amount of effort has been put into the tuning of band gaps, tailoring of absorption onsets, and the optimization of carrier diffusion lengths (The average distance a generated hole or electron travels before recombination) via adjustment of the perovskite composition. For example, the larger ionic radius of the cation FA compared to MA (~ 2 Å and ~ 1.8 Å respectively) results in a $FAPbI_3$ tolerance factor of t = 1.01.[56] It has also been shown to double the electron diffusion length L_e from ~0.1 μm to ~0.18 μm, increase the hole diffusion length L_h from ~0.1 μm to ~0.81 μm[58] and narrow (and red-shift) the optical band gap (absorption edge) from 1.52 eV to 1.47 eV,[55,56,58,63] moving the absorption closer to what is excepted as optimum by the Shockley-Queisser limit (~ 1.34 eV).[63] This occurs at the expense of a lower absorption coefficient α. The optical attenuation coefficient of the methylammonium based perovskites at 550 nm is ~$1.5\text{x}10^{-4}$ cm^{-1},[64] a value that compares to formamidinium based perovskites at 550 nm of ~$1.3\text{x}10^{-4}$ cm^{-1}.[63] FA based perovskites need to be thicker than MA based perovskites due to the weaker absorption of FA.[65,66]

The X halides are also known to affect the electronic band structure of perovskite materials. Analysis of phase states induced by changing the perovskite composition is often performed as function of mixed halide content. Simply, the band gap $MAPbI_3$ can be reduced by ~50 meV and ~150 meV by the direct replacement of iodide for bromide and chloride respectively. The use of such halides results in a contraction of the PbI_6 octahedra, decreases the unit cell size and causes strain in the crystal lattice that blue shifts the absorption range.[55]

2.4: Perovskite Solar Cell Operational Principles

2.4.1: p-n Junctions - Formation of a Depletion Region

The Fermi level of a material is the electrochemical potential – the thermodynamic work required to add one electron to that material. Electrochemical potential must be defined relative to an energy state, here, the electrochemical potential of a semiconductor can be defined as the energy relative to the top of the valance band of that semiconductor. The Fermi level of a material can also be defined as the energy level at which there is a 50% probably of an electronic state being occupied. For conductors with no bandgap, the Fermi level lies within a single band (the overlapping valence and conduction band), close to the work function of the conductor. In an intrinsic semiconductor the Fermi level is located in the middle of the band gap. In an n-type semiconductor there is an increased statistical change of electrons being in the conduction band (relative to holes being in the valence band) and the Fermi level lies closer to the conduction band. Conversely, in a p-type semiconductor there is an increased statistical chance of holes being found in the valence band (relative to electrons being in the conduction band) and the Fermi level lies closer to the valence band.[3,41,67]

When a p-type semiconductor and an n-type semiconductor are brought into contact with each other, there is an induced diffusion of intrinsic charge carriers (with electrons moving to the material with the lower chemical potential) which allow the system to approach equilibrium. Holes from the p-type material migrate to the n-type semiconductor and electrons from the n-type material migrate to the p-type material. This leaves behind positive ions in the n-type material, and negative ions in the p-type material. Carriers from one side of the p-n junction are referred to as majority carries when they are on the side they originate from and minority carriers if they diffuse into the opposite side. As this process continues a region depleted of intrinsic carriers known as the depletion region is formed. The ions either side of the depletion region generate a built-in electric field, which creates an electronic barrier preventing further diffusion of carriers until the equilibrium is perturbed.[9,68] At equilibrium a p-n junction can be said to have a total chemical potential that is constant across the whole diode.

An applied bias can then be applied to the p-n junction. In forward bias the external field opposes the built-in electric field. As the forward bias is increased the net field is reduced, leading to a reduction in barrier height. Now the minority carriers recombine with carriers from the other side of the junction, leading to a dark recombination current. This is the origin of diode like response in p-n junctions, where a large current is observed in forward bias. The opposite case (of applying reverse bias), decreases the probability of carriers diffusing across the depleted region, as the external electric field increases the net field across the depleted region. For large reverse bias conditions, the depleted region also increases in size.

Practical operation of solar cells is performed under illumination at a forward applied bias that does not exceed the open circuit voltage of the solar cell. Characterisation of solar cells is usually performed under steady state conditions, with different illumination intensities or applied biases. These external parameters can also be changed rapidly to investigate solar cell response under transient changes in voltage or illumination intensities. [9]

Figure 8 is a simplistic schematic of a PV p-n junction.

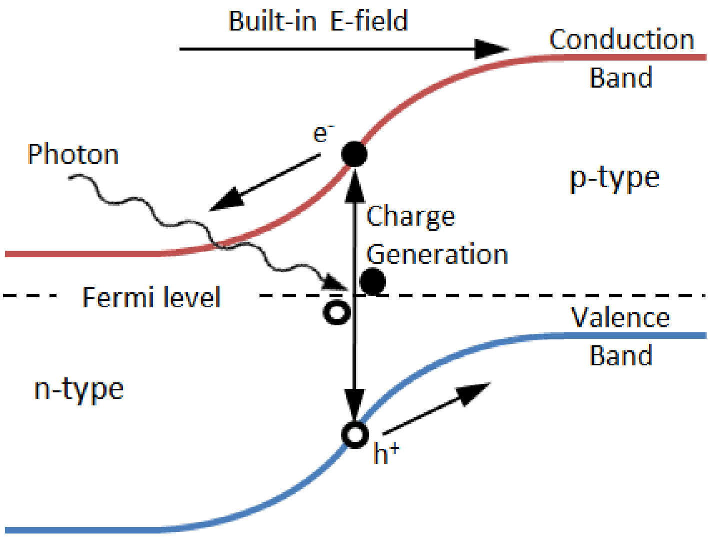

Figure 8: *Simplistic p-n junction solar cell whereby p and n type semi-conducting materials are brought into contact with each other, forming a space charge region and band bending of the conduction and valence bands as the Fermi levels are aligned. Incoming photons generate photocurrent via electron-hole pairs that are separated by the built-in field.*

p-i-n junctions generally have a large (relatively) undoped intrinsic semiconductor (i) between the and p-type and n-type semiconductors that acts as a large depletion region. Both p-i-n or n-i-p junctions are commonly used semiconductor models for PSCs. In fact, p-i-n PSCs are known as inverted PSCs. Here the cell architecture typically has a hole transport layer below the perovskite layer and an electron transporting layer above the perovskite layer. n-i-p PSCs, more commonly known as standard architecture devices have the charge transport layers the opposite way around. The development of early PSC architectures is detailed later in this chapter. As described above, the perovskite band structure enables it to act as an absorbing layer, with incoming photons exciting charges across a band gap.[69,70] However, the simplistic picture of a strong electric field across the depleted region, driving photogenerated charges towards the n and p type contacts, is not an accurate model for the functionality of a PSC.

2.4.2: Charge Transport in a Metal Halide Perovskite Active Layers

On irradiating a semiconductor with a photon, the excitation of an electron from the valence to the conduction band causes the formation of an exciton. Depending on the semiconductor material the exciton can either be a large, weakly-bound Wannier-Mott exciton with a binding energy on the order of ~10 meV or a small tightly bound Frenkel exciton with a binding energy typically between 0.1 and 1 eV. c-Si semiconductors support Wannier-Mott excitons, with the electron and holes having diffusion lengths that are large enough such that they can be extracted to the electrodes as free charges. Exciton binding energy is inversely correlated to the coulombic charge screening within that material, defined as the dielectric constant ε_r of the semiconductor. An increase in temperature will lead to increasingly likelihood for bound excitons to dissociate.

Most lead-halide perovskites generate weakly bound Wannier-Mott excitons, resulting in the generation of free charges. However the value of binding energy (E_B) as determined by experiment and theory vary from 1 to 50 meV.[19,71–78] If excitons did indeed have a binding energy of 50 meV, then it is possible that excitons would remain bound at room temperature, and thus reduce the quantum efficiency of a perovskite device. However, the large PCEs of perovskite devices suggest that the generated excitons are unlikely to be tightly bound.

The calculation of exciton binding energy values usually involves determination of the dielectric constant of the perovskite. There some discussion in how to best interpret the value of the dielectric constant through the use of n-k data and the Kramers-Kronig relations.[79] It has been shown the discrepancies in the Wannier-Mott model result from the use of dielectric constant, specifically the choice of high frequency static values (ε_{ST}), which are typically very large.[72]

Common consensus suggests that $MAPbI_3$ films at room temperature (in the tetragonal phase) may have a binding energy as low as 5 meV, caused by dielectric screening from the MA cations. Mixed halide perovskites have also been found to have reduced excitonic screening due to collective reorientations of MA cations.[71,73] Because of the low exciton binding energy, electrons and holes quickly dissociate much like charges in a fully inorganic semiconductor.

There is some debate as to whether the typical model of a depletion region with charges being swept out by a built-in field is appropriate for a PSC. A built-in field should be generated by well aligned hole and electron transporting levels respective to the perovskite band structure. However, experimental evidence suggests that PSCs still function with badly aligned charge transporting layers, or without charge transport layers at all. These results generate a myriad of potential theoretical issues regarding device junction models.[28,70]

It has been suggested that perovskites do not require a built-in field, and that either Fermi level pinning in the perovskite leads to charge selectivity, or that charge diffusion in the perovskite is so efficient that charges always reach the charge transporting layer interfaces. In the latter case, efficient generation of photocurrent would be entirely reliant on the charge blocking capabilities of the charge selective layers either side of the perovskite. Given that there is evidence of a significant number of free ions present in the perovskite (discussed later in context of perovskite hysteresis), it is likely that photogenerated charges are effectively screened from external electric fields.[28,70]

It is generally accepted that perovskites have remarkable charge transport capabilities. Electron and holes have impressive mobilities. In the case of $MAPbI_3$ perovskites, experimentally determined charge carrier mobilities are around 10-20 $cm^2V^1s^{-1}$,[80,81] with hole mobility often reported as higher than electron mobility. Electron and hole mobilities can be theoretically calculated through the density of states, which takes into account disorder parameters that broaden the density of transport states.[3,41,82]

Perovskite single crystals have been shown to have charge diffusion lengths longer than a millimetre.[75,83] This is not too dissimilar from crystalline silicon which has charge mobilities of around 10^2-10^3 $cm^2V^{-1}s^{-1}$, with diffusion lengths in the 100's of micrometres.[84] As previously discussed the electronic properties of perovskites are likely enhanced due to photon recycling, meaning that charges generated deep in the bulk of the perovskite can radiatively recombine and yet still contribute to photocurrent by generating new charges that eventually reach the charge transport interfaces.[27,85]

The success of the metal lead halide perovskite in PV devices is due to its remarkable optoelectronic properties. Its large absorption coefficients allow photons to be efficiently absorbed even if the perovskite layer is only a few 100 nm thick. For most perovskite active layers the diffusion length is of the order of the typical film thickness (~ 0.5 μm), with FA based multi-cation mixed halide perovskites having the advantage of diffusion lengths greatly exceeding film thickness.[7,86–88] Taken together, a high charge carrier mobility, low bi-molecular charge recombination, and photon recycling allow perovskite PV to function even if the active layer has a thicknesses exceeding a micron. Charge generation occurs on the order of picoseconds whilst most recombination is on the order of microseconds.[61] The low non-radiative recombination rate results in a small difference of under 400 meV between V_{OC} and E_g/q; a value better than many alternative PV semiconductors.[16,61] In Chapter 7, charge collection electrodes separated by over three microns of $MAPbI_3$ are utilised successfully in functional PSCs.

2.4.3: Organic Charge Transport/Blocking Layers

The properties of organic charge transporting layers stem from atomic orbital hybridisation and charge delocalisation processes which are well described elsewhere.[5]

Put simply, the highest energy π bonding orbital that is normally occupied in an organic charge transport layer is known as the highest occupied molecular orbital (HOMO). The next highest orbital (π*) is known as the lowest unoccupied molecular orbital (LUMO). These orbitals are analogous to the valence and conduction bands as found inorganic semiconductors materials.[5,6,89] As with inorganics, photons can excite electrons from the HOMO to the LUMO level. When organics have an electron excited into the LUMO band level, a strongly bound exciton is formed (Frenkel exciton).[7,86–88] Although this exciton is neutral, and its constituent electron and hole are bound, the electron and hole distort the local atomic structure of the polymer. These charges, which cause local energy distortions, are better known as hole and electron polarons. Since excitons are neutral they can only diffuse within the polymer - this is typically through a hopping process along the polymer backbone or from polymer chain to polymer chain.[5,90,91] This diffusion occurs as either a short range electron exchange (Dexter transfer) or a dipole-dipole energy exchange (Förster resonant energy transfer) which are described in detail by Mikhnenko *et al*.[92] Excitons will diffuse until they recombine or they reach an acceptor interface with a band structure mismatch making it energetically favourable for the hole and electron polaron to split apart across the interface.[7,86,87]

In the case of PSCs, organic materials are often used to transport delocalised charge. Since acceptor or donor (hole or electron transporting) polymer layers and accepter fullerenes are significantly disordered, delocalised charges can only travel along and across polymer chains via a short range 'hopping' process.[93,94] Whilst the majority of PV research will refer to band structures in polymers, it is not correct to describe charges in polymers as moving through a conduction band. Firstly, photoexcited charges remain in strongly bound excitonic states that can only diffuse through the polymer. Secondly, delocalised charges moving along charge conjugated polymers have limited delocalisation and hence low charge mobilities.

Typical donor and acceptor organic polymers (and fullerenes) have mobilities not exceeding 10^{-3} $cm^2V^{-1}s^{-1}$, which is several orders of magnitude lower than metal-halide perovskites.[82] As such, when organics are employed as transport layers they either need to be thin (to reduce the length charges travel) or be doped (to increase the conductivity). Whilst inorganic semiconductors are p-type or n-type doped by introducing inorganic impurities, doping of organic semiconductors is typically achieved by the addition of other organic species. These dopants should ideally have band-like structures that either have LUMO levels close to the HOMO level of the material being doped, resulting in p doping, or HOMO levels next to the LUMO level of the organic being doped, resulting in n doping.[95–100] In p doping, the host organic's HOMO level is moved down and in n doping, the host organic's LUMO level is moved up relative to its original position from vacuum energy.

The low coulombic screening in organic semi-conductors (low dielectric constant ε_r),[101,102] means that dopants can easily disturb the original structure of the organic, breaking down ordered bond lengths, generating sub band gap states, and widening the original band gap of the material. Significant doping causes sub-bands to appear inside the band gap. Therefore, dopants can make a significant contribution to the density of states of the host organic. It has been observed that p doping can lead to exciton quenching in donor polymers, leading to a reduced rate of damaging reactions between incident photons and excited states, and hence leading to reduced degradation of the polymers.[95–99]

2.4.4: Interfaces and Charge Transfer

When two materials are brought into contact with each other, the interface that is formed will always have material specific chemical interactions, surface oxides, or other surface defects and traps. When two metals or a metal and a semiconductor are brought together their Fermi levels will tend to align. In the case of a metal-semiconductor, the large number of free charges in the metal relative to the semiconductor means that the band structure of the metal will stay the same whilst the band structure of the semiconductor will accommodate the alignment.[10,11,103]

Figure 9 shows the possible energetics of a metal-metal and a metal-semiconductor interface. Part (a) demonstrates a metal-metal interface where the metals align, causing a potential change Δ at the interface. Part (b) shows a metal-acceptor semiconductor interface where the Fermi level of the acceptor moves up and aligns with the work function of the metal, also causing a change in potential. Part (c) shows a metal-donor semiconductor interface where the Fermi level of the donor moves down and aligns with the work function of the metal, resulting in a negative change in potential. Ideal metal-semiconductor charge extraction cases occur when the work function of a metal cathode (used to extract holes) matches the HOMO level of the donor semiconductor, and the work function of a metal anode (used to extract electrons) matches the LUMO level of the acceptor semiconductor.[10,11,34,103–108] Strictly speaking semiconductors are only affected by an interface in a region close to that interface. In this region, the semiconductor band structure is bent, and an interfacial dipole can be formed. As is indicated in Figure 9, the bulk of the semiconductor does still have a shifted band, but that band is flat at distances far away from the interface. If the bands align well, then there will be a metal-semiconductor ohmic contact, if they do not align then a depletion region will be formed in the semiconducting material. A charge transfer barrier will then form (known as a Schottky barrier), making the interface rectifying in nature. It has been found that Schottky barrier height is mostly independent to the metal work function as the semiconductor Fermi level is usually pinned to the metals Fermi level.[69,109]

For transfer of holes between two semiconductors, alignment of the valence (or HOMO) levels of both is required, and for efficient extraction of electrons alignment of the conduction (or LUMO) levels is required. Charge blocking can be achieved by ensuring a significant energy barrier is present between the conduction levels at the hole extraction interface and the valence levels at the election extraction interface. Charge transport will be significantly reduced if a step up (which will likely manifest as a depletion region and a charge transport barrier) is present on either extraction interface, instead of a step down. Perfect semiconductor charge transfer at interfaces having an ideal alignment are characterised by limited band bending, limited surface depletion region, small barriers to charge transfer, and a small number of surface trap states.[10,11,34,103–108]

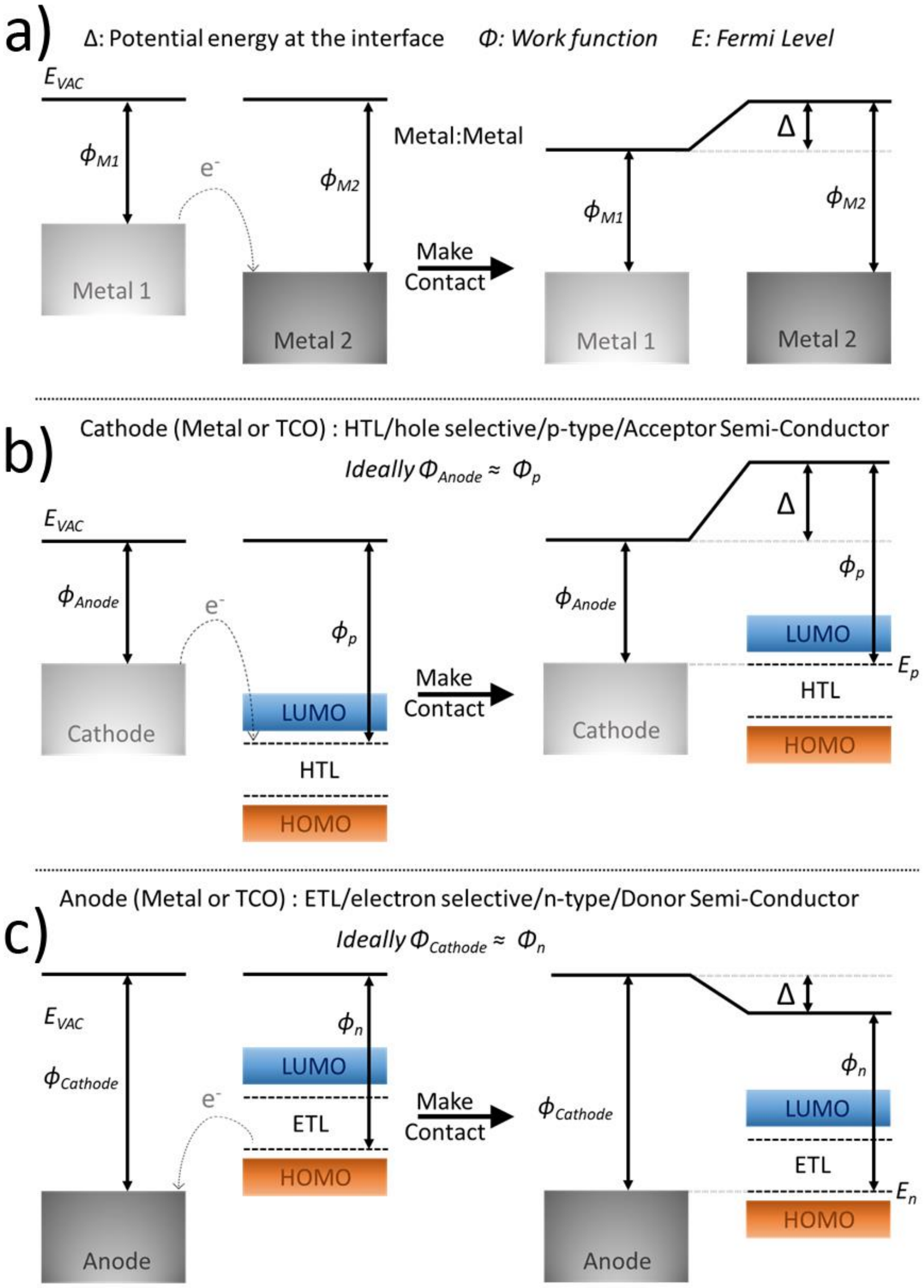

Figure 9: *Energetic alignment (from vacuum energy E_{vac}) before and after metals and organic semi-conductors with different work functions (Φ) are brought into contact with each other: a) metal-metal, b) metal cathode – acceptor semiconductor, c) metal anode – donor semiconductor. The fermi levels are aligned when the materials form an interface, creating an potential change Δ and an interfacial dipole.*

The band structure of layers in a PSC have been established, and the formation of p-i-n, n-i-p and metal-semiconductor junctions have been discussed. Taken together, the functionality of a PSC can be explained using an energy level diagram of all the constituent layers, this is provided at the start of Chapter 3.

2.5: Arrival of Perovskite Solar Cells

Before the materials and device architectures used in this thesis are described, a brief overview of previous perovskite PV developments is provided here.

In typical Dye-Sensitized Solar Cells (DSSCs), a photoactive dye excited charges states (in this case Frenkel excitons) from incoming photons. As described previously, the electrons then transfer into the optically semi-transparent TiO_2 mesoporous scaffold with holes passing through the liquid electrolyte to the counter electrode. In 2006, a $MAPbBr_3$ perovskite was used instead of the dye to produce the first ever perovskite sensitized solar cell (PSSC), with an efficiency of 2.2 % PCE achieved.[110] In 2009 the same group replaced the bromide with iodide in a similar architecture and fabricated a device with 3.8 % PCE.[111] By 2011 another group had reached 6.2 % PCE by sensitizing the TiO_2 with perovskite quantum dots (QDs).[64] It was at this time that perovskites were observed to be easily dissolved in the liquid electrolyte, causing damaging losses to the PCE.[42]

In 2012 the liquid redox electrolyte occurred was engineered out of the PSSC architecture with two major reports by H. Snaith's and M. Grätzel's research groups. Here, the liquid electrolyte was replaced by the hole transport layer (HTL) spiro-MeOTAD, doped with bis(trifluoromethane) sulfonimide lithium (Li-TFSI) and 4-tert-butylpyridine (TBP). The device structure implemented was similar to the schematic shown in Figure 10a. Devices without electrolyte were produced, achieving PCEs of up to 10.9 %.[87,88]

Significant attention was focused on the use of a TiO_2 scaffold as the electron transport material (ETM). In 2012, a Al_2O_3 scaffold was implemented to replace the TiO_2 scaffold and it was shown that open circuit voltage (V_{OC}) was boosted by this change, producing a 10.9 % PCE device. The next big step for perovskite PV was the fabrication of $MAPbI_{3-x}Cl_x$ devices which (at the time) were found to have an electron and hole diffusion length of well over one micron (under low illumination levels). Experimental evidence was clear, the perovskite could act as an active layer, not just as a sensitizing agent (See Figure 10b).[86–88] It was also found that the perovskite later did not have to fill an ETM scaffold, with devices functioning without an ETM scaffold at all (See Figure 10c).[112] In 2013 a planar c-

TiO_2/$MAPbI_{3-x}Cl_x$/Spiro-OMeTAD device demonstrated a PCE above 15 %. With longer diffusion lengths, such perovskite films no longer required a mesoporous scaffold to extract electrons,[61] opening several new avenues of research for the ever growing perovskite PV community.[16]

Device architectures for perovskites from 2013 onwards typically include the mesoporous structure shown in Figure 10b or the planar structure in Figure 10c. Devices are not limited to being produced with the HTL above the perovskite (n-i-p devices), and have also been fabricated with alternative HTLs below the perovskite (p-i-n devices).[113] Choices of material for electron transport layers (ETLs) and HTLs are limited by use of appropriate electron affinity to create an ideal energy landscape for selective charge extraction and also by the fabrication process required to deposit the charge transport materials.[114]

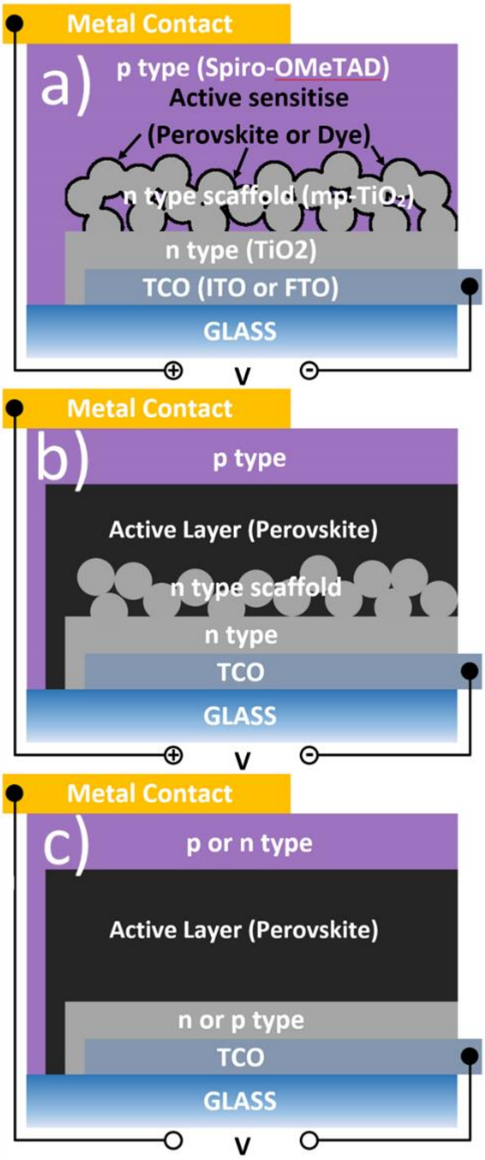

Figure 10: *Adapted from Nat Materials, Grätzel et al.*[115] *the evolution of the PSC from DSSCs. a) The liquid electrolyte replaced by a hole transport layer (HTL), the perovskite coats the titanium dioxide (TiO_2) scaffold or an alternative aluminium oxide (Al_2O_3 scaffold). This all remains upon a transparent conductive oxide layer (TCO) and compact TiO_2 layer. b) The perovskite is a layer above the scaffold material and the HTL is a separate layer above this, due to the highly conductive nature of the perovskite this structure has been proven to function effectively, even without the HTL. c) Thin film planar structure with HTL above and no mesoporous scaffold.*

2.6: Current-Voltage Hysteresis

As has already been established, solar cells are characterised by taking *JV* curves under simulated solar illumination (AM 1.5, 100 mWcm^{-2}). Typically, the solar cell is held under forward bias (FB), then the voltage is reduced to short circuit voltage (SC) at various sweep speed, to obtain a FB-SC sweep. The opposite can be done to produce a SC-FB sweep. Perovskites have been found to exhibit a significant difference in their *JV* curves depending on the direction of the sweep, the speed of sweep, and the recent history of solar cell. This anomaly is known as hysteresis.[116,117] It has been established that the magnitude of hysteresis is also highly dependent on device architecture, materials, deposition techniques, and layer thicknesses.[117]

A recent interpretation of hysteresis leads to the following conclusions: (i) Perovskites have a surprisingly large number of mobile ions which do not act to significantly reduce device performance. (ii) There is a relatively minimal amount of non-radiative recombination occurring in the bulk of a perovskite active later, but the interfaces between the perovskite and surrounding charge transport layers act as sites for significant surface recombination. (iii) Applied bias during PSC testing leads to ionic movement, which in turn modulates the severity of surface recombination (which can influence the efficiency of photogenerated charge extraction). As such, the direction and speed in which the applied bias is changed can affect the measured device performance metrics.

The physical interpretation of PSC (with such large number of mobile ions, and recombination of charges at the interfaces) has been a struggle for the scientific community. Circuit modelling and impedance spectroscopy has led to large capacitors and inductors being used to describe the electronic response of PSCs, both of which have limited meaningful physical interpretation. In yet unpublished work by, Moia *et al*., the electronic response of these interfaces has been successfully modelled as ionically gated transistors

2.7: Optimisation of the Perovskite Active Layer

This section reviews some of the key techniques that have been used in this thesis to obtain high efficiency devices. Solvent engineering of the perovskite solution, post deposition processes performed on the perovskite film and the composition of the perovskite are all discussed, and then applied in Chapters 4-7 of this thesis,

2.7.1: Solvent Engineering

When using solution processing, the choice of solvents used to dissolve the perovskite precursor can change the morphology of the film. Common solvents used to spin-coat perovskites include are dimethylformamide (DMF), γ-butyrolactone (GBL) and dimethyl sulfoxide (DMSO). Many high efficiency perovskite devices use perovskite precursor solutions with DMSO in a solvent blend.[50] A typical device process including a DMSO blend perovskite solution is shown in Figure 11, where an antisolvent wash is spin cast onto the still drying perovskite. The antisolvent washes away excess unreacted organic material whilst the DMSO prevents the perovskite crystal structure from forming by forming MAI-DMSO-PbI_2 complexes. Upon heating at 100 °C DMSO is liberated from the film, and crystallisation of perovskite occurs. This has been associated with large crystal grains and an overall smoother, pin-hole free film morphology.[50,118,119]

A volatile and clean solvent system for the deposition of $MAPbI_3$ active layers,[120] is based on a methylamine bubbled acetonitrile perovskite precursor. This system is used in Chapters 4-7 of this thesis.[120]

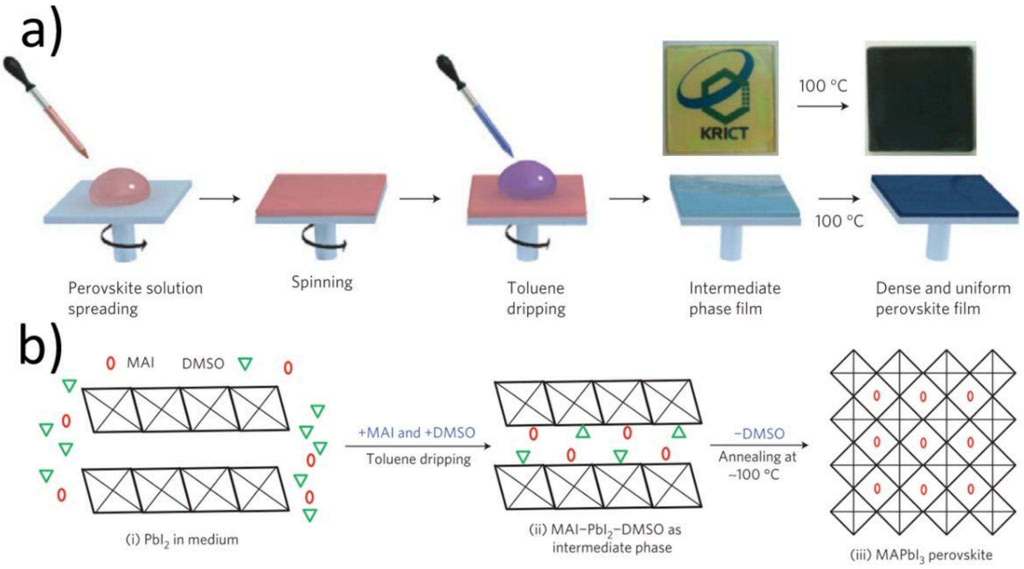

Figure 11: *Taken from Nature Materials, N. Jeon et al.*[119] *Anti-solvent wash with DMSO intermediate phase. a) The steps of the spin coating process. b) A schematic showing how the DMSO retards perovskite formation.*

2.7.2: Post Deposition Engineering

The annealing temperature chosen to remove solvent and crystallise the perovskite layer can affect device performance. Annealing causes crystallisation after any excess organic component is driven out of perovskite. Crystallisation of MA based devices should only be performed at temperatures below 110 °C, as it has been calculated that a large increase in halide deficiencies occurs in films annealing in excess of these temperatures.[121] An improvement in perovskite devices performance has been observed via the implementation of vapour or solvent annealing. Here, the presence of excess solvent generates much larger crystal grain sizes,[122] and resulting in an enhancement of device J_{SC}. This process involves exposing the perovskite to a solvent vapour at an elevated temperature (see Figure 12). During solvent annealing a quasi-stable liquid-phase environment is established between a polar solvent used to dissolve the $MAPbI_3$ surfaces and grain boundaries.[123] This process causes grains to grow until this process is no longer energetically favourable.[124]

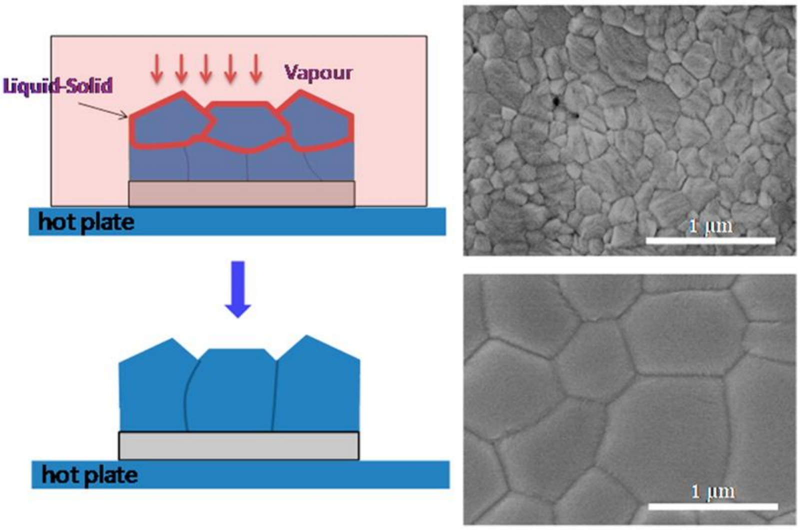

Figure 12: *Taken from ACS Applied Materials & Interfaces, J. Liu et al.*[123] *Schematics of the solvent annealing process and scanning electron microscopy images of perovskite films before and after solvent annealing.*

2.7.3: Compositional Engineering

There are many successful compositions of perovskite solution precursors that enable the fabrication of PV devices having high performance.

MAI:PbX$_2$ (3:1) with X = Cl or Acetate (Ac) perovskites precursor solutions have often be used as a replacement of a MAI:PbI$_2$ (1:1) perovskite precursor. A study directly comparing the different lead sources have found the average PCE of devices using PbAc$_2$, PbI$_2$ and PbCl$_2$ were 14.0 %, 9.3 % and 12 % respectively; demonstrating the improvement from using this alternative lead source.[121] The by-product produced by using lead acetate (PbAc$_2$) in MAI:PbAc$_2$ perovskite films is MAAc, which decomposes at 97.4 °C, making it energetically favourable compared to other potential by-products MACl and MAI. The expected release of organic by-products has been calculated to occur at 226.7 °C for MACl and 245 °C for MAI. Note that it is generally accepted that these organic by-products sublime from a forming perovskite film at temperatures lower than 100 °C, with the perovskite film only approaching a MAPbI$_3$ composition after the organic components have mostly sublimed.[121,125]

Perovskite films obtained from the MAI:$PbAc_2$ route are often ultra-smooth and are of a similar quality to perovskites deposited via vacuum assisted evaporation.[121] However, as shown in Appendix B, perovskites devices prepared from a lead acetate route are highly unstable.

Non-stoichiometric perovskite precursor solutions have been explored to determine their performance when used to create PV devices. Typically, MAI excess perovskite solutions are associated with perovskite films with more ordered grain orientation and large grain sizes,[126,127] whilst excess PbI_2 has been shown to remain in the perovskite film, forming a moisture barrier at grain boundaries and interfaces, which reduces the local density of charge trap states. [126,127] A PbI_2 excess was used for all experiments performed in this thesis.

The addition of cesium to multi-cation PSCs with final composition $CsI_{0.05}((FAPbI_3)_{0.85-0.83}(MAPbBr_3)_{0.15-0.17})_{0.95}$ (a triple-cation active layer), have been shown to enable fabrication of devices with PCEs exceeding 21 %.[52] Potassium has also been added as a molar fraction (0-10 %) of the total monovalent cations (MA, FA, Cs), resulting in quad-cation perovskites. This allowed fabrication of devices with suppressed ion migration and reduced non-radiative losses.[53] These advanced perovskite compositions are reported to achieve larger grain sizes, passivated defect sites (at grain boundaries and interfaces), retarded halide migration and phase segregation, enhanced grain luminesce, and reduced the number of non-luminescent grains. In this work, a multi-cation perovskite composition was used in Chapter 4 whilst Chapter 6 employs the triple-cation perovskite composition.

2.8: Stability of Perovskite Solar Cells

It is difficult to determine the effect of long-term environmental stresses on PV devices in a short period of time, as experiments are required to stress test thin-film PV in way that determines how they will perform over many years under real-world conditions. There are IEC (International Electrotechnical Commission) standards that PV modules must achieve in order to be considered stable.

Stability of PV devices is often measured using T80 and Ts80 lifetimes which are the time taken for the device to fall to 80% of its initial PCE, and the time taken to fall to 80 % of its PCE after a rapid burn-in of initial accelerated degradation.

A typical photovoltaic module (with encapsulation) should aim to retain 80 % of its initial PCE after 25 years by being resistant to continued AM 1.5 illumination (including the UV part of the spectrum). It should also be able to withstand a summer operating temperature of up to 350 K, as well as precipitation and water vapour (up to ~ 80 % relative humidity). Perovskite devices are well known for their instability. It is commonly observed that perovskites will degrade into hydrates or its original constituents PbX_2 and MAX or FAX (X = I, Cl, Br) under these conditions.[16,61,128,129]

2.8.1: Perovskite Degradation Due to Water and Moisture

The effects of liquid water on unencapsulated perovskite films are extreme,[61,128] and have been shown to be an irreversible process. Liquid water travels through the film along grain boundaries and quickly decomposes the crystal structure, visibly changing the perovskite from brown to a yellow-transparent film.[129] The degradation routes that $MAPbI_3$ films undergo are shown in Equation 8.[130]

$$\mathrm{CH_3NH_3PbI_3} \leftrightarrow \mathrm{PbI_2} + \mathrm{CH_3NH_3I} \qquad \text{(Eq. 8)}$$

$$\mathrm{PbI_2} \leftrightarrow \mathrm{Pb(0)} + \mathrm{I_2}$$

$$\mathrm{CH_3NH_3I} \leftrightarrow \mathrm{CH_3NH_2} + \mathrm{HI}$$

$$\mathrm{4HI} + \mathrm{O_2} \leftrightarrow \mathrm{2I_2} + \mathrm{2H_2O}$$

$$\mathrm{2HI} \leftrightarrow \mathrm{H_2} + \mathrm{I_2}$$

These reactions are only reversible when the degradation produces are trapped in the perovskite film. For example, when perovskites are immersed in water, many of their degradation components will be washed away, and thus the perovskite would be physically compromised. Conversely, in an encapsulated film or solar cell, the perovskite will retain more of its constituents during decomposition. Following storage in a dry place or annealing, reversible reactions may take place, and the perovskite may reform.[130] Such recovery of PSCs between cycles of constant testing and resting has been observed.[131]

It has also been observed that water vapour can travel along grain boundaries in a perovskite and form monohydrated crystals ($CH_3NH_3PbI_3H_2O$), or in extreme cases form a dihydrate species ($(CH_3NH_3)_4 PbI_6 2H_2O$). When saturated with water vapour, these hydrates reduce device PCE by an order of magnitude, but after devices are dried in nitrogen for 6 hours, PCEs return to their original value. Without encapsulation, humid environments can cause perovskite PV devices to fluctuate between an efficient and inefficient state. This reversible hydration can however result in an ever-increasing number of defects). Indeed, when water vapour causes the formation of significant concentrations of PbI_2, the PV devices do not recover. In general it has been found that perovskite films with larger grains can have reduced penetration by water vapour and therefore enable increased device stability, and decrease the number of trapped states caused by high levels of humidity.[129]

2.8.2: Perovskite Phase Stability and Degradation Due to Temperature

The maximum operating temperature that a PSC is expected to operate at is approximately 350 K. $MAPbI_3$ films have been shown to degrade in inert atmospheres at temperatures as low as 360K.[132] The $MAPbI_3$ phase state changes between 327K and 330 K, undergoing a change from tetragonal to cubic. This causes a small decrease in band gap and a switch to an acentric structure exhibiting ferroelectric effects.[59,60] Alternatively, FA perovskites have been shown to be more thermally stable with no degradation or discolouration even when exposed to temperatures up to ~ 400 K. $FAPbI_3$ has an ideal tetragonal black phase at temperatures up to ~ 430K, however, this black phase is susceptible to humid environments. In a humid environment the black phase is no longer stable, and it has been shown to convert to a yellow hexagonal structured perovskite. This FA phase change appears to be reversible, with the ideal FA black phase recovered by re-annealing a perovskite film. This unwanted hexagonal phase contains linear chains of PbI_6, has a large optical band gap, and exhibits poor charge separation and transfer properties.[50,133]

The phase instability of perovskites has been addressed by the implementation of mixed MA:FA perovskite films. It has been shown that a $(FAPbI_3)_{0.85}$ $(MAPbBr_3)_{0.15}$ perovskite film contains no hexagonal yellow phase during or after lifetime testing in a humid atmosphere.[50] Mixing $MAPbI_3$ and $FAPbI_3$ stabilises the trigonal black phase effectively and does not limit PCE through the presence of a small amount of bromide.[133]

2.8.3: Other Perovskite Degradation Routes

Deprotonation

Irreversible perovskite degradation routes include deprotonation (see Equation 9); a process that occurs when photoexcited states react with oxides to form super oxides.[134–136] As with moisture, it has been proposed that oxygen migrates through grain boundaries. Whilst methylammonium has been shown to be involved in reversible perovskite degradation and the recovery of perovskite devices, it can break down further as described by Equation 10, causing the perovskite to become permanently degraded.

$$\mathrm{CH_3NH_3PbI_3 + O_2 \rightarrow\ PbI_2 +\ CH_3NH_2 + \frac{1}{2}\ I_2 + H_2O} \tag{9}$$

$$\mathrm{CH_3NH_3PbI_3 \rightarrow\ \ NH_3 +\ CH_3I + PbI_2} \tag{10}$$

Metal Ion Migration and Metal Halide Formation

Metal electrodes can also contribute to PSC instability. For this reason, inert gold and silver contacts are often used instead of copper or aluminium as they are less likely to form charge blocking oxides. Unfortunately, gold has been shown to migrate throughout an entire perovskite cell,[137] and silver has been shown to readily react with perovskite degradation substituents to form silver iodide.[138,139]

Applied Bias

It has been shown that PSCs can degrade from the application of a bias alone. For example, certain grains (those starting with imperfect stoichiometries) have been shown to exhibit significantly faster degradation rates compared to others. This process is accelerated when the humidity surrounding a PSC is increased.[140]

2.8.4: Degradation of Charge Transport Layers

In the interest of achieving good PSC stability, transport layers should not degrade when in the presence oxygen and should therefore be hydrophobic in nature.

Fullerene/electrode interfaces have been known to result in device failure when deposited in the presence of moisture. For this reason, the deposition of fullerenes is usually performed in a dry or inert atmosphere, and PSCs utilising fullerenes are likely to need encapsulation to prevent moisture ingress from degrading the fullerene/electrode interface.[141] PEDOT:PSS has previously been identified as the cause of ITO etching, organic solar cell swelling and delamination, and a source of trapped moisture.[142–144] Figure 13 demonstrates how encapsulated PSCs stored in the dark were still found to degrade over a few hundred hours. This is attributed to moisture trapped inside the encapsulated device because of the use of a hydrophilic PEDOT:PSS HTL.[143]

UV light can introduce trap states on metal oxides; for example when exposed to UV, TiO_2 surface traps will form and act as recombination sites.[145–147] SnO_2 and NiO are less sensitive to UV radiation and are currently being explored as potential alternative metal oxides for charge extraction in stable PSCs.[148–156]

2.8.5: Impressive PSC Stability

Much work has gone into the engineering of stable perovskite materials. Here, the addition of n-butylammonium cation into a perovskite has been shown to generate 2D perovskite crystal structures that form at grain boundaries and interfaces. This 2D phase has been shown to result in reduced non-radiative recombination. Such 2D-3D perovskite hybrids have now achieved T80 lifetimes of 4000 hours when encapsulated.[157] When used in combination with a hydrophobic carbon electrode , PSCs have been proved to be stable for over a year, with no loss in device performance metrics.[158]

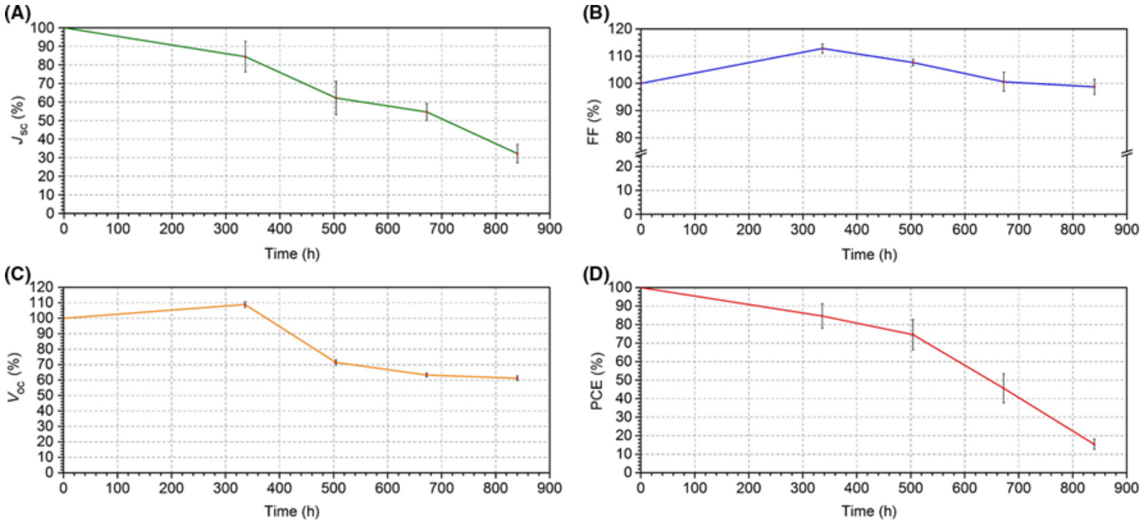

Figure 13: *Taken from Nano Energy, C. Bracher et al.*[143] *Stability measurements of PSCs. The four device performance metrics of encapsulated inverted PSCs containing a PEDOT:PSS HTL are recorded from JV sweeps, and the devices are stored in the dark in air between measurements.*

2.8.6: Encapsulation

Encapsulation should be transparent, low cost, light weight, and a barrier to moisture and oxygen ingress. Encapsulation may be placed on the back or front of a PV module. Any front facing encapsulation should attempt to enhance photon collection by having good transparency, and perhaps incorporate an anti-reflecting coatings. Rear facing encapsulation can also be coated with reflective materials to maximise photon collection.

Encapsulation can stop many of the degradation effects that destabilise PSCs. UV activated epoxies have been demonstrated to fully encapsulate OPVs, resulting in T80 lifetimes in excess of 10,000 hours, whilst successfully operating in real world conditions.[159,160] However, PSCs encapsulated with UV curable epoxies do not generally demonstrate long-term stable device performance metrics.[161–163]

2.9: Back-Contact Perovskite Solar Cells and Modules

Most conventional flat thin-film PV solar cells employ transparent conductive oxides (TCOs) on the front facing illumination side. These TCOs typically have a transmission below 90 %, which means that they absorb photons that would otherwise reach the photoactive absorbing layer.[36,164,165] Such TCOs generally also have sheet resistances between 10-20 Ω/square, which introduces high series resistance in larger area solar modules. To get around poor sheet resistance, thin-film PVs often use grids of metal contacts to increase conductivity, however this reduced the used active area. Such photon loss due to front facing contacts and TCOs is problematic, however there is a thin-film PV architecture that largely circumvents these issues.

Back-contact architectures (such as those shown in Figure 14) place all charge collection electrodes to the rear of the solar cell, minimising the number of photons that are absorbed before entering the photoactive absorbing layer.[36,164,165] These rear electrodes are usually interdigitated back-contacted (IBC) with n and p-type selective materials isolated from each other in order to achieve electron and hole selectivity.[36,165,166] Back contacts can be fabricated from a wide range of conductive and non-transparent materials that removes the series resistance issues that typically occurs when making larger area solar modules with transparent electrodes. However, all electrodes must be made from materials that will not be damaged by the deposition of the perovskite active layer. Whilst the roughness and uniformity of the active material usually dictates performance metrics in flat cells, back-contact cells are less sensitive to the surface coverage of the active material. For example, a hole in the active material does not result in a shunted non-functional solar cell.[164,165] An IBC design also enables in-situ investigations of absorbing layers, where the current-voltage characteristics of the active material can be studied as it is deposited, or as it receives post-deposition treatments.[164,167–169]

Only a few research groups have managed to fabricate working back-contact PSCs, and the best IBC published to date is reported to have a PCE of approximately 4 %, with the module design based on a honeycomb patterning for charge selection layers (See Figure 14b and onwards).[165] Other IBC architectures include ITO fingers separated by 50 μm with electro-deposited TiO_2 and PEDOT coating the electron selective and hole selective fingers respectively (see Figure 14a).[169] Photolithography and masked electron beam evaporation have also been used to produce quasi-interdigitated electrode fingers in a back-contact solar cell with a stable power conversion efficiency output of 3.2 %.[36] Another pseudo back-contact design achieved almost 4 % PCE by positioning an electron extracting TiO_2 material throughout the middle of the perovskite active layer, allowing holes to be collected at the back gold electrode.[164]

Another factor that must be considered when designing perovskite modules is the space used to connect individual cells. Here, cells can either be used to build a voltage (being connected in series) or build a current (being connected in parallel).

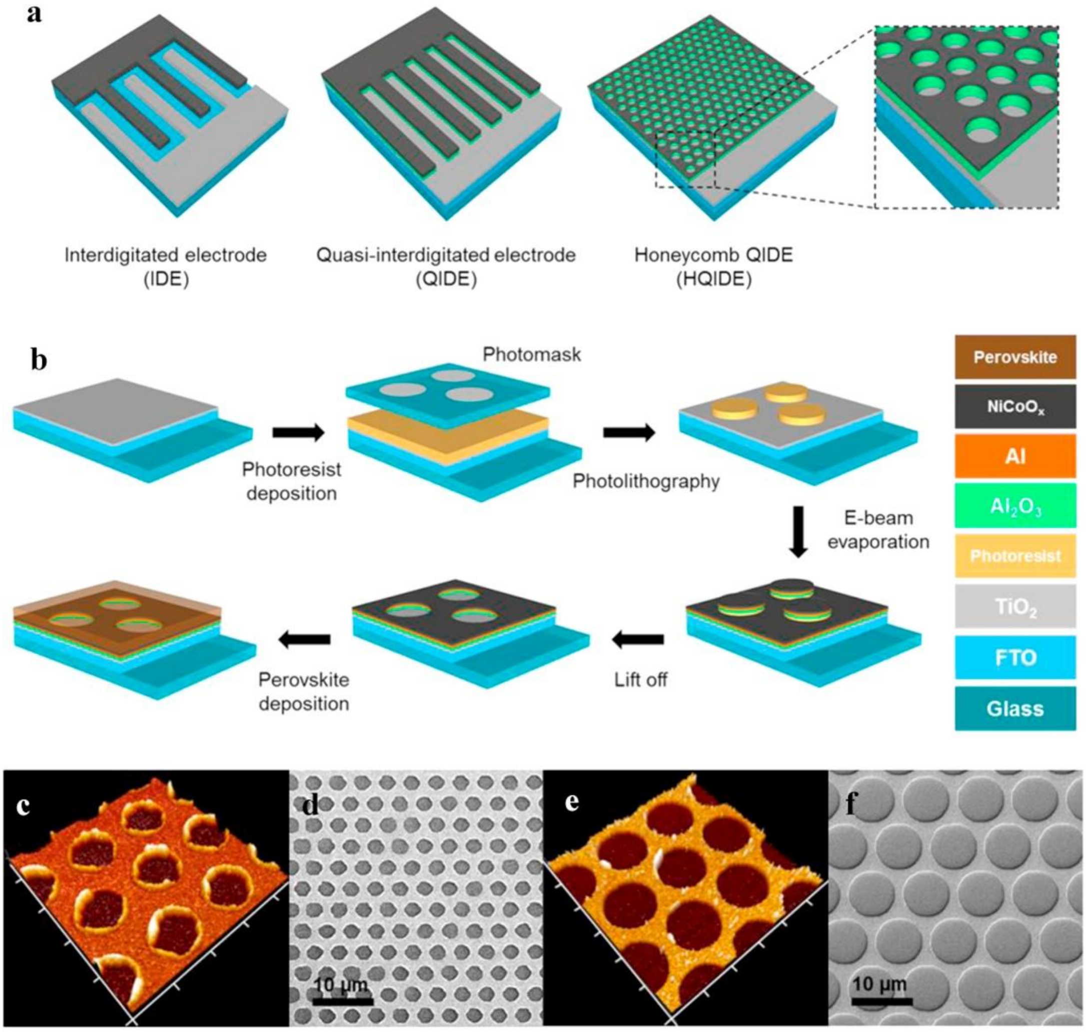

Figure 14: *Taken from Nano Energy, Q. Hou et al.*[165] *Schematics of previous back-contact solar cell architectures including interdigitated back-contacted (IBC), and more recent development of a honeycomb quasi-interdigitated back-contacted cell.*

2.10: Scalable Solution Processing

The ultimate cost-saving aspect of all thin-film PV is the potential for fast and low-temperature fabrication onto flexible substrates.

Solution processing is often described as both scalable and cost-effective. In this thesis all perovskite active layers and many charge transport layers are deposited from solutions via spin-coating. However, spin-coating is a lab-scale deposition technique, which is not scalable to large area deposition and wastes a large proportion of the material. Alternative scalable solution based processes include doctor blade coating, slot-dye coating, spray coating, rotary screen printing, inkjet printing, and flexographic printing.[170] These up-scaling processes are commonly cited as cheap processes, yet they come with many challenges.[34,171–173] These processes are not used in this thesis, although it is expected that the back-contact micro-grove mini-modules described in Chapter 7 could be coated using any one of these scalable deposition techniques.

2.11: Summary

The following experimental chapters (Chapter 4-7) are my own (and collaborating authors) contribution to the continued journey towards a commercial perovskite PV technology, leaping past the many hurdles that perovskite PV must overcome. Chapter 4 continues to search for alternative organic charge transport materials, Chapter 5 takes steps to enable more stable PSCs, Chapter 6 develops a scalable way of depositing metal oxide charge transport layers, and Chapter 7 acts as a proof of concept for an exciting scalable back-contact perovskite module.

2.12: References

[1] A. E. Becquerel, *Comptes Rendus L'Academie Des Sci* **1839**, *9*, 145.

[2] A. Einstein, *Ann. Phys.* **1905**, *17*, 132.

[3] Charles Kittel, *Introduction to Solid State Physics, 8th Edition*, Wiley, **2004**.

[4] R. M. Eisberg and R. Resnick, *Quantum Physics of Atoms, Molecules, Solids, Nuclei, and Particles*, New York: Wiley, **1974**.

[5] N. Greeves, S. Warrem, P. Wothers, J. Clayden, *Organic Chemistry*, Oxford University Press, **2012**.

[6] W. Brütting, *Physics of Organic Semiconductors*, WILEY-VCH Verlag, **2006**.

[7] M. A. Green, A. Ho-Baillie, H. J. Snaith, *Nat. Photonics* **2014**, *8*, 506.

[8] D. R. Lide, *Handbook of Chemistry and Physics, 79th Ed.*, CRC Press, **1998**.

[9] J. Nelson, *The Physics of Solar Cells*, Imperial College Press, **2003**.

[10] S. Braun, W. R. Salaneck, M. Fahlman, *Adv. Mater.* **2009**, *21*, 1450.

[11] H. Ishii, K. Sugiyama, E. Ito, K. Seki, *Adv. Mater.* **1999***, 11(8),* 605-625.

[12] "ASTM Standard G173-03- Standard Tables for Reference Solar Spectral Irradiances: Direct Normal and Hemispherical on 37° Tilted Surface" can be found under https://compass.astm.org/EDIT/html_annot.cgi?G173+03, **2012.**

[13] "NREL - Solar Spectra" can be found under https://www.nrel.gov/grid/solar-resource/spectra.html, **2012.**

[14] W. Shockley, H. J. Queisser, *J. Appl. Phys.* **1961**, *32*, 510.

[15] A. Polman, M. Knight, E. C. Garnett, B. Ehrler, W. C. Sinke, *Science.* **2016**, *352*, 6283

[16] H. J. Snaith, *J. Phys. Chem. Lett* **2013**, *4*, 3623–3630.

[17] "Oxford PV sets world record for PSC," can be found under https://www.oxfordpv.com/news/oxford-pv-sets-world-record-perovskite-solar-cell, **2018**.

[18] D. Zhao, C. Wang, Z. Song, Y. Yu, C. Chen, X. Zhao, K. Zhu, Y. Yan, *ACS Energy Lett.* **2018**, *3*, 305.

[19] C.-W. Chen, S.-Y. Hsiao, C.-Y. Chen, H.-W. Kang, Z.-Y. Huang, H.-W. Lin, *J. Mater. Chem. A* **2015**, *3*, 9152.

[20] C. Chen, S. Bae, W. Chang, Z. Hong, G. Li, Q. Chen, H. Zhou, Y. Yang, *Mater. Horizons* **2015**, *2,* 203-211.

[21] "Nature - A checklist for photovoltaic research" can be found at https://www.nature.com/articles/nmat4473, *Nat. Mater.* **2015**, *14*, 1073.

[22] L. Yalçin, R. Öztürk, *J. Optoelectron. Adv. Mater.* **2013**, *15*, 326.

[23] E. Zimmermann, K. K. Wong, M. Mïüller, H. Hu, P. Ehrenreich, M. Kohlstïädt, U. Wïürfel, S. Mastroianni, G. Mathiazhagan, A. Hinsch, T. P. Gujar, M. Thelakkat, T. Pfadler, L. Schmidt-Mende, *APL Mater.* **2016**, *4*, 091901.

[24] J. A. Christians, J. S. Manser, P. V. Kamat, *J. Phys. Chem. Lett.* **2015**, *6*, 852.

[25] H. J. Snaith, *Nat. Photonics* **2012**, *6*, 337.

[26] H. J. Snaith, *Energy Environ. Sci.* **2012**, *5*, 6513.

[27] L. M. Pazos-Outón, M. Szumilo, R. Lamboll, J. M. Richter, M. Crespo-Quesada, M. Abdi-Jalebi, H. J. Beeson, M. Vrućinić, M. Alsari, H. J. Snaith, B. Ehrler, R. H. Friend, F. Deschler, *Science*, **2016**, *351, 6280,* 1430-1433.

[28] S. Ravishankar, S. Gharibzadeh, C. Roldán-Carmona, G. Grancini, Y. Lee, M. Ralaiarisoa, A. M. Asiri, N. Koch, J. Bisquert, M. K. Nazeeruddin, *Joule* **2018**, *2*, 788.

[29] H. J. Snaith, *Nat. Mater.* **2018**, *17*, 372.

[30] M. Stolterfoht, C. M. Wolff, Y. Amir, A. Paulke, L. Perdigón-Toro, P. Caprioglio, D. Neher, *Energy Environ. Sci.* **2017**, *10*, 1530.

[31] M. W. Denhoff, N. Drolet, *Sol. Energy Mater. Sol. Cells* **2009**, *93*, 1499.

[32] D. Shi, V. Adinolfi, R. Comin, M. Yuan, E. Alarousu, A. Buin, Y. Chen, S. Hoogland, A. Rothenberger, K. Katsiev, Y. Losovyj, X. Zhang, P. A. Dowben, O. F. Mohammed, E. H. Sargent, O. M. Bakr, *Science* **2015,** *347, 6221,* 519-522.

[33] T. S. Sherkar, C. Momblona, L. Gil-Escrig, J. Ávila, M. Sessolo, H. J. Bolink, L. J. A. Koster, *ACS Energy Lett.* **2017**, *2*, 1214.

[34] T. C. Sum, N. Mathews, *Energy Environ. Sci.* **2014**, 2518.

[35] D. Zhao, M. Sexton, H. Y. Park, G. Baure, J. C. Nino, F. So, *Adv. Energy Mater.* **2015**, *5*, 6, 1401855.

[36] A. Jumabekov, E. Della Gaspera, Z. Xu, A. Chesman, J. van Embden, S. Bonke, Q. Bao, D. Vak, U. Bach, *J. Mater. Chem. C* **2016**, *4* 3125.

[37] W. Heisenberg, *Zeitschrift Fur Phys.* **1927**, *43*, 172.

[38] W. Pauli, *Zeitschrift Fur Phys* **1925**, *31*, 765.

[39] M. Fox, *Optical Properties of Solids*, Oxford University Press, **2001**.

[40] W. A. Harrison, *Electronic Structure and the Properties of Solids: The Physics of the Chemical Bond*, Dover Publications, **1989**.

[41] J. S. Blakemore, *Solid State Physics, 2nd Edition*, Cambridge University Press, **2008.**

[42] B. Wang, X. Xiao, T. Chen, *Nanoscale* **2014***, 6*, 12287-12297.

[43] G. Hodes, *Science* **2013**, *342*, 317.

[44] M. Grätzel, *Nat. Mater.* **2014**, *13*, 838.

[45] S. Colella, E. Mosconi, P. Fedeli, A. Listorti, F. Orlandi, P. Ferro, T. Besagni, A. Rizzo, G. Calestani, G. Gigli, F. De Angelis, R. Mosca, F. Gazza, *Chem. Mater.* **2013**, *25*, 4613.

[46] H. Yu, F. Wang, F. Xie, W. Li, J. Chen, N. Zhao, *Adv. Funct. Mater.* **2014**, *24*, 7102–7108.

[47] S. A. Kulkarni, T. Baikie, P. P. Boix, N. Yantara, N. Mathews, S. Mhaisalkar, *J. Mater. Chem. A* **2014**, *2*, 9221.

[48] G. E. Eperon, S. D. Stranks, C. Menelaou, M. B. Johnston, L. M. Herz, H. J. Snaith, *Energy Environ. Sci*, **2014**, 982.

[49] S. Lv, S. Pang, Y. Zhou, N. P. Padture, H. Hu, L. Wang, X. Zhou, H. Zhu, L. Zhang, C. Huang, G. Cui, *Phys. Chem. Chem. Phys.* **2014**, *16*, 19206.

[50] N. J. Jeon, J. H. Noh, W. S. Yang, Y. C. Kim, S. Ryu, J. Seo, S. Il Seok, *Nature* **2015**, *517*, 476.

[51] J. K. Nam, S. U. Chai, W. Cha, Y. J. Choi, W. Kim, M. S. Jung, J. Kwon, D. Kim, J. H. Park, *Nano Lett.* **2017**, *17, 3*, 2028-2033.

[52] M. Saliba, T. Matsui, J.-Y. Seo, K. Domanski, J.-P. Correa-Baena, M. K. Nazeeruddin, S. M. Zakeeruddin, W. Tress, A. Abate, A. Hagfeldt, M. Grätzel, *Energy Environ. Sci.,* **2016,** *9*, 1989-1997.

[53] M. Abdi-Jalebi, Z. Andaji-Garmaroudi, S. Cacovich, C. Stavrakas, B. Philippe, J. M. Richter, M. Alsari, E. P. Booker, E. M. Hutter, A. J. Pearson, S. Lilliu, T. J. Savenije, H. Rensmo, G. Divitini, C. Ducati, R. H. Friend, S. D. Stranks, *Nature* **2018**, *555*, 497.

[54] M. R. Filip, G. E. Eperon, H. J. Snaith, F. Giustino, *Nat. Commun.* **2014**, *5*, 1.

[55] W. Yin, Y. Yan, S. Wei, *J. Phys. Chem. Lett.* **2014**, *5*, 3625–3631.

[56] A. Amat, E. Mosconi, E. Ronca, C. Quarti, P. Umari, M. K. Nazeeruddin, M. Grätzel, F. De Angelis, *Nano Lett.* **2014**, *14*, 3608.

[57] C. Motta, F. El Mellouhi, S. Kais, N. Tabet, F. Alharbi, S. Sanvito, *Nat. Commun.* **2014**, *6*, 1.

[58] S. A. Bretschneider, J. Weickert, J. A. Dorman, L. Schmidt-Mende, *APL Mater.* **2014**, *2,* 040701.

[59] K. Wu, A. Bera, C. Ma, Y. Du, Y. Yang, L. Li, T. Wu, *Phys. Chem. Chem. Phys.* **2014**, *16*, 22476.

[60] A. Poglitsch, D. Weber, *J. Chem. Phys.* **1987**, *87*, 6373.

[61] G. Niu, X. Guo, L. Wang, *J. Mater. Chem. A* **2015**, *3*, 8970.

[62] T. Baikie, Y. Fang, J. M. Kadro, M. Schreyer, F. Wei, S. G. Mhaisalkar, M. Grätzel, T. J. White, *J. Mater. Chem. A* **2013**, *1*, 5628.

[63] T. M. Koh, K. Fu, Y. Fang, S. Chen, T. C. Sum, N. Mathews. *J. Phys. Chem. C* **2014**, *118*, 16458–16462.

[64] J.-H. Im, C.-R. Lee, J.-W. Lee, S.-W. Park, N.-G. Park, *Nanoscale* **2011**, *3*, 4088.

[65] S. D. Stranks, G. E. Eperon, G. Grancini, C. Menelaou, M. J. P. Alcocer, T. Leijtens, L. M. Herz, A. Petrozza, H. J. Snaith, *Science* **2013**, *342*, 341.

[66] W. S. Yang, J. H. Noh, N. J. Jeon, Y. C. Kim, S. Ryu, J. Seo, S. Il Seok, Science **2015**, 348, 6240, 1234-1237.

[67] J. J. Quinn, K.-S. Yi, *Solid State Physics - Principles and Modern Applications*, 8th Edition, Springer, **2018.**

[68] S. E. Braslavsky, *Pure Appl. Chem.* **2007**, *79*, 293.

[69] P. Lopez-Varo, J. A. Jiménez-Tejada, M. García-Rosell, S. Ravishankar, G. Garcia-Belmonte, J. Bisquert, O. Almora, *Adv. Energy Mater.* **2018**, *8*, 1702772.

[70] I. Mora-Seró, *Joule* **2018**, *2*, 585.

[71] J. Even, L. Pedesseau, C. Katan, *J. Phys. Chem. C* **2014**, *118*, 11566.

[72] Q. Lin, A. Armin, R. Chandra, R. Nagiri, P. L. Burn, P. Meredith, *Nat. Photonics* **2014**, *9*, 106.

[73] A. Miyata, A. Mitioglu, P. Plochocka, O. Portugall, J. T. Wang, S. D. Stranks, H. J. Snaith, R. J. Nicholas, **2015**, *11*, *7,* 582-587.

[74] V. D'Innocenzo, G. Grancini, M. J. P. Alcocer, A. R. S. Kandada, S. D. Stranks, M. M. Lee, G. Lanzani, H. J. Snaith, A. Petrozza, *Nat. Commun.* **2014**, *5*, 3586.

[75] G. X. N. Mathews, S. Sun, S. S. Lim, Y. M. Lam, M. Grätzel, S. Mhaisalkar, T. C. Sum, *Science* **2013**, *342*, 344.

[76] P. P. Boix, K. Nonomura, N. Mathews, S. G. Mhaisalkar, *Mater. Today* **2014**, *17*, 16.

[77] J. M. Ball, S. D. Stranks, M. T. Hörantner, S. Hüttner, W. Zhang, E. J. W. Crossland, I. Ramirez, M. Riede, M. B. Johnston, R. H. Friend, H. J. Snaith, *Energy Environ. Sci.* **2015**, *8*, 602.

[78] K. Tanaka, T. Takahashi, T. Ban, T. Kondo, K. Uchida, N. Miura, *Solid State Commun.* **2003**, *127*, 619.

[79] Q. Lin, A. Armin, R. Chandra, R. Nagiri, P. L. Burn, P. Meredith, *Nat. Photonics* **2014**, *9, 2* 106-112.

[80] C. Wehrenfennig, G. E. Eperon, M. B. JohFnston, H. J. Snaith, L. M. Herz, *Adv. Mater.* **2014**, *26*, 1584.

[81] N. K. Noel, B. Wenger, S. N. Habisreutinger, J. B. Patel, T. Crothers, Z. Wang, R. J. Nicholas, M. B. Johnston, L. M. Herz, H. J. Snaith, *ACS Energy Lett.* **2018**, *3,* 1233–1240.

[82] M. Van der Auweraer, F. C. De Schryver, P. M. Borsenberger, H. Bässler, *Adv. Mater.* **1994**, *6*, 199.

[83] Q. Dong, Y. Fang, Y. Shao, P. Mulligan, J. Qiu, L. Cao, J. Huang, *Science* **2015**, *347*, 967.

[84] C. Canali, C. Jacoboni, F. Nava, G. Ottaviani, A. Alberigi-Quaranta, *Phys. Rev. B* **1975**, *12*, 2265.

[85] L. H. Manger, M. B. Rowley, Y. Fu, A. K. Foote, M. T. Rea, S. L. Wood, S. Jin, J. C. Wright, R. H. Goldsmith, *J. Phys. Chem. C* **2017**, *121*, 1062.

[86] J. H. Heo, S. H. Im, J. H. Noh, T. N. Mandal, C.-S. Lim, J. A. Chang, Y. H. Lee, H. Kim, A. Sarkar, M. K. Nazeeruddin, M. Grätzel, S. Il Seok, *Nat. Photonics* **2013**, *7*, 486.

[87] M. M. Lee, J. Teuscher, T. Miyasaka, T. N. Murakami, H. J. Snaith, *Science* **2012**, *338*, 643.

[88] H.-S. Kim, C.-R. Lee, J.-H. Im, K.-B. Lee, T. Moehl, A. Marchioro, S.-J Moon, R. Humphry-Baker, J. H. Yum, J. E. Moser, M. Grätzel, N. Park, *Sci. Rep.* **2012**, *2*, 1.

[89] R. E. Peierls, *Quantum Theroy of Solids*, Clarendon Press, Oxford, **1955**.

[90] N. Tessler, Y. Preezant, N. Rappaport, Y. Roichman, *Adv. Mater.* **2009**, *21*, 2741.

[91] W. R. Salaneck, R. H. Friend, J. L. Brédas, *Phys. Rep.* **1999**, *319*, 231.

[92] O. V. Mikhnenko, P. W. M. Blom, T.-Q. Nguyen, *Energy Environ. Sci.* **2015**, *8*, 1867.

[93] D. Hertel, H. Bässler, *ChemPhysChem* **2008**, *9*, 666.

[94] A. Miller, E. Abrahams, *Phys. Rev.* **1960**, *120*, 745.

[95] J. L. Bredas, *J. Mol. Struct*, **1984**, 107.

[96] V. A. Kolesov, C. Fuentes-Hernandez, W.-F. Chou, N. Aizawa, F. A. Larrain, M. Wang, A. Perrotta, S. Choi, S. Graham, G. C. Bazan, T.-Q. Nguyen, S. R. Marder, B. Kippelen, *Nat. Mater.* **2016**, *16*, 474.

[97] Y. Hu, Z. D. Rengert, C. McDowell, M. J. Ford, M. Wang, A. Karki, A. T. Lill, G. C. Bazan, T. Q. Nguyen, *ACS Nano* **2018**, *12*, 3938.

[98] I. Salzmann, G. Heimel, M. Oehzelt, S. Winkler, N. Koch, *Acc. Chem. Res.* **2016**, *49*, 370.

[99] J. Euvrard, A. Revaux, P. A. Bayle, M. Bardet, D. Vuillaume, A. Kahn, *Org. Electron. physics, Mater. Appl.* **2018**, *53*, 135.

[100] A. Kahn, W. Zhao, W. Gao, H. Vázquez, F. Flores, *Chem. Phys.* **2006**, *325*, 129.

[101] B. Kippelen, J.-L. Brédas, *Energy Environ. Sci.* **2009**, *2*, 251.

[102] Y. W. Su, S. C. Lan, K. H. Wei, *Mater. Today* **2012**, *15*, 554.

[103] M. T. Greiner, M. G. Helander, W. M. Tang, Z. Bin Wang, J. Qiu, Z. H. Lu, *Nat. Mater.* **2012**, *11*, 76.

[104] C. Tao, J. Van Der Velden, L. Cabau, N. F. Montcada, S. Neutzner, A. R. Srimath Kandada, S. Marras, L. Brambilla, M. Tommasini, W. Xu, R. Sorrentino, A. Perinot, M. Caironi, C. Bertarelli, E. Palomares, A. Petrozza, *Adv. Mater.* **2017**, *29*, 1604493.

[105] X. Xu, C. Ma, Y. Cheng, Y. M. Xie, X. Yi, B. Gautam, S. Chen, H. W. Li, C. S. Lee, F. So, S. W. Tsang, *J. Power Sources* **2017**, *360*, 157.

[106] Z. H. Bakr, Q. Wali, A. Fakharuddin, L. Schmidt-Mende, T. M. Brown, R. Jose, *Nano Energy* **2017**, *34*, 271.

[107] S. Ameen, M. A. Rub, S. A. Kosa, K. A. Alamry, M. S. Akhtar, H. S. Shin, H. K. Seo, A. M. Asiri, M. K. Nazeeruddin, *ChemSusChem* **2016**, *9*, 10.

[108] A. Marchioro, J. Teuscher, D. Friedrich, M. Kunst, R. van de Krol, T. Moehl, M. Grätzel, J.-E. Moser, *Nat Phot.* **2014**, *8*, 250.

[109] R. Islam, G. Chen, P. Ramesh, J. Suh, N. Fuchigami, D. Lee, K. A. Littau, K. Weiner, R. T. Collins, K. C. Saraswat, *ACS Appl. Mater. Interfaces* **2017**, *9*, 17201.

[110] A. Kojima, K. Teshima, Y. Shirai, T. Miyasaka, *210th ECS Meet. Abstr #397.* **2008**, *MA2008-02, 1*, 27.

[111] A Kojima, K. Teshima, Y. Shirai, T. Miyasaka, *JACS. Com.* **2009**, *131, 17,* 6050.

[112] M. Liu, M. B. Johnston, H. J. Snaith, *Nature* **2013**, *501*, 395.

[113] Y.-J. Jeon, S. Lee, R. Kang, J.-E. Kim, J.-S. Yeo, S.-H. Lee, S.-S. Kim, J.-M. Yun, D.-Y. Kim, *Sci. Rep.* **2014**, 26.

[114] P. Schulz, E. Edri, S. Kirmayer, G. Hodes, D. Cahen, A. Kahn, *Energy Environ. Sci.* **2014,** *7*, 1377.

[115] M. Grätzel, *Nat. Mater.* **2014**, *13*, 838.

[116] A. Dualeh, T. Moehl, N. Tétreault, J. Teuscher, P. Gao, M. K. Nazeeruddin, M. Grätzel, *ACS Nano* **2014**, *8*, 362.

[117] H. J. Snaith, A. Abate, J. M. Ball, G. E. Eperon, T. Leijtens, N. K. Noel, S. D. Stranks, J. T.-W. Wang, K. Wojciechowski, W. Zhang, *J. Phys. Chem. Lett.* **2014**, *5,* 1511–1515.

[118] J. W. Jung, S. T. Williams, A. K.-Y. Jen, *RSC Adv.* **2014**, *4*, 62971.

[119] N. J. Jeon, J. H. Noh, Y. C. Kim, W. S. Yang, S. Ryu, S. Il Seok, *Nat. Mater.* **2014**, *13*, 1.

[120] N. K. Noel, S. N. Habisreutinger, B. Wenger, M. T. Klug, M. T. Hörantner, M. B. Johnston, R. J. Nicholas, D. T. Moore, H. J. Snaith, *Energy Environ. Sci.* **2017**, 10, 1, 145-152.

[121] W. Zhang, M. Saliba, D. T. Moore, S. Pathak, M. Horantner, T. Stergiopoulos, S. D. Stranks, G. E. Eperon, J. a Alexander-Webber, A. Abate, A. Sadhanala, S. Yao, Y. Chen, R. H. Friend, L. A Estroff, U. Wiesner, H. J. Snaith, *Nat. Commun.* **2014**, *6,* 6142.

[122] L. Q. Zhang, X. W. Zhang, Z. G. Yin, Q. Jiang, X. Liu, J. H. Meng, Y. J. Zhao, H. L. Wang, *J. Mater. Chem. A* **2015**, *3*, 12133.

[123] J. Liu, C. Gao, X. He, Q. Ye, L. Ouyang, D. Zhuang, C. Liao, J. Mei, W. Lau, *ACS Appl. Mater. Interfaces* **2015**, *7*, 24008.

[124] Y. Zhou, O. S. Game, S. Pang, N. P. Padture, *J. Phys. Chem. Lett.* **2015**, *6, 23,* 4827-4839.

[125] E. L. Unger, A. R. Bowring, C. J. Tassone, V. L. Pool, A. Gold-parker, R. Cheacharoen, K. H. Stone, E. T. Hoke, M. F. Toney, M. D. Mcgehee, *Chem. Mater.* **2014,** *26,* 7158–7165.

[126] M. Yang, Y. Zhou, Y. Zeng, C. S. Jiang, N. P. Padture, K. Zhu, *Adv. Mater.* **2015**, *27*, 6363.

[127] M. L. Petrus, Y. Hu, D. Moia, P. Calado, A. M. A. Leguy, P. R. F. Barnes, P. Docampo, *ChemSusChem* **2016**, *9*, 2699.

[128] K. Miyano, M. Yanagida, N. Tripathi, Y. Shirai, K. Miyano, M. Yanagida, N. Tripathi, Y. Shirai, *Appl. Phys. Lett.* **2015***, 106,* 093903.

[129] A. Leguy, Y. Hu, M. Campoy-Quiles, M. I. Alonso, O. J. Weber, P. Azarhoosh, M. van Schilfgaarde, M. T. Weller, T. Bein, J. Nelson, P. Docampo, P. R. F. Barnes, *Chem. Mater.* **2015**, *27, 9,* 3397-3407.

[130] E. J. Juarez-Perez, L. K. Ono, M. Maeda, Y. Jiang, Z. Hawash, Y. Qi, *J. Mater. Chem. A* **2018**, *6*, 9604.

[131] K. Domanski, E. A. Alharbi, A. Hagfeldt, M. Grätzel, W. Tress, *Nat. Energy* **2018**, *3*, 1.

[132] B. Conings, J. Drijkoningen, N. Gauquelin, A. Babayigit, J. D'Haen, L. D'Olieslaeger, A. Ethirajan, J. Verbeeck, J. Manca, E. Mosconi, F. De Angelis, H. Boyen, *Adv. Energy Mater.* **2015***, 5, 15,* 1500477.

[133] A. Binek, F. C. Hanusch, P. Docampo, T. Bein, *J. Phys. Chem. Lett.* **2015**, 1249.

[134] A. J. Pearson, G. E. Eperon, P. E. Hopkinson, S. N. Habisreutinger, J. T. W. Wang, H. J. Snaith, N. C. Greenham, *Adv. Energy Mater.* **2016**, *6*, 1.

[135] D. Bryant, N. Aristidou, S. Pont, I. Sanchez-Molina, T. Chotchunangatchaval, S. Wheeler, J. R. Durrant, S. A. Haque, *Energy Environ. Sci.* **2016**, *9*, 1655.

[136] N. Aristidou, C. Eames, I. Sanchez-Molina, X. Bu, J. Kosco, M. Saiful Islam, S. A. Haque, *Nat. Commun.* **2017**, *8*, 1.

[137] K. Domanski, J. P. Correa-Baena, N. Mine, M. K. Nazeeruddin, A. Abate, M. Saliba, W. Tress, A. Hagfeldt, M. Grätzel, *ACS Nano* **2016**, *10*, 6306.

[138] Y. Kato, L. K. Ono, M. V. Lee, S. Wang, S. R. Raga, Y. Qi, *Adv. Mater. Interfaces* **2015**, *2*, 2.

[139] J. Li, Q. Dong, N. Li, L. Wang, *Adv. Energy Mater.* **2017**, *7*, 1.

[140] J. Barbé, V. Kumar, M. J. Newman, H. K. H. Lee, S. M. Jain, H. Chen, C. Charbonneau, C. Rodenburg, W. C. Tsoi, *Sustain. Energy Fuels* **2018***, 2,* 905.

[141] Y.-Y. Yu, R.-S. Chiang, H.-L. Hsu, C.-C. Yang, C.-P. Chen, *Nanoscale* **2014**, *6*, 11403.

[142] W. Lee, M. Song, S. Park, S. Nam, J. Seo, H. Kim, Y. Kim, *Sci. Rep.* **2016**, *6*, 1.

[143] C. Bracher, B. G. Freestone, D. K. Mohamad, J. A. Smith, D. G. Lidzey, *Energy Sci. Eng.* **2018,** *6*, *1*, 35-46.

[144] A. J. Parnell, A. J. Cadby, A. D. F. Dunbar, G. L. Roberts, A. Plumridge, R. M. Dalgliesh, M. W. A. Skoda, R. A. L. Jones, *J. Polym. Sci. Part B Polym. Phys.* **2016**, *54*, 141.

[145] T. A. Berhe, W.-N. Su, C.-H. Chen, C.-J. Pan, J.-H. Cheng, H.-M. Chen, M.-C. Tsai, L.-Y. Chen, A. A. Dubale, B.-J. Hwang, *Energy Environ. Sci.* **2016**, *9*, 323.

[146] M. A. Henderson, W. S. Epling, C. L. Perkins, C. H. F. Peden, U. Diebold, *J. Phys. Chem. B* **1999**, *103*, 5328.

[147] G. Lu, A. Linsebigler, J. T. Yates, *J. Chem. Phys.* **1995**, *102*, 4657.

[148] J. Sun, J. Lu, B. Li, L. Jiang, A. S. R. Chesman, A. D. Scully, T. R. Gengenbach, Y. B. Cheng, J. J. Jasieniak, *Nano Energy* **2018**, *49*, 163.

[149] W. Chen, Y. Wu, Y. Yue, J. Liu, W. Zhang, X. Yang, H. Chen, E. Bi, I. Ashraful, M. Grätzel, L. Han, *Science.* **2015**, *350*, 944.

[150] S. Sajid, A. M. Elseman, H. Huang, J. Ji, S. Dou, H. Jiang, X. Liu, D. Wei, P. Cui, M. Li, *Nano Energy* **2018**, *51*, 408.

[151] Y. Lv, P. Xu, G. Ren, F. Chen, H. Nan, R. Liu, D. Wang, X. Tan, X. Liu, H. Zhang, Z.-K. Chen, *ACS Appl. Mater. Interfaces* **2018**, *10, 28,* 23928.

[152] H. Lee, Y. T. Huang, M. W. Horn, S. P. Feng, *Sci. Rep.* **2018**, *8*, 1.

[153] J. You, L. Meng, T. Bin Song, T. F. Guo, W. H. Chang, Z. Hong, H. Chen, H. Zhou, Q. Chen, Y. Liu, N. De Marco, Y. Yang, *Nat. Nanotechnol.* **2016**, *11*, 75.

[154] K. Yao, F. Li, Q. He, X. Wang, Y. Jiang, H. Huang, A. K. Y. Jen, *Nano Energy* **2017**, *40*, 155.

[155] M. Najafi, F. Di Giacomo, D. Zhang, S. Shanmugam, A. Senes, W. Verhees, A. Hadipour, Y. Galagan, T. Aernouts, S. Veenstra, R. Andriessen, *Small* **2018**, *14*, 1.

[156] J. Zhao, K. O. Brinkmann, T. Hu, N. Pourdavoud, T. Becker, T. Gahlmann, R. Heiderhoff, A. Polywka, P. Görrn, Y. Chen, B. Cheng, T. Riedl, *Adv. Energy Mater.* **2017**, *7*, 1602599.

[157] Z. Wang, Q. Lin, F. P. Chmiel, N. Sakai, L. M. Herz, H. J. Snaith, *Nat. Energy* **2017**, *17135*, 1.

[158] G. Grancini, C. Roldán-Carmona, I. Zimmermann, E. Mosconi, X. Lee, D. Martineau, S. Narbey, F. Oswald, F. De Angelis, M. Grätzel, M. K. Nazeeruddin, Nat. Commun. **2017,** *8*, 1.

[159] Y. Zhang, E. Bovill, J. Kingsley, A. R. Buckley, H. Yi, A. Iraqi, T. Wang, D. G. Lidzey, *Sci. Rep.* **2016**, *6*, 21632.

[160] Y. Zhang, H. Yi, A. Iraqi, J. Kingsley, A. Buckley, T. Wang, D. G. Lidzey, *Sci. Rep.* **2017**, *7*, 1.

[161] L. Shi, T. L. Young, J. Kim, Y. Sheng, L. Wang, Y. Chen, Z. Feng, M. J. Keevers, X. Hao, P. J. Verlinden, M. A. Green, A. W. Y. Ho-Baillie, *ACS Appl. Mater. Interfaces* **2017**, *9*, 25073.

[162] F. Matteocci, L. Cinà, E. Lamanna, S. Cacovich, G. Divitini, P. A. Midgley, C. Ducati, A. Di Carlo, *Nano Energy* **2016**, *30,* 162-172.

[163] Q. Dong, F. Liu, M. K. Wong, H. W. Tam, A. B. Djurišić, A. Ng, C. Surya, W. K. Chan, A. M. C. Ng, *ChemSusChem* **2016**, *9*, 2518.

[164] Z. Hu, G. Kapil, H. Shimazaki, S. S. Pandey, T. Ma, S. Hayase, *J. Phys. Chem. C* **2017**, *121*, 4214.

[165] Q. Hou, D. Bacal, A. N. Jumabekov, W. Li, Z. Wang, X. Lin, S. H. Ng, B. Tan, Q. Bao, A. S. R. Chesman, Y.-B. Cheng, U. Bach, *Nano Energy* **2018**, *50,* 710-716.

[166] G. W. P. Adhyaksa, E. Johlin, E. C. Garnett, *Nano Lett.* **2017**, *17*, 5206.

[167] S. Weber, I. M. Hermes, S. H. Turren Cruz, C. Gort, V. W. Bergmann, L. Gilson, A. Hagfeldt, M. Grätzel, W. Tress, R. Berger, *Energy Environ. Sci.* **2018**, *11*, 2404.

[168] L. M. Pazos-Outón, M. Szumilo, R. Lamboll, J. M. Richter, M. Crespo-Quesada, M. Abdi-Jalebi, H. J. Beeson, M. Vrućinić, M. Alsari, H. J. Snaith, B. Ehrler, R. H. Friend, F. Deschler, *Science* **2016**, *351*, 1430.

[169] M. Alsari, O. Bikondoa, J. Bishop, M. Abdi-Jalebi, L. Y. Ozer, M. Hampton, P. Thompson, M. T. Hörantner, S. Mahesh, C. Greenland, J. E. Macdonald, G. Palmisano, H. J. Snaith, D. G. Lidzey, S. D. Stranks, R. H. Friend, S. Lilliu, *Energy Environ. Sci.* **2018**, 18.

[170] R. R. Søndergaard, M. Hösel, F. C. Krebs, *J. Polym. Sci. Part B Polym. Phys.* **2013**, *51*, 16.

[171] A. Barrows, A. Pearson, C. Kwak, A. Dunbar, A. Buckley, D. G. Lidzey, *Energy Environ. Sci.* **2014**, *7*, 1.

[172] G. E. Eperon, V. M. Burlakov, P. Docampo, a Goriely, H. J. Snaith, *Adv. Funct. Mater.* **2014**, *24*, 151.

[173] Z. Xiao, C. Bi, Y. Shao, Q. Dong, Q. Wang, Y. Yuan, C. Wang, Y. Gao, J. Huang, *Energy Environ. Sci.* **2014**, *7, 8,* 2619-2623.

Chapter 3

Experimental Methods

3.0: Introduction

This chapter describes the methodology used to characterise charge transport and perovskite materials. In addition, Appendix A contains fabrication details used to make PSCs. The characterisation techniques used in Chapters 4-7 are used with the aim of understanding and optimising the device performance metrics and stability of perovskite photovoltaics.

3.1: Materials

The electronic band structure and relative affinity of semiconductors and metals has been already been discussed in the Chapter 2. Figure 1 presents the band gaps, work functions, conduction bands (CB), valence bands (VB), highest occupied molecular orbitals (HOMO) and lowest occupied molecular orbitals (LUMO) energies from vacuum, for a series of common materials used in perovskite solar cells (PSCs). These have been averaged from values aggregated from literature, where the reported energies from vacuum vary depending on the fabrication route and measurement technique used (including cyclic voltammetry, kelvin probe and UV photoelectron spectroscopy (UPS)).[1-20]

Gold (Au), Silver (Ag), Titanium (Ti), Nickle (Ni), Titanium dioxide (TiO_2), Nickle oxide (NiO), and aluminium oxide (Al_2O_3) are all used in the following chapters. The materials and chemical structures of organics used in following chapters, all of which are contained in Figure 1, are listed below:

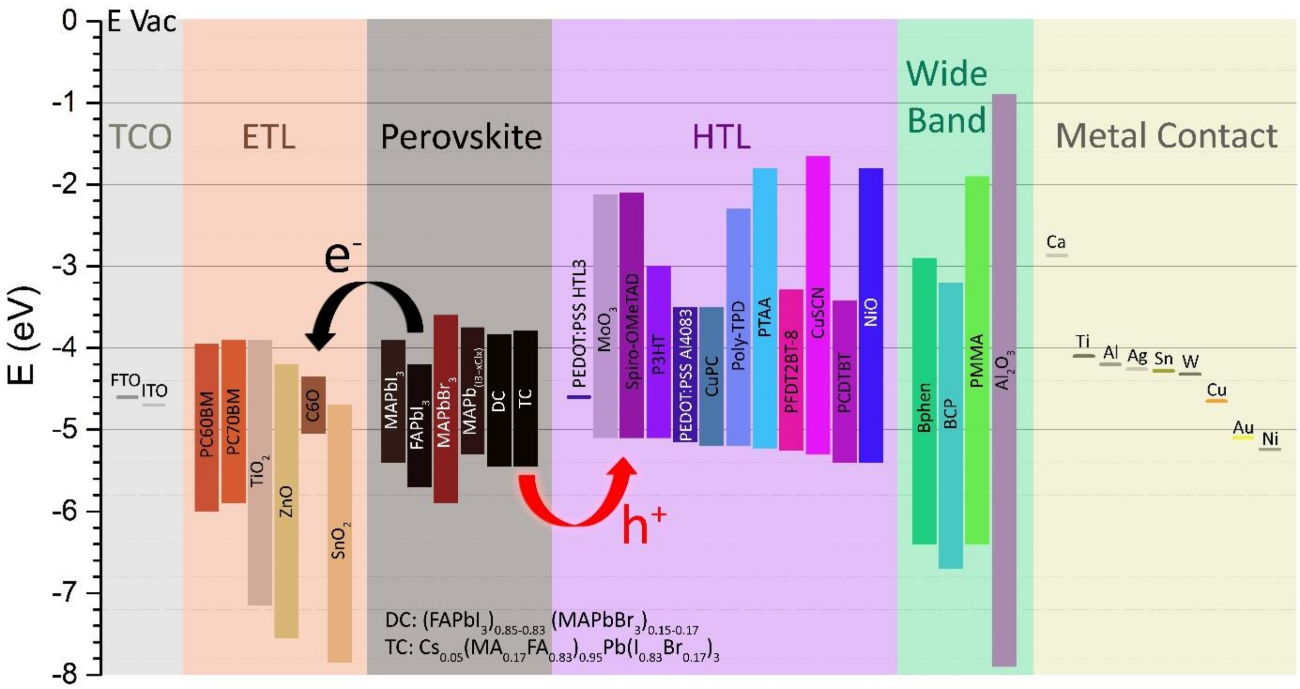

Figure 1: *Conduction bands (CB), valence bands (VB), highest occupied molecular orbital (HOMO) and lowest occupied molecular orbital (LUMO) energies from vacuum, for common materials used in perovskite solar cells.*

Hole transporting Polymers

The chemical structures of polymers used as hole transporting layers (HTLs) in PSCs are shown in Figure 2. These include: poly(3,4-ethylenedioxythiophene)-poly(styrenesulfonate)(PEDOT:PSS), poly[N,N'-bis(4-butylphenyl)-N,N'-bisphenyl benzidine](Poly-TPD), and poly[bis(4-phenyl)(2,4,6-trimethylphenyl)amine Poly(triarylamine) (PTAA).

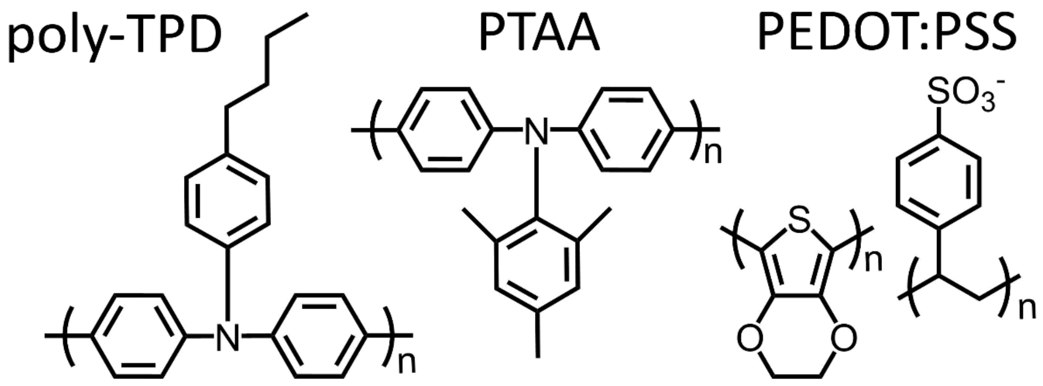

Figure 2: *Chemical structures of organic hole transporting polymers used in this thesis.*

Organic Small Molecules

The chemical structures of organic small molecules used as hole transporting layers (HTLs) in PSCs are provided in Figure 3. These include: 2,2',7,7'-Tetrakis[N,N-di(4-methoxyphenyl)amino]-9,9'-spirobifluorene (spiro-OMeTAD), and copper(II) phthalocyanine (CuPc).

Figure 3 also contains the structure of a large band gap small molecule that is used for electron transporting interfaces as a band bending material resulting in favourable electron extraction: *bathophenanthroline (Bphen)*

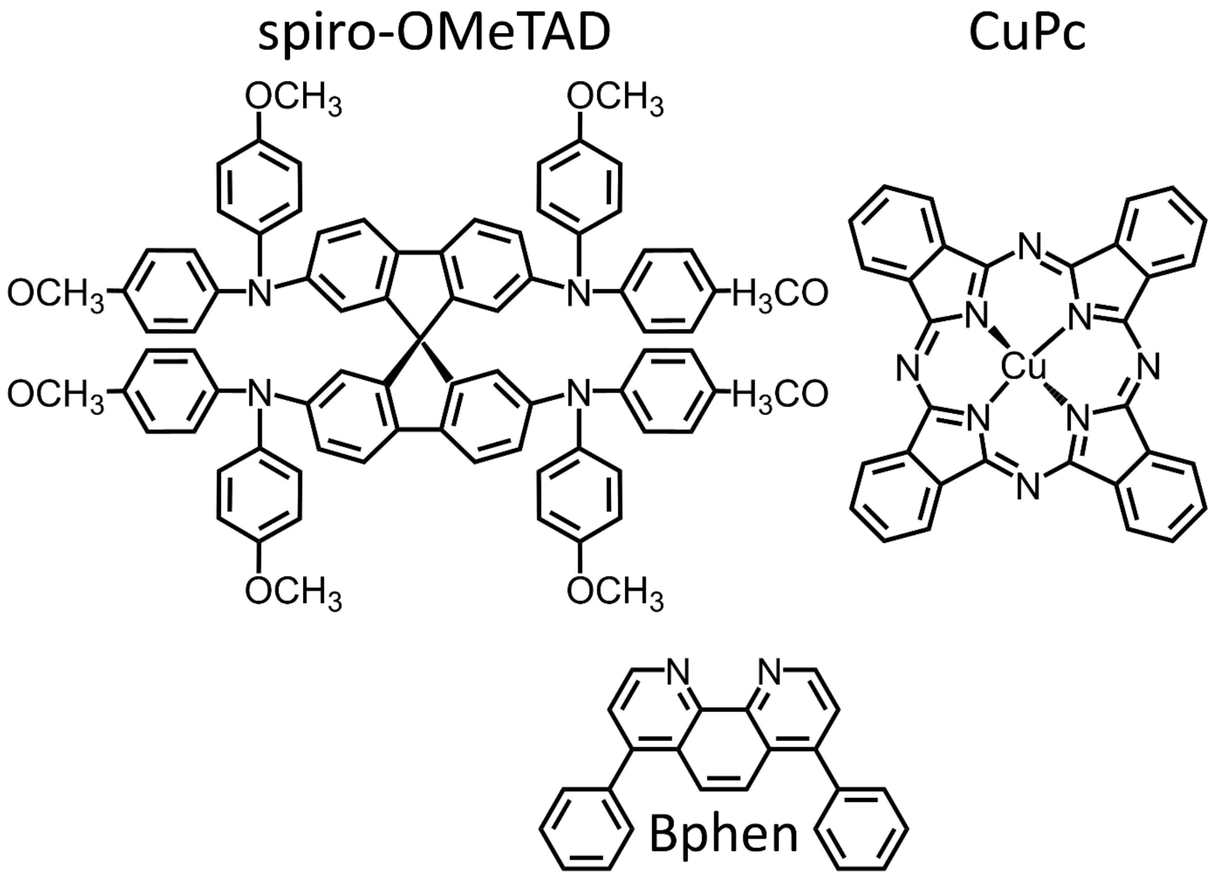

Figure 3: *Chemical structures of organic small molecules used in this thesis.*

Organic Carbazole Based Polymer Donors

The chemical structure of the organic carbazole based polymer donor used as a hole transporting layer (HTL) in PSCs is shown in Figure 4: poly[N-9'-heptadecanyl-2,7-carbazole-alt-5,5-(4',7'-di-2-thienyl-2',1',3'-benzothiadiazole)] (PCDTBT).

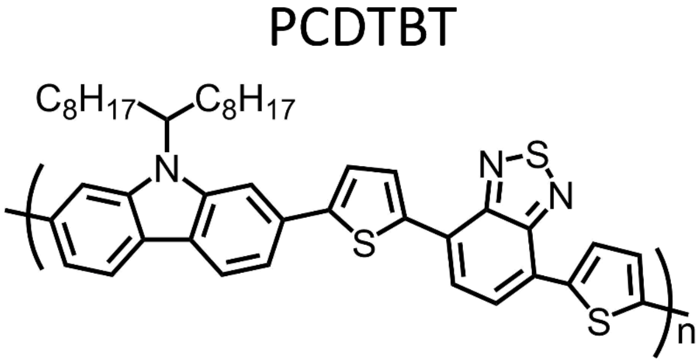

Figure 4: *Chemical structure of organic carbazole based polymer donor used in this thesis.*

Organic Electron Transporting (accepting) Fullerenes.

The chemical structure of organic fullerenes used as electron transporting layers (ETLs) in PSCs are provided in Figure 5. These include:[6,6]-Phenyl-C61/71-butyric acid methyl ester ($PC_{60/70}BM$) and, C60.

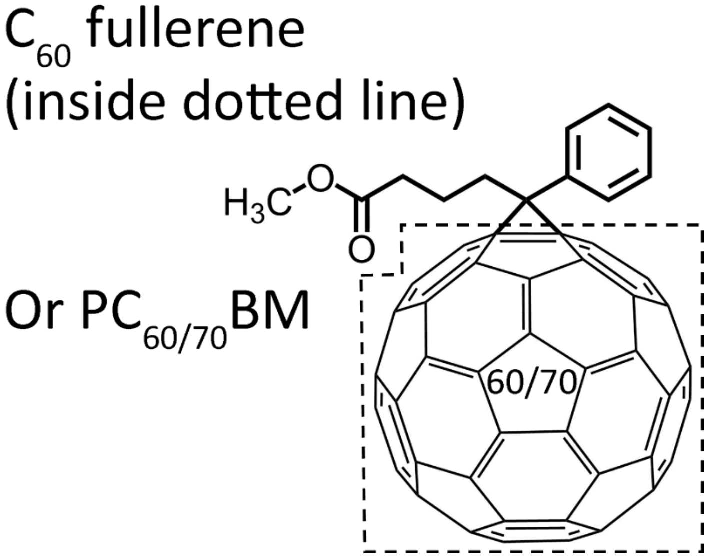

Figure 5: *Chemical structure of fullerene-based electron acceptors used in this thesis.*

Organic Dopants

The chemical structures of organic dopants used in PSCs are shown in Figure 6. These include: tris(2-(1H-pyrazol-1-yl)-4-tert-butylpyridine)cobalt(III) tri[bis(trifluoromethane)sulfonimide] (FK 209 Co(III) with TFSI salt or PF6), 4-tert-butylpyridine (TBP), lithium bis(trifluoromethanesulfonyl)imide (LiTFSI), and 2,3,5,6-Tetrafluoro-7,7,8,8-tetracyanoquinodimethane (F4-TCNQ).

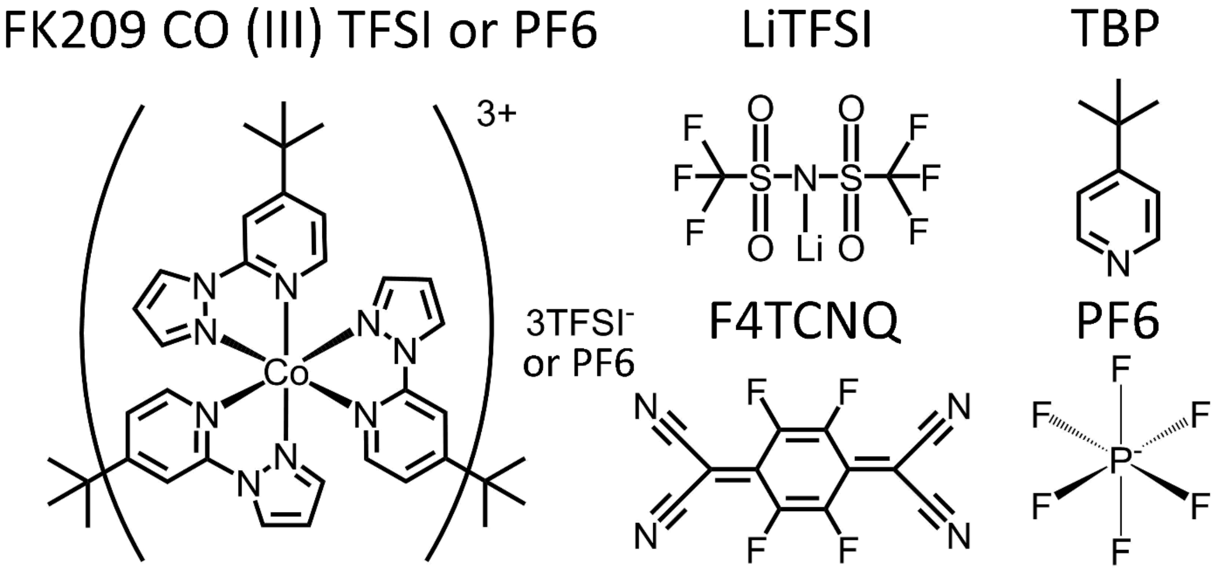

Figure 6: *Chemical structures of organic dopants used in this thesis.*

Organic Encapsulating Interlayer

The chemical structure of the organic encapsulating interlayer used in PSCs is shown in Figure 7:polyvinylpyrrolidone (PVP).

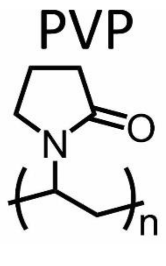

Figure 7: *Chemical structures of polymeric interlayer used in this thesis.*

3.2: Deposition Techniques

3.2.1: Evaporation

Solid materials can be heated to the point at which they vaporise. When this is done inside a vacuum chamber, the high vacuum allows the evaporated material to travel through the vacuum chamber without colliding with any gas molecules, ultimately nucleating on a target surface. Multiple evaporation sources can be used simultaneously, and source materials themselves can be a mixture of materials; e.g. a metal alloys or carbon doped metal oxides.

In thermal evaporation, a high current is passed through a resistive a boat (or a wire holding a crucible) to heat the source material until it evaporates. Once calibrated, a quartz crystal rate monitor vibrating at a target known frequency can detect the rate of material arrival by calculating the change in oscillation frequency upon arrival of evaporated material (the material density is required together with its acoustic impedance). In electron-beam evaporation, electron emission from a heated tungsten filament is accelerated in a beam to reach a hearth. A source material can either be placed directly into the hearth or inside a crucible. The focussed electron-beam is scanned in a pattern across the source material, heating it until it evaporates. Electron-beam evaporation can evaporate materials with very high vaporisation temperatures. Deposition rates can exceed 10s of nanometres a second.

Typically, a stable rate of evaporation is achieved, and the substrates are rotated, enabling the deposition of a uniform and compact film. Some materials will need a base layer to promote adhesion, for example, a layer of chromium is often used as a good first adhesion layer for metals such as gold.

Oxygen can be introduced into the vacuum chamber during evaporation in order to oxidise the vaporised material and create an oxide film. Evaporation of material typically occurs directionally from the source material, a property which is utilised in Chapter 7 of this thesis.

3.2.2: Solution Processing

The printability of materials has been the driving force behind much research related to organic solar cells, organic light emitted diodes and PSCs. When considering a new solvent for a solute it is important consider the density, boiling point, and polarity of that solvent. Ultimately solution processing is reliant on either a material being dispersed evenly throughout a liquid (a suspension), or a solute being well dissolved by a solvent (a solution).

Solvents can be categorised by their dielectric constant, split into polar solvents with high dielectric constants and non-polar solvents with lower dielectric constant (<15 ε_R). The polarity of a molecule is described by its (electric) dipole moment which is a measure of the separation of charge within the molecule. Polar solvents are further categorised into protic and aprotic solvents which solvate negatively charged solutes and positively charged solutes respectively. Generally, the solubility of a solute in a solvent is categorised on a like-for-like basis, where similar solvents are expected to dissolve similar solutes. Hansen-Hildebrand categorisation is most commonly used, where the dispersion (δ_d) and dipolar intermolecular forces between molecules (δ_p), alongside the cohesive energy density (δ_h) of the material, are used as metrics to compare solvents on a like-for-like basis.[21] Donor number is a measure of a solvents ability to solvate Lewis acids and cations.

A stack of solution processed films can be deposited consecutively provided that the solvents used do not dissolve the last layer that came before it. Solvents are typically anhydrous, stored in an inert atmosphere and measured out using needles, syringes, and pipettors of various sizes.

3.2.3: Solvents

Table 1 lists the properties of solvents used in this thesis, whilst Figure 8 shows the chemical structures of these solvents. These include: ethanol (EtOH), methanol (MeOH), isopropyl alcohol (IPA), toluene, chlorobenzene, dimethyl sulfoxide (DMSO), dimethylformamide (DMF), and acetonitrile (ACE).

Solvent	Chemical Formula	Donor Number	Dielectric Constant	Polar, Non-Polar, Alcohol	Protic or Aprotic	Dipole Moment	Bioling Point	Density	Molar Mass	Hansen Solubility Parameters		
		kJmol^{-1}				D	^{o}C	gmL^{-1}	gmol^{-1}	δ_d	δ_p	δ_h
EtOh	CH_3CH_2OH	132.00	24.6	Alcohol	Protic	1.69	78	0.789	46.07	15.8	8.8	19.4
MeOH	CH_3OH	79	32.6	Alcohol (Polar)	Protic	1.69	65	0.792	32.04	14.7	12.3	22.3
IPA	$(CH_3)_2CHOH$	89.00	18.3	Alcohol	Protic	1.66	82	0.786	60.1	15.8	6.1	16.4
Toluene	$C_6H_5CH_3$	0.40	2.38	Non-Polar	n/a	0.36	111.00	0.867	92.14	18	1.4	2
Chlorobenzene	C_6H_5Cl	14.00	5.69	Non-Polar	n/a	1.50	132	1.11	112.56	19	4.3	2
DMSO	$(CH_3)_2SO$	125.00	47	Polar	Aprotic	3.96	189.00	1.1	78.13	18.4	16.4	10.2
DMF	C_3H_7NO	111.00	38.25	Polar	Aprotic	3.86	153.00	0.95	73.10	17.4	13.7	11.3
ACN	CH_3CN	59.00	36.64	Polar	Aprotic	3.92	82	0.786	41.05	15.3	18	6.1

Table 1: *Properties of solvents used in this thesis.*

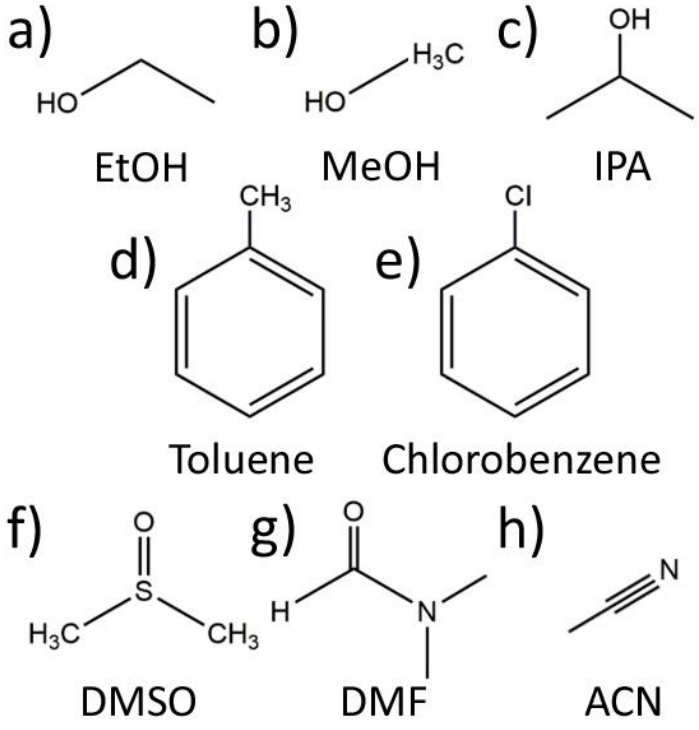

Figure 8: *Chemical structures of solvents used in this thesis.*

3.2.4: Making Solutions

The first step in any perovskite PV development or optimization experiment is to make the perovskite precursor solution. The dry powders and solvents used are detailed in Appendix A. Chemical precursors may be significantly different depending on the supplier, the batch or the purity of that product and so care should be taken when selecting the supplier and product used to produce the perovskite. An example is the solubility of PbI_2 which can be different depending on its purity. The purity and the supplier of research materials were maintained throughout each series of experiments. Given that many of the chemicals that make up the precursor are hygroscopic, it is common practise to only use anhydrous solvents and to avoid humid conditions when storing and weighing out chemicals for perovskite precursors. Solutions and dry powders used here were stored in either a desiccator or a N_2 filled glovebox. Perovskite solutions were always made fresh. Wherever possible a magnetic stir bar or vortex mixer were used to help agitate and dissolve dry powders, rather than heating the solution and generating acids (e.g DMF turning to formic acid)[22] or degraded organic components (e.g acetate degradation). Solutions were typically filtered before use to remove large aggregates that may cause comets and pinholes when deposition is performed. The thickness of a thin-film may be tuned by altering the concentration of the solution. This relationship is linear at low viscosities.

3.2.5: Spin Coating

The primary fabrication technique used here for thin film deposition is spin coating. Figure 9a demonstrates the spin coating process. (i) A substrate is placed onto a chuck with an indentation or a vacuum feed to hold the substrate in place. 10-200ul of solution was deposited onto the substrate before it started spinning (static deposition), (ii) The chuck was then accelerated rapidly (or at a specified lower acceleration) to spin speeds between 800-6000 rotations per minute (rpm). Alternatively, the solution was dripped or quickly dropped onto the substrate whilst it is spinning (dynamic deposition). During the spin coating process the majority of the solution is wasted and flung from the surface. (iii) The remaining film of solvent becomes more concentrated as more solvent is removed, until the solute begins to drop out of the solution. (iv) A thin-film of material is left behind. Depending on the choice of material and solvent the drying process can happen in different ways. For example, a solvent with a higher boiling point will likely remain trapped in the film until the film is thermally annealed. Multiple spin cycles and multiple solvents can be deposited throughout a spin coating deposition process. For example, an anti-solvent is often used to quench the perovskite crystallisation during the spin cycle. Spin coating can be performed in a variety of environments. Substrates can be heated before spin coating to accelerate the formation of a thin-film. In the context of perovskite solar cells, many materials are best solution processed in a dry or inert atmosphere. There are several studies on drying fronts, edge effects and spin coating related defects which describe this process more thoroughly.[23–25]

Spin speed ω (rpm) is often used to tune film thickness t by using the proportional relationship provided in Equation 1.[23]

$$t \propto \frac{1}{\sqrt{\omega}} \qquad (Eq. 1)$$

3.2.6: Contact Angle Goniometry

The ability for a liquid to coat a surface is known as its wettability. When a droplet of liquid touches a surface, the surface energy of the solid and the surface tension of liquid will determine if the liquid stays on the surface, as well as how quickly and how far the liquid spreads out on the surface. The difference in dielectric constant (related to miscibility and solubility) between the solvent and the film, the viscosity and density of the solvent, the density, thickness and roughness of the film, the size of the droplet and the environment in which the measurement is taken all contribute to the nature of the liquid/gas, solid/gas and solid/liquid boundaries, which ultimately determines the resultant contact angle.[26–29]

The surface free energy of the solid (σ_{SG}) is related to the surface tension of the liquid (σ_{LG}), the interfacial tension between the solid and liquid (σ_{SL}) and the contact angle (Θ) as described by Young's equation (Equation 2).

$$\sigma_{\mathrm{SG}} = \sigma_{\mathrm{SL}} + \sigma_{\mathrm{LG}} \cos\theta \qquad (Eq. 2)$$

Figure 9b is a pictorial representation of a typical sessile contact angle measurement. The angle the solution makes relative to the substrate is measured using a lamp and a camera. As a solution is deposited onto a substrate it can wet the surface in several ways: (1) Complete dewetting from the surface forming a droplet. (2) Partial dewetting forming a droplet with contact angle over 90°. (3) Partial wetting of the surface with droplet spreading out and angle less than 90°. (4) Complete wetting of the surface, forming a smooth flat film of solution. Contact angle measurements can be used to determine if the deposition of a solution is suitable for a certain substrate. It is also a good indicator of the affinity of a substrate to certain solvents, the clearest example being the determination of how hydrophobic or hydrophilic a material is.

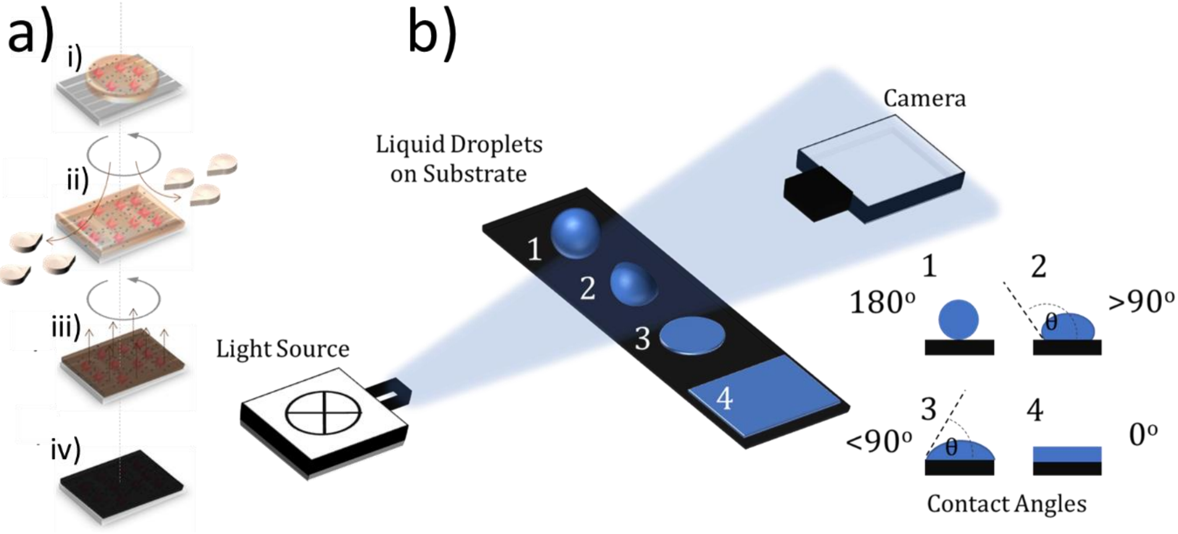

Figure 9: *Solution deposition. a) Spin coating of solution to deposit a film of material. b) Contact angle goniometry.*

3.2.7: Pre/Post-Deposition Treatment

The wettability of solutions and adhesion of evaporation can be improved by the cleaning of surfaces and surface energy modification caused by a UV-ozone (UVO) treatment. Here, a sample is illuminated with UV in air, leading to formation of individual oxygen radicals which go on to form O_3 when combined with other O_2 molecules. Contaminants on the irradiated substrates can undergo photoexcitation followed by reaction with ozone, liberating any organic material from the surface of the substrate. UVO has also been known to change the stoichiometry of metal oxides, for example; the introduction of Ni vacancies in NiO[30], or oxygen vacancies in TiO_2.[31]

Most solvents will not be completely liberated from a thin-film until the thin-film has been heated, placed under a vacuum, or a combination of both. This heating is typically done in an oven or on a hotplate. In the context of perovskite solar cells, the same processes are used to extract solvent from the film and to grow perovskite crystal grains. Upon drying, stoichiometric perovskite solutions will often immediately convert to black,[32] whilst excess organic non-stoichiometric solutions have significantly retarded perovskite crystallisation that requires sublimation of the excess organic material before grain growth starts to occur.[33] Solvent annealing (a process used to grow large crystal grains) is described in detail in Chapter 5.

3.3: Device Characterisation

Typical conventional flat cell perovskite solar cell and flexible back-contact groove solar cells are characterised using the following techniques.

3.3.1: Current-Voltage Measurements

The device performance metrics (described in Chapter 2) are determined as follows. A Newport 92251A-1000 solar simulator was used to illuminate devices through a 0.0256 cm^2 aperture mask. Before each set of measurements, the intensity was calibrated to 100 $mWcm^{-2}$ using an NREL certified silicon reference cell. Typically, the applied bias was swept from 0.0 V to +1.2 V and back again at a scan speed of 0.4 Vs^{-1}, using a Keithley 237 source measure unit. The V_{MPP} of each device was extracted from the JV scans, and the stabilised power output was recorded by holding the devices at their V_{MPP}.

Different sweep speeds are used for the micro-groove mini-modules described in Chapter 7. A stabilised measurement at 0 V was used to determine the charge polarity of groove-based devices. This measurement was also used to check for instability in current output, ensuring that any current detected was not due to electrochemical capacitive reactions.

3.3.2: External Quantum Efficiency (EQE)

The EQE was calculated by the method described previously in Chapter 2. Figure 10a is a schematic of the EQE setup, which comprised of a halogen light source (L.O.T.-Oriel GmbH & Co, 10 - 150 W halogen source), a monochromator grating (Spectral Products, DK 240), and a calibration silicon photodetector (Newport 818-uv). EQE spectra were taken by measuring the generated photocurrent with a source measure unit (Ossila, X-100) while irradiating with the monochromatic source.

3.3.3: Lifetime testing

Device aging was completed using an Atlas Suntest CPS+ with a 1500 W Xenon bulb, quartz IR reducing filters and internal reflectors. It has previously been shown that the lamp spectrum approximately matches AM1.5G (See Figure 10b). The Xenon bulb and internal reflectors produced an irradiance level of 100 $mWcm^{-2}$.

As shown in Figure 10c, seven silicon photodiodes (that can account for fluctuations in the illumination intensity) were used to normalise photocurrent data obtained using the set up. Device performance was determined from reverse sweep *JV* measurements. Here, the applied bias was swept from 1.15 V to 0 V at a scan speed of 0.05 Vs^{-1} using a Keithley 2400 source measure unit. Devices were not swept into deep reverse bias as this was found to reduce device stability (see Appendix B). Devices were held at open circuit between measurements, with every device scanned every 15 minutes. The temperature of the PSCs inside the Suntest was (42 ± 3) °C during operation. The humidity was not controlled, but was found to be within the range of (38 ± 6) % RH over the entire course of device exposure. PSCs mounted in the Suntest were not covered by an aperture mask during lifetime testing, and thus device metrics were normalised to their initial values. T80 lifetimes were extracted directly (when possible) or extrapolated using a linear fit applied to the post burn-in region.

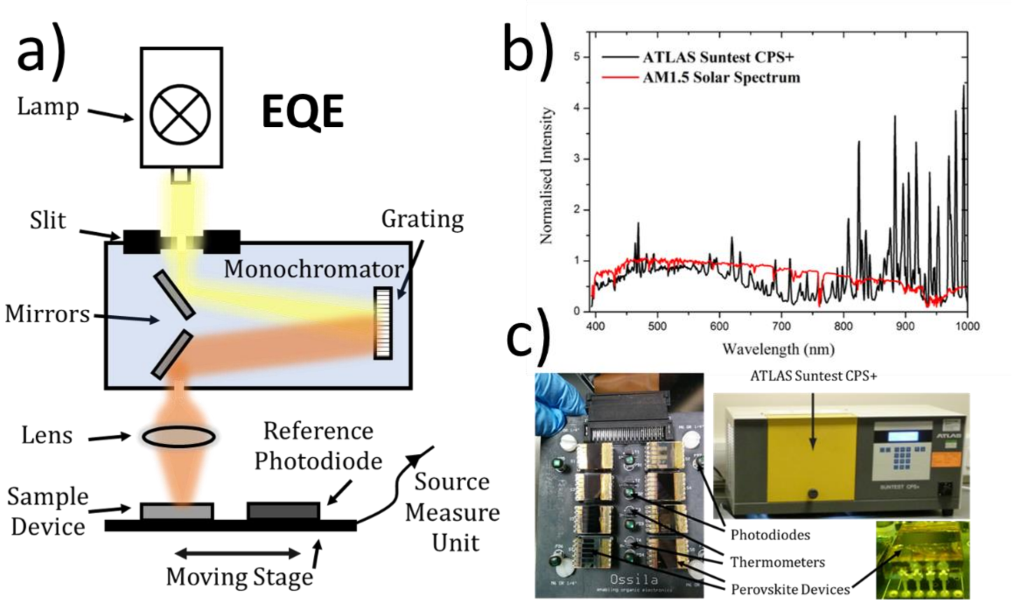

Figure 10: *Device characterisation. a) Schematic of external quantum efficiency (EQE). b) The ATLAS Suntest CPS+ Xenon lamp spectra compared to the AM1.5 solar spectra, from Edward S. R. Bovill's thesis 'The Air Stability and Operational Lifetime of Organic Photovoltaic Materials and Devices'. c) Picture of Atlas Suntest CPS+ with photodiodes, thermometers and mounted perovskite devices.*

3.3.4: Conductivity

Conductivity measurements were prepared on interdigitated (ID) indium tin oxide (ITO) substrates with channel widths varying from 50 to 200 μm. The conductivity was extracted from the high electric-field region, beyond the charge injection inflections of I-V scans measurements. These were taken using a Keithley 237 source measure unit, sweeping from -10 V to +10V and back again at various scan speeds on samples with various channel widths.

3.4: Microscopy and Profilometry

3.4.1: Focussed Ion Beam-Scanning Electron Microscopy (FIB-SEM)

Fractured flat devices were attached to 1 cm diameter stubs using electrically-conductive silver paint and allowed to dry before being loaded into a scanning electron microscope (SEM). Flexible plastic groove devices were mounted on carbon adhesive discs and sputter coated with 10 nm of gold-palladium using a Cressington 108 auto coating unit.

A schematic of a focussed ion beam (FIB)-SEM is shown in Figure 11a. A heated tungsten filament emits electrons which are directed by a strong electric field (anode) and focused by a series of magnetic lenses. The beam passes through a scanning coil which raster scans the beam across a sample surface. The entire setup is pumped down to high vacuum so that the electrons do not interact with gas molecules. Higher resolution is typically obtaining from using higher accelerating voltages. Higher voltages also cause faster charge build up in samples, which results in enhanced sample degradation. Both electrons and X-rays are given off when the sample is bombarded with the electron-beam. Electrons are typically detected with a scintillator and photomultiplier. Electrons are emitted as either back-scattered or secondary emission elections. Back-scattered electrons provide elemental contrast on the image of the sample, as their intensity is dependent on atomic number.[34,35] A separate set of magnetic optics and an ion source is used to create a focused ion beam, which can also be used to mill the surface of a sample, enabling the imaging of sample cross-sections.

An Inspect F, FEI Helios NanoLab G3 UC and Nova Nano 450 scanning electron microscope (SEM) was used to image flat thin-films and PSC devices. Here, all the samples were imaged using a through-lens detector (TLD) with a beam current of ~21 pA and an accelerating voltage of around 1-2 keV. For top view samples, perovskite was deposited on ITO/poly-TPD substrates. FEI Helios 600 Nanolab was used to image plastic groove devices. Milling of the cross-sections was carried out using a 30 kV gallium ion beam with currents of 2.8 or 6.5 nA. Electron-beam imaging of the milled cross-section was performed at 3 kV, 0.17 nA using an in-lens imaging mode.

3.4.2: Atomic Force Microscopy (AFM)

Figure 11b demonstrates how AFM can be used to characterise the surface of a sample. A probe which is typically ~10nm in size is attached to a cantilever and scanned across a surface. The thin-film causes the cantilever to move, which in turn deflects a laser that is illuminated onto the surface of the cantilever. A quadrant photodiode which has been aligned to capture the reflected beam can then be used to determine the height over which the cantilever is deflected as it moves.[36,37] AFM can be operated in contact mode or tapping mode. In tapping mode, an oscillating tip is brought into contact with the film, at which point the oscillation becomes dampened. This change in oscillation is monitored by a feedback loop, which modulates the tip height to maintain its initial oscillation amplitude. The height change required to always maintain this amplitude is recorded. Tapping mode is typically used to avoid issues that occur when tips are dragged along soft or very rough samples.[38] A Veeco Dimension 3100 operated in tapping mode was used to characterise thin-films.

3.4.3: Dektak Surface Profilometry

A step in a film is created by either using an evaporation mask for evaporated thin-films, or by scratching a trench in a solution-processed thin-film. As Figure 11c shows, a Dektak stylus can be scanned or mapped across the film to determine the surface roughness of the flat areas and thickness of the film.

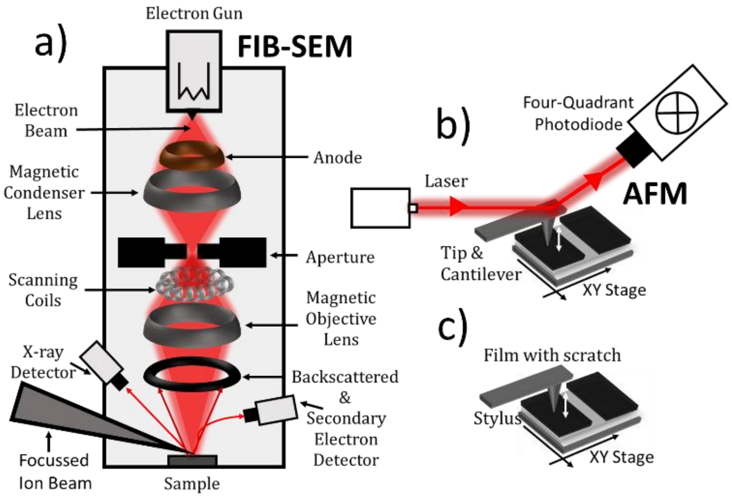

Figure 11: *Surface and cross-section morphology characterisation. Schematics of: a) focussed ion beam-scanning electron microscopy (FIB-SEM), b) atomic force microscopy (AFM), and c) surface profilometry.*

3.5: Spectroscopy

Schematics for all spectroscopic techniques used in this thesis are presented in Figure 12 below:

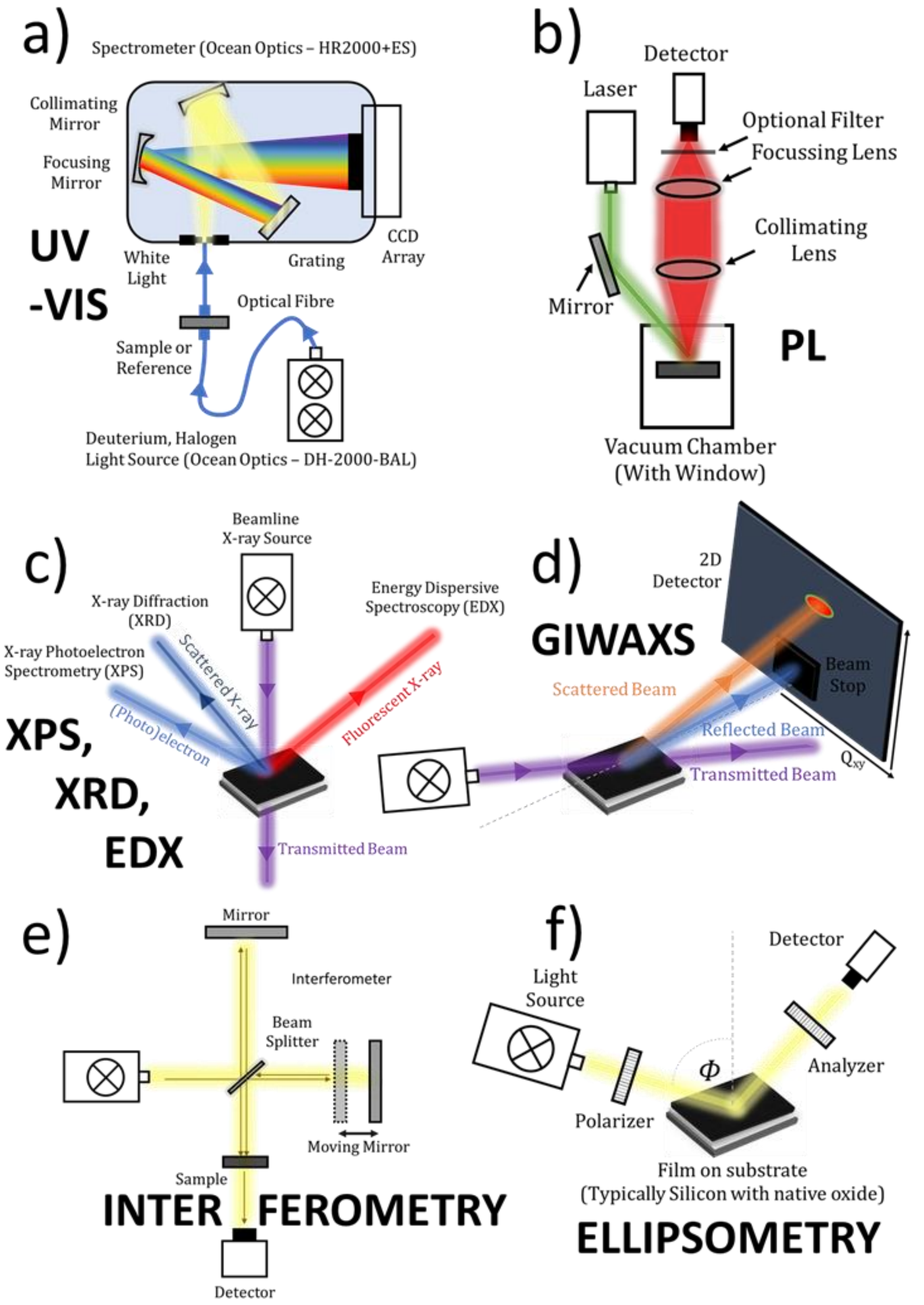

Figure 12: *Schematics of the following spectroscopy setups: a) UV-vis absorption or transmission spectroscopy, b) steady-state photoluminescence (PL), c) X-ray based photoelectron spectrometry (XPS), diffraction (XRD), and dispersive spectroscopy (EDX), d) grazing-incidence wide-angle x-ray scattering (GIWAXS), e) interferometry and f) ellipsometry.*

3.5.1: Absorption: UV-vis

A deuterium-halogen UV-VIS-NIR light source (Ocean Optics – DH-2000-BAL), collection fibre optic cables (Ocean Optics) and spectrometer (Ocean Optics – HR2000+ES) with a grating and charge-coupled device (CCD) were used to perform transmission and absorbance measurements (See Figure 12a). A sample was placed between the source and spectrometer, and the difference between the illumination intensity measured as a function of wavelength $I_0(\lambda)$ with the intensity measured by the spectrometer $I(\lambda)$ used to calculate the sample transmission $T(\lambda)$ (see Equation 3).[39]

$$T(\lambda) = \frac{I(\lambda)}{I_0(\lambda)} \qquad (Eq. 3)$$

The absorbance of the film can be calculated using Equation 4.[39]

$$A(\lambda) = -log_{10}\big(T(\lambda)\big) = -log_{10}\left(\frac{I(\lambda)}{I_0(\lambda)}\right) \qquad (Eq. 4)$$

Equation 5 can be used to calculate the attenuation coefficient α if the absorbance and thickness of film (t) is known. This is known as the Beer-Lambert law.

$$\alpha t = A \ln 10 \qquad (Eq. 5)$$

This relationship is only valid when the reflection of all surfaces, emission of the thin-films, and any interference effects are accounted for. If the thickness of the thin-film is known and the reference background is properly removed, then absorbance can be used to calculate the attenuation coefficient.

Samples for absorption measurements were prepared on quartz-coated glass using the same deposition methods as used in device fabrication unless otherwise stated.

3.5.2: Steady State Photoluminescence

A laser was focussed onto the surface of a sample. Here the sample was mounted behind a window in a vacuum chamber. Provided that the sample has a band gap with energy less than or equal to the energy of incoming laser, it will become photoexcited as it absorbs the incident light. Upon radiative recombination of excited states, the sample emits photoluminescence at a wavelength equivalent to the band gap of the sample. The intensity will depend on the incident power of the laser light (determined by the power of the laser and the optics), the wavelength of the light (here a 512 nm green laser was used for perovskites) and the absorption of the sample at that wavelength. The distribution of the photoluminescence will depend on the sample temperature and structural disorder. Figure 12b demonstrates this process. Lenses were used to collect and collimate as much as the photoluminescence as possible, which was subsequently focused down onto a detector (either a monochromator or CCD). The detected spectra will therefore also depend on the collection efficiency. An optical filter was often used to block any laser light that was scattered into the detector.

3.5.3: UV photoelectron spectroscopy (UPS) or X-ray photoelectron spectroscopy (XPS)

As shown in Figure 12c, a beam of photons of various known energies is focussed onto a sample. Electrons are liberated from the material, each with a kinetic energy that is dependent on the electron orbital it originated from and the energy of the photon that knocked it free from its nucleus. Photoelectron spectroscopy is the measurement of the spectra of electron kinetic energies, which are determined from the resultant Lorentz force generated when electrons pass through the magnetic field of a hemispherical analyser.[40–42] The maximum depth an electron can be liberated from within a sample and still escape from that sample is typically ~ 5 nm. Only the top surface of thin-films are analysed. UPS utilises UV photons and XPS is performed with X-rays with energies higher than 1.5 keV.[40–42]

Photoelectron spectroscopy can be used to characterise the composition and stichometry of thin-film materials. It is also sensitive enough to detect fine structure associated with the vibrational levels of molecular orbitals. The spectrum width is the distance between the highest kinetic energy observed (lowest binding energy or Fermi level) and the low kinetic energy cut-off (a tail). The work function of a sample can be calculated by subtracting the observed spectrum width from the known energy the incident photons.[40–42]

Analysis was carried out using a Kratos Supra instrument with a monochromated aluminium source, with measurements performed at two locations, each of area 700 μm by 300 μm. Survey scans were collected between 1200 to 0 eV binding energy, at 160 eV pass energy, 1 eV intervals, and 300 seconds/sweep with one sweep being collected. High-resolution O 1s, C 1s, Ni 2p or Ti 2p XPS spectra, and Ni LMM Auger spectra, were also collected at 20 eV pass energy and 0.1 eV intervals for each analysis point over an appropriate energy range, with one 300 second sweep for all spectra except the Ni LMM Auger which, given the extended eV range necessary, was collected for 450 seconds. The data collected was calibrated in intensity using a transmission function characteristic of the instrument (determined using software from NPL) to make the values instrument independent. The data could then be quantified using theoretical Schofield relative sensitivity factors. The high-resolution spectra were all calibrated in eV by fixing the main C 1s peak to be 285.0 eV.

3.5.4: X-ray Diffraction (XRD)

XRD is also shown in Figure 12c. Here X-rays that are targeted onto the sample are diffracted by any periodic surface features. Specific repeating lattices of different crystalline or semi-crystalline materials produce specific diffraction patterns, scattered at a variety of angles. This scattering follows Bragg's diffraction law (Equation 6), where n is any integer, λ is the wavelength of the incident X-ray and the repeating crystal lattice of atoms has a distance d between diffraction planes.[43]

$$n\lambda = 2dsin\theta \qquad (Eq. 6)$$

By scanning a detector around a chosen range of 2θ angles, the intensity at each angle can be found. By observing the angles at which diffraction patterns occur, the spacing between the planes (d) can be obtained. This d-spacing is typically compared against the d-spacing of other known materials, or the peaks are indexed and placed into a model to solve and find the crystal structure of the material.

X-ray diffraction data was collected on a Cu Kα Bruker D8 ADVANCE X-ray powder diffractometer. The instrument was fitted with a motorised variable slit optic set to 0.3° opening and a high-resolution energy-dispersive Lynxeye XE detector. Scans were collected at room temperature and at angles ranging between 20° and 70° 2θ, using a step size of 0.04° and step time of 12 s giving a total exposure time of 3.5 or

4.5 h. Reference samples were used to determine the background signal from the sample holder and uncoated quartz coated glass reference slide. The height of the samples was optimised to improve signal intensity of a known reference substrate.

3.5.5: Energy-Dispersive X-ray Spectroscopy (EDX)

EDX is also shown in Figure 12c. In this case, the beam of X-rays is used to excite inner shell electrons. As these electrons are liberated from the inner shells, an outer shell electron will drop the fill the now empty lower electron orbital. As the outer shell electron drops, it emits a photon with an energy equivalent to the energy drop. Multiple shell orbitals will undergo this process and the elemental composition of a sample can built up by detecting the emitted photons.

Compositional analysis was performed using a Helios NanoLab at 10 keV accelerating voltage, with the signal measured using an Oxford Instruments EDX spectrometer and analysed using AZtecEnergy spectral analysis software.

3.5.6: Grazing Incidence Wide-Angle X-ray Scattering (GIWAXS)

Like XRD, GIWAXS makes use of diffraction patterns produced when incident X-rays are scattered from a sample. As the name suggests, GIWAXS is a performed with the X-ray source aligned at a grazing incidence relative to the sample. Again, Bragg's law of diffraction (Equation 6) provides an understanding of how X-rays will diffract through a crystalline or semi-crystalline material. The incident angle dictates how deep into the material will probe; there is a critical angle at which the X-rays will interact with the bulk of the material instead of its top surface. GIWAXS is typically used to observe structures in the range of nm's -to Å's.[44–47]

Figure 12d is a simplified schematic of a GIWAXS experiment. To ensure the X-rays reaching the detector are only from scattering (orange) and not from the reflected (blue) or transmitted (purple) beam, a beam-stop is used near the base of the detector. This occludes the direct beam and also some of the reflected intensity. Unlike most XRD setups (where a series of angles are scanned around a sample using a point detector) GIWAXS typically utilises a two-dimensional detector, making it possible to collect the full diffraction pattern simultaneously. Equation 7 demonstrates how the reciprocal space parameter q is related to angle of detected diffraction pattern and wavelength of incident X-rays.[44–47]

$$q = \frac{2\pi}{d} = \frac{4\pi sin\theta}{\lambda} \qquad (Eq. 7)$$

Using these values, GIWAXS can be used to identify the strengths of various crystal orientations and phases, identify materials (by comparison), and collect data for indexing and modelling of crystal structures. For highly oriented samples the diffraction pattern will appear as spots. For ordered samples with many directions of orientation, the diffraction pattern will manifest as arcs or rings on a 2D detector. The width of diffraction patterns is a good indication of a level of disorder of the various crystal structures within a sample.[44–47]

Measurements were carried out using a Xenocs Xeuss 2.0 SAXS/WAXS machine equipped with was a liquid Gallium MetalJet (Excillum) x-ray source emitting x-rays with an energy of 9.2 keV. Samples were mounted on an angular positioning stage for alignment. The measurements were then performed in a vacuum chamber to reduce background scatter. The scattered X-rays were measured with a Pilatus3R 1M detector over a count time of 10 minutes. The 2D detector image were processed using Foxtrot software, which was used to produce the 1D line profiles for both the azimuthal or radial integrations.

3.5.7: Fourier transform infrared spectroscopy (FTIR)

A Michelson interferometer (Figure 12e) can be used produce a continuously modulated spectrum of wavelengths from an IR lightsource, which is illuminated onto a sample. Several ranges of IR light and types of detectors can be used to determine different material properties. In attenuated total reflectance (ATR) mode, the light reflected from a surface (probing ~ 2 μm deep) is analysed using a Fourier transform to determine features that can be associated with known materials.[48]

In the context of this thesis, FTIR was used to explore whether residual solvent remained in $MAPbI_3$ films after solvent annealing. The films were removed from the substrate using a razor blade, and the resultant powder was investigated using a PerkinElmer 100 attenuated total reflection-IR (ATR-IR) spectrometer.

3.5.8: Ellipsometry

Ellipsometry is a non-intrusive technique, used to measure the thickness and optical properties of a thin-film. As is shown in Figure 12f, linearly polarized light was reflected off the surface of the film, and was passed through an analysing polarized filter.[49–51] The ratio of amplitude of light oscillating perpendicular to the plane of incidence (R_s) to light oscillating parallel to the plane of incidence (R_p) is measured. Using Equation 8, this reflectance ratio (ρ) can be used to calculate the optical constants (Ψ), the ratio of the amplitude of incident and reflected light, and (Δ), the ratio of the phase lag between incident and reflected light.[49–51]

$$\rho = \frac{R_s}{R_p} = \tan(\Psi)\exp(i\Delta) \qquad (Eq. 8)$$

Ellipsometry was performed using a spectroscopic ellipsometer (M2000v, J. A. Woollam Co., USA). Materials were deposited onto silicon substrates covered with a 410-420 nm thick thermal oxide. Data was collected over a wavelength range of 370 to 1000 nm. The metal oxides used are considered to be homogeneous and have negligible absorbance across this range (often leading to indeterminable extinction coefficients (k)). Using these approximations, a Cauchy model was considered appropriate to determine the thickness and optical properties of the materials. The model was then used to extract the refractive index (n) and (when possible) the extinction coefficients (k) of the film.

3.5.9: Laser-Beam-Induced Current (LBIC)

In LBIC the photocurrent induced by a focussed beam of laser light is measured. The laser light is chopped and passed across the surface of a solar cell. This technique typically enables the identification of defects and non-uniformities in solar cell active areas. In the context of micro-groove mini modules, explained in Chapter 7, LBIC has been proven useful to identify an upper limit for the size of a groove device active area.

As can be seen from Figure 13, an LBIC mapping system is comprised of a mechanically chopped laser excitation that is passed through a spatial filter before being focussed to a spot size of around 2 μm onto the sample via a 100x objective (Mitutoyo, infinity-corrected for long working distances). The sample was mounted on a computer controlled XY-stage and raster-scanned in a sawtooth pattern in steps of 0.5 or 1 μm. A 4.5 mW, 635 nm diode laser (Thor Labs, CPS635) was used to generate the photocurrent.

A reference silicon photodiode collects like reflected from the neutral density filter in order to account for laser intensity fluctuations. The repeating chopped laser signal is used to aid photocurrent signal detection (V_{signal}) by a Stanford Research Systems SR830 lock-in amplifier - which is provided with the frequency signal of the optical chopper as a reference signal ($V_{reference}$).

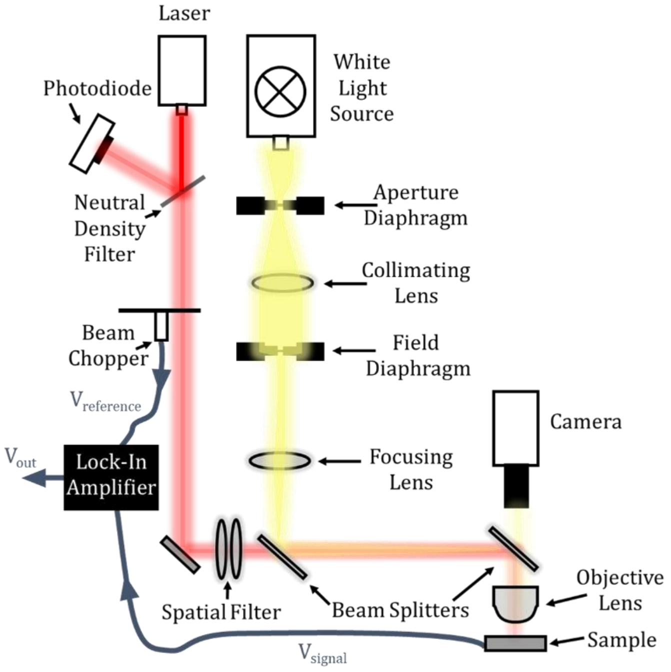

Figure 13: *Schematic of laser beam induced current (LBIC) mapping setup.*

3.6: Device Fabrication

Each chapter uses a specific PSC fabrication methodology. General fabrication details are provided in Appendix A. The device architectures used were adapted from those developed by other PV research groups.[32,52,53] Conventional planar solar cells with a standard (n-i-p) and inverted (p-i-n) architecture were built as stacks of material on top of transparent conductive oxide (TCO) coated glass with a standardised 15 mm x 20 mm size. Schematics and photographs of device processing and finished devices are presented in Figure 14, where the fabrication routines for n-i-p (part a) and p-i-n (part c) are used to complete devices with the same or similar structures to those shown in Figure 14b and Figure 14d respectively. Photographs of finished devices are given in Figure 14e, 14f and 14g.

Samples for spectroscopic characterisation were either prepared in the same way as devices (on TCOs), or on quartz coated glass, or on silicon substrates (with a thermal or native silicon oxide). Conductivity measurements were performed by using interdigitated ITO substrates. All layer thicknesses reported in this thesis and shown in Figure 14 were measured using a Bruker DektakXT profilometer and confirmed (when possible) with cross-sectional SEM as detailed above.

Whilst optimising materials choice and fabrication routines for Chapter 4-7, it was discovered that lead acetate route perovskite active layers enabled PCEs of up to 18 % PCE. Appendix B contains stability data and a brief discussion regarding PSCs with lead acetate route perovskites. Unfortunately, it is found that these PSCs are very unstable. It is for this reason that this thesis avoids the use of acetate route perovskite.

The architecture and fabrication of solar grooves are given in detail in Chapter 7. Conventional planar cells are fabricated to select appropriate electrode and charge transport materials for back-contact solar grooves. Part of this materials screening process is provided in Appendix C.

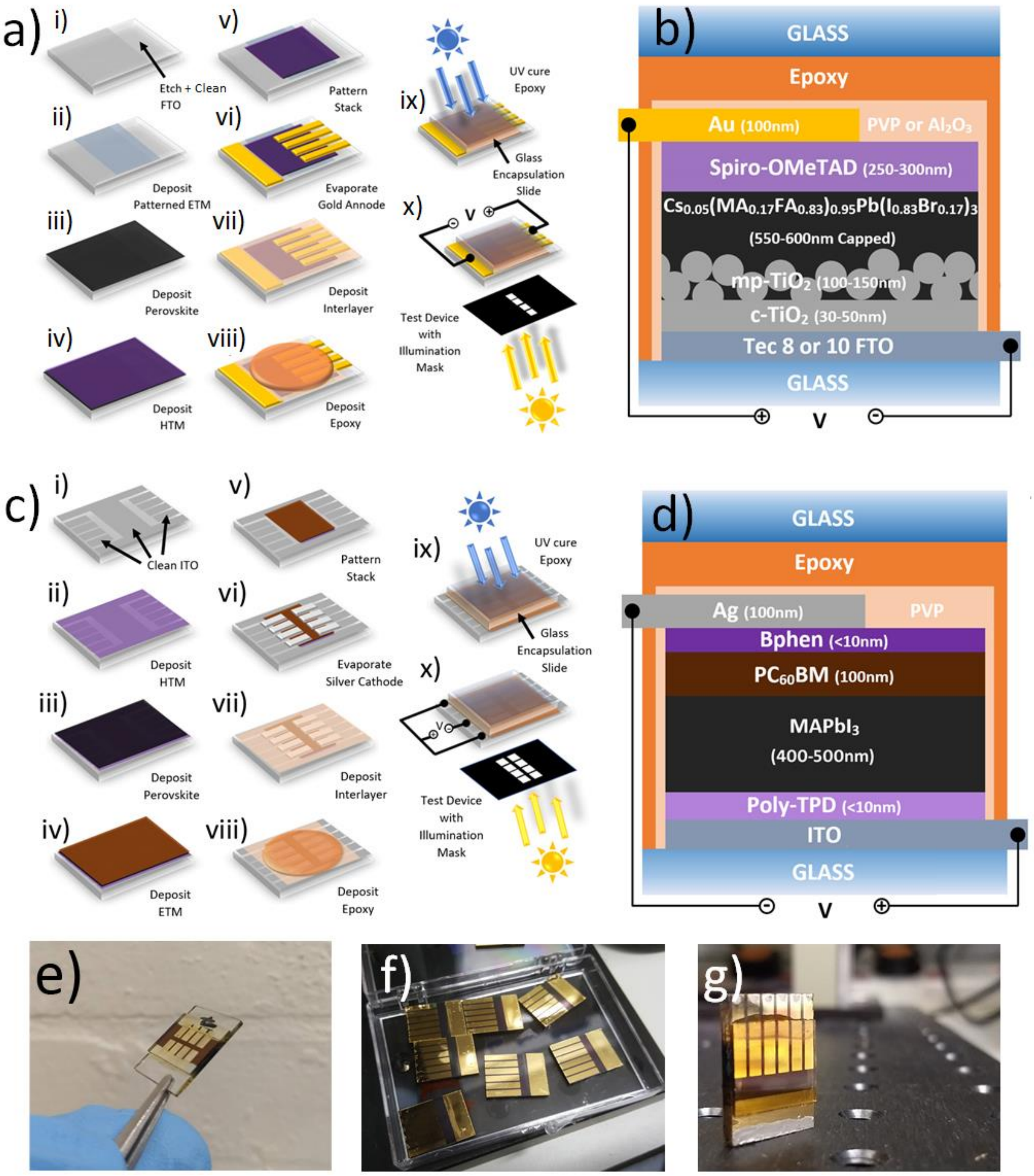

Figure 14: *Fabrication of solar cells. a) A schematic of the fabrication and testing routine used to create 6-pixel standard n-i-p architecture perovskite solar cells incorporating a* Al_2O_3*/epoxy encapsulation. b) Resultant n-i-p device showing all layers, together with their approximate thicknesses. c) A schematic of the fabrication and testing routine used to create 8-pixel inverted p-i-n architecture perovskite solar cells incorporating a PVP/epoxy encapsulation. d) Resultant p-i-n device showing all layers, together with their approximate thicknesses. e) Photo of fully encapsulated p-i-n device. f) Photo of sample box containing finished n-i-p devices. g) Photo of fully encapsulated n-i-p device.*

3.7: References

[1] D. Bi, W. Tress, M. I. Dar, P. Gao, J. Luo, C. Renevier, K. Schenk, A. Abate, F. Giordano, J.-P. Correa Baena, J.-D. Decoppet, S. M. Zakeeruddin, M. K. Nazeeruddin, M. Grätzel, A. Hagfeldt, *Sci. Adv.* **2016**, *2*, e1501170.

[2] D. C. Watters, H. N. Yi, a J. Pearson, J. Kingsley, a Iraqi, D. Lidzey, *Macromol. Rapid Commun.* **2013**, *34*, 1157.

[3] S. Ameen, M. A. Rub, S. A. Kosa, K. A. Alamry, M. S. Akhtar, H. S. Shin, H. K. Seo, A. M. Asiri, M. K. Nazeeruddin, *ChemSusChem* **2016**, *9*, 10.

[4] J. Liu, S. Pathak, T. Stergiopoulos, T. Leijtens, K. Wojciechowski, S. Schumann, N. Kausch-busies, H. J. Snaith, *J. Phys. Chem. Lett.* ***2015**, 6*, *9*, 1666-1673.

[5] V. Zardetto, B. L. Williams, A. Perrotta, F. Di Giacomo, M. A. Verheijen, R. Andriessen, W. M. M. Kessels, M. Creatore, *Sustain. Energy Fuels* **2017**, *1*, 30.

[6] Y. Zhang, X. Wang, Y. Liu, S. Song, D. Liu, *J. Mater. Chem.* **2012**, *22*, 11971.

[7] M. Salado, R. K. Kokal, L. Calio, S. Kazim, M. Deepa, S. Ahmad, *Phys. Chem. Chem. Phys.* **2017**, *19*, 22905.

[8] M. Deepa, M. Salado, L. Calio, S. Kazim, S. M. Shivaprasad, S. Ahmad, *Phys. Chem. Chem. Phys.* **2017**, *19*, 4069.

[9] A. J. Pearson, D. C. Watters, H. Yi, M. S. Sarjadi, L. X. Reynolds, P. P. Marchisio, J. Kingsley, S. A. Haque, A. Iraqi, D. G. Lidzey, *RSC Adv.* **2014**, *4*, 43142.

[10] C. C. Chen, W. H. Chang, K. Yoshimura, K. Ohya, J. You, J. Gao, Z. Hong, Y. Yang, *Adv. Mater.* **2014**, *26*, 5670.

[11] X. Yao, W. Xu, X. Huang, J. Qi, Q. Yin, X. Jiang, F. Huang, X. Gong, Y. Cao, *Org. Electron. physics, Mater. Appl.* **2017**, *47*, 85.

[12] K. Zhao, R. Munir, B. Yan, Y. Yang, T. Kim, A. Amassian, *J. Mater. Chem. A* **2015**, *3*, 20554.

[13] F. Hou, Z. Su, F. Jin, X. Yan, L. Wang, H. Zhao, J. Zhu, B. Chu, W. Li, *Nanoscale* **2015**, *7*, 9427.

[14] T. M. Koh, K. Fu, Y. Fang, S. Chen, T. C. Sum, N. Mathews, S. G. Mhaisalkar, P. P. Boix, T. Baikie, *J. Phys. Chem. C* **2014,** *118, 30*, 16458-16462

[15] Y.-J. Jeon, S. Lee, R. Kang, J.-E. Kim, J.-S. Yeo, S.-H. Lee, S.-S. Kim, J.-M. Yun, D.-Y. Kim, *Sci. Rep.* **2014**, 26.

[16] H. Zhou, Q. Chen, G. Li, S. Luo, T. Song, H.-S. Duan, Z. Hong, J. You, Y. Liu, Y. Yang, *Sci. (Washington, DC, U. S.)* **2014**, *345*, 542.

[17] J. Burschka, N. Pellet, S.-J. Moon, R. Humphry-Baker, P. Gao, M. K. Nazeeruddin, M. Grätzel, *Nature* **2013**, *499*, 316.

[18] J. H. Noh, N. J. Jeon, Y. C. Choi, M. K. Nazeeruddin, M. Grätzel, S. Il Seok, *J. Mater. Chem. A* **2013**, *1*, 11842.

[19] P. Schulz, E. Edri, S. Kirmayer, G. Hodes, D. Cahen, A. Kahn, *Energy Environ. Sci.* **2014**, *7*, 1377

[20] P. P. Boix, K. Nonomura, N. Mathews, S. G. Mhaisalkar, *Mater. Today* **2014**, *17*, 16.

[21] A. M. Gaikwad, Y. Khan, A. E. Ostfeld, S. Pandya, S. Abraham, A. Claudia, *Org. Electron.* **2016**, *30*, 18.

[22] N. K. Noel, M. Congiu, A. J. Ramadan, S. Fearn, D. P. McMeekin, J. B. Patel, M. B. Johnston, B. Wenger, H. J. Snaith, *Joule* **2017**, *1*, 328.

[23] Ossila, "Spin-Coating Guide" can be found under https://www.ossila.com/pages/spin-coating.

[24] University of Louisville, "Spin-Coating Information" can be found under *https://louisville.edu/micronano/files/documents/standard-operating-procedures/SpinCoatingInfo.pdf/view*

[25] N. Sahu, B. Parija, S. Panigrahi, Indian. *J. Phys*. **2009**, *83*, 493.

[26] A. S. Dimitrov, P. A. Kralchevsky, A. D. Nikolov, H. Noshi, M. Matsumoto, *J. Colloid Interface Sci.* **1991**, *145*, 279.

[27] K. Kabza, J. E. Gestwicki, J. L. Mcgrath, *J. Chem. Educ.* **2000**, *77*, 63.

[28] A. Krishnan, Y. Liu, P. Cha, R. Woodward, D. Allara, E. A. Vogler, *Colloids and Surfaces B: Biointerfaces*, **2005**, *43*, 95.

[29] D. Bonn, J. Eggers, J. Indekeu, J. Meunier, *Rev. Mod. Phys.* **2009**, *81*, 739.

[30] R. Islam, G. Chen, P. Ramesh, J. Suh, N. Fuchigami, D. Lee, K. A. Littau, K. Weiner, R. T. Collins, K. C. Saraswat, *ACS Appl. Mater. Interfaces* **2017**, *9*, 17201.

[31] Z. Wang, J. Fang, Y. Mi, X. Zhu, H. Ren, X. Liu, Y. Yan, *Appl. Surf. Sci.* **2018**, *436*, 596.

[32] N. K. Noel, S. N. Habisreutinger, B. Wenger, M. T. Klug, M. T. Hörantner, M. B. Johnston, R. J. Nicholas, D. T. Moore, H. J. Snaith, *Energy Environ. Sci.* **2017**, *10*, 145-152.

[33] W. Zhang, M. Saliba, D. T. Moore, S. Pathak, M. Horantner, T. Stergiopoulos, S. D. Stranks, G. E. Eperon, J. a Alexander-Webber, A. Abate, A. Sadhanala, S. Yao, Y. Chen, R. H. Friend, L. a Estroff, U. Wiesner, H. J. Snaith, *Nat. Commun.* **2014**, *6*, 6142.

[34] I. Minkoff, *J. Mat. Sci.* **1967**, *2*, 388-394

[35] V. Kumar, W. L. Schmidt, G. Schileo, R. C. Masters, M. Wong-Stringer, D. C. Sinclair, I. M. Reaney, D. Lidzey, C. Rodenburg, *ACS Omega* **2017**, *2*, 2126.

[36] E. Meyer, *Prog. Surf. Sci.* **1992**, *41*, 3.

[37] G. Binnig, C. F. Quate, *Phys. Rev. Lett.* **1986**, *56*, 930.

[38] S. N. Magonov, V. Elings, M. H. Whangbo, *Surf. Sci.* **1997**, *375*, L385-L391.

[39] E. Hecht, *Optics (5th Edition*), Pearson*,* **2016.**

[40] K. A. I. Siegbahn, *Pure. App. Chem.* **1976**, *48,* 77-97.

[41] D. R. Penn, *J. Electron Spectros. Relat. Phenomena* **1976**, *9*, 29.

[42] K. Siegbahn, *Rev. Mod. Phys.* **1982***, 54, 3*, 709 .

[43] C. G. Pope, *J. Chem. Educ.* **1997**, *74*, 129.

[44] G. Renaud, R. Lazzari, F. Leroy, *Surf. Sci. Rep.* **2009**, *64*, 255.

[45] D. Altamura, T. Sibillano, D. Siliqi, L. De Caro, C. Giannini, *Nanomater. Nanotechnol.* **2012**, *2*, 16.

[46] B. L. Henke, E. M. Gullikson, J. C. Davis, *At. Data Nucl. Data Tables* **1993**, *54*, 181.

[47] P. Müller-Buschbaum, *Anal. Bioanal. Chem.* **2003**, *376*, 3.

[48] Chemistry LibreTexts, N. Birkner, Q. Wang, “How an FTIR Spectrometer Operates” can be found under https://chem.libretexts.org/Textbook _Maps/Physical_and_Theoretical_Chemistry_Textbook_Maps/Supplemental_Modules_(Physical_and_Theoretical_Chemistry)/Spectroscopy/Vibrational_Spectroscopy/Infrared_Spectroscopy/How_an_FTIR_Spectrometer_Operates

[49] H. G. Tompkins, E. A. Irene, *HANDBOOK OF ELLIPSOMETRY*, William Andrew & Springer, **2005**.

[50] A. Rothen, *Review of Scientific Instruments,* **1998,** *16,* 26.

[51] P. Petrik, B. Fodor, E. Agocs, P. Kozma, J. Nador, N. Kumar, J. Endres, *SPIE Optical Metrology Proceedings, Modeling Aspects in Optical Metrology V*, **2015**, *9526*, 1.

[52] N. J. Jeon, J. H. Noh, W. S. Yang, Y. C. Kim, S. Ryu, J. Seo, S. Il Seok, *Nature* **2015**, *517*, 476.

[53] M. Saliba, T. Matsui, J.-Y. Seo, K. Domanski, J.-P. Correa-Baena, M. K. Nazeeruddin, S. M. Zakeeruddin, W. Tress, A. Abate, A. Hagfeldt, M. Grätzel, *Energy Environ. Sci.* **2016,** *9***,** 1989-1997.

Chapter 4

Volume 5, Issue 30

July 08, 2017

15714

Journal of Materials Chemistry A

Efficient Perovskite Photovoltaic Devices Using Chemically Doped PCDTBT as A Hole-Transport Material

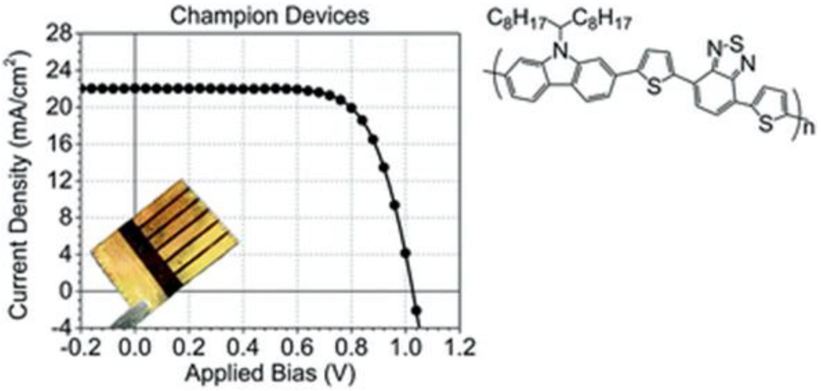

For the journals PDF:

DIO: 10.1039/c7ta03103c

Cite this: J. Mater. Chem. A,2017, 5, 15714

4.0: Publication Forward: Choosing A Hole Transport Material

There are many materials that have the correct hole affinity to align with multi-cation perovskites. Indeed, inorganic metal oxides, organometallic complexes, organic small molecules and conjugated polymers have all been utilised as HTLs in PSCs. Many variations of semiconducting conjugated polymers have also been explored for applications in bulk-heterojunction organic solar cells, having ideal optoelectronic properties to act as photoactive donor materials. Amongst these polymers, carbazole-based conjugated polymer based OPVs have been demonstrated to produce efficient OPVs. In this chapter we use poly[N-9'-heptadecanyl-2,7-carbazole-alt-5,5-(4',7'-di-2-thienyl-2',1',3'-benzothiadiazole)] (PCDTBT), which has been widely explored as a absorber material in organic PV, and investigate it as a potential material for use as an HTL in standard architecture PSCs. At the time of writing, the following publication has been cited 8 times, indicating that it has contributed and inspired further research in the perovskite PV community.

4.1: Publication Main Body

Efficient perovskite photovoltaic devices using chemically doped PCDTBT as a hole-transport material

Michael Wong-Stringer[1], James E. Bishop[1], Joel A. Smith[1], David K. Mohamad[1],
Andrew J. Parnell[1], Vikas Kumar[2], Conny Rodenburg[2] and David G. Lidzey[1]*

1) Department of Physics & Astronomy, University of Sheffield, Hicks Building,
Hounsfield Road, Sheffield, S3 7RH, U.K.
2) Department of Chemical and Biological Engineering, University of Sheffield,
Mappin St, Sheffield, S1 3JD
*Corresponding author, email d.g.lidzey@sheffield.ac.uk

Keywords: PCDTBT, perovskite solar cells, p-doping, conductivity, hole-transport materials

Abstract

It is shown that by chemically doping the carbazole-based conjugated polymer PCDTBT using the molecular materials TBP, LiTFSI and FK209, its conductivity can be increased by a factor of 10^5 times. Such doped PCDTBT films are used as a hole transport material (HTM) for standard architecture $(CH(NH_2)_2PbI_3)_{0.85}(CH_3NH_3PbBr_3)_{0.15}$ perovskite solar cells (PSCs). We show that devices with optimised PCDTBT thickness and doping level achieve a peak power conversion efficiency (PCE) of 15.9%. We expect a number of related doped conjugated polymers to also be capable of acting as efficient HTMs for PSCs.

Introduction

Over the last few years, perovskite solar cells (PSCs) have shown promising progress in terms of efficiency and stability. Stabilised power conversion efficiencies (PCEs) reaching 21.6% have been reported,[1] with devices operating for > 10,000 hours with no loss in performance demonstrated.[2] The choice of hole-transport materials (HTMs) used in perovskite devices is receiving increasing scrutiny, with research focused on maximizing charge-transport efficiency and operational stability, but minimising the cost and complexity of the HTM layer.[3,4]

In standard structure perovskite devices incorporating a device architecture of [glass/fluorine-doped tin oxide (FTO)/electron transport material (ETM)/perovskite/HTM/metal contact], the most commonplace HTM remains 2,2',7,7'-tetrakis[N,N-di(4-methoxyphenyl)amino]-9,9'-spirobifluorene (spiro-OMeTAD). However, to act as an efficient HTM, spiro-OMeTAD usually requires chemical doping. This involves adding a combination of several key chemicals, namely; 4-*tert*-Butylpyridine (TBP), bis(trifluoromethane)sulfonimide lithium salt (LiTFSI), and FK 209 Co(III) - TFSI salt (FK209), with the amounts added varying between publications.[5-7] A complete understanding on how exactly this cocktail of dopants affects the HTM and the rest of the device stack is not yet available. It is widely agreed that LiTFSI and FK209 dopants create a p-doped state on spiro-OMeTAD.[8-12] Here, the LiTFSI doping requires optical-radiation and oxygen to p-dope the spiro-OMeTAD; a process that increases its conductivity by over three orders of magnitude.[9,10] However recent work on the use of FK209 to dope other

HTMs demonstrates that it can generate similar p-doped states in an inert atmosphere, without relying on light and oxygen.[1,6,9] It has been proposed that the additive TBP migrates through the perovskite stack and becomes located at the interface between the perovskite and the TiO_2; this passivates trap states at the TiO_2 surface, resulting in a negative shift in the TiO_2 conduction band states which increases the device open circuit voltage (V_{oc}).[13] However, other work suggests that the LiTFSI passivates the TiO_2 surface, whilst TBP provides an increase in J_{sc} (and hence charge-collection efficiency) regardless of the choice of ETM or HTM.[14,15] Indeed, using the additive TBP in an HTM is thought to lead to an increase in hole selectivity via band bending at the perovskite/HTM interface; a process that is evidenced by a significant improvement (5.5% to 12%) in the stabilised power output of TBP-doped PSC devices.[15] It has also been demonstrated that TBP helps solubilize other dopants added to the HTM, thereby improving the wetting of the HTM onto the perovskite surface.[14] Gaining a deeper understanding of how these dopants and additives affect an entire device stack is thus an important part of the development of an efficient and stable PSC.

There have recently been reports that certain tailored “dopant-free” HTMs can almost match the efficiencies of spiro-OMeTAD,[11,16] however, the use of dopants generally appears to be an effective strategy to improve the charge-transport properties of many HTM materials.[3,4,17] Here, we explore the use of a chemically-doped film of the donor-acceptor carbazole co-polymer poly[N-9'-heptadecanyl-2,7-carbazole-alt-5,5-(4',7'-di-2-thienyl-2',1',3'-benzothiadiazole)] (PCDTBT) as a HTM in a perovskite solar cell. Organic heterojunction solar cells that use the popular material PCDTBT generally have excellent operational stability, with devices demonstrated to have Ts80 lifetimes of up to 6,200 hours when operating in outdoor conditions.[18] This stability results from its low-lying highest-occupied molecular orbital (HOMO) level, which is positioned at 5.45 eV[3,18-22]. We note that the HOMO-level of PCDTBT is in fact lower than that of the spiro-OMeTAD HOMO level (which has been reported in the range of 5.0 to 5.22 eV),[3,23] suggesting that it may have improved oxidative stability when incorporated as the HTM in PSC devices. Importantly, recent development of simpler routes to synthesize PCDTBT now allow it to be made in high yields (>90%) at targeted molecular weights.[24]

To explore the suitability of PCDTBT as a solution-processable HTM in perovskite solar cells, we have fabricated devices employing an efficient multi-cation, multi-halide perovskite active layer based on formamidinium lead iodide ($FAPbI_3$) and methylammonium lead bromide ($MAPbBr_3$), as adapted from previous work.[7] We note that doped-PCDTBT has previously been used as an HTM in standard architecture (n-i-p) PSCs; however, device efficiency was relatively low at 4.2%.[17] Here, we show that by optimising both PCDTBT thickness and doping level, devices based on the structure [FTO/c-TiO_2/mp-TiO_2/$(FAPbI_3)_{0.85}$ $(MAPbBr_3)_{0.15}$/PCDTBT/Au] can be created having a peak efficiency of 15.9% PCE. This efficiency compares very well with our control PSC devices incorporating a spiro-OMeTAD HTM (doped with LiTFSI, TBP and FK209) that have a peak efficiency of 17.4%. To achieve such performance, PCDTBT is combined with the materials most commonly used in high efficiency spiro-OMeTAD-PSCs; namely LiTFSI, FK209 and TBP. Our champion devices also employ a LiTFSI layer above the mesoporous (mp) TiO_2 electron-selective contact. This approach is based on other recent reports, whereby such an LiTFSI layer generated an improvement in device metrics via a reduction in nonradiative recombination at defect sites at the surface of the TiO_2.[25,26] As part of our optimisation studies, we explore the optical, electronic and structural properties of doped and undoped PCDTBT using a range of techniques, including UV-vis absorption spectroscopy, grazing-incidence wide-angle X-ray scattering (GIWAXS), atomic force microscopy (AFM), and thin-film conductivity measurements. Our approach allows us to determine the effect of the dopants on the polymer and the doping level required to optimise device efficiency. We also compare the photo-stability of doped and undoped PCDTBT with that of spiro-OMeTAD and present preliminary findings that suggest that PCDTBT may well allow perovskite solar cells to be fabricated having enhanced operational stability.

Results and Discussion

We first describe the effects that doping PCDTBT has on its optical and electronic structure. In Figure 1 we present the chemical structures of PCDTBT (a) and spiro-OMeTAD (b) together with the materials added to the HTMs: FK209 (c), TBP (d), and LiTFSI (e). Figure 1(f) shows the UV-Vis absorption of FK209 and a 1:5.6 molar ratio blend of LiTFSI:TBP dissolved into acetonitrile. It can be seen that FK209 is characterised by an absorption band with an onset located at 550 nm, while the LiTFSI:TBP has a weaker absorption peaking at 440 nm with an absorption onset also occurring at 550 nm. In Figure 1(g), we plot the absorption of a thin-film PCDTBT (red) and spiro-OMeTAD (black) when they are doped with LITFSI, TBP and FK209 at a molar ratio (normalised to the molar concentration of PCDTBT monomer) of 1:0.4:2.4 for PCDTBT:LiTFSI:TBP and 1:0.2:0.8:0.03 for spiro-OMeTAD:LiTFSI:TBP:FK209. The absorbance spectra PCDTBT is characterised by broad absorption bands at 390 and 510 nm, corresponding to electronic transitions from the S_0 ground state to S_2 and S_1 (charge-transfer like) excited states.[27] We see very little difference between the absorption spectra of the doped and undoped PCDTBT, and conclude that at the concentration used, the dopants do not appear to modify its absorbance spectra. In Figure S1, we confirm that the molar attenuation of LiTFSI and TBP dopants is insignificant relative to that of PCDTBT.

Figure 1(h) compares to the photo-stability of doped and undoped PCDTBT and spiro-OMeTAD with 1:0.4:2.4:0.052 PCDTBT:LiTFSI:TBP:FK209 and 1:0.2:0.8:0.03 spiro-OMeTAD:LiTFSI:TBP:FK209 respectively. Here, films of equivalent thickness were placed in air under a halogen lamp emitting light having a brightness equivalent to 1 sun. Samples were then periodically removed from under the lamp and their optical absorption re-measured. It can be seen that the peak optical absorption of the undoped PCDTBT reduces to 80% of its initial value after 10 hours. The absorption of the undoped spiro-OMeTAD however reduces less rapidly, and falls to 80% of its initial value after around 30 hours of illumination. It is clear that compared to spiro-OMeTAD, PCDTBT has a significantly increased absorption across the visible spectrum, and thus the more rapid photo-degradation observed here is consistent with an enhanced rate of excited state generation that increases photo-oxidation.

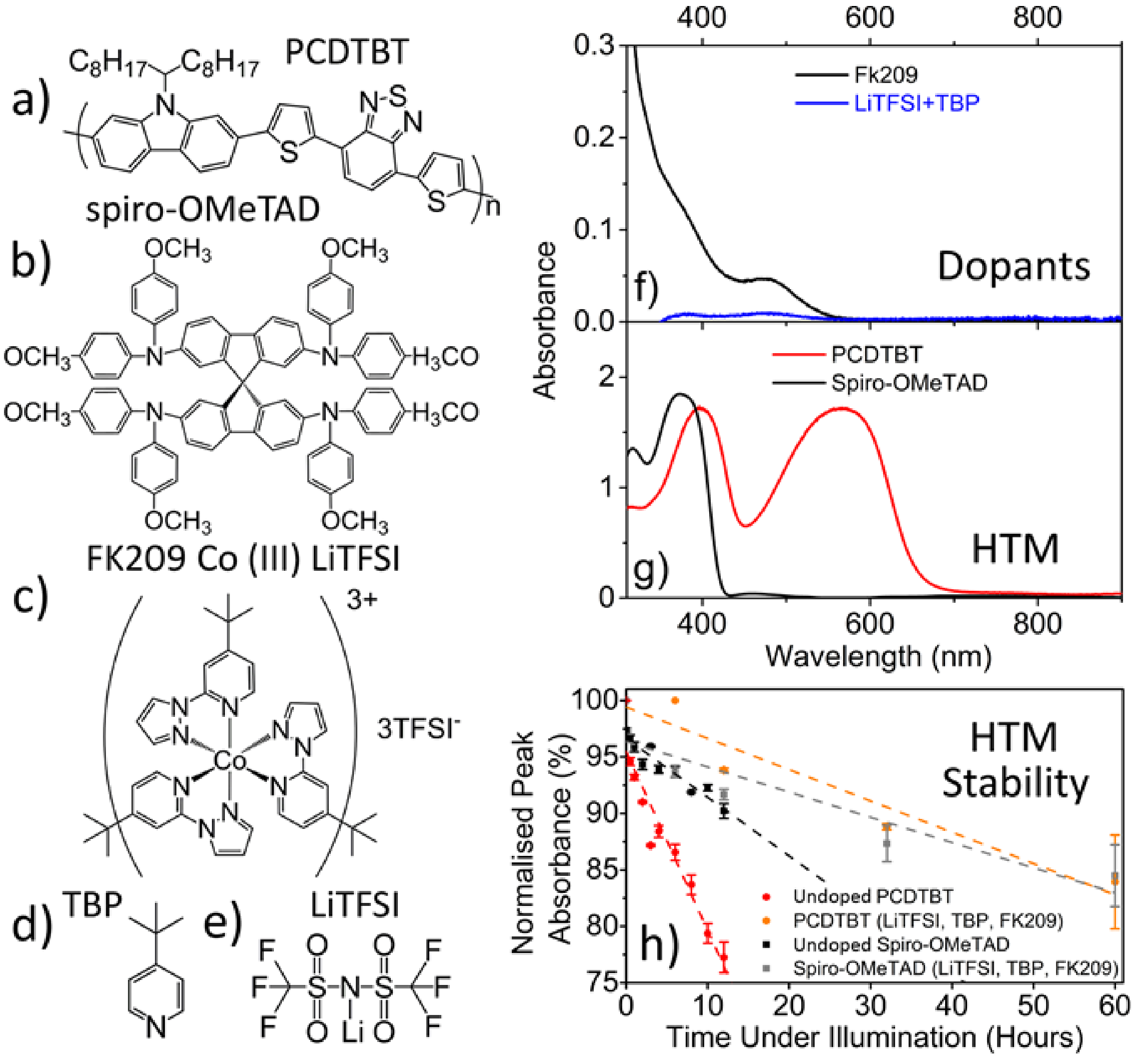

Figure 1: *Chemical structures of (a) PCDTBT, (b) spiro-OMeTAD, (c) FK209 Co (III) LiTFSI, (d) TBP and (e) LiTFSI, and absorbance of (f) a solution of 0.78mM FK209 (black) and 4.1mM LiTFSI+ 22.8mM TBP (blue) in acetonitrile, (g) absorbance of doped PCDTBT (black) and doped spiro-OMeTAD (red). Part (h) shows the decay of the peak absorbance in films of undoped and doped PCDTBT and spiro-OMeTAD films when stored in air under constant AM 1.5 illumination. Details of the doping levels and film thickness are given in the experimental section.*

Upon doping however, both spiro-OMeTAD and PCDTBT films are more photostable, with the absorption of doped PCDTBT and spiro-OMeTAD films estimated to reduce to 80% of their initial value after 75 hours. Interestingly, the doped PCDTBT film has a similar photostability to that of the doped spiro-OMeTAD despite the fact that it absorbs a greater flux of the incident photons. We attribute the increased photostability of the films on doping to exciton quenching by the dopants; a process that appears to reduce the rate of excited-state photochemical reactions that generate non-radiative defects. This is confirmed by steady state photoluminescence measurements (see Figure S2) made on doped and undoped PCDTBT films, that indicate a partial quenching (by 33%) of PCDTBT luminescence.

In the supplementary information (see Figure S3) we compare the contact angle of doped and undoped PCDTBT and spiro-OMeTAD films to deionised water using a sessile drop technique. This demonstrates that in both its doped and undoped forms, PCDTBT is significantly more hydrophobic than spiro-OMeTAD. Indeed, upon addition of the hydrophilic dopants into the films, the contact angle of spiro-OMeTAD drops by over 20º, while the contact angle of PCDTBT undergoes a negligible change (limited to a reduction of 2º). This indicates that spiro-OMeTAD is more likely to absorb water onto its surface than PCDTBT, and may thus present a less effective barrier to the migration of moisture in an operational device.

To further understand the effect of the dopants on the PCDTBT we have performed GIWAXS measurements to determine the effect of the dopants on molecular packing. Typical data is shown in Figure S4. We find that the doping levels used do not apparently result in significant shifts of either the lamella-separated side chains or the π-π stacked backbones, indicating that the dopant molecules are unlikely to directly intercalate between chains. However we find a degree of broadening of all scattering features that is accompanied by a relative reduction in intensity of the lamella-scattering peak, indicative of a general increase in film disorder.[28,29] We propose therefore that the molecular dopants mix with the PCDTBT at a mesoscopic level which leads to partially disrupted molecular packing.

To prepare doped PCDTBT films for use as an HTM layer, the LiTFSI, TBP, FK209 were added to the solutions at different concentrations, with the solutions then cast into thin-films by spin-coating. However, it was found that when FK209 was added to PCDTBT (in excess of a molar ratio PCDTBT:FK209 of 1:0.052 in a

20mg/ml PCDTBT CB solution), the solid component of the solution underwent aggregation as evidenced by increased solution turbidity. Indeed, this effect can be evidenced through AFM and optical images of doped and undoped spin-cast PCDTBT thin films as shown in Figure 2. For films doped containing LiTFSI and TBP, the AFM image shown in Figure 2(b) and optical image shown in Figure 2(e) indicate the presence of small aggregates that increase film roughness by approximately four times compared to that of undoped PCDTBT (corresponding to a surface roughness of 2.6 nm and 0.61 nm respectively). Upon addition of FK209, at a FK209 doping ratio of 1:0.03 PCDTBT:FK209, doped films of PCDTBT form a continuous film having a roughness of 3.1 nm, as determined using AFM (see Figure 2(c)). However, at longer length-scales (see Figure 2(f)), it is apparent that such films contain aggregates having length-scales as large as 100 μm, making them unsuitable for PV applications.

To understand the effect of chemical doping on the electronic properties of PCDTBT, we have measured its electronic conductivity in both its doped and undoped states. This was done by spin-casting PCDTBT solutions containing the various dopants at different concentrations onto interdigitated ITO electrodes (supplied by Ossila Ltd), in which the lateral spacing between electrode contacts varied between 50 and 200 μm. Current-voltage scans were then performed, and the effective film conductivity was extracted.

Figure 3(a) plots the conductivity of a PCDTBT film when doped with LiTFSI, TBP or FK209, or with a blend of LiTFSI and TBP, or with LiTFSI, TBP and FK209. It can be seen that PCDTBT films doped with TBP have a conductivity that its less than 1 order of magnitude greater than undoped PCDTBT.

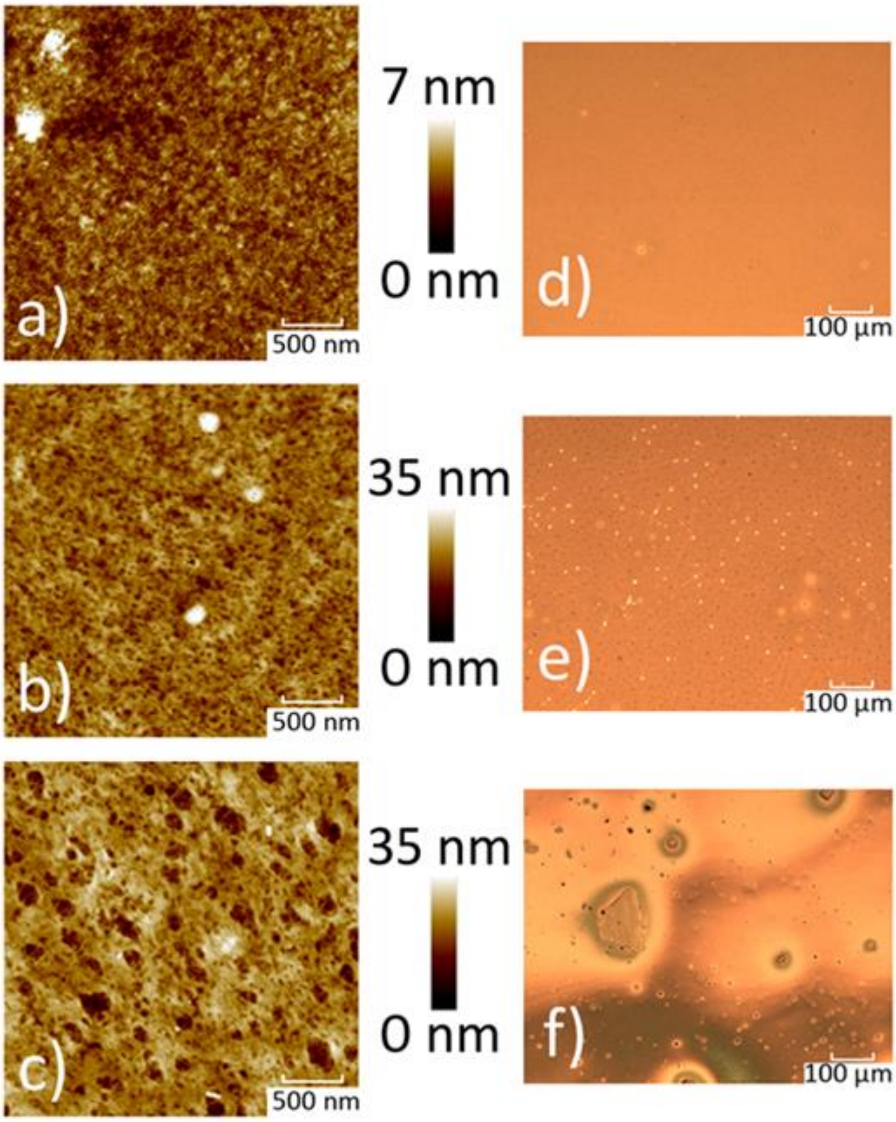

Figure 2: *AFM topographs of (a) pure PCDTBT, (b) PCDTBT when doped with LiTFSI + TBP doped, and (c) a PCDTBT film doped with LiTFSI + TBP + FK209. (d), (e) and (f) are optical microscope images of the same films respectively. The film Ra roughness averages are 0.61 nm, 2.6 nm and 3.1 nm respectively.*

We believe however that the conductivity quoted here for the undoped PCDTBT must be seen as an upper-limit of its actual conductivity, as our measurement is limited by the current resolution of the source-measure unit used to perform the measurement. Doping PCDTBT with either LiTFSI or FK209 results in a significant increase in conductivity of between 6 and 7 orders of magnitude. Notably, the additional inclusion of TBP does not result in a significant further increase in conductivity, with the conductivity of the LiTFSI:TBP doped PCDTBT film being around 6×10^{-4} S m^{-1}. Upon further addition of FK209, we find the conductivity of the film with all three dopants increases to 4×10^{-3} S m^{-1}. Such increased conductivity as a result of p-doping is well-known; for example the conductivity of spiro-OMeTAD increases from between 10^{-6} to 10^{-3} S m^{-1} when doped with LiTFSI and/or FK209.[9.30] To demonstrate that the observed increase in PCDTBT conductivity results from p-doping (rather than being caused by some electro-chemical or ionic current resulting from the field-induced migration of the dopant ions), we have dispersed a similar quantity (grams dopant into grams of polymer) of LiTFSI and TBP into the insulating polymer PMMA. The results of this experiment are shown in Figure 3(b). Here, it can be seen that the conductivity of PMMA increases on addition of dopants from around 2×10^{-9} S m^{-1} to 6×10^{-8} S m^{-1}. Again, the conductivity reported here for the undoped polymer is most likely determined by the sensitivity floor of our source-measure unit used to record the current-voltage trace. PMMA is a high band-gap insulator material that is characterised by fully saturated bonds along its molecular backbone. Thus, the increase in conductivity seen here most likely originates from the migration of dopants and ions within the film, rather than the formation of a conductive p- doped state. This conductivity level is significantly smaller than that of the doped PCDTBT; a result suggesting that while there may be some small component of ionic movement or electro-chemical current in the doped PCDTBT, it is likely that a different process is responsible for its increased conductivity. We therefore attribute the 10^5 times increase in conductivity in the doped PCDTBT films to electronic conduction via p-doped states.

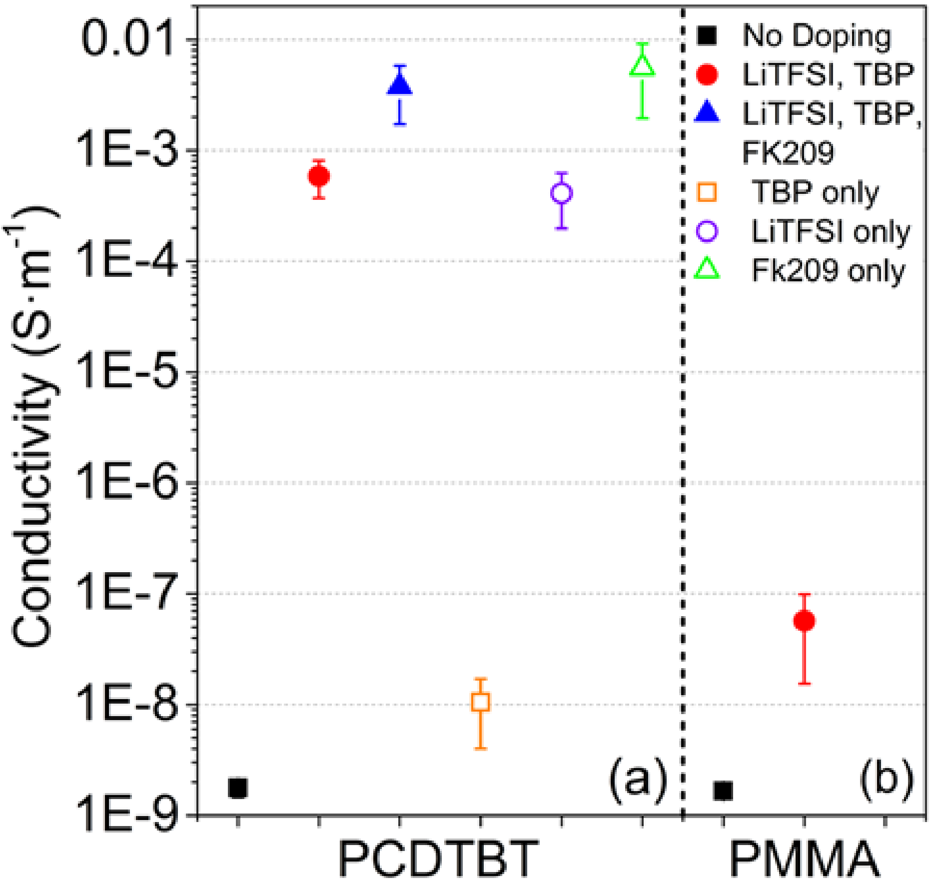

Figure 3: *The conductivities of a series of PCDTBT thin films as determined from the high voltage region of I-V traces of films coated on interdigitated ITO substrates. Part (a) shows the conductivity of a pure PCDTBT film (black), and PCDTBT when doped with LiTFSI + TBP (red), LiTFSI + TBP + FK209 (blue), TBP (orange), LiTFSI (purple) and FK209 (green). Part (b) plots the conductivity of a pure PMMA film (black), and PMMA when doped with LiTFSI + TBP (red).*

Note we have also explored the apparent p-doping of PCDTBT films stored under various conditions and find a slight increase in PCDTBT conductivity when films have been stored in dry air for 24 hours or exposed to A.M 1.5 radiation for 30 minutes, as shown in Figure S5.

We now discuss the use of a doped-PCDTBT polymer as a HTM in standard structure n-i-p architecture PSC. Here, devices were based on the architecture: glass / TEC 10 FTO / c-TiO_2 / mp-TiO_2 / $(FAPbI_3)_{0.85}(MAPbBr_3)_{0.15}$ / HTM / Au as illustrated in the schematic diagram shown in Figure 4(a). To optimise device efficiency, extensive experiments were conducted to optimise the PCDTBT thickness and doping level. For initial thickness optimisation experiments, the dopant level was fixed at 1:0.4:2.4 (PCDTBT monomer:LiTFSI:TBP), with the total solids concentration in the chlorobenzene solution varying between 5 and 30 mg/ml (see Table S1 for full fabrication details for each PCDTBT layer). As a benchmark, devices are compared with devices incorporating a (470 ± 50) nm thick spiro-OMeTAD HTM doped with LiTFSI:TBP:FK209 (1:0.2:0.8:0.03). Again, the data presented on spiro-OMeTAD based devices was collected after optimisation of thickness and dopant levels.

We display the results of the optimisation experiments for PCDTBT-HTM devices in Figure 5 as a series of box-plots, showing device metrics (PCE, short circuit current (J_{sc}), open circuit voltage (V_{oc}) and fill factor (FF)) as a function of PCDTBT thickness as measured by a Bruker DektakXT profilometer. Figure S6 plots typical J-V sweeps for devices with each thickness of PCDTBT. It can be seen that as the thickness of the PCDTBT is increased from 40 to 170 nm, there is a general increase in all device metrics. Beyond a PCDTBT thickness of 170 nm, the J_{sc} and V_{oc} plateau at around 21 mA/cm^2 and 1V respectively. The FF and PCE attain peak values of 70% and 15.9% respectively at a PCDTBT thickness of (170 ± 20) nm, after which they reduce as thickness increases. Table S1 in supplementary information details the shunt and series resistance for each PCDTBT thickness.

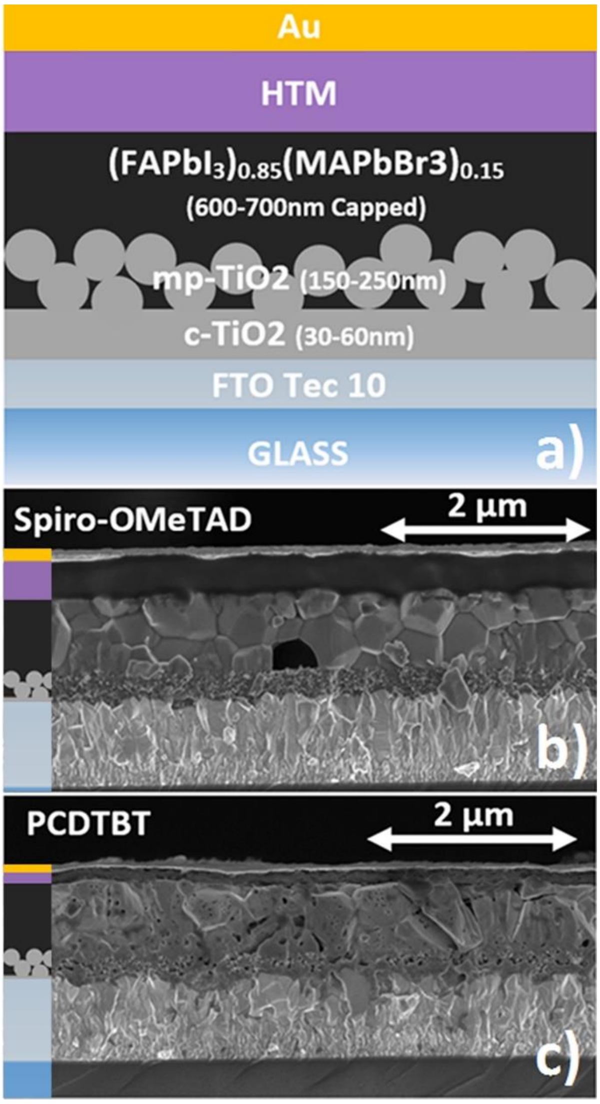

Figure 4: *PSC device layout. Part (a) is a schematic figure showing device structure. Part (b) is a cross-sectional scanning electron microscope (SEM) of a reference device using a spiro-OMeTAD HTM (purple). Part (c) shows an SEM image of a device utilising an optimised PCDTBT HTM (purple).*

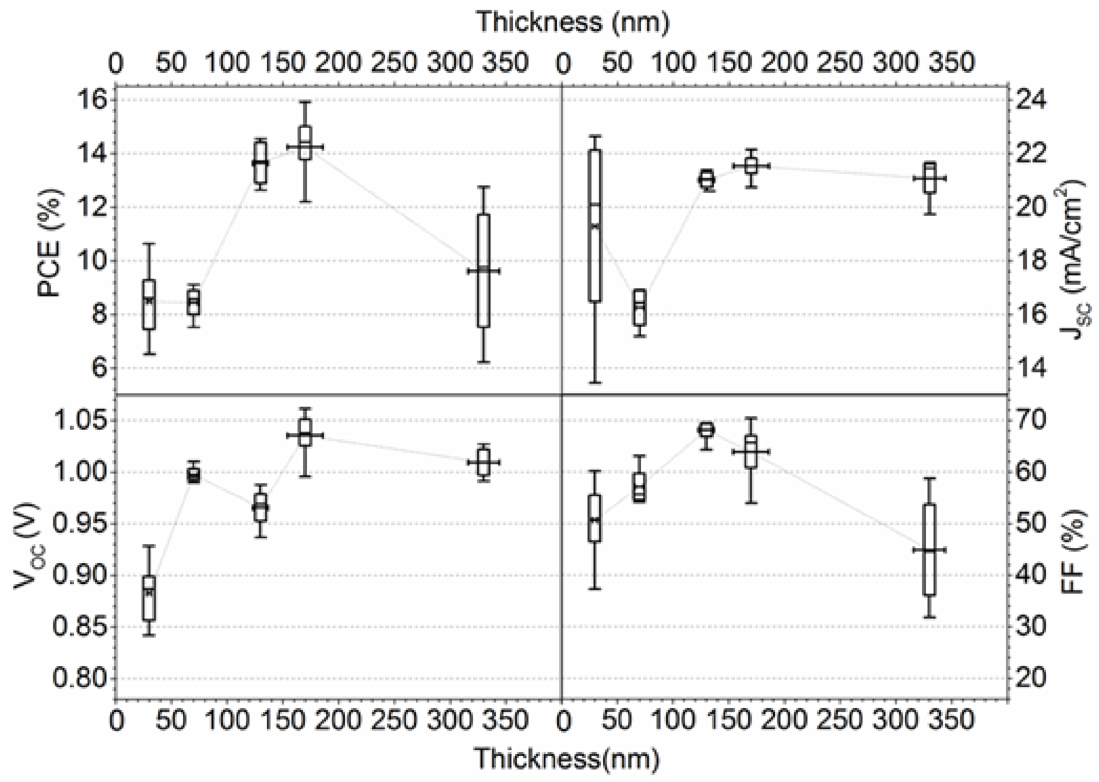

Figure 5: *Boxplots of device metrics for a PSC as a function of doped PCDTBT film thickness.*

For completeness, we present cross-sectional scanning electron microscope (SEM) images of optimised PSCs based on spiro-OMeTAD and PCDTBT based HTMs in Figure 4(b) and (c) respectively. It can be seen that the SEM images confirm that the optimum PCDTBT thickness is significantly thinner (170 nm) than that used in the spiro-OMeTAD (470 nm) devices. Nevertheless, the PCDTBT films appear to be uniform and successfully form a continuous film over the perovskite active layer. The cross-sectional SEM was performed on champion devices with device metrics in the top quartile of a batch of similar devices. Despite the good performance of these devices, we observe the presence of darker spots in the perovskite layer in both spiro-OMeTAD and PCDTBT devices. An intensity line profile of these spots (see Figure S7) indicates that they are not voids, but contain some material. It is well known that a reduced signal of back-scattered electrons may indicate a specimen with lower average atomic number.[31] However, under the imaging conditions used here, n-type material would also appear darker than undoped or p-doped regions.[32,33] These darker regions could therefore be either residual organic material from fabrication, an onset of perovskite degradation into its organic components, or dopant-heavy regions of the perovskite. We also note the presence of a darker region of the HTM near the perovskite/HTM interface, which we attribute to a build-up of n-doped material. It is likely this is further evidence for the origin of band bending which is likely beneficial to hole extraction. Further investigation is needed to understand the origin of these darker regions, and their presence indicates that further improvements in device performance, beyond those reported here, may be possible.

We have explored the effects of doping the PCDTBT HTM at various levels on the performance of a PSC device. In all cases, the thickness of the PCDTBT HTM was fixed at 170 nm. Table 1 summarises key metrics of devices constructed using PCDTBT doped with a combination of materials at different concentrations. It can immediately be seen that the undoped PCDTBT HTM results in devices having very low PCEs of (0.37 ± 0.04)% as a result of low J_{sc} and FF. It is likely that the low conductivity and lack of band bending in the undoped PCDTBT film impedes hole transport from the perovskite active layer to the Au contact. It can be seen that devices incorporating PCDTBT doped with LiTFSI or FK209 have improved performance, however, the device PCE is limited to (0.98 ± 0.5)% and (1.94 ± 0.7)% respectively. This indicates that hole extraction from devices without TBP is still highly inefficient despite the large increase in conductivity observed in PCDTBT films doped with either LiTFSI or FK209, as evidenced in Figure 3. Interestingly, devices in which the PCDTBT is doped with TBP perform much better, having a PCE of (6.6 ± 1.5)%, indicating that it is the most critical of the dopants explored. Here, such gains in efficiency result from significantly increased J_{sc}. We note that previous work has suggested that a build-up of TBP at the interface between the perovskite and various HTMs (e.g. spiro-OMeTAD and single-walled carbon nanotubes capped by the polymer PMMA) may induce band bending and enhance the band alignment between the perovskite valance band and the HTM HOMO level,[15] resulting in more effective hole transfer. Here we assume that a similar effect occurs, with the low values for device FF being consistent with the low conductivity of the TBP-doped PCDTBT without LiTFSI.

When both LiTFSI and TBP are doped into the PCDTBT at a concentration of (1:0.4:2.4) and at an enhanced concentration of (1:0.8:4.8) (referred to as x2 in Table 1), we find a significant enhancement of device metrics. Here, devices utilising the PCDTBT at the 'standard' doping level have a PCE of (14.4 ± 0.7)%; a value that is apparently reduced to (11.8 ± 1.0)% at the x2 concentration. Here, the reduction in efficiency at the enhanced doping level results from a reduction in all device metrics apart from V_{oc}. It has been proposed that LiTFSI passivates trap states at the TiO_2 surface, increasing the V_{oc} but increasing charge recombination rates at the perovskite/TiO_2 interface,[10,34] which may explain the reduction in x2 doped device performance. We also find that as the concentration of dopants is increased, the doped PCDTBT solution becomes increasingly harder to wet to the perovskite surface.

Upon addition of all dopants (LiTFSI, TBP and FK209) to the PCDTBT, we find a reduction in all device metrics, with the PCE reducing to (12.7 ± 1.2)%. It appears that despite the fact that such films have the highest conductivity (see Figure 3), the enhanced film inhomogeneity (see Figure 2) acts to reduce device efficiency. We believe this is consistent with an increase in the number short circuit pathways between the perovskite and metal contact.

It appears, therefore, that PCDTBT achieves best performance as a HTM when it is used at a thickness of around (170 ± 20) nm and doped with LiTFSI and TBP at a molar ratio of 1:0.4:2.4 for PCDTBT monomer:LiTFSI:TBP. We compare the performance of batches of these device with a batch of devices incorporating a spiro-OMeTAD HTM, in addition to champion metrics for devices that incorporate an additional LiTFSI interlayer above the mp-TiO_2 in Table 2. As has been previously reported, there is an increase in FF upon the inclusion of the LiTFSI interlayer,[26] but no significant change in other device metrics. For completeness, we plot JV curves under AM1.5 illumination for PSCs based on a PCDTBT and spiro-OMeTAD HTMs, containing a LiTFSI interlayer, in Figure 6(a), and include stabilised measurements of output power in Figure 6(b). It can be seen that devices incorporating the PCDTBT HTM have a slightly reduced performance compared to those using the spiro-OMeTAD HTM (peak PCE of 15.9% compared with 17.4%). This reduction in efficiency mainly occurs as a result of lower FF (70% compared to 73% for PCDTBT and spiro-OMeTAD HTMs respectively).

	No Dope	LiTFSI	TBP	LiTFSI,TBP	x2 LiTFSI, x2 TBP	Fk209	Fk209, LiTFSI, TBP
PCE [%]	**0.42** (0.37 ± 0.04)	**2.04** (0.98 ± 0.52)	**8.56** (6.63 ± 1.46)	**15.7** (14.4 ± 0.7)	**12.8** (11.8 ± 1.0)	**3.30** (1.94 ± 0.71)	**15.2** (12.7 ± 1.2)
J_{sc}[mA/cm^2]	**3.8** (3.6 ± 0.3)	**7.9** (5.8 ± 1.3)	**21.2** (20.2 ± 0.8)	**21.6** (20.7 ± 0.7)	**18.5** (17.6 ± 0.9)	**8.3** (5.7 ± 1.6)	**22.4** (21.2 ± 0.9)
V_{oc}[V]	**0.72** (0.69 ± 0.03)	**0.93** (0.83 ± 0.07)	**1.04** (1.01 ± 0.02)	**1.02** (1.01 ± 0.01)	**1.02** (1.00 ± 0.01)	**1.00** (0.90 ± 0.13)	**1.05** (1.02 ± 0.01)
FF [%]	**18** (15 ± 2)	**28** (19 ± 5)	**39** (32 ± 5)	**71** (69 ± 2)	**68** (66 ± 2)	**39** (32 ± 5)	**65** (59 ± 4)

Table 1: *Key device metrics for a series of PSCs using a PCDTBT HTM. Data shown in bold text are the peak values obtained with data in parenthesis being the average value ± standard deviation. For the optimum thickness of PCDTBT (170 nm) different PCDTBT data is given for films that are either un-doped, or doped with LiTFSI only, TBP only, LiTFSI + TBP, double the regular concentration of LiTFSI and TBP, FK209 only, and finally all dopants.*

Finally, we have made preliminary measurements of operational stability on devices utilising doped PCDTBT (see Figure S8) that are compared to benchmark devices utilising a doped spiro-OMeTAD HTM. Here, devices were deliberately left unencapsulated, and operated in air under a constant 1 sun equivalent halogen lamp. It was found that after 75 hours, the PCE of PCDTBT had reduced to 50% of its initial value. In comparison, devices utilising a spiro-OMeTAD HTL had reduced to 30% of their initial efficiency over the same period. We suspect that the enhanced stability of devices incorporating a PCDTBT HTM may result from its hydrophobic nature (even upon doping) that reduces the ingress of moisture into the perovskite active layer.

	Spiro-OMeTAD	PCDTBT	Spiro-OMeTAD + LiTFSI Interlayer	PCDTBT + LiTFSI Interlayer
PCE [%]	**16.6** (15.3 ± 0.8)	**15.6** (14.3 ± 0.8)	**17.36**	**15.92**
J_{SC} [mA/cm]	**22.4** (22.0 ± 0.2)	**21.7** (20.7 ± 0.2)	**22.43**	**22.04**
V_{oc} [V]	**1.08** (1.04 ± 0.03)	**1.06** (1.04 ± 0.01)	**1.05**	**1.03**
FF [%]	**70** (67 ± 2.3)	**68** (63 ± 4)	**73**	**70**

Table 2: *Key device metrics of optimized PCDTBT-PSCs and reference spiro-OMeTAD-PSCs. Data shown in bold text is peak value obtained with data in parenthesis being the average value ± standard deviation. Key device metrics of our champion devices are also presented, here the devices implement a LiTFSI interlayer above the mp-TiO*$_2$.

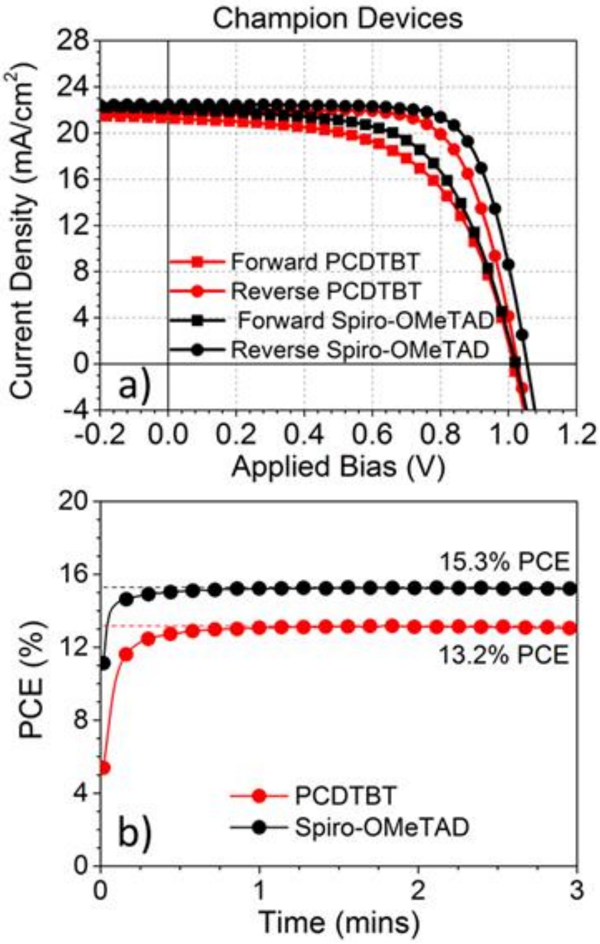

Figure 6: *Champion Devices. Part (a) shows J-V curves obtained for champion devices utilising a spiro-OMeTAD HTM (black) and a PCDTBT HTM (red). Forward sweeps indicated by square points and reverse sweeps indicated by circular points. J-V curves were measured at a sweep speed 0.4 Vs*$^{-1}$*. (b) Stabilised PCE measurements taken for 3 minutes under constant simulated AM1.5 illumination for spiro-OMeTAD-PSCs (black) and PCDTBT-PSCs (red). These devices implement a LiTFSI interlayer above the mp-TiO2.*

Conclusions

We have explored doping the conjugated polymer PCDTBT with a series of dopant molecules to improve its functionality as a hole-transport material in a perovskite solar cell. Electrical measurements indicate that the conductivity of PCDTBT thin films was increased by a factor of $\sim 10^5$ times upon doping with LiTFSI and TBP, making it ideal a material for efficient charge transport. Comparative light-soaking measurements suggest that the photostability of doped PCDTBT is comparable to that of doped spiro-OMeTAD, while contact angle measurements suggest that doped PCDTBT has a more hydrophobic surface, suggesting an enhanced barrier to the ingress of moisture. X-ray scattering measurements on doped and undoped thin films of PCDTBT indicated that both the lamelle and π–π stacking peaks were broadened in the doped films suggesting that the chemical doping may partially disrupt molecular packing. The LiTFSI and TBP doped PCDTBT films were then used as a HTM in standard architecture PSCs. Here, it was found that using either LiFISI and TBP alone did not markedly improve device performance, however it was the combined use of such dopants that was necessary to improve device efficiency. By optimising the doping level and thickness of the doped PCDTBT HTM layer, PSC devices were created with a champion PCE of 15.9%, with stabilised measurements performed under ambient conditions revealing device efficiencies of 13.2%. Our work confirms that doped PCDTBT is a promising HTM in high-performance perovskite solar cell devices.

Experimental Methods

Device fabrication: All solvents used were purchased from Sigma Aldrich. Devices were fabricated on TEC 10 FTO/glass substrates (XOP glass). FTO was patterned by etching each substrate with zinc powder and 4M HCl, after which they were dumped in DI water, dried and swabbed with cotton buds and then sonicated for 10 minutes in hot Helmanex detergent solution, twice in deionised water, and IPA. The c-TiO_2 layer was deposited by spray-pyrolysis from a dilution of 1.72ml of Titanium diisopropoxide bis(acetylacetonate) (75wt % Sigma Aldrich) in 18.28ml of IPA (Sigma Alrich) onto a hotplate at 450°C and left to sinter for 30 minutes.

A meso-porous TiO_2 (mp-TiO_2) layer was fabricated from a titanium oxide paste (18-NRT Dyesol) that was first diluted to 15 wt% in ethanol. The resulting solution was spin coated in air (< 35% RH) at room temperature on top of the c-TiO_2 at 5000 rpm for 15s. After deposition, the substrates were left at room temperature for 10 minutes before being sintered in air for 1 hour at 450°C. For final champion devices a 19mg/ml solution of bis(trifluoromethane)sulfonimide lithium salt, LiTFSI (Sigma Aldrich) in acetonitrile was spun onto the substrates in air (<35% RH) at 3000rpm and the substrates were re-sintered in air at 450°C for a further 30 minutes before being passed into a nitrogen filled glove box.

To prepare the perovskite layer, formamidinium iodide FAI (>99.5%, Ossila), lead iodide PbI_2 (99%, Sigma Aldrich), methylammonium bromide MABr (Dyesol) and lead bromide $PbBr_2$ (99.999%, Sigma Aldrich) were dissolved in a 4:1 v/v DMF:DMSO solvent blend at a concentration of 1.31M, 1.38M, 0.24M, 0.24M for FAI, PbI_2, MABr and $PbBr_2$ respectively. This produced a ~50% wt $(FAPbI_3)_{0.85}(MAPbBr_3)_{0.15}$ perovskite solution, however the 0.95:1 FAI:PbI_2 molar ratio used resulted in a slight excess of lead in the final solution. The resultant ink was not heated and has not yet been shown to be stable beyond 1 week when stored in air.

To process the perovskite precursor, the $(FAPbI_3)_{0.85}(MAPbBr_3)_{0.15}$ solution was deposited inside an N_2 filled glovebox using a 2-step anti-solvent spin routine adapted from Bi, D. et al.[7] Firstly 50μl of the perovskite solution was dispensed onto the stationary substrate from a pipette. The substrate was then spun at 2000 rpm for 10 s with a ramp-up of 200 $rpms^{-1}$ then at 6000 rpm for 30 s with a ramp-up of 2000 $rpms^{-1}$. A near continuous stream of 100μl of chlorobenzene was then rapidly deposited onto the spinning substrate after 10 seconds into the second stage of the spin cycle (corresponding to 20 seconds after the perovskite was originally dispensed). Immediately after spin-casting, the substrate was placed on a hotplate at 100°C and annealed for 90 minutes.

To prepare the PCDTBT layer, A low palladium content poly[N-9'-heptadecanyl-2,7-carbazole-alt-5,5-(4',7'-di-2-thienyl-2',1',3'-benzothiadiazole)], PCDTBT with Mw ~ 34,900 (Ossila) (synthesised as described in ref [19] and purified as described in ref [21]) was first dissolved in chlorobenzene (CB) at 20mg/ml. Similarly, spiro-OMeTAD (2,2',7,7'-Tetrakis[N,N-di(4-

methoxyphenyl)amino]-9,9'-spirobifluorene) (> 99.5% Ossila) was first dissolved in CB at 96.6mg/ml. Stock dopant solutions of LiTFSI (Sigma) and FK 209 Co(III) - TFSI (Dyesol) were made at 175mg/ml in acetonitrile. To achieve the standard (optimum) doping level, 20μl of LiTFSI stock and 10μl of TBP (96%, Sigma) were added to 1ml of PCDTBT solution. The optimum spiro-OMeTAD solutions were created by adding 30μl of LiTFSI stock, 10μl of TBP and 20μl of FK209 stock to 1ml of spiro-OMeTAD solution. This was equivalent to a molar ratio of 1:0.4:2.4 for PCDTBT monomer:LiTFSI:TBP and 1:0.2:0.8:0.03 for spiro-OMeTAD:LiTFSI:TBP:FK209. For PCDTBT thickness screening the dopant ratio was held constant and solution concentrations were scaled as indicated in Table S1. For PCDTBT HTMs using FK209, 3.2μl of stock FK209 was added to 250 μl of doped PCDTBT solution. All solutions were kept at room temperature and vortex mixed before use. For optimum device performance, HTMs were spun at 2000rpm for 30s onto a static perovskite coated substrate in a nitrogen filled glovebox. For thickness tuning measurements the spin speed was changed as indicated in Table S1. Thicknesses were measured using a Bruker DektakXT profilometer.

To deposit the device anode, the devices were returned into air and placed in an Edwards Auto 306 bell-jar evaporator. An 80nm thick gold layer was evaporated onto the device surface at a pressure of *ca* 10^{-6} mbar. The final device layout is shown in Figure S9.

Absorption: UV-vis measurements were performed under ambient conditions using UV-VIS-NIR light source (Ocean Optics – DH-2000-BAL), collection fibre optic cables (Ocean Optics) and spectrometer (Ocean Optics – HR2000+ES). Samples for absorption measurements were prepared on quartz-coated glass using the same deposition methods as used in device fabrication. Doped samples were made with doping levels that match those described in device fabrication. Doped and undoped HTM films of 120-140nm, matching the doping level used in champion devices, were aged under a constant 1 sun equivalent halogen lamp containing a UV component.

Solution absorption measurements of the dopants were recorded in a clean cuvette having a 0.4 cm path length, using doping levels equivalent to 1/3 the dopant level used to make champion PCDTBT devices. Supplementary solutions were taken with diluted 0.0125mg/ml PCDTBT solution in CB with doping concentrations of x320 LiTFSI, TBP and x240 FK209 relative to device doping levels.

Contact Angle: A goniometer tensiometer coupled with Attension Theta software package was used to take images of static droplets of deionized water on doped and undoped PCDTBT and spiro-OMeTAD films and determine the sessile contact angle.

GIWAX S: Grazing Incidence Wide-Angle X-ray Scattering (GIWAXS) measurements were carried out using a Xenocs Xeuss 2.0 SAXS/WAXS machine equipped with was a liquid Gallium MetalJet (Excillum) x-ray source emitting x-rays with an energy of 9.2 keV. PCDTBT samples with (~120 nm thick) and without the dopants (~90 nm thick) were mounted on an angular positioning stage to align the samples. The measurements were performed in a vacuum chamber to reduce the background signal. The scattered X-rays were measured with a Pilatus3R 1M detector over a count time of 10 minutes. The 2D detector image was processed using Foxtrot software, which was used to produce the 1D plots.

Atomic Force Microscopy: A Veeco Dimension 3100 operated in tapping mode with was used to characterise undoped, LiTFSI and TBP doped and FK209 doped PCDTBT films equivalent to those used in device fabrication.

Conductivity: Samples for conductivity measurements were prepared on Interdigitated (ID) ITO Substrates with variable channel width, 50 to 200 μm (Ossila). Undoped and doped ITO/PCDTBT/ITO samples were made with doping levels that also match those described in device fabrication. The conductivity was extracted from the high E-field region, beyond the charge injection inflections of I-V scans measurements, taken using a Keithley 237 source measure unit to sweep from -10 V to +10V and back again at various scan speeds on samples with various channel widths. For the poly(methyl methacrylate) PMMA measurements a 5mg/ml solution of Mw ~ 120,000 (Sigma) in CB was dispensed with and without 5μl of LiTFSI stock and 2.5μl of TBP. Since the density of a film of PMMA and PCDTBT are similar (both ~ 1.2 g.cm^{-3}),[35,36] the same ratio of doping concentrations was used for both materials and are assumed comparable.

SEM: An FEI Nova Nano 450 scanning electron microscope (SEM) was used to image PSC devices. Here, fractured samples were attached to 1 cm diameter stubs using electrically conductive silver paint and allowed to dry before being loaded into the SEM. All the samples were imaged using through-lens detector (TLD) with a beam current of ~21 pA and an accelerating voltage of 1.5 kV.

Device characterisation: Device performance was determined by measuring J-V curves under ambient conditions using a Newport 92251A-1000 solar simulator. A NREL certified silicon reference cell was used to calibrate the simulated AM1.5 light to 100 $mWcm^{-2}$ at 25°C. The un-encapsulated devices were covered with an illumination aperture mask that defined an illuminated area of 0.0256 cm^2. J-V measurements were recorded using a Keithley 237 source measure unit that swept the applied bias from -1.2 V to +1.2V and back again at a scan speed of 0.4 Vs^{-1}. The J-V scans were typically recorded on the second or third day after device fabrication. The performance metrics were extracted from the J-V scan and then used to determine the V_{mpp} of the best devices. Stabilised current/power measurements were taken by holding the devices at their V_{mpp} for several minutes. For supplementary device stability data, several PSCs of starting PCEs equivalent to those reported here, implementing PCDTBT (doped with FK209 in addition to LiTFSI and TBP) and spiro-OMeTAD as HTMs, are repeatedly tested in air at 45^{o}C with uncontrolled humidity, under a constant AM 1.5 light source. Devices are left without encapsulation to accelerate the degradation process. The device metrics are normalised to several reference diodes.

Acknowledgements

This work was funded by the UK Engineering and Physical Sciences Research Council (EPSRC) via grants EP/M025020/1 ‘High resolution mapping of performance and degradation mechanisms in printable photovoltaic devices’, EPSRC grant EP/N008065/1 ‘SECONDARY ELECTRON EMISSION - MICROSCOPY FOR ORGANICS WITH RELIABLE ENGINEERING-PROPERTIES’, and EP/M014797/1 ‘Improved Understanding, Development and Optimization of Perovskite-based Solar Cells’. We also thank the EPSRC for PhD studentships via the University of

Sheffield DTG account (J.B.) and from the Centre for Doctoral Training in New and Sustainable PV, EP/L01551X/1 (M.S.). We also would like to thank Dr Andrew J Musser and Dr David Coles for useful discussions. The GIWAXS measurements were made possible by the recently installed Xeuss 2.0 instrument, and we are grateful to Xenocs for their help and support in the user program at Sheffield.

4.2: Additional Discussion and Supplementary Information

Original Supplementary Information

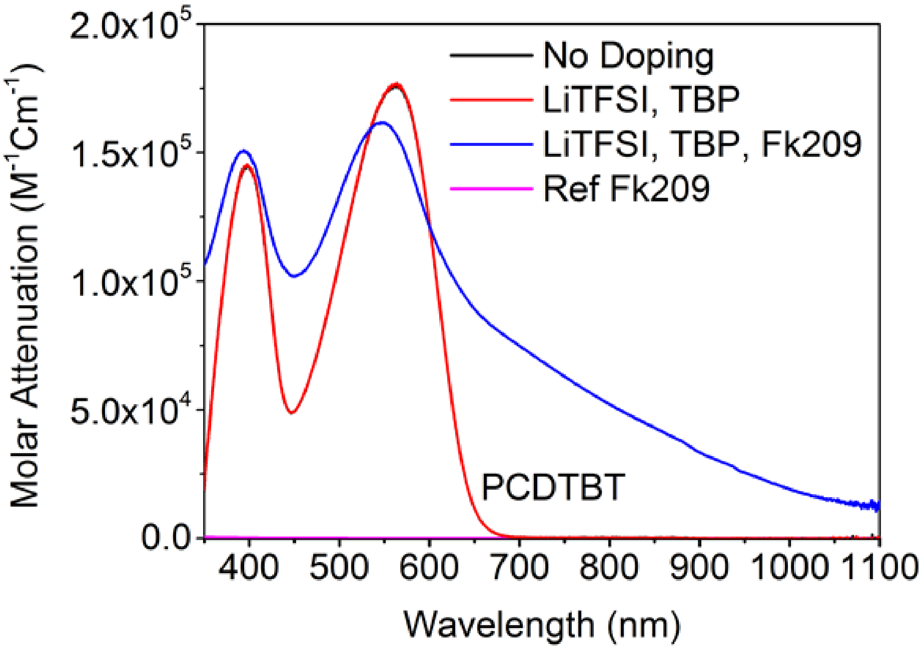

Figure S1: *The (monomer) molar attenuation spectra of a solution of 0.0125mg/ml PCDTBT in CB (path length = 0.4cm), without doping (black, hidden behind red), with LiTFSI and TBP (red) and with LiTFSI, TBP and FK209 (blue). The relative amount of dopants are x320 LiTFSI, TBP and x240 FK209 compared to those used in device fabrication. The reference dopant solution (pink) demonstrates the relatively low molar attenuation of dopants. As the FK209 concentration was increased, it began to aggregate in solution. The large background on the absorption spectra for PCDTBT doped with FK209 most likely originates from enhanced optical scattering.*

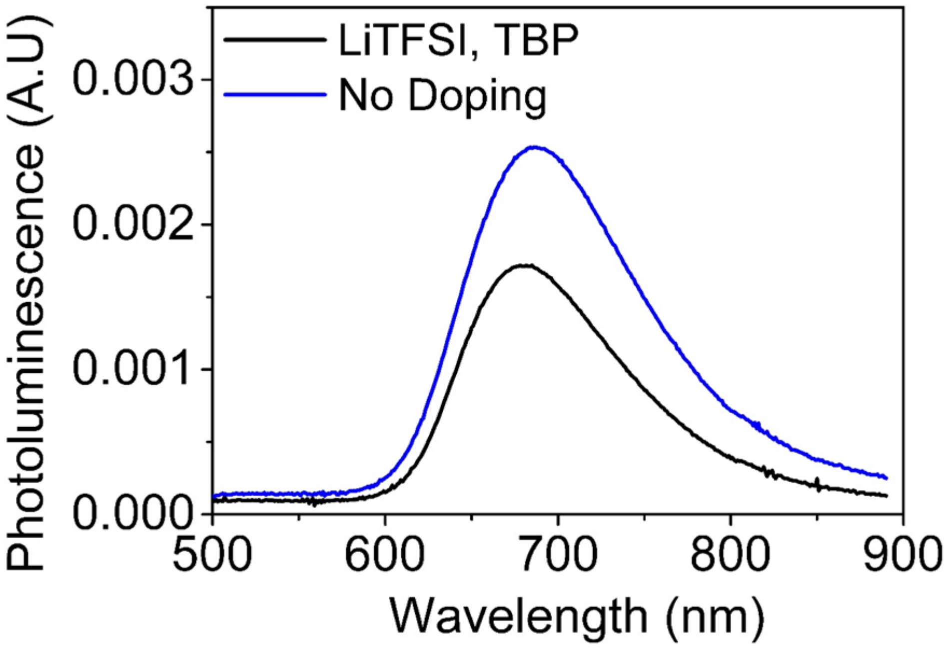

Figure S2: *Steady-State Photoluminescence of PCDTBT and PCDTBT doped with LiTFSI and TBP, with both films having the same thickness. The quantity of dopants in the film were equivalent to the amount used in device fabrication. The PL emission from doped PCDTBT is partially quenched PL relative to an undoped PCDTBT film.*

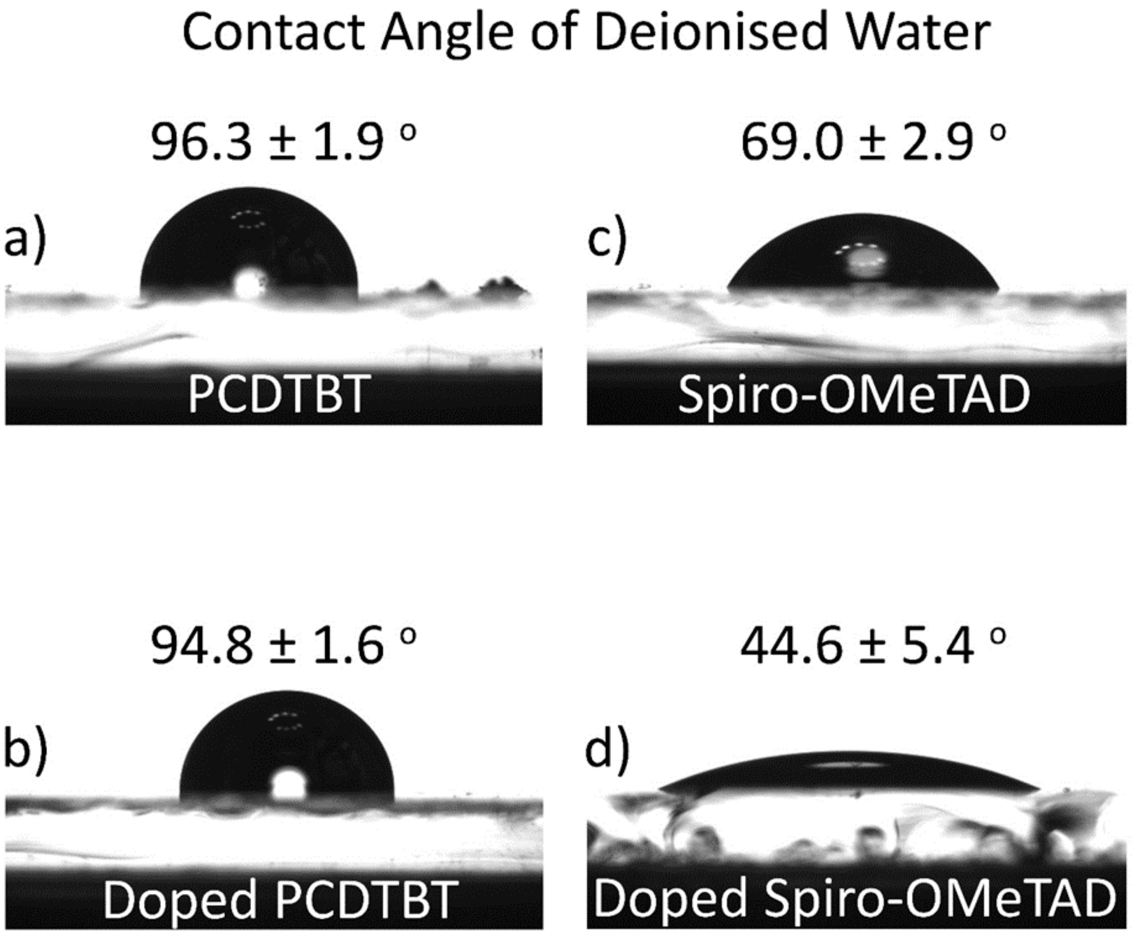

Figure S3*: Contact angle of deionised water on both neat and doped PCDTBT and spiro-OMeTAD films. PCDTBT is hydrophobic in both cases, which will prevent moisture ingress through the back surface to the active layer. Upon doping, the wettability of the HTM materials increases; a finding that is particularly significant for spiro-OMeTAD. This is attributed to increased hydrophilicity upon addition of the dopants, particularly the hygroscopic LiTFSi.*

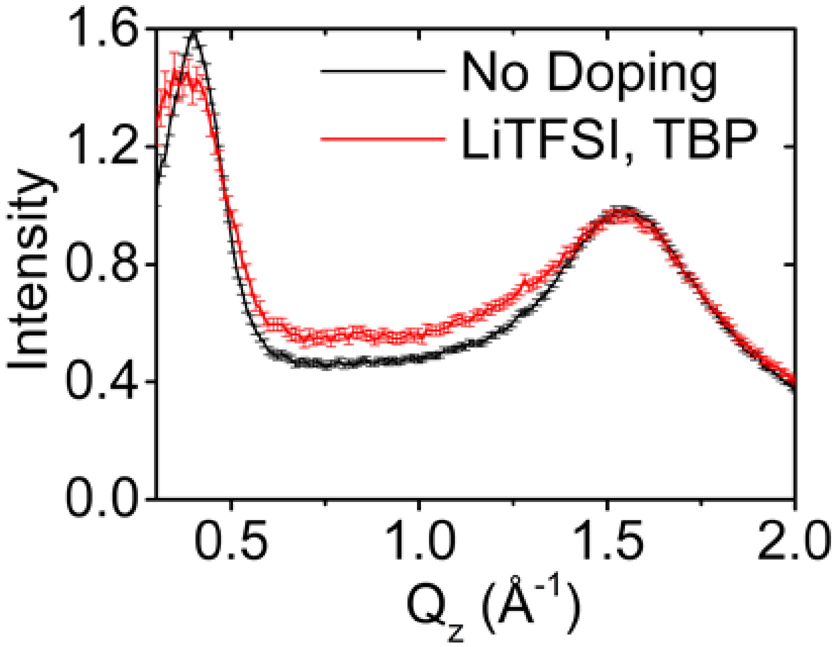

Figure S4: *Typical GIWAXS scattering spectra determined in the out-of-plane direction for both undoped PCDTBT, and PCDTBT doped with LiTFSI:TBP at the same molar ratio as used in device studies. Here, measurements were made at an incidence angle of α = 0.16° (above the critical angle of PCDTBT).*[28] *In the undoped material, we observe scattering maxima at Qz = 0.41 Å^{-1} and 1.56 Å^{-1}, which correspond to scattering from lamella-separated side chains (d = 15.5 Å) and π-π stacked backbones (d = 4.02 Å) respectively.*[28,29] *On doping the PCDTBT, we detect a small increase in π-π stacking distance to 4.05 Å, accompanied by a broadening of the scattering band, signifying a reduction in scattering coherence length from 11.95 Å to 11.27 Å, as determined from the Scherrer equation.*[28] *This is accompanied by a reduction in the amplitude of the lamella-scattering peak, together with a small increase (15.5 Å to 15.8 Å) in the lamella-stacking distance upon addition of the dopants. Taken together, the small increase in stacking length-scales, the relative reduction in the amplitude of lamella-scattering signal and increased disorder in π-π packing indicates that the dopants are able to interact with the PCDTBT, and partially disrupt molecular packing.*

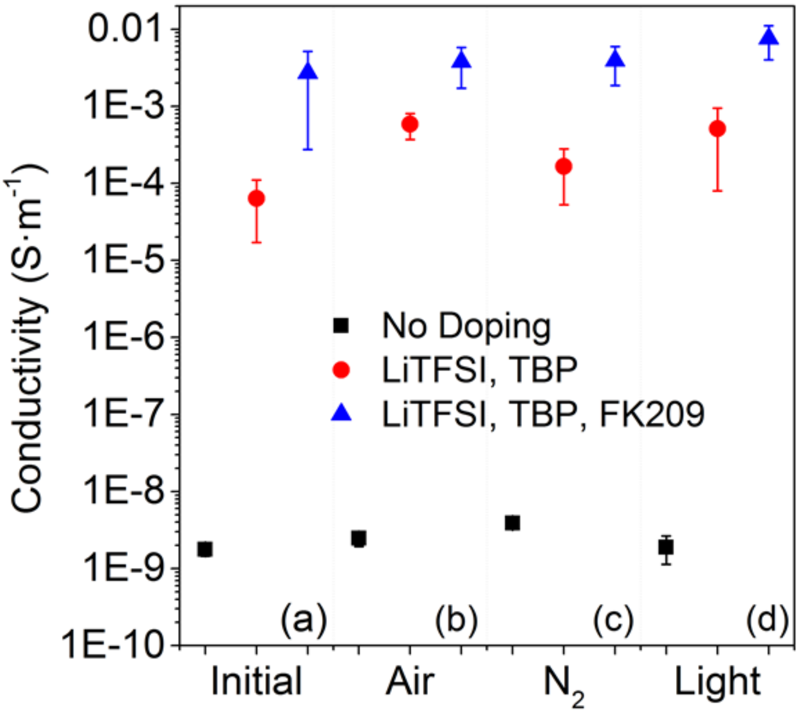

Figure S5: *The conductivity of PCDTBT samples without doping (black), with LiTFSI and TBP (red) and with LiTFSI, TBP and FK209 (blue). Measurements were taken after the films were made (a), after being stored for 24 hours in air (b), after being stored in* N_2 *for 24 hours and after being left under a Newport 92251A-1000 solar simulator for 30 minutes. The quantity of dopants in the film were equivalent to the amount used in device fabrication. We observed a small increase in conductivity relative to the initial doped (red) conductivity after both being stored in air for 24 hours (b) and after being under illumination for 30 minutes (d). We observe a small loss of conductivity for PCDTBT films doped without FK209 (red) after being stored under* N_2 *for 24 hours (c). Films with FK209 (blue) changed very little between storage conditions (b,c) but also underwent a small increase in conductivity under illumination (d).*

Spin Speed	Solution	Thickness [nm]	Pa Roughness [nm]	Stnd Dev [nm]	Estimated Rs [Ohms cm^2]	Estimated Rsh [Ohms cm^2]
2k	5 mg/ml	28	1	1	10	160
2k	10mg/ml	65	3	4	11	580
4k	20mg/ml	127	3	7	7	1460
2k	20mg/ml	166	17	16	7	3720
2k	30mg/ml	332	3	14	13	1770

Table S1: *A list of all of the combinations of PCDTBT solution concentrations (in CB with dopants) and spin speeds, and the resultant thicknesses and roughnesses of the final PCDTBT film each combination of parameters produced. Also shown is the aproximate shunt and series reistance of devices made with each combination of parameters. Shunt resistance increases with thickness up until 20 mg/ml PCDTBT spun at 2k rpm, which was the process conditions used to fabricate champion PCDTBT-PSCs.*

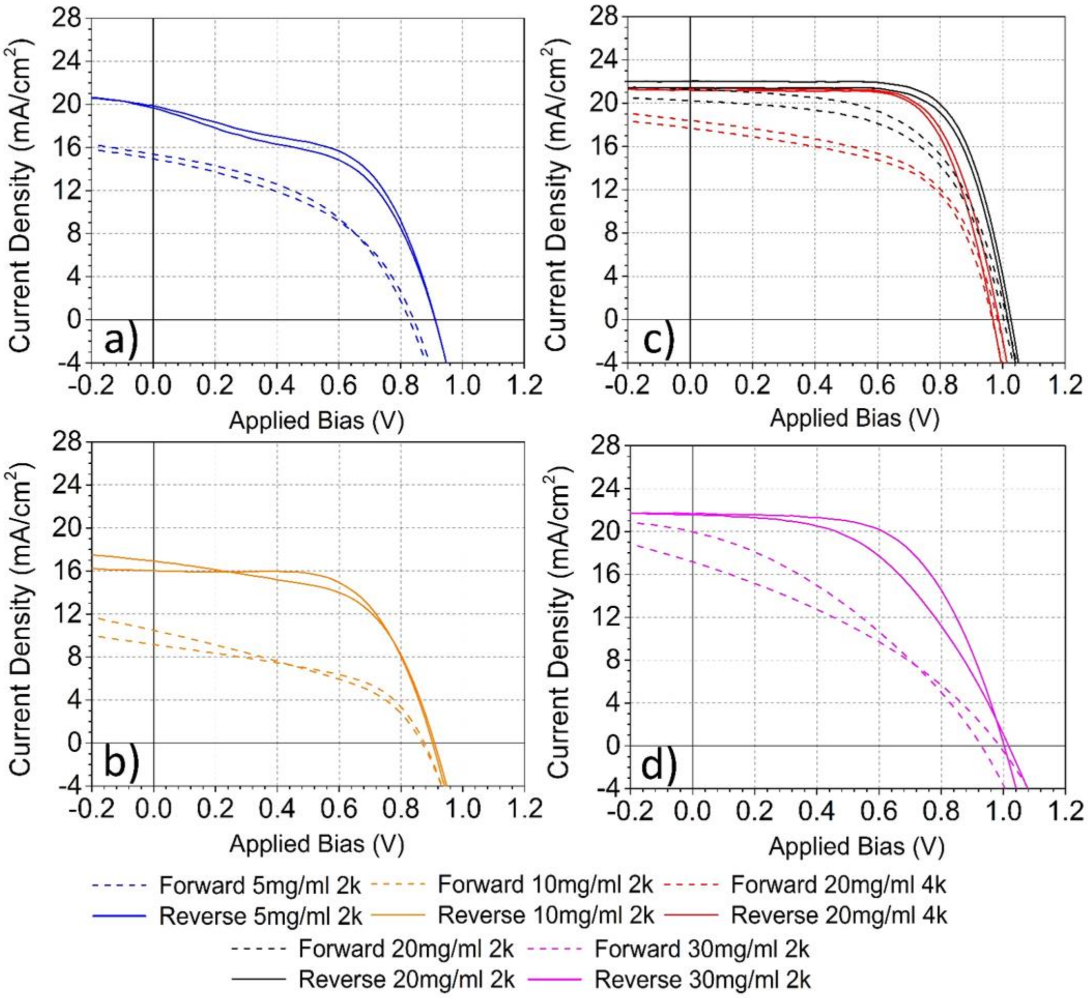

Figure S6: *Two representative forward and reverse J-V sweeps for perovskite devices using PCDTBT deposited using all conditions listed in table S1, taken at 0.4 Vs^{-1}. 5 mg/ml PCDTBT 2k rpm (a), 10 mg/ml PCDTBT 2k rpm (b), 20 mg/ml PCDTBT 2k & 4k rpm (c), and 30 mg/ml PCDTBT 2k rpm (d).*

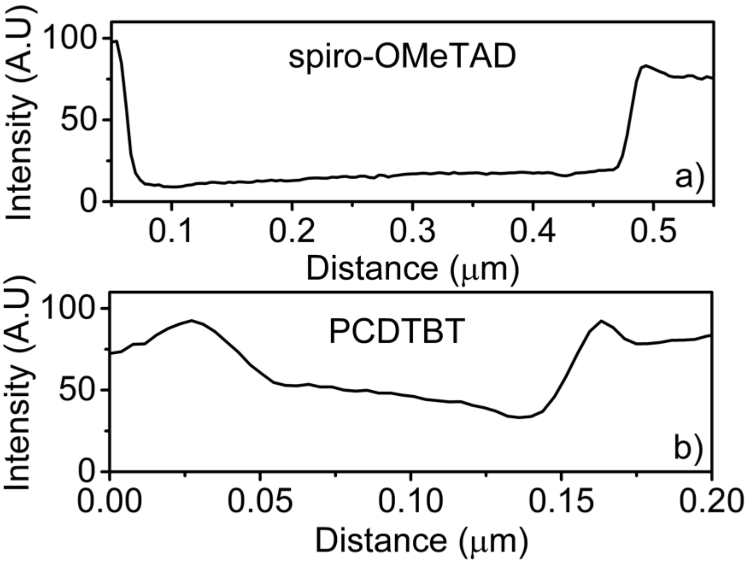

Figure S7: *Line profiles of the intensity of dark regions in SEM images (see Figure 5) in (a) spiro-OMeTAD and (b) PCDTBT, showing that dark regions are not voids but contain some material.*

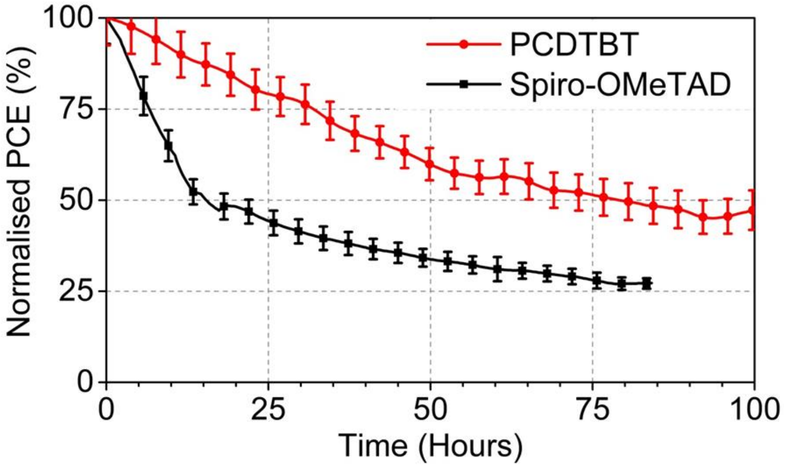

Figure S8*: Stability of PSCs with PCDTBT and spiro-OMeTAD HTMs. Devices are left without encapsulation to accelerate the degradation process. Devices are continuously tested with J-V measurements under a constant 1 sun equivalent halogen lamp. Devices based on the PCDTBT HTM have a relatively enhanced stability compared to those incorporating spiro-OMeTAD.*

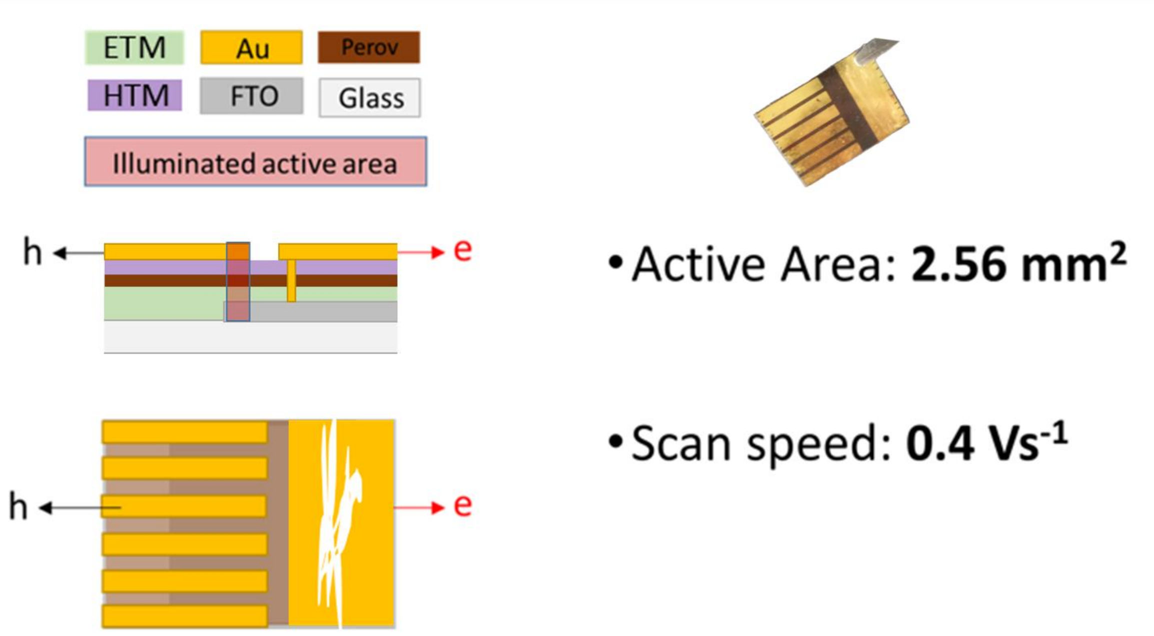

- Active Area: **2.56 mm^2**
- Scan speed: **0.4 Vs^{-1}**

Figure S9: *Device layout used to fabricate PSCs. Devices were mounted on a testboard along with a 2.56mm^2 illumination mask ready for testing under a solar simulator.*

Additional Discussion

To further investigate the doping of PCDTBT with LiTFSI, TBP and FK209, the series and shunt resistances of the devices provided in Table 1 of the original manuscript are given in Table S2. In addition to this, the current-voltage sweeps from characteristic devices in each doping category are given in Figure S10.

It is clear that the introduction of LiTFSI, TBP and FK209 individually into the PCDTBT all reduce the series resistance of the PSCs, with TBP alone acting to reduce series significantly from 1040 Ω to 68 Ω. However, only the TBP and FK209 act to increase the shunt resistance. Upon combination of both LiTFSI and TBP, the series resistance is minimised (7.5 Ω) and the shunt resistance is large (830 Ω), enabling the impressing device metrics in the original manuscript. As with the PCE, the R_S is not improved further upon the addition of FK209. This data indicates that dopants act together to increase the conductivity of PCDTBT (low R_S) whilst also maintaining high shunt resistance, however the PCDTBT does not adequately select charge (high R_{SH}) without addition of the TBP or FK209.

	No Dope	**LiTFSI**	**TBP**	**LiTFSI,TBP**	**Fk209**	**Fk209, LiTFSI, TBP**
R_S (Ω)	1040 ± 200	530 ± 150	68 ± 6	7.5 ± 0.3	110 ± 15	11.8 ± 0.8
R_{SH} (Ω)	110 ± 5	130 ± 10	1350 ± 420	830 ± 130	820 ± 140	1050 ± 380

Table S2: *Series and shunt resistance for a series of PSCs using a PCDTBT HTM. Data shown is average value ± standard deviation. For the optimum thickness of PCDTBT (170 nm) different PCDTBT data is given for films that are either un-doped, or doped with LiTFSI only, TBP only FK209 only, and finally all dopants.*

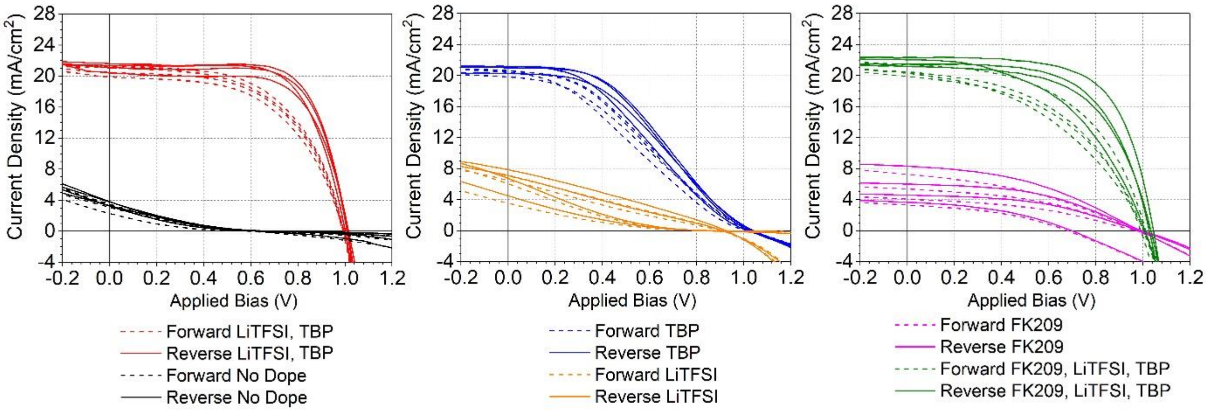

Figure S10: *Four representative forward and reverse J-V sweeps for perovskite devices using PCDTBT deposited using all conditions listed in Table S2, taken at 0.4 Vs^{-1}.*

The dopants (TBP, LiTFSI, FK209) used to increase the conductivity of spiro-OMeTAD and PCDTBT have been shown to increase the photostability of the hole transport layer. However, it is unclear whether these dopants are associated with decreased PSC stability. Cross-sectional SEM images show in Figure S11 presents an additional piece of evidence, indicating that these dopants can accelerate device degradation. Here, an LiTFSI interlayer was directly deposited onto an FTO substrate. Figure S11a is an image of an FTO substrate recorded before LiTFSI deposition, whilst Figure S11b is taken after LiTFSI deposition. A large contrast in FTO crystal quality is observed, whereby LiTFSI appears to have caused non-uniform degradation of FTO crystals.

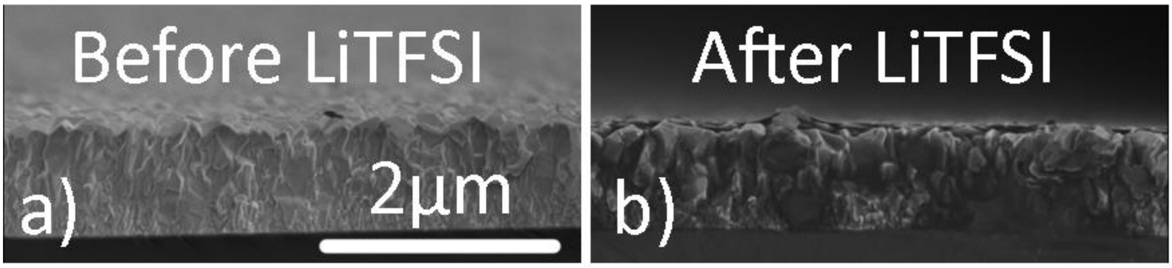

Figure S11: *SEM image of cross-section of FTO substrate before (a,b) and after (c,d) deposition of 19mg/ml acetonitrile LiTFSI solution. FTO appears degraded due to LiTFSI. All scale bars are 2μm.*

4.3: Further Context

Each material that makes up a perovskite solar cell contributes to its performance metrics and stability. This chapter identified a potential HTL replacement, PCDTBT, which can be used to make efficient PCSs.

In order to fully understand the effects of the chemical dopants on the PCDTBT, further measurements may be required. Arrhenius plots of doped PCDTBT films, and conductivity measurements on neat films of organic dopants might support or counter the argument that p-doped PCDTBT states are indeed being generated.

Regardless, this reliance on organic dopants is undesirable, and it is vital that methods to retain efficient charge transport without the need of dopants are developed. Such organic dopants can migrate throughout the PSCs, with such dopants being potentially associated with PSC instability. Metal oxides charge transport layers that are free of organic dopants are investigated in Chapter 6. Combining such metal oxides with neat PCDTBT to form multilayer charge transport stacks may also prove to be a future fabrication route for hole-transport in PSCs.

It is clear that finding a PSC device architecture that is stable is important if perovskites are to be used in a commercial PV technology. Inverted architecture PSCs that are fabricated and encapsulated in order to to maximise PSC stability are described in Chapter 5.

4.4: References

[1] M. Saliba, T. Matsui, K. Domanski, J.-Y. Seo, A. Ummadisingu, S. M. Zakeeruddin, J.-P. Correa-Baena, W. R. Tress, A. Abate, A. Hagfeldt, M. Gratzel, *Science (80).* **2016**, *5557*.

[2] G. Grancini, C. Rolda´n-Carmona, I. Zimmermann, E. Mosconi, X. Lee, D. Martineau, S. Narbey, F. Oswald, F. De Angelis, M. Graetzel. M. K. Nazeeruddin, *Nat. Commun.* **2017**, *8,* 15684.

[3] S. Ameen, M. A. Rub, S. A. Kosa, K. A. Alamry, M. S. Akhtar, H. S. Shin, H. K. Seo, A. M. Asiri, M. K. Nazeeruddin, *ChemSusChem* **2016**, *9*, 10.

[4] S. F. Völker, S. Collavini, J. L. Delgado, *ChemSusChem* **2015**, *8*, 3012.

[5] M. M. Lee, J. Teuscher, T. Miyasaka, T. N. Murakami, H. J. Snaith, *Science* **2012**, *338*, 643.

[6] M. Saliba, T. Matsui, J.-Y. Seo, K. Domanski, J.-P. Correa-Baena, N. Mohammad K., S. M. Zakeeruddin, W. Tress, A. Abate, A. Hagfeldt, M. Gratzel, *Energy Environ. Sci.* **2016**, *9*.

[7] D. Bi, W. Tress, M. I. Dar, P. Gao, J. Luo, C. Renevier, K. Schenk, A. Abate, F. Giordano, J.-P. Correa Baena, J.-D. Decoppet, S. M. Zakeeruddin, M. K. Nazeeruddin, M. Gra tzel, A. Hagfeldt, *Sci. Adv.* **2016**, *2*, e1501170.

[8] T. Leijtens, G. E. Eperon, S. Pathak, A. Abate, M. M. Lee, H. J. Snaith, *Nat. Commun.* **2013**, *4*, 2885.

[9] J. H. Noh, N. J. Jeon, Y. C. Choi, M. K. Nazeeruddin, M. Grätzel, S. Il Seok, *J. Mater. Chem. A* **2013**, *1*, 11842.

[10] S. Wang, W. Yuan, Y. S. Meng, *ACS Appl. Mater. Interfaces* **2015**, *7*, 24791.

[11] Y. Liu, Q. Chen, H.-S. Duan, H. Zhou, Y. Yang, H. Chen, S. Luo, T.-B. Song, L. Dou, Z. Hong, Y. Yang, *J. Mater. Chem. A* **2015**, *3*, 11940.

[12] W. H. Nguyen, C. D. Bailie, E. L. Unger, M. D. Mcgehee, *JACS* **2014**, *136*, 10996.

[13] G. Schlichthörl, S. Y. Huang, J. Sprague, a J. Frank, *J. Phys. Chem. B* **1997**, *101*, 8141.

[14] S. Wang, M. Sina, P. Parikh, T. Uekert, B. Shahbazian, A. Devaraj, Y. S. Meng, *Nano Lett.* **2016**, acs. nanolett.6b02158.

[15] S. N. Habisreutinger, N. K. Noel, H. J. Snaith, R. J. Nicholas, *Adv. Energy Mater.* **2016**, 1601079.

[16] Y.-K. Wang, Z.-C. Yuan, G.-Z. Shi, Y.-X. Li, Q. Li, F. Hui, B.-Q. Sun, Z.-Q. Jiang, L.-S. Liao, *Adv. Funct. Mater.* **2016**, *26*, 1375.

[17] J. H. Heo, S. H. Im, J. H. Noh, T. N. Mandal, C.-S. Lim, J. A. Chang, Y. H. Lee, H. Kim, A. Sarkar, K. NazeeruddinMd, M. Gratzel, S. Il Seok, *Nat Phot.* **2013**, *7*, 486.

[18] Y. Zhang, E. Bovill, J. Kingsley, A. R. Buckley, H. Yi, A. Iraqi, T. Wang, D. G. Lidzey, *Sci. Rep.* **2016**, *6*, 21632.

[19] N. Blouin, A. Michaud, M. Leclerc, *Adv. Mater.* **2007**, *19*, 2295.

[20] S. Beaupré, M. Leclerc, *J. Mater. Chem. A* **2013**, *1*, 11097.

[21] C. Bracher, H. Yi, N. W. Scarratt, R. Masters, A. J. Pearson, C. Rodenburg, A. Iraqi, D. G. Lidzey, *Org. Electron.* **2015**, *27*, 266.

[22] E. S. R. Bovill, J. Griffin, T. Wang, J. W. Kingsley, H. Yi, A. Iraqi, A. R. Buckley, D. G. Lidzey, *Appl. Phys. Lett.* **2013**, *102*.

[23] S. S. Reddy, K. Gunasekar, J. H. Heo, S. H. Im, C. S. Kim, D. H. Kim, J. H. Moon, J. Y. Lee, M. Song, S. H. Jin, *Adv. Mater.* **2016**, *28*, 686.

[24] S. Wakim, S. Beaupré, N. Blouin, B.-R. Aich, S. Rodman, R. Gaudiana, Y. Tao, M. Leclerc, *J. Mater. Chem.* **2009**, *19*, 5351.

[25] M. Saliba, T. Matsui, J.-Y. Seo, K. Domanski, J.-P. Correa-Baena, M. K. Nazeeruddin, S. M. Zakeeruddin, W. Tress, A. Abate, A. Hagfeldt, M. Grä Tzel, **2016**, *9*, 1989.

[26] F. Giordano, A. Abate, J. Pablo, C. Baena, M. Saliba, T. Matsui, S. H. Im, S. M. Zakeeruddin, M. K. Nazeeruddin, A. Hagfeldt, M. Graetzel, *Nat. Commun.* **2016**, *7*, 1.

[27] N. Banerji, E. Gagnon, P. Y. Morgantini, S. Valouch, A. R. Mohebbi, J. H. Seo, M. Leclerc, A. J. Heeger, *J. Phys. Chem. C* **2012**, *116*, 11456.

[28] T. Wang, A. J. Pearson, A. D. F. Dunbar, P. A. Staniec, D. C. Watters, D. Coles, H. Yi, A. Iraqi, D. G. Lidzey, R. A. L. Jones, *Eur. Phys. J. E* **2012**, *35*, 2.

[29] T. Wang, A. J. Pearson, A. D. F. Dunbar, P. A. Staniec, D. C. Watters, H. Yi, A. J. Ryan, R. A. L. Jones, A. Iraqi, D. G. Lidzey, *Adv. Funct. Mater.* **2012**, *22*, 1399.

[30] A. Abate, T. Leijtens, S. Pathak, J. Teuscher, R. Avolio, M. E. Errico, J. Kirkpatrik, J. M. Ball, P. Docampo, I. McPherson, H. J. Snaith, *Phys. Chem. Chem. Phys.* **2013**, *15*, 2572.

[31] J. Cazaux, *J. Microsc.* **2004**, *214*, 341.

[32] C. Schönjahn, R. F. Broom, C. J. Humphreys, A. Howie, S. A. M. Mentink, *Appl. Phys. Lett.* **2003**, *83*, 293.

[33] C. Schönjahn, C. J. Humphreys, M. Glick, *J. Appl. Phys.* **2002**, *92*, 7667.

[34] Q. J. Yu, Y. H. Wang, Z. H. Yi, N. N. Zu, J. Zhang, M. Zhang, P. Wang, *ACS Nano* **2010**, *4*, 6032.

[35] J. Ackermann, M. Juda, D. Hirsch, *Kunststoffe Int.* **2014**, *2014*, 59.

[36] A. J. Clulow, A. Armin, K. H. Lee, A. K. Pandey, C. Tao, M. Velusamy, M. James, A. Nelson, P. L. Burn, I. R. Gentle, P. Meredith, *Langmuir* **2014**, *30*, 1410.

Chapter 5

Volume 8, Issue 24

August 27, 2018

1801234

High Performance Multi-Layer Encapsulation for Perovskite Photovoltaics

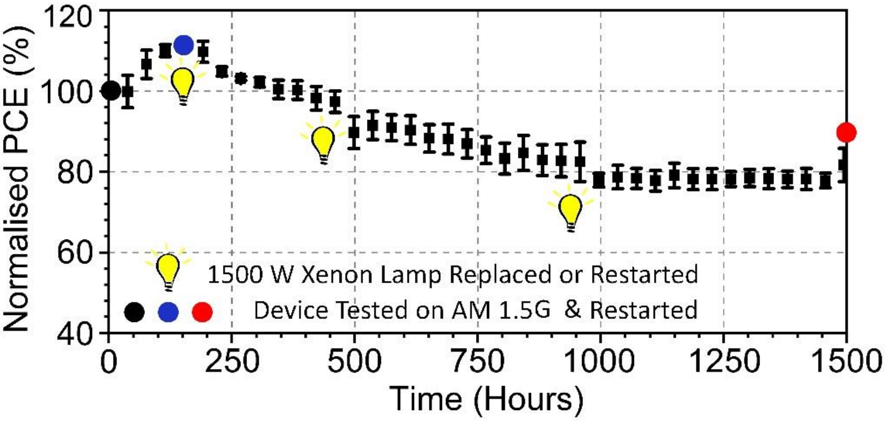

For the journals PDF:

DIO: 10.1002/aenm.201801234

Cite this: Advanced Energy Materials, 2018, 8, 24

5.0: Publication Forward: Finding a Stable Architecture

In this chapter it is established that F4-TCNQ doped poly-TPD can be used to fabricate stable PSCs based on the architecture (ITO)/poly-TPD(F4-TCNQ)/$MAPbI_3$/ $PC_{60}BM$/Bphen/Ag. However, the long-term stability of such PSCs is still reliant on its encapsulation which supresses the formation of silver iodide complexes. Lead acetate and methylamine bubbled route perovskite depositions were investigated for PSC stability measurements. Appendix B details how lead acetate route perovskite resulted in unstable PSCs, and hence was not used for this study. Appendix B also includes some details on *J-V* measurement regimes for PSC aging studies. Here, a multi-layer encapsulation system is developed which, when used on inverted $MAPbI_3$ based PSCs, enables the testing of long-term PSC operational stability in a lifetime testing chamber.

5.1: Publication Main Body

High performance Multi-Layer Encapsulation for Perovskite Photovoltaics

Michael Wong-Stringer[1], Onkar S. Game[1], Joel A. Smith[1], Thomas J. Routledge[1], Bakhet A. Alqurashy[2], Benjamin G. Freestone[1], Andrew J. Parnell[1], Naoum Vaenas[1], Vikas Kumar[3], Majed O. A. Alawad[4], Ahmed Iraqi[4], Cornelia Rodenburg[3] and David G. Lidzey[1]*

[1]Department of Physics & Astronomy, University of Sheffield, Hicks Building, Hounsfield Road, Sheffield, S3 7RH, UK

[2]Department of Basic Science and Technology, Community Faculty, Taibah University, 30002 Al-Madina Al-Mounawara, Saudi Arabia

[3]Department of Materials Science and Engineering, University of Sheffield, Mappin St, Sheffield, S1 3JD, UK

[4]Department of Chemistry, University of Sheffield, Brook Hill, Sheffield, S3 7HF, UK

*Corresponding author, email d.g.lidzey@sheffield.ac.uk

Keywords: PVP, epoxy, perovskite solar cells, stability, lifetime, T80, encapsulation, solvent anneal

Abstract

An encapsulation system comprising of a UV-curable epoxy, a solution processed polymer interlayer, and a glass cover-slip, is used to increase the stability of methylammonium lead triiodide ($CH_3NH_3PbI_3$) perovskite planar inverted architecture photovoltaic (PV) devices. We find this encapsulation system acts as an efficient barrier to extrinsic degradation processes (ingress of moisture and oxygen), and that the polymer acts as a barrier that protects the PV device from the epoxy before it is fully cured. This results in devices that maintain 80% of their initial power conversion efficiency after 1000 hours of AM1.5 irradiation. Such devices are used as a benchmark and are compared with devices having initially enhanced efficiency as a result of a solvent annealing process. We find that such solvent-annealed devices undergo enhanced burn-in and have a reduced long-term efficiency; a result demonstrating that initially enhanced device efficiency does not necessarily result in long-term stability.

Introduction

The power conversion efficiency (PCEs) of perovskite solar cells (PSCs) fabricated using various process routines now routinely exceed 20%,[1–7] with a highest certified PCE reported being 22.7%.[7] Such enhanced efficiency results from both detailed device optimisation studies and materials engineering. Perhaps the most significant development has been the introduction of inorganic cations (including potassium, caesium and rubidium) into the more ubiquitous methylammonium ($CH_3NH_3^+$) and formamidinium ($HC(NH_2)_2^+$) based perovskites. Such cations can result in a range of effects, including enhanced perovskite crystal growth,[6] enhanced material stability at elevated temperature,[4,6] and supressed light-induced ion migration or segregation.[5,8,9] Further enhancements in device stability have been gained from the use of thinner, hydrophobic, UV stable and dopant-free electron and hole transport materials (ETMs and HTMs).[10–17] For example titanium dioxide (TiO_2) has been replaced by tin dioxide (SnO_2),[10,18,19] which has reduced UV sensitivity, and the water soluble and acidic material poly(3,4-ethylenedioxythiophene) polystyrene sulfonate (PEDOT:PSS)[2,20] has been replaced by hydrophobic polymers such as poly[bis(4-phenyl)(2,5,6-

trimethylphenyl)amine (PTAA) or poly(N,N'-bis-4-butylphenyl-N,N'-bisphenyl)benzidine (poly-TPD). Other work has explored reducing trap state density and enhancing charge transport across interfaces within a PSC device.[1–6,21–24] Such progress indicates that with careful design, PSCs have the capability to achieve not only high PCE, but also acquire long-term stability.

An important component of a photovoltaic (PV) device is its encapsulation, as this protects it from the damaging effects of oxygen and moisture. In silicon-based PV, this is typically achieved using glass together with laminated ethylene vinyl acetate (EVA) layers. However this level of protection is not sufficient for PSCs and it is believed that perovskites are sensitive to decomposition products of EVA (acetic acid).[25] For this reason, there is a clear need to develop effective encapsulation strategies for PSCs and to explore their role in extending the operational lifetime of the device. Indeed, effective encapsulation systems permit the study of intrinsic cell degradation mechanisms, such as those caused by light, temperature and processing route without unwanted effects resulting from moisture-induced degradation.

PV T80 device lifetime is defined as the time taken over which the PCE falls to 80% of its initial value.[26,27] In our previous work on organic PCDTBT-based bulk heterojunction solar cells, we demonstrated that the use of a glass cover-slip and a UV curable epoxy can protect the device to such an extent that T80 lifetimes (measured after an initial burn-in) exceeding 10,000 hours can be demonstrated.[26,28] We have also applied this encapsulation technique to PSCs, and concluded that the relatively short T80 lifetimes determined (280 hours after burn-in) resulted from the acidic[29] and hydrophilic nature of the PEDOT:PSS hole extraction layer that was used.[27] During this study however, it became apparent that some degradation occurred to the PSC during the UV curing of the epoxy, and it was speculated that either some polar solvent or initiators in the epoxy underwent a reaction with the perovskite. We note that other work using UV curable epoxies to encapsulate PSCs has also not demonstrated devices having long-term stability.[30–32]

In this paper, we demonstrate that perovskites can be degraded by the deposition and curing of typical epoxy materials. To mitigate this effect, we use a solution-processable polymer interlayer (polyvinylpyrrolidone (PVP)) placed between the PSC and the epoxy, which we demonstrate reduces direct degradation from the epoxy. This allows us to establish a significantly improved yield of high-performing, stable PSCs, with devices having a T80 lifetime of 1000 hours. Using our most stable process as a 'baseline', we then explore the effect of a solvent-annealing process that is often used to enhance device efficiency. Interestingly, we find that solvent annealed devices suffer from a large negative burn-in, such that 40% of their initial PCE is lost within the first 10 hours of aging under AM1.5 illumination. Our measurements demonstrate that devices must be separately optimised for efficiency and stability, and that efficient PSC devices are not necessarily operationally stable.

Devices were based on an indium tin oxide (ITO)/poly-TPD(F4-TCNQ)/$MAPbI_3$/$PC_{60}BM$/Bphen/Ag architecture and were fabricated as illustrated schematically in Figure 1a,b. Here, all layers (except the 100 nm thick silver cathode) were deposited by spin-coating. We have used the hydrophobic hole-transport polymer poly-TPD, doped with 2,3,5,6-Tetrafluoro-7,7,8,8-tetracyanoquinodimethane (F4-TCNQ). The use of such materials is expected to minimise the level of trapped moisture within the device. The $MAPbI_3$ perovskite was deposited by spin-coating from the low boiling-point, non-toxic solvent acetonitrile. Here, the perovskite ink was created by bubbling methylamine through an acetonitrile solution containing $MAPbI_3$ nanocrystals. During the bubbling the nanocrystals dissolve, forming a yellow-coloured solution. This solvent system was originally developed by Noel *et al,* and allows facile wettability of the perovskite precursor ink onto a poly-TPD surface.[33] We acknowledge other reported techniques to improve wettability such as UV ozone treatments,[34] dimethylformamide (DMF) rinsing[35] and the use of ultra-thin amphiphilic polymer layers in order to increase the wettability of DMF-based perovskite solutions.[36,37] However, we find that using $MAPbI_3$ deposited from an acetonitrile solution is a highly reproducible and reliable route to deposit perovskite layers on thin (<10nm) hydrophobic HTMs. Finally, $PC_{60}BM$ and bathophenanthroline (BPhen) layers were deposited from chlorobenzene and IPA solutions respectively.

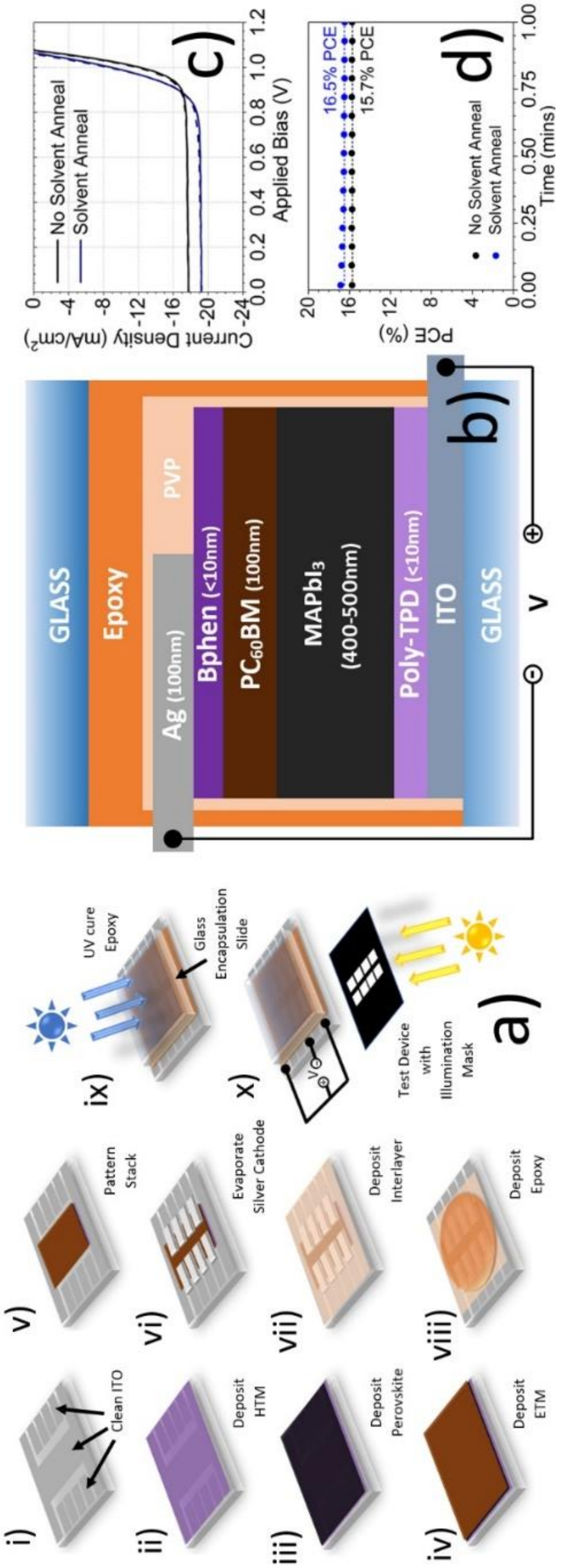

Figure 1: *(a) A schematic of the fabrication and testing routine used to create perovskite solar cells incorporating a PVP/epoxy encapsulation. (b) Device architecture showing all layers, together with their approximate thicknesses. (c) Current-voltage sweeps and (d) stabilised power outputs for champion devices with the thermally annealed* $MAPbI_3$ *active layer (black) and with additional solvent annealing (blue). Dashed and solid lines represent forward and reverse sweep directions respectively.*

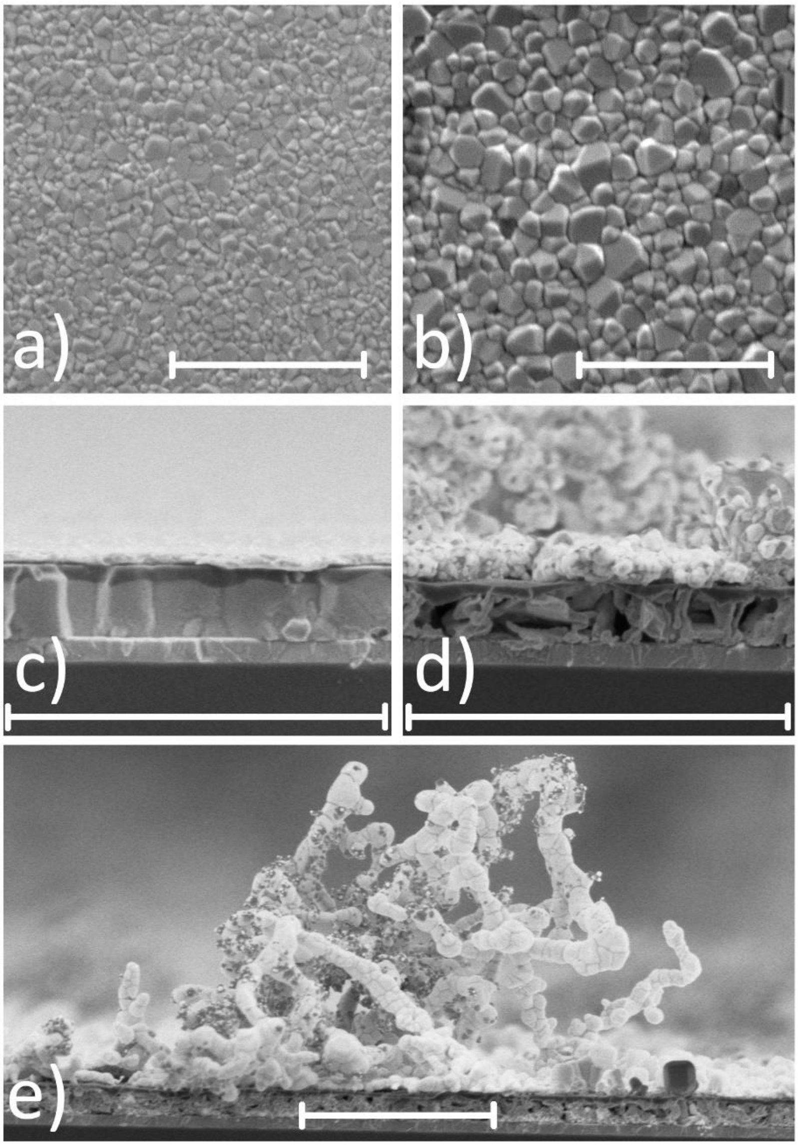

Figure 2: *Parts (a) and (b) show a top view scanning electron microscopy (SEM) images of* $MAPbI_3$ *prior to solvent annealing in (a), and after solvent annealing in (b). Parts (c) and (d) show cross-sectional SEM images: fresh solvent annealed device in (c), and a solvent annealed device aged without encapsulation in (d). The growth of silver iodide dendrites on another degraded device (as confirmed in Figure S6) can be clearly seen in part (e). All scale bars are 2µm.*

We have used our device architecture to explore the use of solvent annealing to grow perovskite grain size and thereby improve device efficiency. This process involves exposing the perovskite to a solvent vapour at an elevated temperature (100ºC). This establishes a quasi-stable liquid-phase environment between the polar solvent dissolving the $MAPbI_3$ surfaces and grain boundaries, permitting the growth of perovskite grains.[38] This process continues until the growth of larger grains is no longer energetically favourable - for example when the grain extends throughout the entire film and can no longer maximise its surface area at the base and top of the film[39]. To incorporate solvent annealing into the device preparation process, we held freshly prepared ITO/poly-TPD(F4-TCNQ)/$MAPbI_3$ multilayers at 100ºC for 15 minutes in a dimethylformamide (DMF) solvent atmosphere. Following this, they were further annealed under nitrogen to remove any residual DMF, after which device processing proceeded as normal. We henceforth refer to solvent annealed and non-solvent annealed films as SA and non-SA respectively. We can evidence the growth of perovskite grains following solvent annealing using scanning electron microscopy as shown in Figure 2a,b (images recorded before and after solvent annealing). Here, it can be seen that the average size of $MAPbI_3$ grains increased from (140 ± 10) nm to (370 ± 30) nm following solvent annealing. This increase in grain size is also accompanied with an increase in surface roughness from 6.5 nm to 19 nm (calculated from AFM images presented in Figure S1).

	Solvent Anneal	**No Solvent Anneal**
PCE [%] *(Stabilised)*	**17.55** *(16.5)*	**15.31** *(15.7)*
J_{SC} [mA/cm^2]	**20.21**	**17.77**
V_{oc} [V]	**1.08**	**1.08**
FF [%]	**79.81**	**80.12**

Table 1: *Solar cell performance parameters for champion devices either with or without solvent annealing.*

We have characterised all devices using current-voltage (*J*-*V*) sweeps, together with stabilised power outputs (SPOs) (see example data for SA and non-SA devices in Figure 1c,d). Very little hysteresis is observed in the *JV* scan, as has been reported for other comparable inverted architecture PSCs.[2] Full device metrics (PCE, J_{SC}, open-circuit voltage (V_{OC}) and fill factor (FF)) for 'champion' PSCs are shown in Table 1. We find that non-SA PSCs have a FF of 80% but have a lower J_{SC} of ~18 mA/cm^2, yielding a maximum PCE of 15.3%. As expected, SA PSCs had a PCE of 17.6%, explained largely as a result of their higher J_{SC} (20 mA/cm^2). Here, we attribute the initially larger values of device J_{SC} in SA films to a reduction in the density of grain boundaries[38,40,41]. However, we cannot exclude the possibility that increased light scattering (from a rougher top surface) or increased interface area between the $MAPbI_3$ and $PC_{60}BM$ might also result in increased charge generation and extraction.

Devices were finally encapsulated in a nitrogen atmosphere using a one-part epoxy resin incorporating a UV-activated initiator (supplied by Ossila Ltd). Encapsulation involved placing a drop of epoxy on top of the device to create a seal over the whole PSC with a glass cover-slip, with the UV-epoxy being 'cured' by exposure to a UV lamp. Here, the epoxy is deposited such that it covers the PSC to the edge of substrate, and had a thickness of (70 ± 10) μm. This created a seal that is just over 2 mm between the edge device active-area and the surrounding atmosphere. Typical epoxies similar to the one employed here have a water vapour transmission rate (WVTR) of 0.7 – 0.94 gmm/m^2day.[42] Alternately, a (135 ± 5) nm layer of the polymer PVP dissolved in methanol (see chemical structure in Figure 3e) was first spin-cast onto the device, after which the device was sealed using epoxy and glass. Here, PVP was selected as it can be processed from methanol, which due to its low boiling point (65ºC) evaporates rapidly during spin-coating, leaving very little time for it to interact with the PSC stack. Note that control experiments have shown (see Figure S2a) that the exposure of $MAPbI_3$ PSCs to methanol does not affect their electronic properties. A schematic of an encapsulated device is shown in Figure 1b.

We now examine the interaction between the epoxy and the different materials within the PSC device stack. Figure 3a shows comparative UV-Vis absorbance spectra of a control $MAPbI_3$ film on a quartz substrate, and a $MAPbI_3$ film that has been encapsulated using epoxy and glass. It can be seen that the unencapsulated $MAPbI_3$ control is characterised by a strong absorbance over the whole UV-Vis region with a sharp band edge around 780 nm. The absorbance of the encapsulated $MAPbI_3$ film is however reduced by more than a factor of three. This reduced absorption is clearly indicative of undesirable chemical reactions between the epoxy and $MAPbI_3$. We expect however that in a full PSC device stack, the perovskite layer would be partially protected from direct contact with the epoxy by the $PC_{60}BM$ and silver electrodes.

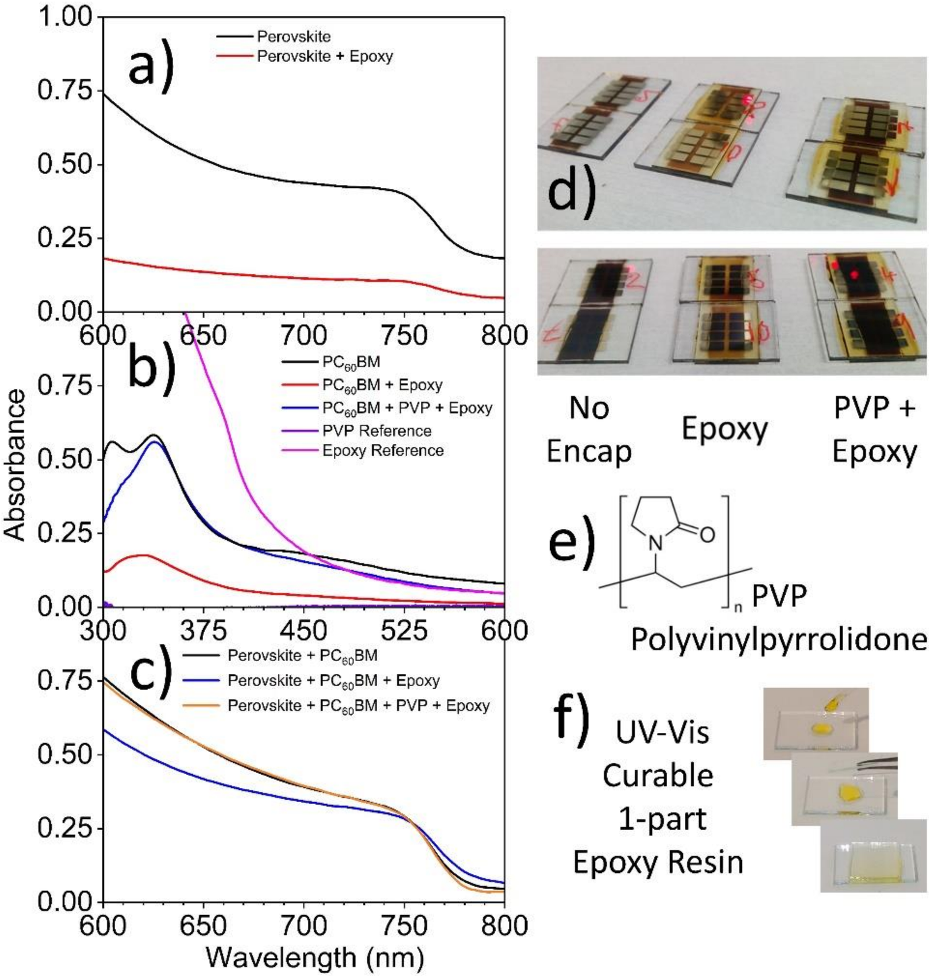

Figure 3: *Absorbance spectra of various material combinations. Part (a) shows absorbance spectra recorded for* $MAPbI_3$ *(black) and epoxy encapsulated* $MAPbI_3$ *(red). (b) Absorbance spectra for pure* $PC_{60}BM$ *(black), and* $PC_{60}BM$ *after encapsulation with epoxy (red) and with a PVP interlayer placed between* $PC_{60}BM$ *and epoxy (PVP/epoxy encapsulated, blue). Reference absorbance spectra of epoxy (pink) and PVP (purple) are also shown (note that PVP has negligible absorbance across all observed wavelengths). (c) Absorbance spectra of* $MAPbI_3$ */*$PC_{60}BM$ *before (black) and after encapsulation with epoxy (blue) and with PVP/epoxy (orange). (d) Photographs of completed devices using different encapsulation routines, (e) the chemical structure of PVP and (f) the epoxy deposition process.*

To explore possible interactions between the epoxy and the $PC_{60}BM$, we have again measured changes in its relative UV-Vis absorption on encapsulation. We plot the absorbance spectrum of a pure $PC_{60}BM$ film in Figure 3b, together with that of an encapsulated $PC_{60}BM$ film. Here, the absorption of the epoxy encapsulation has been subtracted, as it is strongly absorbing at wavelengths < 450 nm. Again, we find a significant reduction in the absorption of the $PC_{60}BM$ film on encapsulation; a result indicative of chemically-induced degradation. While the exact origin of this degradation mechanism is unclear, we suspect that either a photo-initiator or a polar-species within the epoxy reacts with the $MAPbI_3$ and $PC_{60}BM$ during UV-curing, causing them to undergo decomposition. We believe that this degradation process is unlikely to result from direct UV-induced photo-oxidation, as the curing process was performed in a nitrogen atmosphere. We found that a multi-layer of perovskite/$PC_{60}BM$ still loses some absorption if encapsulated with an epoxy that had been left under vacuum for 48 hours (Figure S3). This suggests that it is a component of the epoxy itself (such as a photo-initiator) that is most likely responsible for the degradation rather than absorbed moisture within the epoxy.

To demonstrate that the PVP polymer is able to protect the active layers within the device from chemical species present in the epoxy during curing, we repeated the encapsulation experiments described above. Here, PVP was first coated onto a film of $PC_{60}BM$. The results of this experiment are shown in Figure 3b, where it can be seen that the presence of the PVP coated onto the $PC_{60}BM$ almost completely protects it from the effects of the epoxy, with the absorption of the $PC_{60}BM$ being very similar in both the control and epoxy/PVP/$PC_{60}BM$ films. Figure 3c similarly compares the absorption of a $MAPbI_3$/$PC_{60}BM$ control, together with a $MAPbI_3$/$PC_{60}BM$/epoxy multilayer in which a PVP protection layer was either present or absent. Interestingly, we find that the absorption of the $MAPbI_3$/$PC_{60}BM$/epoxy multilayer is significantly reduced compared to the $MAPbI_3$/$PC_{60}BM$ control, however the combined presence of the PVP/$PC_{60}BM$ layers appears to completely protect the $MAPbI_3$ from damaging species within the epoxy. This protection can be clearly visualised in the images shown in Figure 3d. Here, a bleaching of the $MAPbI_3$ absorption can be seen in devices that did not incorporate the PVP interlayer.

We now discuss the effect of the PVP interlayer on device efficiency and stability. Here, we have measured *J-V* sweeps and SPOs of PSCs that were recorded before encapsulation, after encapsulation and after 200 hours of aging under continuous illumination in an Atlas Suntest CPS+ chamber.[27,43] Such measurements were made on non-SA and SA $MAPbI_3$ devices, both with and without the PVP interlayer. Metrics for all devices studied are presented in Figure 4 and in Table 2, with SPO measurements for devices shown in Figure S4.

In Figure 4a, we present device metrics for non-SA devices. We find that non-SA PSCs that were encapsulated using PVP/epoxy have a higher PCE (12.9 ± 1.5) % than devices that were either unencapsulated (11.6 ± 1.5) %, or encapsulated with epoxy alone (11.0 ± 0.9) %. This appears to result from a non-reversible increase in device J_{SC} from (15.9 ± 0.2) mA/cm^2 to (17.0 ± 0.2) mA/cm^2 before and after encapsulation with PVP/epoxy respectively. A similar improvement in J_{SC} is also observed upon illuminating unencapsulated PSCs with the UV curing lamp as shown in Figure S2b. Intriguingly, the J_{SC} of PVP/epoxy encapsulated devices further increases on aging to an average value of (18.0 ± 0.1) mA/cm^2. This is accompanied by an increase in average V_{OC} from (1.05 ± 0.01) V to (1.1 ± 0.01) V. We suspect these increases in J_{SC} and V_{OC} may originate from reduced recombination at the perovskite / transport layer interfaces. This is likely due to illumination causing a photo-generated electric field which drives ion migration, with such ions reducing the density of trap-state and recombination-rates at the transport layer interfaces.[44,45] In supplementary Figure S5(a) we plot the EQE of PSCs before and after aging where it can be seen that the integrated J_{SC} increases from 17.66 to 19.78 mA/cm^2. Figure S5(a-c) also demonstrates that changes in J_{SC} upon aging do not result from: (i) changes in the energetic-location of the perovskite band-edge, or (ii) changes in the morphology and distribution of grain-sizes.

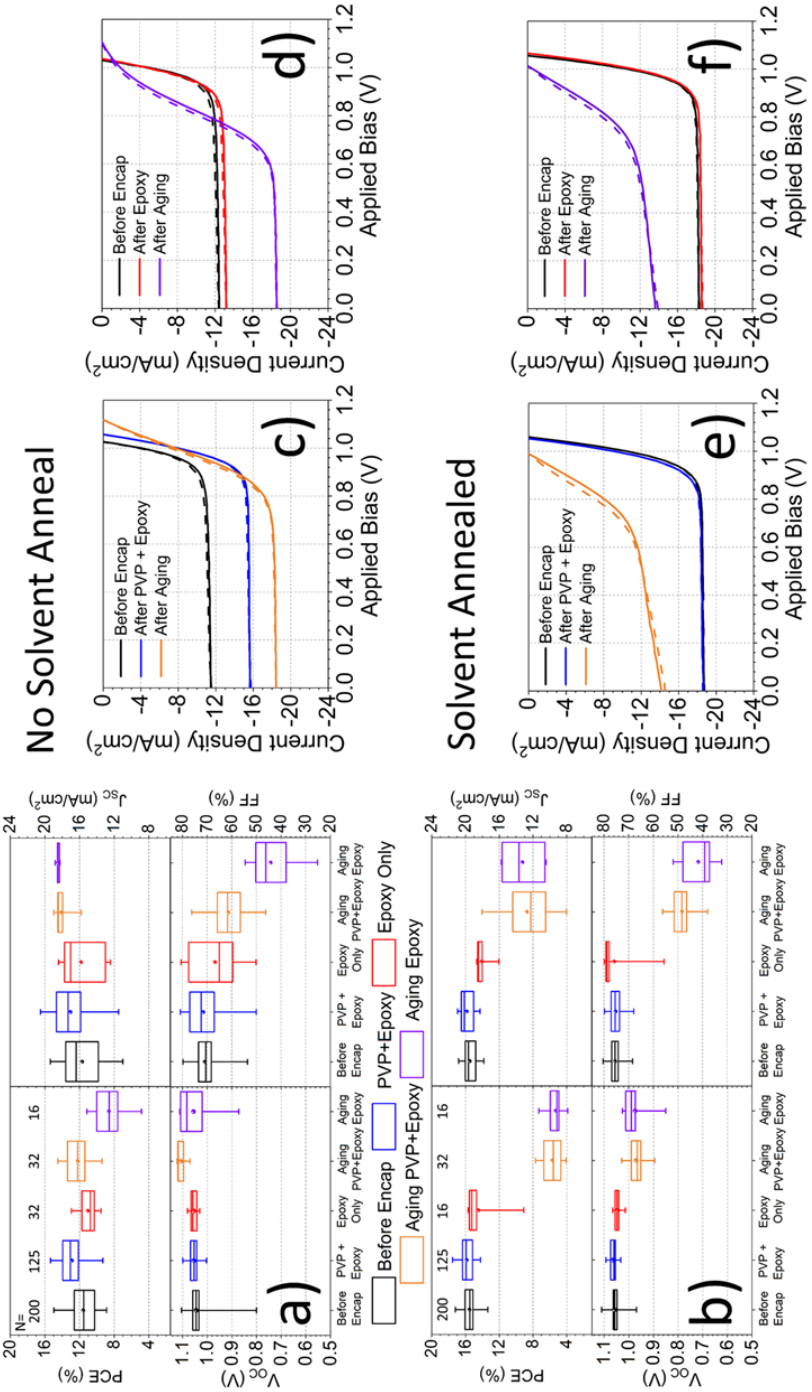

***Figure 4:** Parts (a) and (b) present box plots of all performance metrics from both forward and reverse sweeps for PSCs. Specifically, part (a) shows data for PSCs without solvent annealing, and part (b) shows data for solvent annealed devices. In both cases, data is presented at various stages of encapsulation and after 200 hours aging under 1 sun illumination. Data recorded before encapsulation is shown using black symbols, after encapsulation with epoxy only (red symbols), epoxy-only after aging (purple), with a PVP interlayer and epoxy (blue) and PVP/epoxy after aging (orange). The number of cell measurements recorded for each condition are presented in the PCE plot in parts (a) and (b). Extreme outliers, such as cells that have fully degraded due to encapsulation failure are not included. Representative J-V sweeps before and after encapsulation and subsequent aging are presented in parts (c) to (f). Specifically, devices in which no solvent anneal was used are summarised in parts (c) and (d), with solvent annealed devices in (e) and (f). In all cases, we show data for devices that were either encapsulated with epoxy only, or with epoxy and PVP.*

In devices that were encapsulated using just epoxy, we observe a decrease in average PCE from (11.0 ± 0.1)% to (8.7 ± 0.4)% after aging, with this loss in efficiency occurring due to a reduction in FF, although this is also accompanied by an increase in J_{SC}. It appears therefore that even though the active area of the PSC is largely protected by a silver electrode, this is not sufficient to prevent device degradation – a process manifested by a 'flick' in the *J-V* sweep above V_{OC}, (see Figure 4d). This observation is generally indicative of inefficient charge extraction at one of the interfaces (most likely the top MAPbI$_3$-PC$_{60}$BM interface). It is possible that the degradation of MAPbI$_3$ – even in regions away from the cell area – has a negative impact on the stability of device pixels that are largely protected by the silver contact. Devices that were encapsulated by PVP/epoxy appear significantly more stable, with the PSC demonstrating no statistically-significant change in efficiency over the testing period. Such results highlight the ability of the PVP interlayer to protect the active device layers from the epoxy and thereby resulting in enhanced PSC stability.

	PVP + Epoxy			Epoxy		
No Solvent Anneal	**Before Encapsulation**	**After Encapsulation**	**After 200 Hours Aging**	**Before Encapsulation**	**After Encapsulation**	**After 200 Hours Aging**
PCE [%] *(Stabilised)*	**9.21**	**13.14** *(12.8)*	**13.75** *(14.1)*	**10.11**	**10.63** *(10.4)*	**11.16** *(12.4)*
J_{SC} [mA/cm^2]	**11.48**	**15.62**	**18.46**	**12.45**	**13.19**	**18.53**
V_{oc} [V]	**1.03**	**1.05**	**1.12**	**1.02**	**1.03**	**1.11**
FF [%]	**78.16**	**79.94**	**66.66**	**78.87**	**77.84**	**54.51**
Solvent Anneal						
PCE [%] *(Stabilised)*	**15.62**	**15.26** *(14.7)*	**7.4** *(7.2)*	**15.55**	**15.70** *(14.7)*	**7.32** *(7.2)*
J_{SC} [mA/cm^2]	**18.75**	**18.67**	**14.18**	**18.32**	**18.58**	**13.91**
V_{oc} [V]	**1.05**	**1.05**	**0.99**	**1.06**	**1.07**	**1.01**
FF [%]	**78.67**	**77.63**	**52.79**	**80.38**	**79.31**	**51.95**

Table 2: *Performance metrics for representative devices. Here, data includes PVP/epoxy and epoxy-only devices that are either solvent annealed (SA) or non-solvent annealed (non-SA). We use the following colour-scheme for the text: before encapsulation (black), after encapsulation (blue and red) and after aging (orange and purple). Stabilised measurements were not performed before encapsulation to minimise device degradation.*

In Figure 4b we present device metrics for devices that were solvent annealed. Such devices start with an initially higher PCE and J_{SC} and are also characterised by a narrower distribution of device metrics. Again, no hysteresis is observable in the JV scans (see Figure 4e,f) and we find that there is no significant change in device performance upon encapsulation (even without the PVP interlayer). However, it appears that all SA devices degrade rapidly, and undergo a reduction in all performance metrics (most notably losing shunt resistance). Our measurements on non-SA PSCs described above indicate that the PVP/epoxy encapsulation is highly robust, and thus extrinsic (moisture and oxygen induced) degradation pathways in SA devices can most likely be excluded. We conclude therefore that the observed instability in encapsulated SA PSCs most likely has an intrinsic origin.

In Figure 5, we plot device metrics for SA and non-SA devices during aging over a period of up to 220 hours. The PCE of non-SA devices that were unencapsulated is presented in Figure 5a. Here, it can be seen that such devices undergo complete degradation within around 2 hours. We expect this process results from the use of a silver electrode, which has been reported to react with $MAPbI_3$ decomposition products (methylammonium iodide (MAI), hydriodic acid (HI) or iodide (I^-))[46–48]. Such degradation products initially originate from exposed perovskite grain boundaries as a result of reactions involving moisture and oxygen,[48] and then diffuse through pinholes, along grain boundaries and through the $PC_{60}BM$. Whilst ion migration may initially be beneficial for device performance, the device performance decreases when a significant accumulation of ions and degradation components occurs at the silver electrode. Cross-sectional SEM images of SA PSCs without encapsulation were used to better understand degradation (see Figure 2c-e). It can be seen that on aging, we evidence the presence of localised dendrite-like structures on the silver electrode surface which EDX measurements indicate contain an excess of silver and halide compared to regions of the PSC that are less degraded (Figure S6); a finding consistent with previous reports.[44,47,49,50]

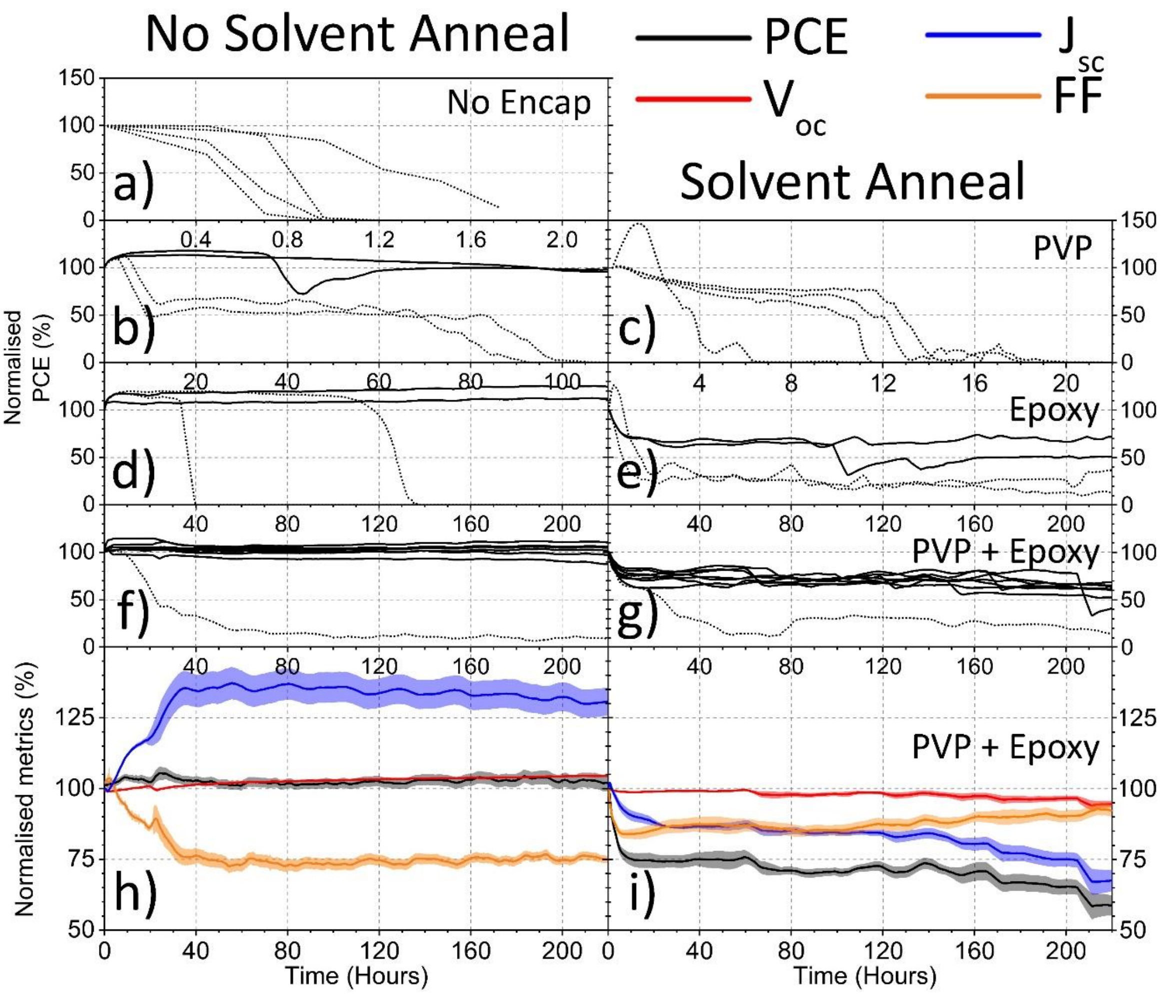

Figure 5: The effect of aging under illumination and load on device performance. The figures plot the normalised PCE (black) over time for individual cells. Here, data is split into non-solvent annealed devices (left column) and solvent annealed devices (right column). Devices are either (a) without encapsulation, (b) and (c) PVP encapsulated, (d) and (e) encapsulated with epoxy only or (f) and (g) encapsulated with PVP/epoxy. Solid lines are used to plot data for individual devices that we consider to be stable, with dotted lines indicating devices that have degraded much faster than other stable devices. For each sub-plot, we present data recorded from 4 devices, except for the plot summarising PVP/epoxy encapsulated devices, where data for 8 devices is shown. Parts (h) and (i) present normalised device metrics (JSC - blue, Voc - red, FF - orange) over time for PVP/epoxy encapsulated devices. Here, part (h) corresponds to devices that were not solvent annealed with part (i) corresponding to with solvent annealed devices. In all cases, the plotted line represents the mean of device measurements with the translucent band representing the standard deviation of all cells.

Figure 5b plots the time dependent PCE of non-SA PSCs that were encapsulated using just PVP. It can be seen that devices are characterised by a significant improvement in stability, with 50% of devices maintaining their initial PCE after 100 hours. The remaining devices, (data plotted using dotted lines), undergo a rapid decline in efficiency and fail after around 100 hours of operation. This indicates that despite PVP being soluble in many polar materials[51-53], it provides some protection from oxygen and moisture ingress. Given the fact that PVP is hydrophilic and has a high WVTR (>2000 g/m^{2}day when used in hydrogels),[53] we conclude that the protection it provides may result from it preferentially absorbing moisture that would otherwise migrate into the device. However without additional epoxy/glass encapsulation, it is apparent that PVP alone does not act as an effective moisture barrier-layer. For SA PSCs that were only encapsulated using PVP (see 4c), we find that all devices fail after around 12 hours.

Figures 5d,f and 4e,g compares the stability of non-SA and SA PSCs that were encapsulated with epoxy and PVP/epoxy respectively. We find that the yield and reproducibility of devices encapsulated using PVP/epoxy is improved compared to devices encapsulated using epoxy alone. For example, from a total of 8 SA and 8 non-SA PVP/epoxy encapsulated cells, we find that only one device fails out of each device set over the 220 hour testing window. The evolution of average device metrics for non-SA and SA devices encapsulated using PVP/epoxy is shown in Figure 5h,i respectively. For non-SA devices, there is clear positive burn-in of J_{SC} that occurs over the first 30 hours of aging, however this is accompanied by a reduction in FF that results in no change in PCE during this time. Notably the PVP/epoxy encapsulation does not prevent SA devices experiencing a significant negative burn of around 40% over the first 10 hours of testing.

We have performed an extensive analysis of the lifetime of SA and non-SA devices as shown in Figure 6a. Here, we plot a histogram of extrapolated T80 lifetimes for 45 SA and 82 non-SA PSCs, with devices fabricated over a series of independent device runs. It can be seen that no SA device has a T80 above 200 hours, while a number of non-SA devices have an (extrapolated) T80 lifetime of over 2000 hours.

It is interesting to speculate on the origin of the more rapid degradation of SA PSCs. One possible explanation comes from the presence of residual DMF solvent within the perovskite that remains from the solvent annealing treatment. Studies on perovskites cast from a DMF precursor solvent suggest that residual DMF can be difficult to remove as a result of its high boiling point (153ºC).[54] To explore whether residual solvent is left in the perovskite films, we have used Fourier transform infrared spectroscopy measurements to study the non-SA and SA perovskite films (as shown in Figure S7), however we failed to detect even trace amounts of DMF in such films. We note that recent work has demonstrated a differential degradation of individual (and even adjacent) perovskite grains. Indeed, grains with different defect densities or stoichiometry can result in some grains being more stable than others.[55] It can be seen in the SEM cross-section image of a SA-device shown in Figure 2d that some grains are dark and completely degraded whilst others likely remain as $MAPbI_3$ even after aging. We have also found (see Figure S6) that there is also a large variation in the quality and uniformity of the silver contact after aging. We speculate that the quasi-stable liquid-phase environment established during solvent annealing increases the mobility of ions such that the larger resultant grains have a wider distribution of stoichiometric and ionic defects relative to a non-SA $MAPbI_3$ film. Indeed, Figure 2c demonstrates that some grains in the fresh SA device appear smaller and brighter than other larger grains. This inhomogeneity will likely lead to an increased tendency for instability, particularly in grains having a PbI_2 deficit.[55] It is also possible that the increased roughness of the SA $MAPbI_3$ relative to non-SA $MAPbI_3$ (from 6.5nm to 19nm - see Figure 2a,b and S2) might result in reduced device stability. Here, increased roughness of the interface between the $MAPbI_3$ and the $PC_{60}BM$ may facilitate the diffusion of MAI, HI and I^- into the $PC_{60}BM$ and then to the silver top contact, resulting in enhanced device degradation.

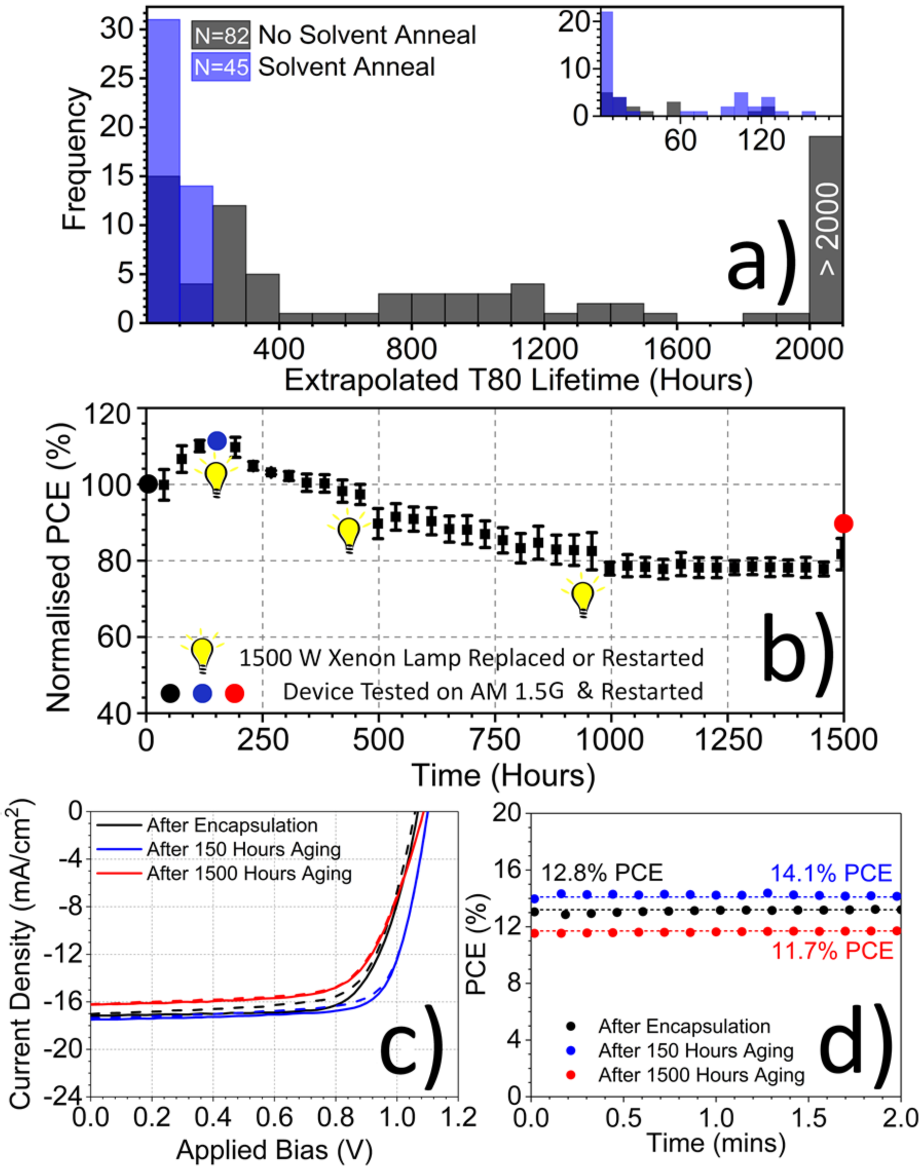

Figure 6: *Part (a) shows a histogram of extrapolated PSC T80 lifetime for devices containing solvent-annealed (blue) or non-solvent annealed (black) perovskite films. The inset highlights device data recorded over the first 200 hours of measurement. Part (b) shows normalised PCE recorded over 1500 hours for one device having particularly high stability. Bulb symbols represent breaks in the measurement due to the lamp being restarted or replaced. Calibrated current-voltage measurements (circles) were taken at 0 hours (black), 150 hours (blue) and 1500 hours (red). The result of these measurements is shown in part (c); J-V sweeps and part (d); stabilised power outputs. Dashed and solid lines represent forward and reverse J-V sweeps respectively.*

Our previous study on the stability of PSC devices incorporating a PEDOT:PSS hole-extraction layer demonstrated that device lifetime was limited to ~300 hours. Here, we ascribed this instability to the presence of moisture trapped within the hydroscopic and acidic PEDOT:PSS.[27,29,56] The PVP/epoxy system developed here allows us to test this hypothesis, and we therefore explored replacing the poly-TPD HTM with PEDOT:PSS. The enhanced hydrophilic nature of PEDOT:PSS can be evidenced from contact-angle measurements, with relative contact angles for PEDOT:PSS and poly-TPD being 15.1 ± 2.1º and 60.2 ± 4.1º respectively (see Figure S8). We find such devices incorporating PEDOT:PSS undergo a rapid reduction in device metrics, with devices completely failing after 24 hours (see Figure S9). This result highlights a clear correlation between the use of hydrophobic charge extraction layers and long term operational stability in PSCs.

Finally, using our encapsulation system we can explore the stability of non-SA $MAPbI_3$ devices over an extended time-period. This is shown in Figure 6b, where we follow the efficiency of a device encapsulated with epoxy/PVP over a period of 1500 hours. It can be seen that after 1000 hours of testing, the device retained 80% of its starting efficiency; a result that was expected given the expected extrapolated T80 lifetimes in Figure 6a. After this long burn, the device efficiency stabilised, indicating that its T80 lifetime after burn-in is likely to in in the range of 1000s of hours. Note that the device was periodically removed from the aging setup to record calibrated AM1.5G *J-V* measurements as shown in Figure 6c. This confirmed that device PCE had dropped from 13.2% to 11.9% after 1500 hours of aging, corresponding to a burn-in of 15%. These values were obtained from both *J-V* sweeps as well as SPO measurements (see Figure 6d) that were recorded at the same time (see data summary presented in Table 3).

	After Encapsulation	**After 150 Hours Aging**	**After 1500 Hours Aging**
PCE [%] *(Stabilised)*	**13.21** *(12.8)*	**14.52** *(14.1)*	**11.98** *(11.7)*
J_{SC} [mA/cm^2]	**17.18**	**17.50**	**16.25**
V_{oc} [V]	**1.07**	**1.10**	**1.09**
FF [%]	**72.01**	**75.42**	**67.87**

Table 3: *Performance metrics for champion PSCs recorded at three points during 1500 hours aging (data taken from Figure 6a).*

Conclusions

In summary, we have demonstrated that PVP not only acts as a protective interlayer to protect $MAPbI_3$ based solar cells from the epoxy used to encapsulate such devices, but is also able to provide partial protection from moisture and oxygen. By combining PVP, epoxy and glass we develop a highly effective multi-layer encapsulation system, achieving T80 lifetimes of 1000 hours for inverted architecture $MAPbI_3$ PSCs. We expect that such a solution-processable interlayer system could be integrated into a cheap roll-to-roll process suitable for manufacture. We highlight the importance of isolating PSCs from the damaging effects of epoxy and expect there are other materials (both polymeric and dielectric) that could also be used as barrier interlayers for PSC encapsulation, provided that the deposition of such interlayers does not damage the PSC. We demonstrate that these impressive lifetimes for inverted architecture PSCs are reliant on the use of a hydrophobic polymer hole transport material, poly-TPD, instead of the more commonly utilized hydrophilic PEDOT:PSS. We use this encapsulation system to explore the comparative stability of PSCs containing a $MAPbI_3$ active layer that had been initially exposed to solvent vapour (a solvent-annealing process) which we show increases the average size of the perovskite crystal grains. This annealing process results in an initial increase in device PCE, with the non solvent-annealed control and the solvent annealed device having a peak efficiency of 15.3% and 17.6% respectively. We find however that this initial efficiency gain is rapidly lost over a 10-hour burn-in period, with the efficiency of the solvent annealed device falling below that of the non-solvent annealed control. Our results indicate that more research is required to understand what steps may be required to stabilise solvent annealed PSC and that higher efficiency PSC devices do not necessarily have long-term intrinsic-stability. Optimisation of device stability should be viewed as an important separate task to the optimisation of efficiency. With encapsulation equivalent to our successful multi-layer sealing and device optimisation driven to obtain stability, $MAPbI_3$ based PSCs can operate effectively for thousands of hours. Combining these developments with perovskite compositional advancements paves the way for stability lasting many years.

Experimental Methods

Materials and handling: All solvents, except those used for cleaning, were purchased from Sigma Aldrich in their anhydrous form and stored in a nitrogen filled glovebox. All dry powders were stored under vacuum. Dry powders were weighed out in air, with all solvents added to the dry powders in the glovebox. All solutions were filtered with a 0.45 µm polytetrafluoroethylene (PTFE) filter shortly before deposition with spin-coating performed in the glove-box using a dynamic technique.

Device fabrication: Perovskite Solar Cells (PSCs) were fabricated on 20 Ω / square pre-patterned ITO glass photovoltaic substrates. Substrates were first sonicated for 10 minutes in hot Hellmanex detergent solution, then placed in boiling deionised (DI) water, sonicated for 10 minutes in hot DI water, followed by a final 10 minute sonication in isopropyl alcohol (IPA). Shortly before deposition of the hole-transport layer, substrates were dried with a nitrogen gun and UV ozone cleaned for 15 minutes. Poly(N,N'-bis-4-butylphenyl-N,N'-bisphenyl)benzidine (poly-TPD) and 2,3,5,6-tetrafluoro-7,7,8,8-tetracyanoquinodimethane (F4-TCNQ) were dissolved in toluene at 1 mg/ml and 0.2 mg/ml respectively. The poly-TPD solution was heated to 80ºC to fully dissolve the solution. Following Wang e*t al.*[20], the poly-TPD was spin-coated from a hot solution onto a recently UV-ozone cleaned substrate at a speed of 4000 rpm to create a uniform ultra-thin poly-TPD film. This was then annealed at 110ºC for 10 minutes before being transferred to the glovebox. The methylamine bubbled acetonitrile $MAPbI_3$ was made following the procedure described by Noel *et al.*[33] A 0.5M solution composed of methylammonium iodide to lead iodide (99.99%) at a ratio of 1:1.06 was then spin-coated on the poly-TPD at 4000 rpm in the glovebox.[33] The resulting 350-400 nm thick $MAPbI_3$ film was then annealed at 100ºC for 45 minutes in the glovebox. To solvent anneal the PSCs, the $MAPbI_3$ films were held at 100ºC for a further 30 minutes. During the first 15 minutes of this anneal, they were sealed under a glass petri dish in a solvent atmosphere created using 20 µl of dimethylformamide (DMF). After 15 minutes, the petri-dish lid was then removed. After the ITO/poly-TPD/$MAPbI_3$ films had cooled to room temperature a 30 mg/ml [6,6]-phenyl-C61-butyric acid methyl ester ($PC_{60}BM$) solution in chlorobenzene (which had been stirred overnight at 70ºC and then left to cool before deposition) was spin-coated at 3000 rpm to produce a 100 nm thick $PC_{60}BM$ layer. The substrates were annealed again for 10 minutes at 90ºC in a glovebox. After the ITO/poly-TPD/$MAPbI_3$/$PC_{60}BM$ films had cooled to room temperature an ultra-thin bathophenanthroline (Bphen) layer was spin-coated from a 0.5 mg/ml IPA solution at 6000 rpm in a glovebox. Before completing the PSCs the entire ITO/poly-TPD/$MAPbI_3$/$PC_{60}BM$/BPhen stack was brought into a humidity controlled clean room (<35% RH) and held at 80ºC whilst being patterned with a DMF coated cotton bud to swab the sides and edges of the substrate (see an image of the swabbed films in Figure 1a:v). After cooling and returning to the glovebox, the patterned substrates were placed in a thermal evaporator and left overnight under a < $2x10^{-6}$ pa vacuum. The following day a 100 nm Ag cathode was thermally evaporated onto the film surface at a rate of 1 $Ås^{-1}$. The final device layout for an encapsulated PSC is shown in Figure 1b. Here we show a completed PSC device has 8 cells formed by the overlap between Ag cathodes and ITO anode, with each cell having an active area of 0.04 cm^2. The PSCs were taken back into the glovebox and either left without encapsulation, or coated with 135 ± 5 nm of polyvinylpyrrolidone (Sigma Aldrich) spin-coated at 6000 rpm from a 25 mg/ml methanol solution, or coated with a drop of UV initiated one part epoxy (Ossila), covered with a glass encapsulation slide and cured under a UV light for 20 minutes, or encapsulated with both PVP and epoxy. The encapsulation materials were deposited to cover the whole PSC stack. Note that the glass slide can usually only be removed with force (a process that which often also results in the removal of other PSC layers), indicating that the epoxy makes a strong seal to the PSC, even in the presence of a PVP interlayer. All layer thicknesses reported here and shown in Figure 1b were measured using a Bruker DektakXT profilometer and confirmed with cross-sectional SEM as detailed below.

Device characterisation: Device performance was determined under ambient conditions by measuring *J-V* curves using a Newport 92251A-1000 solar simulator, with devices illuminated through a 0.0256 cm^2 aperture mask. Before each set of measurements, the intensity was calibrated to 100 $mWcm^{-2}$ using an NREL certified silicon reference cell. The applied bias was swept from 0.0 V to +1.2 V and back again at a scan speed of 0.4 Vs^{-1} using a Keithley 237 source measure unit. The V_{mpp} of each device was extracted from the *J-V* scans, and the stabilised power output was recorded by holding the devices at their V_{mpp}.

Lifetime testing: Device aging was completed using an Atlas Suntest CPS+ with a 1500W Xenon bulb, quartz IR reducing filters and internal reflectors. We have previously shown that the lamp spectrum approximately matches AM1.5G.[27,43] The Xenon bulb in combination with internal reflectors produce an irradiance level of ~100 mW/cm^2. This bulb was replaced several times during the longest lifetime-testing experiments. All lifetime PCE and J_{SC} measurements reported here are normalised to 7 silicon photodiodes that take into account fluctuations in the illumination intensity. Device performance was determined from reverse sweep *J-V* measurements. Here, the applied bias was swept from 1.15 V to 0 V at a scan speed of 0.05 Vs^{-1} using a Keithley 2400 source measure unit. Devices were not swept into negative voltage as we have found this reduces device stability, and were held at open circuit between measurements, with every device being scanned every 15 minutes. The temperature of the PSCs inside the Suntest was (42 ± 3) ºC during operation. The humidity was not controlled, but was found to be within the range (38 ± 6)% RH over the entire course of the exposure. PSCs mounted in the Suntest were not covered by an aperture mask during lifetime testing, and thus device metrics are normalised to their initial values. T80 lifetimes were extracted directly when possible or extrapolated using a linear fit applied to the post burn-in region.

Absorbance: UV-vis absorption measurements were performed under ambient conditions using a UV-VIS-NIR light source (Ocean Optics – DH-2000-BAL), and spectrometer (Ocean Optics – HR2000+ES). All data reported here is presented as absorbance. Samples for absorption measurements were prepared on quartz-coated glass, using the same deposition methods as used in device fabrication. All absorbance measurements of films that have been encapsulated have had the absorbance of the reference encapsulation system subtracted.

Contact angle: A contact angle goniometer (Ossila) was used to determine the sessile contact angle from images of droplets of deionized water on poly-TPD and PEDOT:PSS.

Scanning electron microscopy (SEM) & energy dispersive x-ray spectroscopy (EDX): An Inspect F, FEI Helios NanoLab G3 UC and Nova Nano 450 were used to image the surfaces of $MAPbI_3$ (at 2keV) and cross-section of PSCs device stacks (at 1keV). For top view samples, $MAPbI_3$ was deposited on ITO/poly-TPD substrates. Further details of the mounting of samples and use of the SEM are given in our previous work.[17] Compositional analysis was performed using energy dispersive X-ray spectroscopy (EDX-SEM) using the Helios NanoLab at 10 keV accelerating voltage, with the signal measured using an Oxford Instruments EDX spectrometer and analysed using AZtecEnergy spectral analysis software.

Atomic force microscopy: A Veeco Dimension 3100 with a nanoscope IIIA controller operated in tapping mode was used to characterise the surface topography of the non-solvent annealed and solvent annealed samples.

Fourier transform infrared spectroscopy (FTIR): To explore whether residual solvent remained in the $MAPbI_3$ films, they were deposited on quartz glass and annealed for 60 minutes. They were then solvent annealed for 5 minutes with solvent volume increased to 100 µl. No subsequent annealing was applied in order to maximise the quantity of any residual solvent. Films were then removed from the substrate using a razor blade, with the resultant powder investigated using a PerkinElmer 100 attenuated total reflection-IR (ATR-IR) spectrometer.

External Quantum Efficiency (EQE): External quantum efficiencies were measured using a white light source that was monochromated using a Spectral Products DK240 monochromator that was then imaged on the PSC active-area. The intensity of the monochromated light was determined using a calibrated silicon photodiode having a known spectral response. The external quantum efficiency was measured across two scanning ranges (380 - 700 nm and 600-850 nm) using an Xtralien X100 (Ossila) source measure unit to determine the PSC photocurrent.

Supporting Information: Supporting Information is available online.

Acknowledgements This work was funded by the UK Engineering and Physical Sciences Research Council (EPSRC) via grants EP/M025020/1 'High resolution mapping of performance and degradation mechanisms in printable photovoltaic devices', EPSRC grant EP/N008065/1 'Secondary Electron Emission - Microscopy for Organics With Reliable Engineering-Properties', and EP/M014797/1 'Improved Understanding, Development and Optimization of Perovskite-based Solar Cells'. We also thank the EPSRC for PhD studentships via the University of Sheffield DTG account (T.R.) and from the Centre for Doctoral Training in New and Sustainable PV, EP/L01551X/1 (M.S., B.F., J.S.). We also would like to thank Dr James Kingsley, Dr Nick Scarratt, Claire Greenland, Emma Spooner, and Rachel Kilbride for useful discussions.

5.2: Additional Discussion and Supplementary Information

Original Supplementary Information

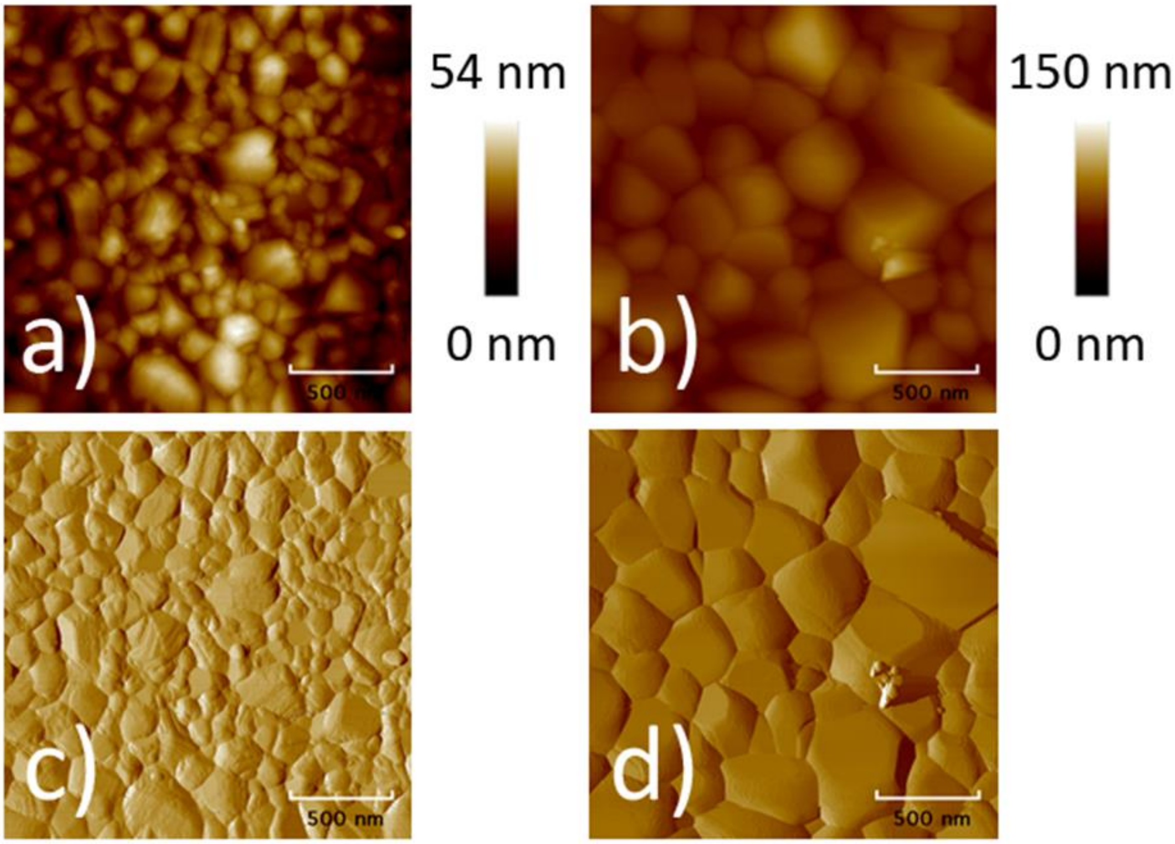

Figure S1: *Atomic force microscopy height images of (a) MAPbI3 following thermal annealing and (b) MAPbI3 following an additional solvent anneal. The film Ra roughness average is 6.5 nm and 19 nm respectively. Films were deposited on ITO/poly-TPD. For completeness, the corresponding phase maps for (a) and (b) are shown in (c) and (d) respectively.*

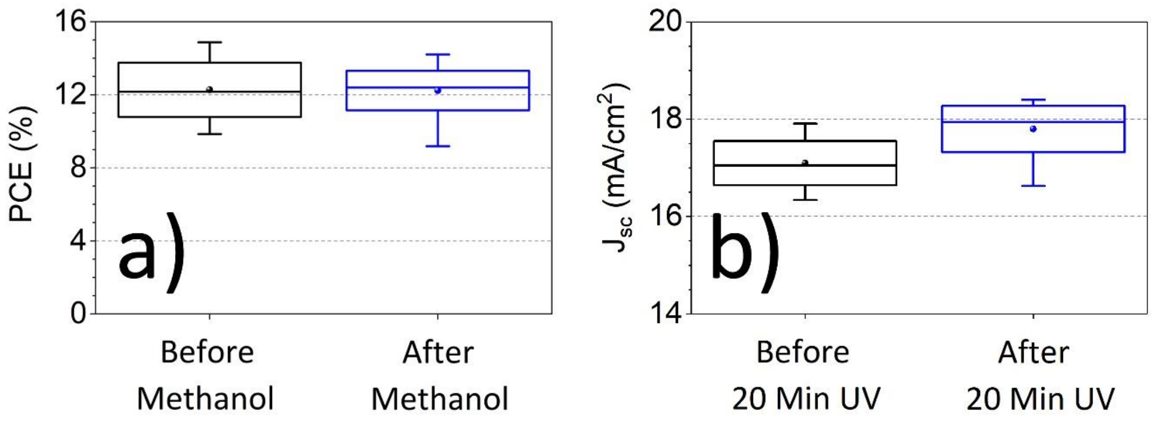

Figure S2: *(a) PCE boxplots of PSCs with no solvent anneal and no encapsulation before (black) and after (blue) dynamically spin coating methanol at 6000 rpm on the completed PSCs. This confirms that the methanol used to deposit the PVP encapsulation does not alter the device performance. Data was obtained from N = 50 device measurements across 3 substrates (8 devices per substrate, metrics from reverse and forward sweeps included). (b)* J_{SC} *boxplots before (black) and after (blue) exposure to 20 minutes of UV light in* N_2*-GB. Here, devices were not encapsulated nor were they solvent annealed. This demonstrates that the UV light used to cure the epoxy does induce a statistically significant increase in* J_{SC}*.*

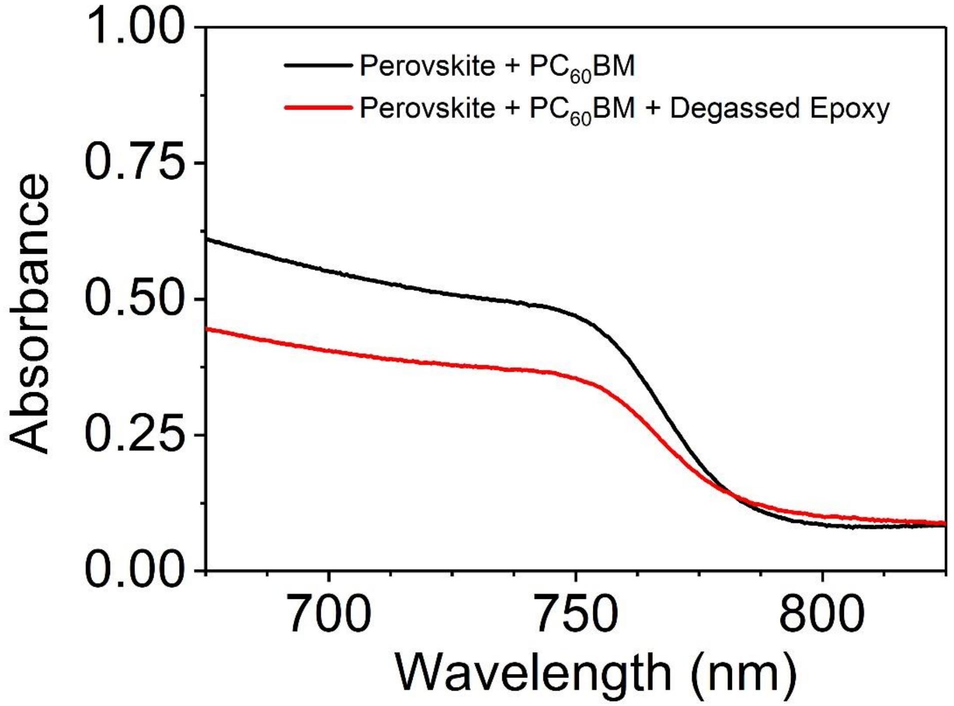

Figure S3: *Absorbance of thin films on quartz coated glass of a thick* $MAPbI_3$ */*$PC_{60}BM$ *stack before (black) and after (red) encapsulation with epoxy. Here, the epoxy has been 'degassed' under vacuum for 48 hours. This process is found to reduce (but not completely suppress) the effect of the encapsulation process that degrades the perovskite. The inset photograph shows the same effect for completed devices. Here, a device encapsulated with degassed epoxy appears darker (more absorbing) than a device encapsulated with untreated (non-degassed) epoxy. We find that the simple inclusion of a PVP interlayer prevents the damaging effect of the epoxy more than does the degassing procedure. Here, we have subtracted the absorbance of the encapsulation from that of the* $MAPbI_3$ *film.*

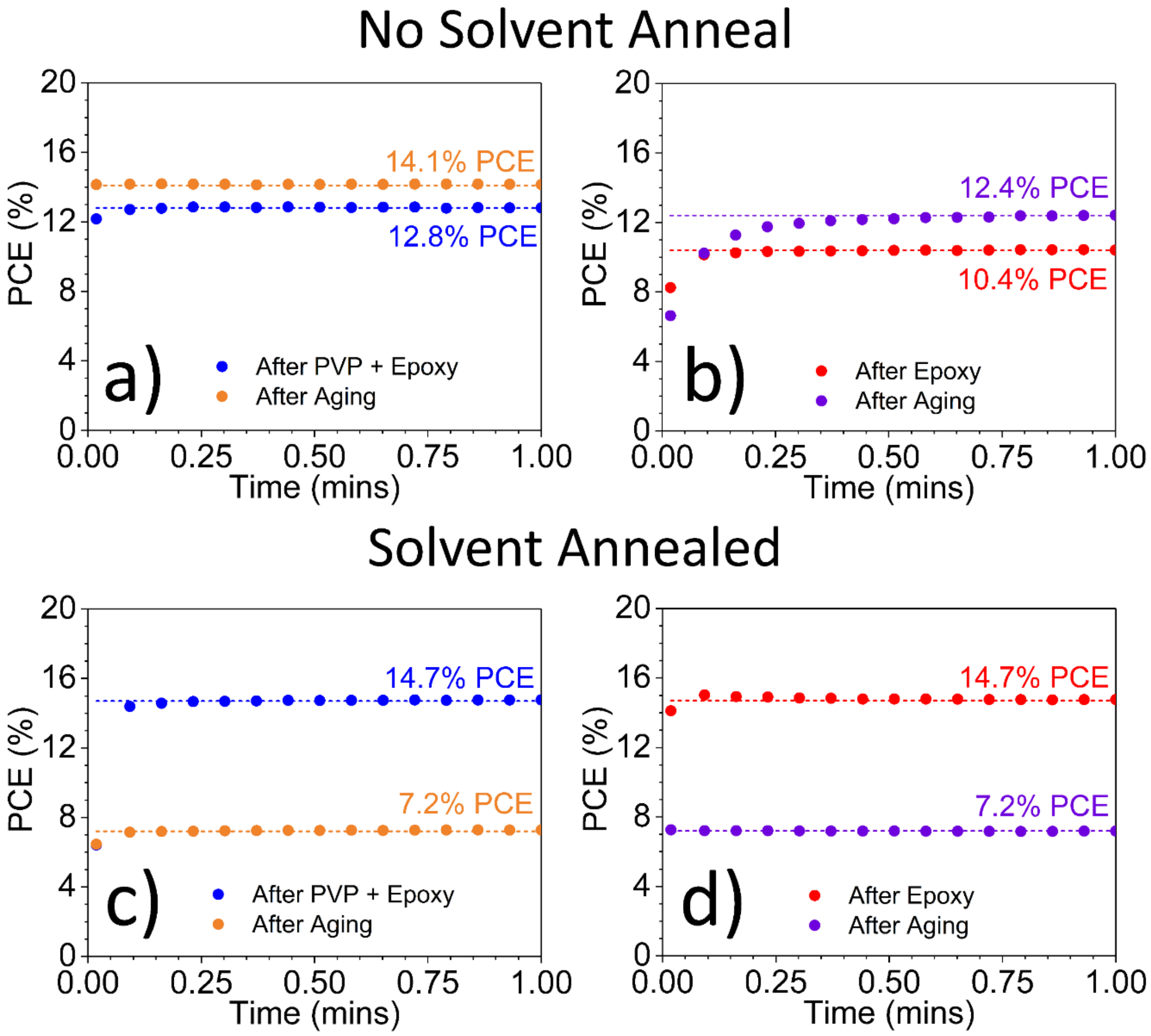

Figure S4: *Stabilised PCE measurements of representative PSC sweeps shown in Figure 4c-f using the same plot colours as used in Figure 4. Part (a) shows stabilised PCEs of devices with no solvent anneal (non-SA) with devices encapsulated with PVP/epoxy, part (b) shows non-SA devices encapsulated with epoxy, part (c) shows solvent annealed (SA) devices encapsulated with PVP/epoxy and (d) SA encapsulated using just epoxy. Stabilised measurements were not recorded before encapsulation to minimise aging of the device.*

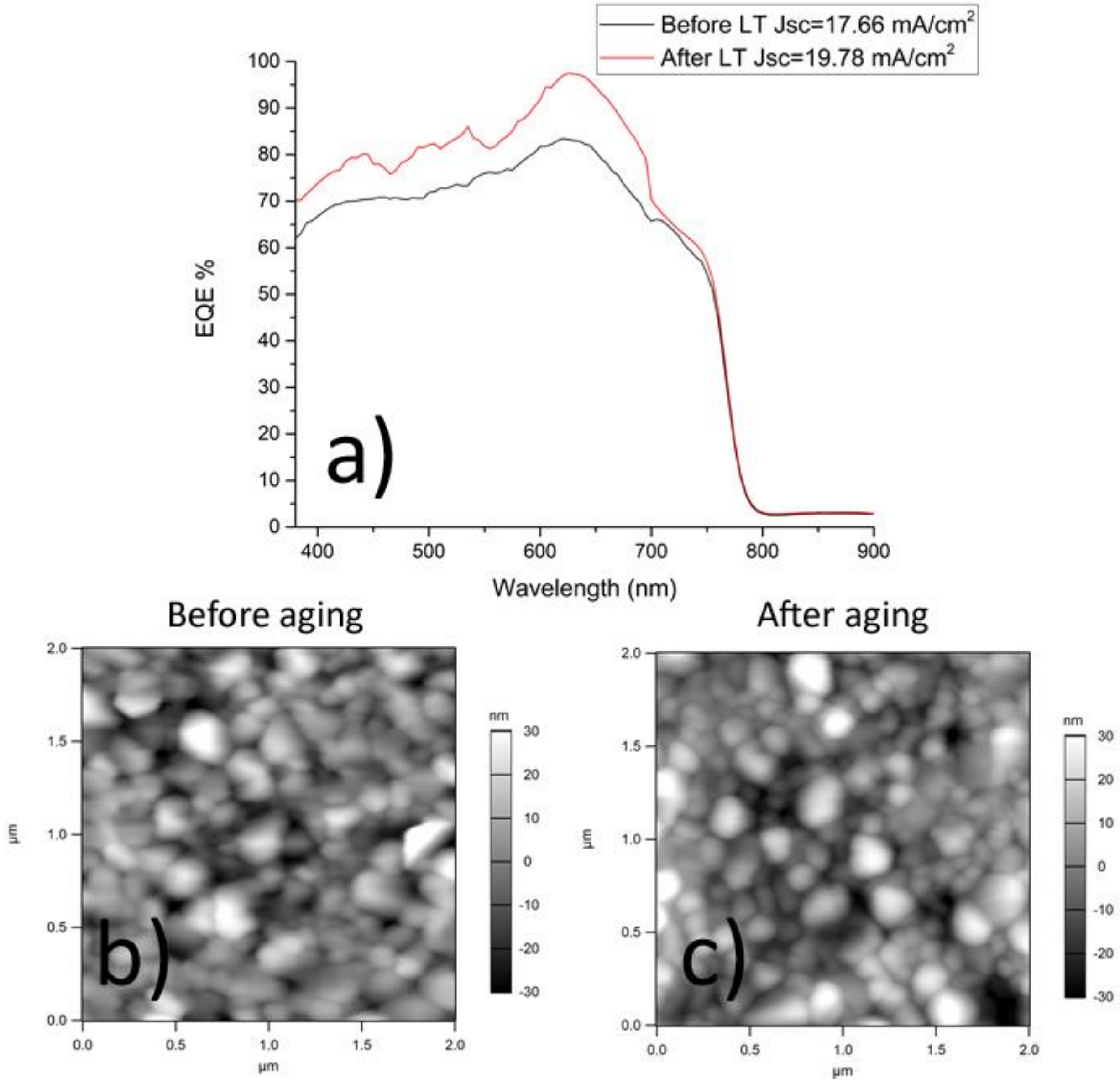

Figure S5: *(a) EQE of a typical non-solvent annealed device (encapsulated with PVP and Epoxy) before (black) and after 18 hours of aging (red). No shift in the band edge is observed. (c) Atomic force microscopy height images before aging and (d) directly after aging, indicating that average grain size has not changed. Films were encapsulated with PMMA before overnight aging and then washed off before AFM measurement.*

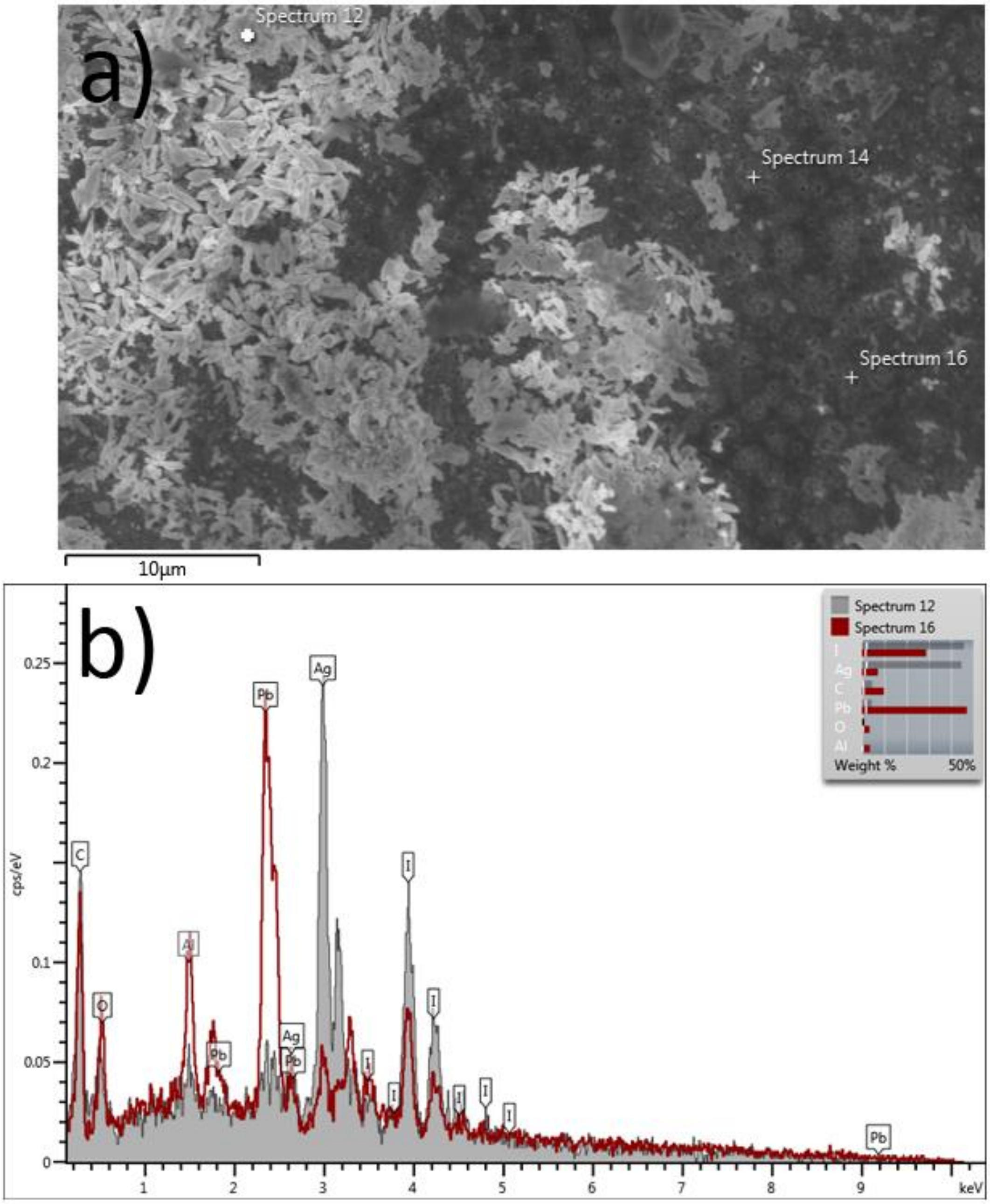

Figure S6: *(a) Top view SEM showing locations of energy dispersive X-ray spectra presented in (b), showing an excess of silver and iodine in the dendrite features (spectrum 12) as compared to less degraded* $MAPbI_3$ *areas (spectrum 16).*

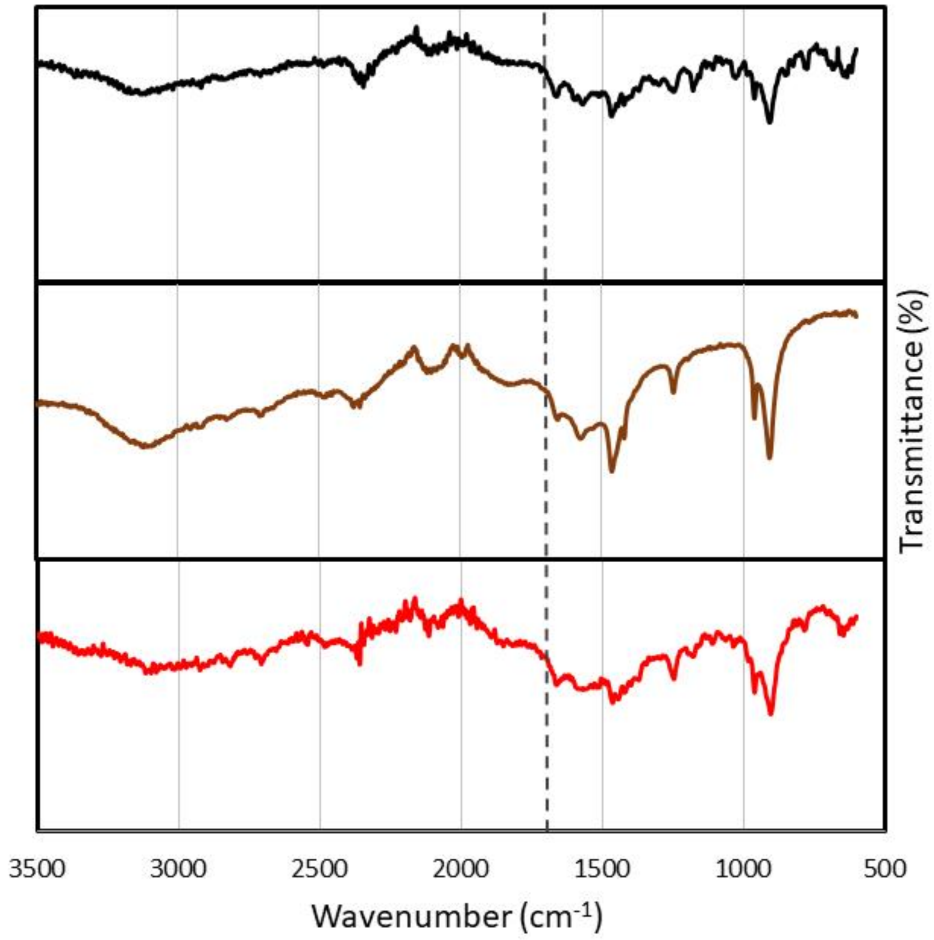

***Figure S7**: Fourier transform infrared (FTIR) spectra for a) MA:AC deposited MAPbI$_3$ (black), b) solvent annealed MAPbI$_3$ (brown) and c) "extreme" solvent annealed MAPbI$_3$ (high solvent volume and no subsequent annealing). We find that there is no observable carbonyl (C=O) stretch apparent around 1660-1690cm^{-1} (grey dashed line) as would be expected for dimethylformamide (DMF), indicating that there is very little residual solvent in the films following solvent annealing. All other frequencies are comparable to previous reports of MAPbI$_3$.[57] Full material preparation and analysis is described in methods.*

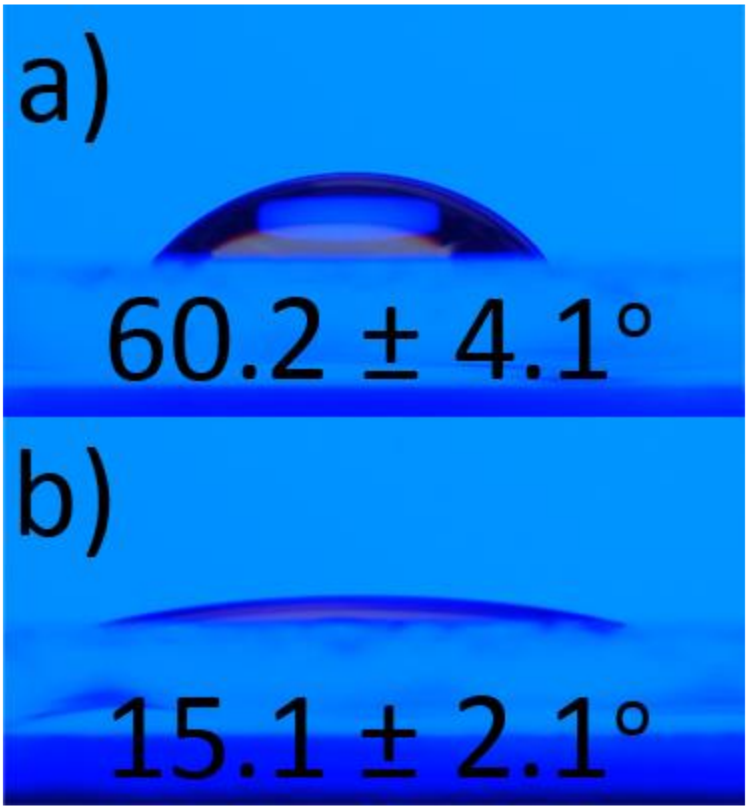

Figure S8: *Contact angles of deionised water on both poly-TPD and PEDOT:PSS. The high contact angle of water upon poly-TPD demonstrates the hydrophobic nature of poly-TPD, while PEDOT:PSS is soluble in water and extremely hydrophilic. Because of the polar nature of solvents used with typical perovskites, the perovskite solution tends to dewet from a poly-TPD surface, however poly-TPD is largely moisture free and will thus improve PSC stability.*

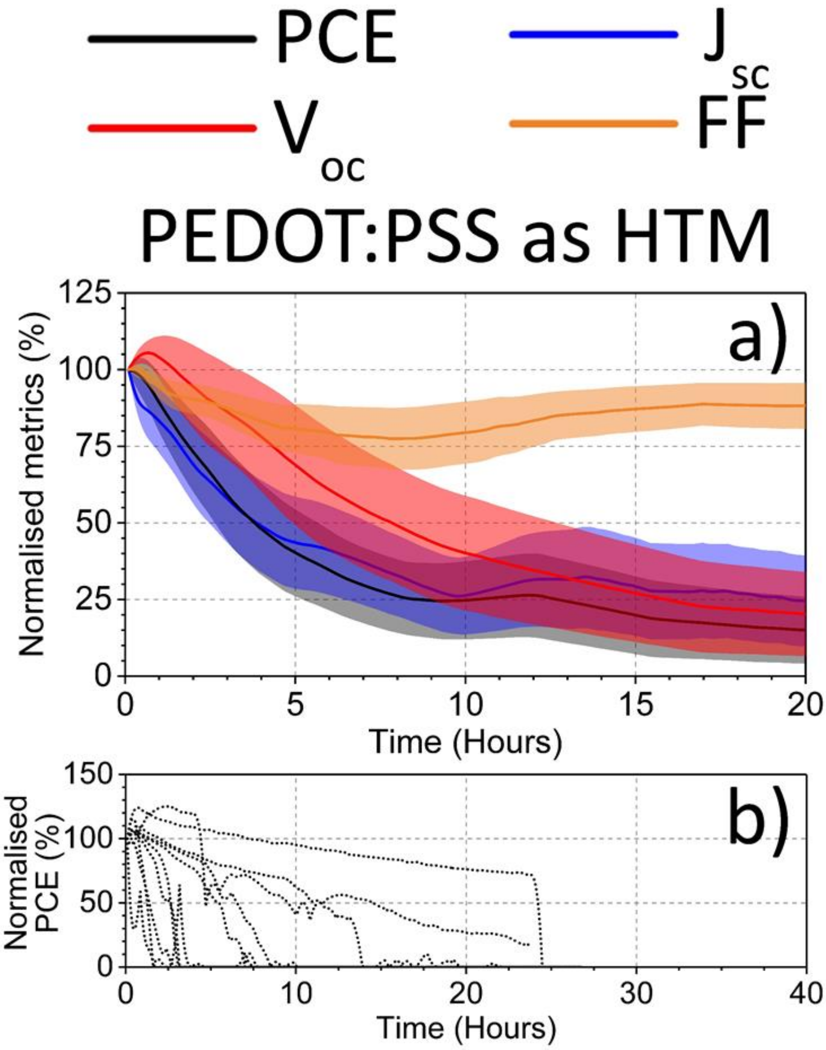

Figure S9: *(a) Performance metrics (Black - PCE, J_{sc} - blue, V_{oc} - red, FF - orange) for PEDOT:PSS containing devices during device operation. This highlights the rapid decay of PSCs despite encapsulation with PVP and epoxy. We attribute the fast decay of these PCSs to moisture adsorbed onto the PEDOT:PSS surface that was sealed into the device during fabrication, and/or the acidic nature of PEDOT:PSS etching the ITO[27,29]. Solid lines represent the mean of each metric and the translucent band represents the standard deviation across all the devices. In part (b) dotted lines indicate the performance of individual devices over time.*

Additional Discussion

During this research it was found that such multi-layer encapsulation techniques can also be applied to standard architecture PSCs. Devices with structure FTO/c-TiO_2/mp-TiO_2/$Cs_{0.05}(MA_{0.17}FA_{0.83})_{0.95}Pb(I_{0.83}Br_{0.17})_3$/spiro-OMeTAD/Au were fabricated for PSC aging studies. Here, a solution processed PVP encapsulation layer was found to damage the spiro-OMeTAD HTL, with performance metrics dropping signifcantly. Instead, an electron-beam evaporated 250 nm thick Al_2O_3 encapsulation interlayer was developed to protect standard architecture PSCs (in combination with epoxy and glass) from moisture and oxygen ingress.

Figure S10 presents current-voltage sweeps (a) and stabilised power outputs (b) of a champion FTO/c-TiO_2/mp-TiO_2/$Cs_{0.05}(MA_{0.17}FA_{0.83})_{0.95}Pb(I_{0.83}Br_{0.17})_3$/spiro-OMeTAD/Au/$Al_2O_3$/epoxy/glass PSC before encapsulation, after encapsulation and after 100 hours of aging in the ATLAS lifetime tester. It was found that the encapsulation process still reduced the PCE of the PSC, with stabilised PCE's falling from 18.4 % to 14.7 % after the encapsulation process. Once encapsulated however, the device was highly stable, exhibiting no loss in PCE after 100 hours of aging. To determine the cause of the drop in performance upon encapsulation, PSC *JV* sweeps were taken before and after the Al_2O_3 deposition (see Figure S10c) and before and after the epoxy was deposited (see Figure s10d). As can be seen, it is the deposition of the epoxy that caused a drop in both V_{OC} and J_{SC}, indicating that the Al_2O_3 is unable to fully protect PSC from the epoxy during the curing process.

Figure S11 presents the performance metrics during 100 hours of aging of FTO/c-TiO_2/mp-TiO_2/$Cs_{0.05}(MA_{0.17}FA_{0.83})_{0.95}Pb(I_{0.83}Br_{0.17})_3$/spiro-OMeTAD/Au PSCs sealed with: a) Al_2O_3/epoxy/glass, b) Al_2O_3, c) epoxy, and d) no encapsulation. We find that using epoxy alone causes the devices to degrade faster than those without any encapsulation, again indicating that the epoxy causes significant damage to the PSCs and reduces their stability. Surprisingly, all four device performance metrics fall when they are encapsulated with epoxy and glass, whilst V_{OC} is still maintained for PSCs without encapsulation.

As Figure S11b indicates, Al_2O_3 acts as an effective encapsulant for around 1 day of aging before the encapsulation fails and photocurrent begins to fall rapidly. It is only the Al_2O_3/epoxy/glass multilayer that enables all four performance metrics to remain largely unchanged for the entire aging process.

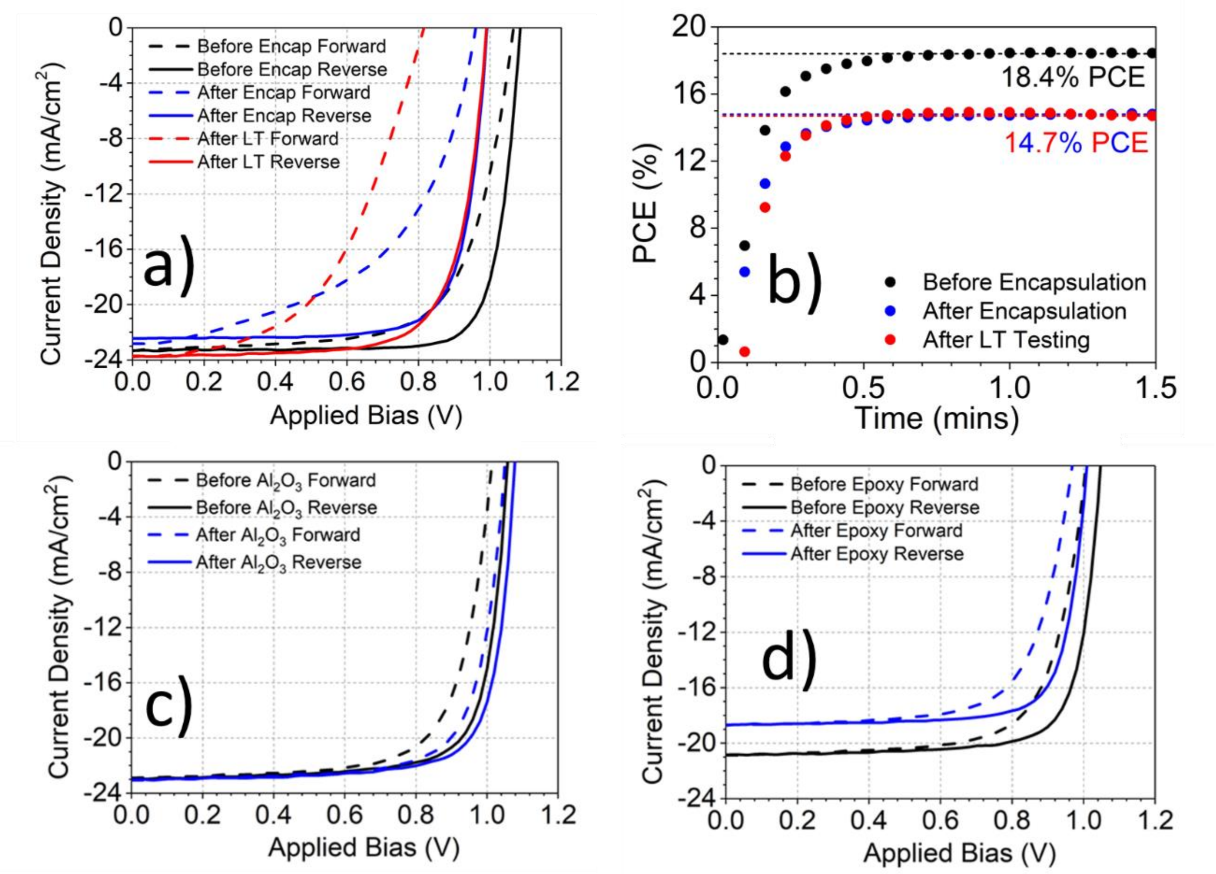

Figure 10: *The effect of encapsulation and aging under illumination and load on standard structure FTO/c-*TiO_2*/mp-*TiO_2*/* $Cs_{0.05}(MA_{0.17}FA_{0.83})_{0.95}Pb(I_{0.83}Br_{0.17})_3$*/spiro-OMeTAD/Au device performance. a) Current-voltage sweeps of a champion device before encapsulation, after* Al_2O_3 *and epoxy encapsulation and after 100 hours of testing. b) The stabilised power outputs of the same device at each stage. The encapsulation apparently reduces the PCE, but the aging does not. c) Current-voltage sweeps of a device before and after electron-beam deposition of* Al_2O_3*. d) Current-voltage sweeps of a device before and after encapsulation with epoxy.*

Regardless of the loss of performance due to the encapsulation process, it is evident that the Al_2O_3/epoxy/glass multi-layer encapsulation can enable stable perovskite device operation. Unfortunately, a technique to supress the drop-in performance upon encapsulation with epoxy has yet to be developed, and the reproducibility of stable standard architecture perovskite solar cells has so far been poor. Whilst the inclusion of an Al_2O_3 interlayer consistently improved the lifetime of standard architecture PSCs, the lack of reproducibility in long-term stability is not yet understood and requires further experimental research. Note that Al_2O_3 can also be used as an encapsulation interlayer for inverted structure PSCs, however a full lifetime study with a large sample size has yet to be performed.

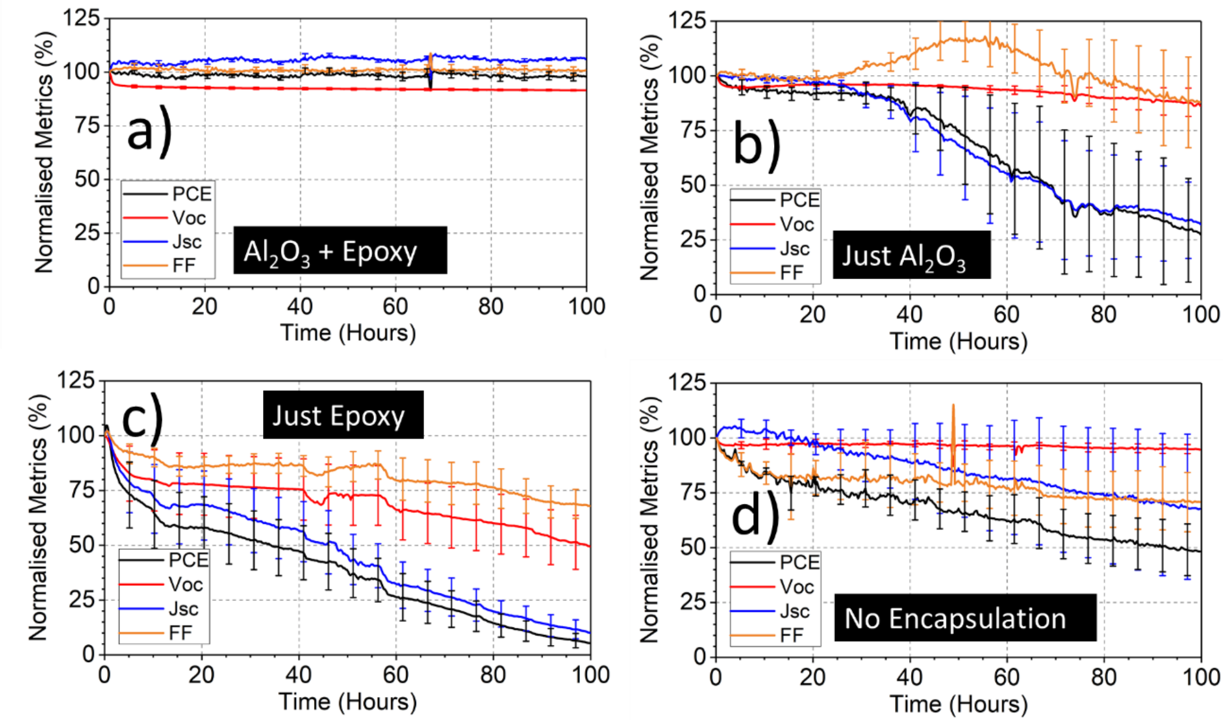

Figure S11: *The effect of aging under illumination and load on standard structure FTO/c-TiO_2/mp-TiO_2/ $Cs_{0.05}(MA_{0.17}FA_{0.83})_{0.95}Pb(I_{0.83}Br_{0.17})_3$/spiro-OMeTAD/Au device performance. The figures plot the normalised performance metrics (PCE – black, J_{SC} - blue, V_{OC} - red, FF - orange) over 100 hours. In all cases, the plotted line represents the mean of device measurements with error bars representing standard deviation across all cells. Devices are encapsulated with either: a) AL_2O_3/epoxy/glass encapsulation, b) Al_2O_3 c) epoxy or d) no encapsulation.*

5.3: Further Context

This chapter highlights that caution must be taken upon choosing and introducing an encapsulation system for perovskite solar cells. As discussed above, an inert interlayer could be PVP (as used in the paper), or a wide variety of other materials (such as Al_2O_3 used in the additional discussion) may suit the need of an encapsulation interlayer. Ultimately the material and deposition method used must not damage the perovskite solar cell during the encapsulation process. The same requirements should be considered for any encapsulation component. Here, a UV curable epoxy was used as the main barrier to moisture ingress. However, there are a many alternative commercial curable epoxies and glues. Prior, during and after completion of this work, several encapsulation products that are advertised as 'non-damaging' to organic thin-film electronics have been screened. It was found that most of these products reduce the performance of perovskite solar cells during or shortly after the encapsulation process. Any commercial encapsulation material should be treated with caution when used in perovskite photovoltaics. Any active process that initiates the encapsulation, any contaminants in the encapsulant, and any resultant stress produced during encapsulation can all lead to decomposition or delamination of the individual active and charge extraction layers. Future studies on the encapsulation and stability of perovskite solar cells should holistic.

The hydrophobic polymers discussed in this chapter have been proven useful for avoiding moisture ingress into PSCs. However, the surface energy of such polymers can also lead to difficulty in wetting uniform and pin-hole free perovskites; an issue that will be particularly problematic when PSCs are scaled to much large area cells and modules. In addition, these polymers are the most expensive components of a PSC.

The novel back-contact perovskite solar cells discussed in Chapter 7 require the implementation of evaporable charge transport layers. Low-cost metal oxides are therefore favourable to poly-TPD (or other similar polymer HTLs) when developing scalable PSC technologies. Drawing upon this, Chapter 6 establishes the use of evaporated metal oxide charge transport layers as replacements for organic transport layers.

5.4: References

[1] W. S. Yang, B.-W. Park, E. H. Jung, N. J. Jeon, Y. C. Kim, D. U. Lee, S. S. Shin, J. Seo, E. K. Kim, J. H. Noh, S. Il Seok, *Science* **2017**, *356*, 1376.

[2] M. Stolterfoht, C. M. Wolff, Y. Amir, A. Paulke, L. Perdigón-Toro, P. Caprioglio, D. Neher, *Energy Environ. Sci.* **2017**, *10*, 1530.

[3] M. Saliba, T. Matsui, K. Domanski, J.-Y. Seo, A. Ummadisingu, S. M. Zakeeruddin, J.-P. Correa-Baena, W. R. Tress, A. Abate, A. Hagfeldt, M. Gratzel, *Science* **2016**, *354*, 206-209

[4] M. Saliba, T. Matsui, J.-Y. Seo, K. Domanski, J.-P. Correa-Baena, M. K. Nazeeruddin, S. M. Zakeeruddin, W. Tress, A. Abate, A. Hagfeldt, M. Grä Tzel*, Energy Environ. Sci.* **2016**, 9, 1989.

[5] M. Abdi-Jalebi, Z. Andaji-Garmaroudi, S. Cacovich, C. Stavrakas, B. Philippe, J. M. Richter, M. Alsari, E. P. Booker, E. M. Hutter, A. J. Pearson, S. Lilliu, T. J. Savenije, H. Rensmo, G. Divitini, C. Ducati, R. H. Friend, S. D. Stranks, *Nature* **2018**, *555*, 497.

[6] T. Bu, X. Liu, Y. Zhou, J. Yi, X. Huang, L. Luo, J. Xiao, Z. Ku, Y. Peng, F. Huang, Y.-B. Cheng, J. Zhong, *Energy Environ. Sci.* **2017**, *10*, 2509.

[7] NREL Efficiency Chart, March **2018**.

[8] D.-Y. Son, S.-G. Kim, J.-Y. Seo, S.-H. Lee, H. Shin, D. Lee, N.-G. Park, *J. Am. Chem. Soc.* **2018**, *140*, 1358.

[9] E. T. Hoke, D. J. Slotcavage, E. R. Dohner, A. R. Bowring, H. I. Karunadasa, M. D. McGehee, *Chem. Sci.* **2015**, *6*, 613.

[10] J. A. Christians, P. Schulz, J. S. Tinkham, T. H. Schloemer, S. P. Harvey, B. J. T. de Villers, A. Sellinger, J. J. Berry, J. M. Luther, *Nat. Energy* **2018**, *3*, 68-74

[11] Z. H. Bakr, Q. Wali, A. Fakharuddin, L. Schmidt-Mende, T. M. Brown, R. Jose, *Nano Energy* **2017**, *34*, 271.

[12] S. N. Habisreutinger, B. Wenger, H. J. Snaith, R. J. Nicholas, *ACS Energy Lett.* **2017**, *2*, 622.

[13] F. Wang, M. Endo, S. Mouri, Y. Miyauchi, Y. Ohno, A. Wakamiya, Y. Murata, K. Matsuda, *Nanoscale* **2016**, *8*, 11882.

[14] L. Calió, S. Kazim, M. Grätzel, S. Ahmad, *Angew. Chemie Int. Ed.* **2016**, 55, 14522-1454.

[15] Q. Wang, C. Bi, J. Huang, *Nano Energy* **2015**, *15*, 275.

[16] D. Zhao, M. Sexton, H. Y. Park, G. Baure, J. C. Nino, F. So, *Adv. Energy Mater.* **2015**, *5*, 1401855.

[17] M. Wong-Stringer, J. E. Bishop, J. A. Smith, D. K. Mohamad, A. J. Parnell, V. Kumar, C. Rodenburg, D. G. Lidzey, *J. Mater. Chem. A* **2017**, *5*, 15714.

[18] Q. Liu, M. C. Qin, W. J. Ke, X. L. Zheng, Z. Chen, P. L. Qin, L. Bin Xiong, H. W. Lei, J. W. Wan, J. Wen, G. Yang, J. J. Ma, Z. Y. Zhang, G. J. Fang, *Adv. Funct. Mater.* **2016**, *26*, 6069.

[19] B. Roose, J. P. C. Baena, K. C. Gödel, M. Graetzel, A. Hagfeldt, U. Steiner, A. Abate, *Nano Energy* **2016**, *30*, 517.

[20] J. T.-W. Wang, Z. Wang, S. K. Pathak, W. Zhang, D. deQuilettes, F. Wisnivesky, J. Huang, P. Nayak, J. Patel, hanis yusof, Y. Vaynzof, R. Zhu, I. Ramirez, J. Zhang, C. Ducati, C. Grovenor, M. Johnston, D. S. Ginger, R. Nicholas, H. Snaith, *Energy Environ. Sci.* **2016**, *9*, 2892.

[21] J. Kim, M. A. M. Teridi, A. R. bin M. Yusoff, J. Jang, W. S. Yang, G. Niu, X. Guo, L. Wang, C.-G. Wu, J. H. Heo, M. Jørgensen, K. Norrman, F. C. Krebs, L. S. C. Pingree, B. A. MacLeod, D. S. Ginger, Z. Wu, J. T.-W. Wang, H. Choi, M. Liu, M. B. Johnston, H. J. Snaith, P.-W. Liang, N. J. Jeon, H.-B. Kim, H. J. Snaith, M. R. Filip, G. E. Eperon, H. J. Snaith, F. Giustino, *Sci. Rep.* **2016**, *6*, 1234.

[22] L. Yang, A. T. Barrows, D. G. Lidzey, T. Wang, *Reports Prog. Phys.* **2016**, *79*, 026501.

[23] H. J. Snaith, *J. Phys. Chem. Lett* **2013**, *4*, 3623.

[24] Z. Zhou, S. Pang, Z. Liu, H. Xu, G. Cui, *J. Mater. Chem. A* **2015**, *3*, 19205.

[25] R. Cheacharoen, N. J. Rolston, D. Harwood, K. A. Bush, R. H. Dauskardt, M. D. McGehee, *Energy Environ. Sci.* **2017**, *11*, 144.

[26] Y. Zhang, H. Yi, A. Iraqi, J. Kingsley, A. Buckley, T. Wang, D. G. Lidzey, *Sci. Rep.* **2017**, *7*, 1.

[27] C. Bracher, B. G. Freestone, D. K. Mohamad, J. A. Smith, D. G. Lidzey, *Energy Sci. Eng.* **2017**, *6*, 35

[28] Y. Zhang, E. Bovill, J. Kingsley, A. R. Buckley, H. Yi, A. Iraqi, T. Wang, D. G. Lidzey, *Sci. Rep.* **2016**, *6*, 21632.

[29] W. Lee, M. Song, S. Park, S. Nam, J. Seo, H. Kim, Y. Kim, *Sci. Rep.* **2016**, *6*, 1.

[30] L. Shi, T. L. Young, J. Kim, Y. Sheng, L. Wang, Y. Chen, Z. Feng, M. J. Keevers, X. Hao, P. J. Verlinden, M. A. Green, A. W. Y. Ho-Baillie, *ACS Appl. Mater. Interfaces* **2017**, *9*, 25073.

[31] F. Matteocci, L. Cinà, E. Lamanna, S. Cacovich, G. Divitini, P. A. Midgley, C. Ducati, A. Di Carlo, *Nano Energy* **2016**, *30*, 162.

[32] Q. Dong, F. Liu, M. K. Wong, H. W. Tam, A. B. Djurišić, A. Ng, C. Surya, W. K. Chan, A. M. C. Ng, *ChemSusChem* **2016**, *9*, 2518.

[33] N. K. Noel, S. N. Habisreutinger, B. Wenger, M. T. Klug, M. T. Hörantner, M. B. Johnston, R. J. Nicholas, D. T. Moore, H. Snaith, *Energy Environ. Sci.* **2017**, *10*, 145.

[34] X. Xu, C. Ma, Y. Cheng, Y. M. Xie, X. Yi, B. Gautam, S. Chen, H. W. Li, C. S. Lee, F. So, S. W. Tsang, *J. Power Sources* **2017**, *360*, 157.

[35] X. Zheng, B. Chen, J. Dai, Y. Fang, Y. Bai, Y. Lin, H. Wei, X. C. Zeng, J. Huang, *Nat. Energy* **2017**, *2*, 17102.

[36] N. Tripathi, Y. Shirai, M. Yanagida, A. Karen, K. Miyano, *ACS Appl. Mater. Interfaces* **2016**, *8*, 4644.

[37] J. Lee, H. Kang, G. Kim, H. Back, J. Kim, S. Hong, B. Park, E. Lee, K. Lee, *Adv. Mater.* **2017**, *29*, 1.

[38] J. Liu, C. Gao, X. He, Q. Ye, L. Ouyang, D. Zhuang, C. Liao, J. Mei, W. Lau, *ACS Appl. Mater. Interfaces* **2015**, *7*, 24008.

[39] Y. Zhou, O. S. Game, S. Pang, N. P. Padture, *J. Phys. Chem. Lett.* **2015**, *6*, 4827.

[40] Y. Wang, S. Li, P. Zhang, D. Liu, X. Gu, H. Sarvari, Z. Ye, J. Wu, Z. Wang, Z. D. Chen, *Nanoscale* **2016**, *8*, 19654.

[41] Z. Xiao, Q. Dong, C. Bi, Y. Shao, Y. Yuan, J. Huang, *Adv. Mater.* **2014**, *26*, 6503.

[42] W. Woishnis, Permeability and Other Film Properties of Plastics and Elastomers, Plastics Design Library, 1995,

[43] E. Bovill, N. Scarratt, J. Griffin, H. Yi, A. Iraqi, A. R. Buckley, J. W. Kingsley, D. G. Lidzey, *Appl. Phys. Lett.* **2015**, *106*, 073301.

[44] P. Calado, A. M. Telford, D. Bryant, X. Li, J. Nelson, B. C. O'Regan and P. R. F. Barnes, Nat. Commun., 2016, 7, 13831.

[45] T. Zhang, S. H. Cheung, X. Meng, L. Zhu, Y. Bai, C. H. Y. Ho, S. Xiao, Q. Xue, S. K. So, S. Yang, J. Phys. Chem. Lett. 2017, 8, 5069.

[46] J. Li, Q. Dong, N. Li, L. Wang, *Adv. Energy Mater.* **2017**, *7*, 1.

[47] Y. Kato, L. K. Ono, M. V. Lee, S. Wang, S. R. Raga, Y. Qi, *Adv. Mater. Interfaces* **2015**, *2*, 2.

[48] Y. Han, S. Meyer, Y. Dkhissi, K. Weber, J. M. Pringle, U. Bach, L. Spiccia, Y.-B. Cheng, *J. Mater. Chem. A* **2015**, *3*, 8139.

[49] Q. Sun, P. Fassl, D. Becker-Koch, A. Bausch, B. Rivkin, S. Bai, P. E. Hopkinson, H. J. Snaith, Y. Vaynzof, *Adv. Energy Mater.* **2017**, *7*, 170097.

[50] Y. Kato, L. K. Ono, M. V Lee, S. Wang, S. R. Raga, Y. Qi, *Adv. Mater. Interfaces* **2015**, 2, 1500195.

[51] K. Nasouri, A. M. Shoushtari, M. R. M. Mojtahedi, *Adv. Polym. Technol.* **2015**, *34*, 1.

[52] M. Teodorescu, M. Bercea, *Polym. - Plast. Technol. Eng.* **2015**, 54, 923.

[53] A. Zheng, Y. Xue, D. Wei, S. Li, H. Xiao, Y. Guan, *Soft Mater.* **2014**, 12, 297.

[54] A. E. Williams, P. J. Holliman, M. J. Carnie, M. L. Davies, D. a. Worsley, T. M. Watson, *J. Mater. Chem. A* **2014**, *2*, 19338.

[55] J. Barbé, V. Kumar, M. J. Newman, H. K. H. Lee, S. M. Jain, H. Chen, C. Charbonneau, C. Rodenburg, W. C. Tsoi, *Sustain. Energy Fuels* **2018**, *2*, 905.

[56] A. J. Parnell, A. J. Cadby, A. D. F. Dunbar, G. L. Roberts, A. Plumridge, R. M. Dalgliesh, M. W. A. Skoda, R. A. L. Jones, *J. Polym. Sci. Part B Polym. Phys.* **2016**, *54*, 141.

[57] X. Guo, C. McCleese, C. Kolodziej, A. C. S. Samia, Y. Zhao, C. Burda, *Dalt. Trans.* **2016**, *45*, 3806.

Chapter 6

Advanced Article

Journal of Materials Chemistry A

Low-Temperature, High-Speed Reactive Deposition of Metal Oxides for Perovskite Solar Cells

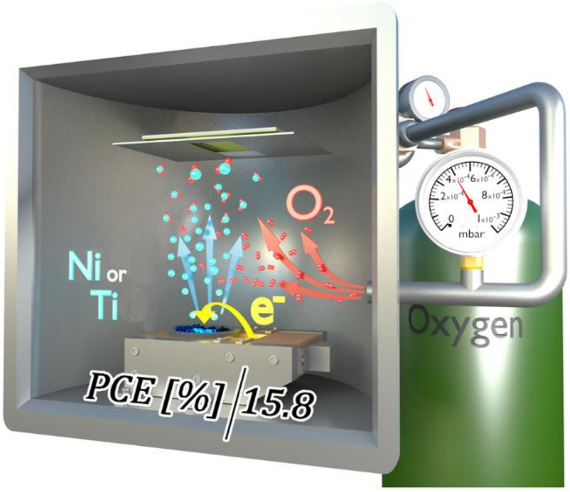

For the journals PDF:

DIO: 10.1039/C8TA10827G

Cite this: J. Mater. Chem. A,2019, Advance Article.

6.0: Publication Forward: Why Evaporated Metal Oxides?

As previously shown in Chapter 3, NiO and TiO_2 have near ideal electronic band structures relative to that of many perovskite active layers, making them ideal HTL and ETLs respectively. This chapter explores the deposition of metal oxides using low-cost techniques. Here, NiO and TiO_2 are deposited using reactive electron-beam evaporation; a process that is compatible with heat sensitive polymeric substrates.

6.1: Publication Main Body

Low-Temperature, High-Speed Reactive Deposition of Metal Oxides for Perovskite Solar Cells

Michael Wong-Stringer[1,α], Thomas J. Routledge[1,α], Onkar S. Game[1], Joel A. Smith[1], James E. Bishop[1], Naoum Vaenas[1], Benjamin G. Freestone[1], David M. Coles[1,3], Trevor McArdle[2], Alastair R. Buckley[1,3] and David G. Lidzey[1,3]*

[1]Department of Physics & Astronomy, University of Sheffield, Hicks Building, Hounsfield Road, Sheffield, S3 7RH, United Kingdom

[2]Power Roll Limited, Washington Business Centre, 2 Turbine Way, Sunderland, SR5 3NZ, United Kingdom

[3]Ossila Limited, Windsor Street, Sheffield, S4 7WB, United Kingdom

[α]These authors contributed equally to this work

*Corresponding author, email d.g.lidzey@sheffield.ac.uk

Keywords: perovskite solar cells, metal oxide, NiO, nickel oxide TiO_2, titanium dioxide
electron-beam evaporation, reactive, scalable, low-temperature.

Abstract

Nickel oxide (NiO) and titanium dioxide (TiO_2) charge-extraction layers are fabricated under a partial pressure of O_2 from nickel and titanium metals using a reactive electron-beam evaporation process. Using such materials, inverted architecture perovskite solar cells incorporating a NiO hole-transport layer achieve power conversion efficiencies up to 15.8 %, whilst standard architecture devices using a TiO_2 electron-transport layer achieve a power conversion efficiency up to 13.9 %. Critically, we find that such metal oxides can be deposited at high speed (nm/s) and at low substrate-temperature, and do not require a high-temperature anneal step after deposition, making reactive electron-beam evaporation compatible with roll-to-roll processing on sensitive flexible polymeric substrates.

Introduction

The efficiency of perovskite solar cells (PSCs) has increased rapidly, with recently reported power conversion efficiencies (PCEs) commonly exceeding 20 %.[1,2] Such advances have been driven by the synthesis of new perovskite materials, and by the development of superior charge-transporting materials. Indeed, high PCE PSCs are reliant on the use of charge-transporting materials that have high conductivity (leading to low resistance losses) and good charge selectivity (leading to low parasitic losses). This role is currently dominated by small molecules and thin polymer films that have been chemically-doped to achieve high conductivities.[3–6] It is known that these dopants can undergo migration within a PSC, resulting in reduced device stability.[4,7] For this reason, there is growing interest in the development of metal oxides for use as charge-transporting layers in PSCs. Such materials (which are free from mobile dopants) can be used to create efficient PSCs, and crucially, have increased thermal and photo-chemical stability compared to their doped organic counterparts.[8–15] Unfortunately, many metal oxides are prepared using high-temperature processes to create effective charge-extraction materials.[9,16–24] While this is not problematic when fabricating devices on substrates such as fluorine-doped tin oxide (FTO) coated glass, it is an issue for device fabrication on polymeric substrates (e.g. polyethylene terephthalate) that are often used in high throughput roll-to-roll (R2R) processes.[15]

In this paper, we explore the deposition of the metal oxides NiO and TiO_2 using a reactive electron-beam (e-beam) evaporation technique that is compatible with the low temperature requirements of flexible polymeric substrates. TiO_2 and NiO are of significant interest for applications in PSCs due to their favourable conduction and valance band (CB and VB) energies, reported from -3.6 to -4.2 eV and -5.0 and -5.5 eV respectively.[10,13,25–32] These values align with the conduction and valance bands of many ubiquitous perovskites active layers.[10,13,25–32] The high CB of NiO (1.85 eV)[33] and deep VB of TiO_2 (7.2 eV)[32] also make them effective at blocking electrons and holes respectively. For this reason, TiO_2 and NiO have been used as effective electron- and hole-transporting materials (ETM/HTM) in high-performance PSCs. Here, we deposit TiO_2 and NiO using a process that utilises metallic pellets which are evaporated using an electron-beam, with an oxygen partial pressure within the deposition chamber oxidising the vaporized metals. We show that this process is compatible with high-speed R2R manufacturing by fabricating efficient PSCs in which the metal oxide charge-transporting layers were deposited at rates up to 1 nm/s.

We note that a number of alternative processes have been used to deposit NiO and TiO_2, however many of these techniques have issues with manufacture scalability. For example NiO and TiO_2 have previously been deposited from sol-gel or nanoparticle suspensions,[20,22,26,27,33–36] using chemical bath deposition (CBD), atomic layer deposition (ALD), magnetron sputtering, pulsed laser deposition and e-beam deposition. However techniques such as CBD require elevated temperatures either during[37] or post deposition.[8] Such temperatures can be reduced below 100 °C, although this is at the cost of extended reaction times, thereby reducing the capacity for R2R deposition.[38] Slow deposition rates are also a major limitation of ALD; indeed TiO_2 films deposited via ALD can take up to 100 minutes (over 200 cycles) to form a 20 nm layer.[11] Despite their potential for scalability, metal oxide films deposited from nanoparticle solutions usually contain residual organic ligands or stabilisers that cannot be removed by low temperature annealing.[39] This issue can be avoided by depositing a metallic film (e.g. Ni) which is then oxidized using a post-deposition high-temperature anneal in air to create a HTM.[23,24] Alternatively NiO or TiO_2 can be directly deposited from stoichiometric source pellets using techniques such as magnetron sputtering, pulsed laser or e-beam deposition.[12,25,30,33,40–45] However the interaction of source metal oxide pellets with high-energy electron beams, lasers or plasmas quickly changes their initial stoichiometry, leading to batch-to-batch inconsistencies in the optical and electronic properties of the resultant oxide-materials.

In contrast, the reactive e-beam technique used here to produce metal oxides is inherently low-cost in nature,[10,46,47] and combines both reduced substrate temperature, and high-speed deposition. It is therefore well suited for R2R fabrication. Using this technique, we demonstrate the fabrication of inverted architecture (p-i-n) PSCs with NiO, and standard architecture (n-i-p) PSCs with TiO_2, and report champion PCEs of 15.8 % and 13.9 % for PSCs incorporating NiO and TiO_2 respectively. We also fabricate PSCs with a PCE of 14.2 % (NiO) and 13.5 % (TiO_2) when using a fast (1 nm/s) deposition rate. Finally, we demonstrate that this technique can also be used to create devices that require no thermal annealing (i.e. all process steps are carried out at room temperature), with TiO_2-based PSCs achieving a PCE of 11.3 %. We emphasize that the use of a vacuum in this process is not expected to present a barrier to manufacture, as vacuum-deposition techniques are well established in R2R processing; e.g. the production of low-cost metallized plastic for food packaging applications.[48]

Results and discussion

The reactive e-beam process used to deposit NiO and TiO_2 is detailed in Figure 1a. Metal pellets were placed in a deposition crucible and melted using an electron-beam, while oxygen gas was bled into the chamber at a partial pressure from $5x10^{-5}$ mbar to $1.9 x10^{-4}$ mbar. The oxygen gas oxidised the evaporating metal-vapour, resulting in the deposition of a metal oxide film onto the substrate (here a patterned indium tin oxide [ITO] electrode). Evaporation rates were adjusted through control of beam current, with film deposition rates (measured using a quartz-crystal microbalance) between 0.3 and 10 Å/s utilised. To understand the deposition-process in more detail, we have used temperature-sensitive label indicators to directly monitor the temperature of the substrates. This measurement indicated that the temperature of the substrate did not exceed 70 °C at any point during deposition, confirming that this process is in principle compatible with sensitive polymeric-substrates.

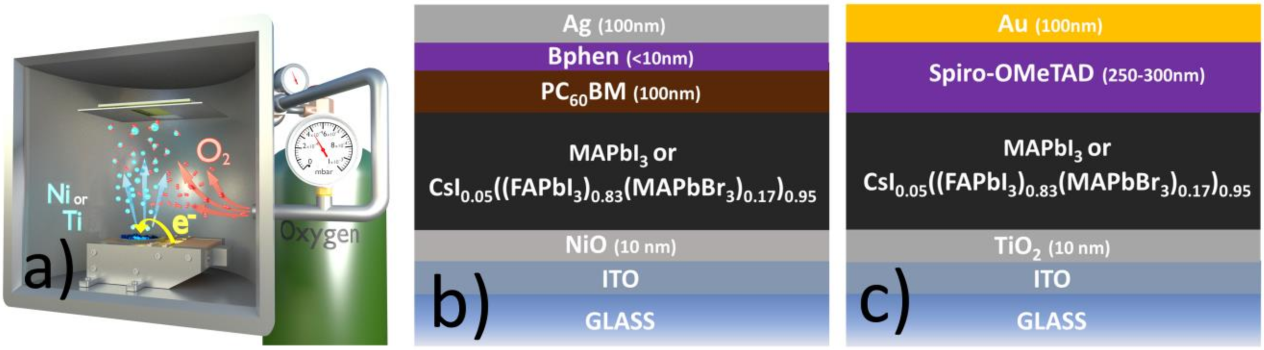

Figure 1: *a) Reactive electron-beam deposition of metal oxides. The beam (yellow) heats the metal source material (blue) causing evaporation of the material (light blue), whilst oxygen (red) is fed into a vacuum system. The rate and oxygen partial pressure can be controlled. The substrate is rotated and covered with an evaporation mask. b) Inverted p-i-n perovskite solar cell used here, incorporating NiO deposited via reactive electron-beam deposition. c) Standard n-i-p perovskite solar cell used here, incorporating* TiO_2 *deposited via reactive electron-beam deposition.*

We have also investigated the effect of exposing such metal oxide films to a 15-minute UV-ozone treatment immediately before perovskite deposition. Inverted architecture (p-i-n) PSCs were fabricated based on the structure ITO/NiO/perovskite/$PC_{60}BM$/bathophenanthroline (BPhen)/Ag as shown in Figure 1b. Standard-architecture (n-i-p) PSCs were fabricated using the structure ITO/TiO_2/perovskite/spiro-OMeTAD/Au as shown in Figure 1c. Further fabrication and measurement details are provided in the supplementary information.

Metal oxide films on ITO were used to create PSC devices using two different perovskite materials. The first was a triple cation perovskite $CsI_{0.05}((FAPbI_3)_{0.83}(MAPbBr_3)_{0.17})_{0.95}$ (referred to as TC), which has been widely used in the literature since it was first used to create devices having a PCE of 21 %.[49] The second perovskite used was the material $MAPbI_3$, which was deposited from an acetonitrile solution (referred to as AC). This process route was first reported by Noel *et al.*[50] and can be used to create highly compact and uniform perovskite films. The devices fabricated were characterised using current-voltage

(J-V) sweeps under calibrated 100 mW/cm^2 AM1.5 irradiation. Additional characterisation techniques are also employed to explore the optoelectronic and morphological properties of the metal oxide films, including atomic force microscopy (AFM), UV-vis absorption, x-ray diffraction (XRD), X-ray photoelectron spectroscopy (XPS), and spectroscopic ellipsometry.

We first discuss the optical and morphological properties of the films that were deposited. Here, films were deposited on quartz-coated glass at an oxygen partial pressure of 1 x 10^{-4} mbar at a rate of 1.5 - 2 Å/s and had an average thickness of 10 nm. Figure 2a, 2b and 2c presents AFM topographs of ITO, NiO and TiO_2 respectively. These indicate an RMS roughness of 2.17 nm, 1.69 nm, and 2.03 nm for ITO, NiO and TiO_2 respectively. It is apparent that such films do not planarise the ITO substrate, however as they reduce RMS roughness, it is likely that they form a semi-conformal coating.

To further understand the physical structure of the films, XRD measurements were performed on 100 nm thick metal oxide films deposited on quartz-covered glass, with typical data shown in Figure 2d. Here a reference scan recorded on a quartz-coated glass substrate is included for reference. XRD measurements of the NiO film identify crystalline components as evidenced by the appearance of reflections observed at 37° and 63° respectively. Here, the peaks at 37° and 63° coincide with the (111) and (220) reflections, however the expected (200) peak at 43° coincides with a large background peak from the quartz substrate that is apparent at the same angle. To determine whether the (200) peak contributes to the measured NiO XRD spectra, we have determined the full width at half maximum (FWHM) linewidth of the peaks around 43° in both the quartz-reference and in the NiO-coated quartz-glass. In both cases, we find the linewidth of these peaks to be very similar (quartz $FWHM_{43^\circ} = 0.34^\circ \pm 0.04^\circ$ and NiO $FWHM_{43^\circ} = 0.31^\circ \pm 0.04^\circ$), suggesting that that any scattering from the (200) plane-direction is very weak. We note that previous work by Park *et al* [25] used the relative ratio of the (111) and (200) scattering features in NiO films to evidence preferential alignment of crystal planes. Here, we believe that the apparent absence of the expected NiO (200) diffraction peak also suggests a preferential alignment of NiO crystallites along the (111) plane direction. In contrast, we find no clear crystal reflections are observed from TiO_2 (the positions where the (101) and (200) reflections are expected are also shown). This indicates that such TiO_2 films are largely amorphous.

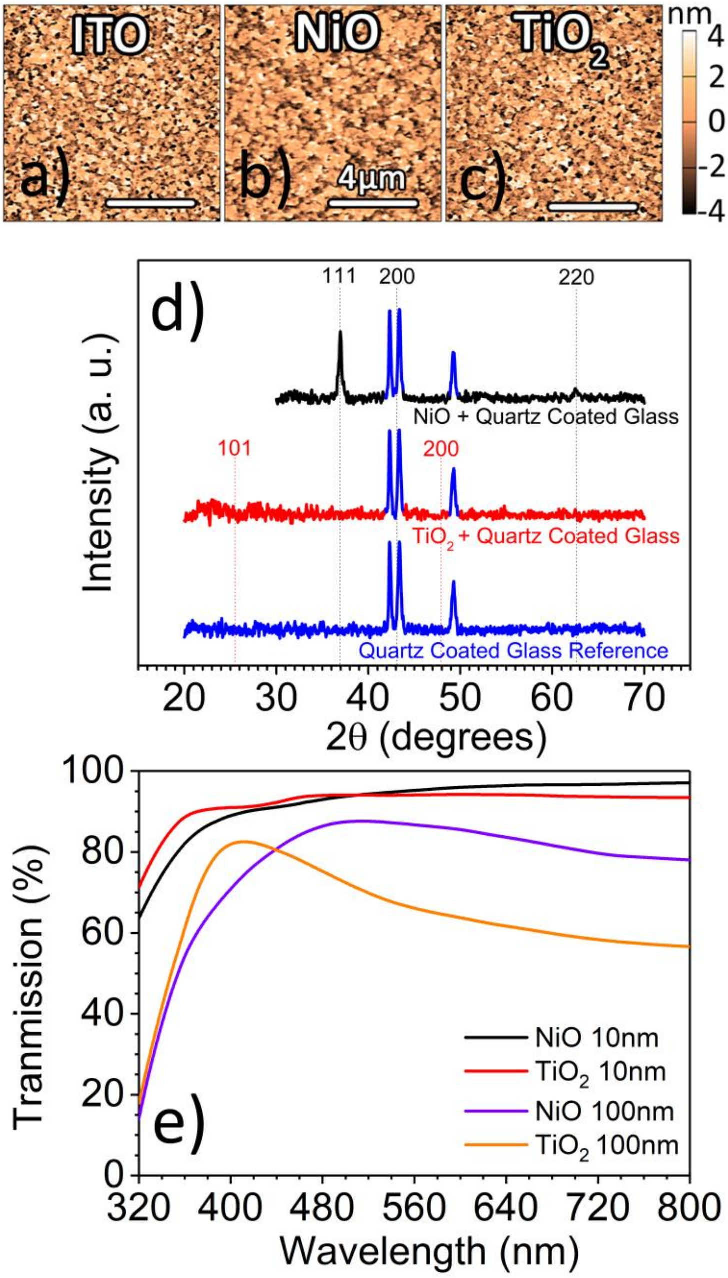

Figure 2: *Characterisation of metal oxide films. Atomic force microscope topographs of a) ITO, b) ITO/NiO (10 nm) and c) ITO/TiO_2 (10 nm). d) X-ray diffraction patterns of our NiO and TiO_2 deposited onto quartz coated glass using the reactive e-beam process. Labelled dotted lines indicate known NiO and TiO_2 reflections with crystallographic planes labelled. e) Transmission UV-vis spectra of 10 nm and 100 nm NiO and TiO_2 films, deposited onto quartz coated glass using the reactive e-beam process.*

Figure 2e shows the optical transmission of 10 nm thick NiO and TiO_2 films. We find that such films have high optical transmissivity (> 90 %) across the visible spectrum; a favourable property that is likely to reduce parasitic optical absorption in a PV device that would otherwise causes losses in photocurrent. To determine the optical band-gap of the materials deposited, the optical transmission measurements were taken of films that were significantly thicker (100 nm) than would be used in a practical device. This was then used to produce Tauc plots (see Figure S1) from which we determine optical band gaps of (3.64 ± 0.04) eV and (3.61 ± 0.04) eV for NiO and TiO_2 respectively. In Figure S2a and S2b we present the refractive index, *n*, obtained for 10 nm NiO and TiO_2 films as determined by ellipsometry. Here a Cauchy model was used to confirm film thickness of 10 nm.

We have also characterised the elemental composition of NiO and TiO_2 films using XPS, with data presented in Figure S3 and Figure S4. Here, full survey scans (parts a and b) as well as high-resolution metal 2p (parts c and d) and O 1s (parts e and f) spectra of both NiO and TiO_2 are provided. These spectra closely match those of previous XPS studies performed on NiO and TiO_2,[18,51–54] and indicate that there is no oxygen deficiency in either e-beam deposited materials. Taken together, our characterisation of the reactive e-beam deposited metal oxide films demonstrate that the NiO films are semi-crystalline and the TiO_2 films are largely amorphous, with the optical properties of both closely matching that of previous reports of low temperature processed metal oxides.[40–42]

We now consider the application of the metal oxide films created as HTM and ETM materials. Firstly, we discuss the effect of film thickness on device performance. Inverted architecture p-i-n PSC devices were fabricated utilising an AC perovskite with two different thicknesses (10 and 20 nm) of NiO. Table 1 tabulates key device metrics including PCE, fill factor (FF), short circuit current density (J_{SC}), open circuit voltage (V_{OC}), shunt resistance (R_{SH}), and series resistance (R_S) for the two thicknesses. Characteristic J-V curves from PSCs are presented in Figure S5a. We find that PSCs containing a 10 nm thick NiO (deposited at 1 Å/s) had a 60 % lower R_S than equivalent devices containing a 20 nm thick film, and similar R_{SH} values. This resulted in an overall PCE enhancement of around 10 % for PSCs containing a 10 nm NiO layer compared to those containing thicker NiO. It is therefore apparent that the thicker NiO films introduced series losses via its limited conductivity. For this reason, 10 nm thick metal oxide films were used in all devices described below.

p-i-n NiO AC	PCE [%]	J_{SC} [mA/cm^2]	V_{OC} [V]	FF [%]	R_S [Ωcm^2]	R_{SH} [Ωcm^2]
10 nm NiO, 1 Å/s	11.5 ± 0.6	15.7 ± 0.8	1.05 ± 0.02	69.7 ± 3.0	6.05 ± 0.9	1540 ± 960
20 nm NiO, 1 Å/s	10.5 ± 1.1	16.5 ± 1.1	0.98 ± 0.02	64.1 ± 2.1	9.96 ± 1.7	1250 ± 630

Table 1: *Performance metrics (average ± standard deviation) for p-i-n PSCs with a reactive e-beam deposited NiO HTM and AC perovskite active layer. PSCs are made with NiO thicknesses of 10 nm and 20 nm.*

PSCs with p-i-n configuration were fabricated using a TC perovskite and a NiO HTM. Interestingly, it was found that when the TC perovskite is converted using an anneal temperature of 100 °C (a standard process condition for this material), devices had a relatively poor performance, with low FF (<50 %) and J_{SC} (<16 mA/cm^2) leading to a PCE of <6 % (see characteristic J-V curves in Figure S5b). However, such metrics improve significantly when the TC perovskite was instead annealed at a lower temperature (80 °C) in vacuum – see Figure 3a. Using an 80 °C vacuum anneal for inverted architecture PCSs and a standard 100 °C anneal for standard architecture PSCs, we then explored (i) a range of O_2 partial pressures (5x10^{-5} mbar, 1x10^{-4} and 1.9 x10^{-4} mbar) during the metal oxide depositions, and (ii) different evaporation rates (0.5 Å/s and 1.5 or 2 Å/s), with all data presented in Table S1. It was found that across all oxygen partial pressures TC PSCs had similar performance metrics and efficiencies; a result that suggests the deposition process could be easily transferred between different e-beam systems.

We have also explored the effect of exposing the metal oxide films to a UV-Ozone (UVO) treatment for 15 minutes before the perovskite was deposited. This low-temperature and scalable technique is well known to modify surface energy and improve the wettability of materials deposited upon its surface. UVO treatment has also previously been reported to change the stoichiometry of metal oxides by introducing Ni vacancies in NiO[54], oxygen vacancies in TiO_2[55] and to induce the formation of NiO(OH) (nickel oxide hydroxide) and $Ni(OH)_2$ (nickel hydroxide) in NiO films.[51,54,56] Figure 3b presents data for PSCs that contain a TC perovskite, with devices utilising either a NiO HTM or a TiO_2 ETM. Characteristic J-V curves of devices used to collect the data are shown in Figure S6a. A vacuum anneal is used to convert the perovskite for all NiO based inverted PSCs for the reasons discussed above.

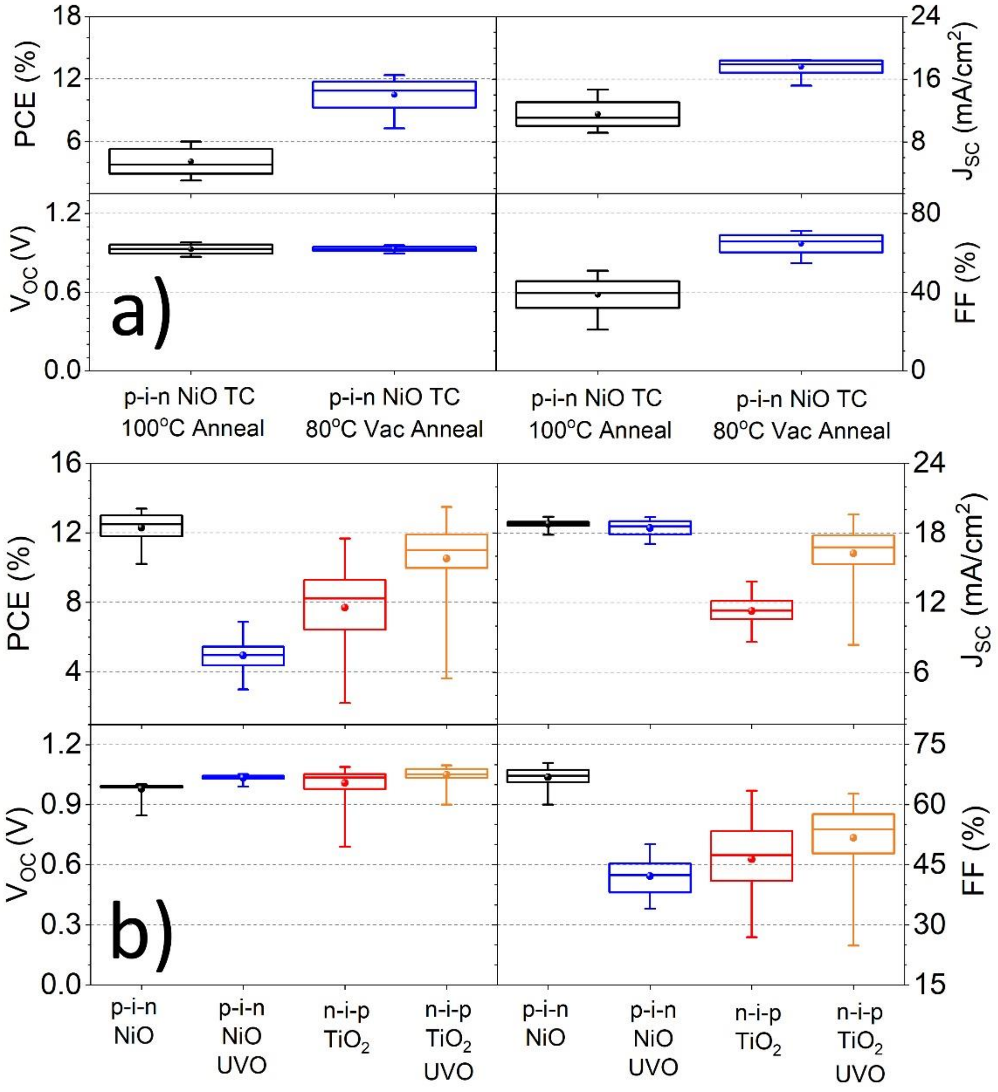

Figure 3: *a) Box plot of performance metrics for p-i-n PSCs with a reactive e-beam deposited NiO HTM and TC active layer, PSCs are fabricated with a 100 °C anneal (black) or an alternative 80 °C vacuum anneal (blue) for conversion of the perovskite. b) Boxplots of performance metrics for p-i-n (black, blue) and n-i-p (red, orange) PSCs with reactive e-beam deposited NiO HTM and* TiO_2 *ETM respectively. The perovskite precursor is either deposited directly onto the metal oxides (black, red) or treated with UV-Ozone for 15 minutes (blue, orange) prior to deposition of the perovskite.*

We firstly discuss the effect of UVO on the NiO HTM; it is found that all device performance metrics are significantly reduced when NiO films are exposed to the UVO (PCE falls from 12 % to 5 % as a result of reduction in both FF and J_{sc}). A reduction in the optical transmission of the NiO across all wavelengths (see Figure S6b), with a greater reduction in transmission occurring for a thicker film, coupled with a reduction in its apparent optical band gap by 120 meV (see Figure S1) suggests a change in the stoichiometry of the film.

High resolution XPS scans of Ni 2p spectra reveal an increase in Ni^{3+} relative to Ni^{2+} after UVO treatment (see Figure S3c and S3d), a result consistent with an increase in Ni vacancies or the incorporation of Ni_2O_3 or NiO(OH) into the film. A peak in the O 1s spectra that is associated with OH^- is also observed to increase after UVO treatment (see Figure S3e and S3f). As Ni_2O_3 and NiO(OH) are optically 'black', their formation is consistent with the loss in transmission observed in NiO film after UVO treatment. The NiO films are only 10 nm thick, therefore it is likely that such states are located through the entire film, resulting in a reduction in device performance as observed for UVO treated NiO HTMs.

We now consider the effect of UVO treatment on the TiO_2 ETM. Here, we find that a 15-minute UVO exposure improves the average device PCE from 7.5 % to 10.5 %, with all metrics (particularly FF) increasing. It appears that the UVO process results in an increase in the optical transmittance of TiO_2 (see Figure S6c). It is also likely that this process improves the wettability of the perovskite to the TiO_2 surface via a increase in the surface energy, improving the quality of the resultant interface. Our XPS measurements indicate that the UVO treatment results in a significant reduction in contaminants but does not significantly change the stoichiometry of the TiO_2. Here O 1s spectra (see Figure S4e and S4f), indicate that a shoulder associated with OH^- contamination is apparently suppressed after UVO treatment. The full survey scan spectrum also directly indicates that UVO removes sodium, potassium and phosphate contaminants. Note, however that we find no changes in the XRD diffraction spectra of TiO_2 and NiO following UVO treatment, suggesting that this process does not result in any substantive change in film crystallinity (See Figure S7).

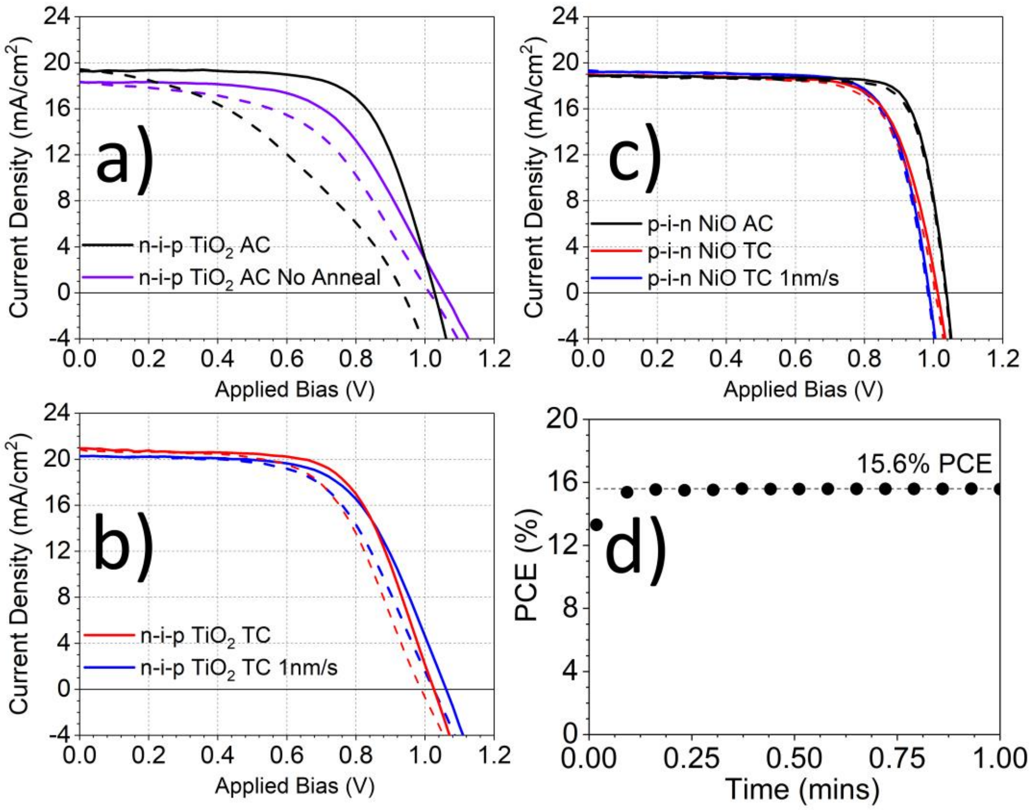

Figure 4: *Current-Voltage sweeps for champion standard (n-i-p) and inverted (p-i-n) PSCs with AC and TC perovskite active layers. a) n-i-p with TiO_2 ETM and AC perovskite. b) n-i-p with TiO_2 ETM and TC perovskite. c) p-i-n with NiO HTM with AC and TC perovskite. Part a) also contains a champion n-i-p PSC without any anneal during fabrication (purple). For both architectures, PSCs with a TC perovskite and high rate of metal oxide evaporation (1 nm/s) are also included (blue). Dotted lines represent forward sweeps and solid lines represent reverse sweeps. d) A stabilised efficiency output for champion 15.8 % p-i-n with reactive e-beam deposited NiO and AC active layer.*

	p-i-n NiO AC	**p-i-n NiO TC**	**p-i-n NiO 1 nm/s TC**	**n-i-p TiO2 AC**	**n-i-p TiO2 TC**	**n-i-p TiO2 1 nm/s TC**	**n-i-p TiO2 AC no Anneal**
PCE [%]	15.8	14.0	14.2	13.6	13.9	13.5	11.3
J_{SC} [mA/cm^2]	18.9	18.9	19.2	19.3	20.9	20.3	18.3
V_{OC} [V]	1.04	1.01	0.99	1.03	1.03	1.06	1.05
FF [%]	80.5	73.0	74.8	68.6	64.8	62.5	58.4

Table 2: *Performance metrics for champion p-i-n and n-i-p PSCs given in Figure 4.*

In Figure 4 we present current-voltage curves of our champion PSCs. Here n-i-p architecture PSCs are prepared with the TiO_2 exposed to a UVO for 15 minutes before the deposition of either AC or TC perovskites, with the perovskite films then annealed at 100 °C for 60 minutes. Both AC and TC perovskites were also processed in p-i-n architecture with an NiO HTM. Here UVO treatment was not applied to the NiO, and after TC perovskite deposition the devices were annealed under vacuum at 80 °C (with AC perovskite annealed at 100 °C). We also make use of a multi-layer encapsulation technique, which we have previously demonstrated to increase and stabilise the photocurrent of AC based inverted PSCs.[57] We present the performance metrics of all PSCs discussed in Table 2. Here, standard n-i-p PSCs (Figures 4a and 4b) and inverted p-i-n PSCs (Figure 4c) achieve a maximum PCE of 13.9 % and 15.8 % respectively. We find that the champion PSC using NiO has an impressive FF of 80 %, although the J_{SC} is below 19 mA/cm^2.

Previous reports on inverted PSCs utilising NiO as a HTM have shown that the choice of solvent and perovskite stoichiometry (particularly the DMSO:PbI_2 ratio), is critical in creating large, columnar perovskite crystal grains.[58] We expect that further optimisation of the perovskite deposition process on NiO fabricated by reactive e-beam is likely to lead to further increases in photocurrent in our inverted PSCs. Furthermore, we note that our champion PSCs did not achieve V_{OC} values exceeding 1.06 V; a result that may be consistent with a preferential orientation as suggested by XRD measurements. We expect that selective doping of the nickel source with either cobalt, magnesium or copper may offer a route to increase the V_{OC} of inverted PSCs by lowering the NiO valence band energy.[14,20,28,59]

Our measurements suggest that devices containing a TiO_2 ETM are characterised by high series resistance that limits the FF and PCE. Here such effects may either result from a lack of oxygen vacancies (required for n-type doping) as indicated by the XPS measurements, or may originate from the largely amorphous nature of the TiO_2. It is apparent that the UVO exposure used considerably improves the performance of such devices, and we believe that additional (low-temperature) surface treatments of reactive e-beam deposited TiO_2 may allow us to achieve some additional crystallization of the TiO_2 and further improve its conductivity. Further tuning of the density of oxygen vacancies by optimising the reactive evaporation deposition conditions may also result in a reduction in the electronic barrier to electron extraction.

We have also used our process to explore the rate at which metal oxide films can be deposited and still retain their electronic functionality. Here, NiO and TiO_2 layers were fabricated at a high deposition rate of 1 nm/s, with such films then used as charge-extraction layers in PSC devices incorporating a TC perovskite. The current-voltage curves of champion PSCs with these rapidly deposited metal oxides are shown in Figures 4b and 4c, with accompanying device metrics presented in Table 2 (averages and standard deviation are listed in Table S1). We find that PSCs incorporating rapidly deposited metal oxides have PCEs that are equivalent to those obtained with slowly deposited metal oxides. This suggests that the deposition of metal oxides via reactive e-beam is compatible with a high-speed R2R manufacture process.

Finally, we have explored whether it is possible to fabricate PSC devices by removing all annealing steps in the device fabrication route entirely. Figure 4a presents a J-V curve of a standard architecture PSC incorporating a 10 nm thick largely amorphous TiO_2 ETM, and an AC $MAPbI_3$ perovskite that was not thermally annealed. Using this route, we achieve a reasonable device PCE of 11.3 %.

Conclusions

We have used a reactive electron-beam evaporation process to deposit two different metal oxides from a metal source material under a low partial pressure of oxygen. We find that NiO and TiO_2 deposited using this technique can be used to efficiently extract charge from perovskite solar cells, realising peak efficiencies of 15.8 % for inverted structure PSCs using a NiO HTM, and 13.9 % for standard structure PSCs using a TiO_2 ETM. We show that control of deposition parameters, choice of perovskite annealing routine and the use of UV-ozone treatment applied to the metal oxides affects the performance metrics of the PSCs created. Critically, our low-temperature deposition process is compatible with sensitive, flexible polymeric substrates, as we demonstrate that reactive electron-beam deposited metal oxides do not need high temperature annealing to function as effective charge-transporting materials. Our work suggests therefore that metal oxide films can be deposited quickly, ensuring that the process is compatible with high throughput roll-to-roll manufacturing. Indeed, we have recently found that this technique can be successfully implemented onto flexible PET substrates.[60] It is an open question as to whether metal oxide films prepared using this rapid processing method have similar adhesion properties compared to comparable materials prepared using more conventional deposition techniques. Indeed, our future work will address this issue, and will determine the extent to which such materials can be used in more demanding applications in which device stability is limited by thin-film mechanical properties and delamination effects.

Acknowledgments: This work was funded by the UK Engineering and Physical Sciences Research Council (EPSRC) via grants EP/M025020/1 'High resolution mapping of performance and degradation mechanisms in printable photovoltaic devices' and EP/M014797/1 'Improved Understanding, Development and Optimization of Perovskite-based Solar Cells', and EP/I032541/1 'Solar Energy in Future Societies'. We also thank the U.K. EPSRC for PhD studentships via the University of Sheffield DTG account (T.R., J.B) and from the Centre for Doctoral Training in New and Sustainable PV, EP/L01551X/1 (M.S., J.S., B.F.). XPS analysis was performed in the Sheffield Surface Analysis Centre.

Conflict of Interest: D.G.L. and A.R.B. are co-directors of the company Ossila Ltd that retail materials used in perovskite photovoltaic research. T.M. is an employee of PowerRoll Ltd who are developing solar cell technology based on perovskites and metal oxides.

6.2: Additional Discussion and Supplementary Information

Original Supplementary Information

Experimental methods:

Device fabrication

Materials – All materials were purchased from Sigma Aldrich unless otherwise stated. All solvents are anhydrous unless otherwise stated. All dry powders were stored in a N_2 glovebox antechamber.

Cleaning & Substrate Preparation – Patterned Tec 20 indium tin oxide (ITO) glass (Ossila) with 8 cells per substrate were cleaned by sonication in dilute 2 % Hellmanex solution, followed by dump rinsing in DI water and then sonication in isopropyl alcohol (IPA) for 15 minutes. Substrates were dried with N_2 and then UV-Ozone cleaned for 15 minutes to remove final organic residues prior to subsequent layer deposition. ITO substrates were then moved into an electron beam evaporation system inside a N_2 glovebox and pumped down to pressures not exceeding $2x10^{-6}$ mbar. An evaporation mask was used such that the metal oxides were deposited over the patterned ITO active area, but not on the ITO contacts. A quartz crystal microbalance was used to monitor the rate and thickness of each metal oxide deposition.

Reactive Oxide deposition – Nickel and titanium pellets were purchased from Kurt Lesker (¼ by ¼ inch, 99.995 % purity). For deposition, Ni pellets were placed directly in a copper hearth, while titanium pellets were placed inside a carbon crucible. The deposition sources were first preconditioned through a long, high power electron beam exposure using a wide sweep pattern. This created a pool of melted metal that was free from initial oxide impurities. During deposition, O_2 was first fed into the chamber at a partial pressure between from $5x10^{-5}$ to $1.9\ x10^{-4}$ mbar. During evaporation the O_2 flow rate was maintained at the chosen constant partial pressure and substrates were rotated at approximately 10 rpm. Evaporation of the metal oxides was performed using a smaller electron beam pattern, at rates ranging from 0.3 to 10 Å/s, creating a 10 nm (unless otherwise stated) transparent film.

Triple Cation Perovskite (TC) – Triple-cation perovskites having a composition $CsI_{0.05}((FAPbI_3)_{0.83}(MAPbBr_3)_{0.17})_{0.95}$ were deposited from solution via the one-step antisolvent quenching method. The solution was prepared with 1 ml of mixed solvent (anhydrous n,n-dimethylformamide: dimethyl sulfoxide (DMF:DMSO) 4:1 volume ratio) containing formamidinium iodide, (FAI, 1 M, Greatcell), methylammonium bromide (MABr, 0.2 M, Greatcell), lead(II) iodide, (PbI_2, 1.1 M, TCI) and lead(II) bromide ($PbBr_2$, 0.2 M, TCI) which was heated at 70 °C and intermittently vortex mixed for around 30 minutes before adding 50 µl/ml of caesium iodide (CsI) in DMSO (1.5M concentration). This solution was filtered through a 0.2 µm PTFE filter before being spin coated at 1000 rpm for 10 seconds then 6000 rpm for 20 seconds. 100 µl of chlorobenzene (CB) was then rapidly dripped on the film surface 5 seconds before the end of the program. Films were annealed at 80 °C for 60 minutes inside a vacuum chamber or at 100 °C for 60 minutes in a N_2 atmosphere.

Acetonitrile Perovskite (Ac) – Methylamine bubbled acetonitrile perovskite solutions with composition $MAPbI_3$ were deposited via dynamic spin coating. A 0.5M suspension was prepared using 4 – 10 ml of anhydrous acetonitrile containing PbI_2 and methylammonium iodide (MAI, Greatcell) at a ratio of 1:1.06. The black suspension of powder in acetonitrile was then bubbled with dry methylamine to create a clear-yellow solution, as first demonstrated by Noel *et al.*[50] This solution was then filtered through a 0.2 µm PTFE filter before spin coating at 4000 rpm for 30 seconds. Films were annealed at 100°C for 60 minutes in a N_2 atmosphere.

$PC_{60}BM$/BPhen/Ag (*p-i-n* only) – a [6,6]-phenyl-C61-butyric acid methyl ester ($PC_{60}BM$) solution (Ossila, 30 mg/ml in CB) which had been stirred overnight at 70 °C and then left to cool was filtered through a 0.2 µm PTFE filter before spin coating at 4000 rpm onto the perovskite film for 20 seconds. The substrates were annealed for 10 minutes at 90 °C in a N_2 filled glovebox. After cooling, a bathophenanthroline (Bphen) solution (0.5 mg/ml in IPA) was spin coated at 6000 rpm onto the substrates for 20 s. Devices were patterned using razor blade to allow contact to the

ITO as required. Devices were completed by thermally evaporating a 100 nm Ag contact onto the surface of the Bphen.

Spiro-OMeTAD/Au (*n-i-p* only) – a 2,2',7,7'-Tetrakis[N,N-di(4-methoxyphenyl)amino]-9,9'-spirobifluorene (spiro-OMeTAD) solution (Ossila, 86 mg/ml in CB) was prepared with each ml additionally containing 34 µl of 4-tert-butyl-pyridine (tBP, 96.6%), 20 µl of lithium bis(trifluoromethanesulfonyl)imide (Li-TFSI, 500 mg/ml in acetonitrile) and 11 µl of tris(2-(1H-pyrazol-1-yl)-4-tert-butylpyridine)cobalt(II) di[hexafluorophosphate] (FK 209 Co(II) PF6, Dyesol, 300 mg/ml in acetonitrile). The solution was vortex mixed until dissolved and filtered through a 0.2 µm PTFE filter before being spin coated at 4000 rpm onto the perovskite films for 30 seconds. Devices were left in a dark, dry desiccant chamber overnight and patterned using a razor blade to allow contact to the ITO as required. Devices were completed by thermally evaporating 80 nm Au patterned contacts onto the surface of the spiro-OMeTAD.

Device Encapsulation – Inverted p-i-n Devices were encapsulated as detailed in our previous work,[57] using a layer of polyvinylpyrrolidone, UV curable epoxy and a glass cover slip.

Device and Film Characterisation

AFM – An Asylum Research MFP 3D scanning probe microscope was used in AC mode with Bruker TESPA-V2 cantilevers (f_0 : 320 kHz and k: 42 N/m) for imaging. Typical scanning parameters included a scan rate of 0.5 – 1 Hz with 256 scan points/line.

XRD – X-ray diffraction data was collected on a Cu Kα Bruker D8 ADVANCE X-ray powder diffractometer. The instrument was fitted with a motorised variable slit optic set to 0.3° opening and a high-resolution energy-dispersive Lynxeye XE detector. Scans of 100 nm metal oxide films on quartz, along with a quartz reference were collected at room temperature between 20° - 70° 2θ, using a step size of 0.04° and step time of 12 s giving a total exposure time of 3.5 or 4.5 h.

XPS **-** The ITO substrates coated with NiO and TiO_2 before and after UVO treatment were mounted onto the sample holder with double sided carbon tape. For XPS analysis the samples were considered insulating despite their conductive coating as no path was made between the uppermost surface and the sample mount, so charge neutralisation was used. XPS analysis was performed using a Kratos Supra instrument with a monochromated aluminium source, with two analysis points taken per sample, each of area 700 μm by 300 μm. Survey scans were collected between 1200 to 0 eV binding energy, at 160 eV pass energy, 1 eV intervals, and 300 seconds/sweep with one sweep being collected. High-resolution O 1s, C 1s, Ni 2p or Ti 2p XPS spectra, and Ni LMM Auger spectra, were also collected at 20 eV pass energy and 0.1 eV intervals for each analysis point over an appropriate energy range, with one 300 second sweep for all spectra except the Ni LMM Auger which - given the extended eV range necessary - was collected for 450 seconds. The data collected was calibrated in intensity using a transmission function characteristic of the instrument (determined using software from The National Physical Laboratory) to make the values instrument independent. The data was then quantified using theoretical Schofield relative sensitivity factors. All high-resolution spectra were calibrated in units of eV by fixing the main C 1s peak to be 285.0 eV.

UV-Vis Transmission – An Ocean Optics DH-2000-BAL UV-VIS-NIR light source and HR2000+ES spectrometer were used to determine transmission of metal oxide films deposited onto quartz coated glass. The optical band gaps were determined by first calculating the absorption coefficient α (assuming zero reflection and interference) on 100 nm thick film using the Beer-Lambert law. This allowed a Tauc plot of $(\alpha h\upsilon)^2$ $[1/(cm^2\ eV^2)]$ against hυ (eV) to be constructed.

Ellipsometry – Ellipsometry was performed using a spectroscopic ellipsometer (M2000v, J. A. Woollam Co., USA). Nickel oxide and titanium dioxide were deposited onto silicon substrates with a 410-420 nm thermal oxide (Ossila). Ψ, the ratio of the amplitude of incident and reflected light, and Δ, the ratio of the phase lag between incident and reflected light, were recorded over a wavelength range of 370 to 1000 nm. The metal oxide was considered to be homogeneous and the film had negligible absorbance across this range, and hence low extinction coefficients (k). As such, we were able to determine the thickness using a Cauchy model. The model was then used to extract the refractive index (n) of the film. The resultant fits for nickel oxide and titanium dioxide had mean square errors (MSEs) of 4.4 and 11.5 respectively.

Device Characterisation – Device performance metrics were determined in air using a Newport 92251A-1000 solar simulator, calibrated against an NREL certified silicon reference cell to an intensity of 100 mW/cm^2. Devices were illuminated through a 0.0256 cm^2 aperture mask. J-V curves were obtained using a Keithley 237 source measure unit, sweeping the applied bias at 0.4 V/s from 0.0 V to +1.2 V and 1.2 V to 0 V. The stabilised power output was measured by holding devices at their V_{mpp}. For all tables and boxplots, a minimum of 24 pixels were tested to determine average efficiency and standard deviation.

Supplementary Figures and Table

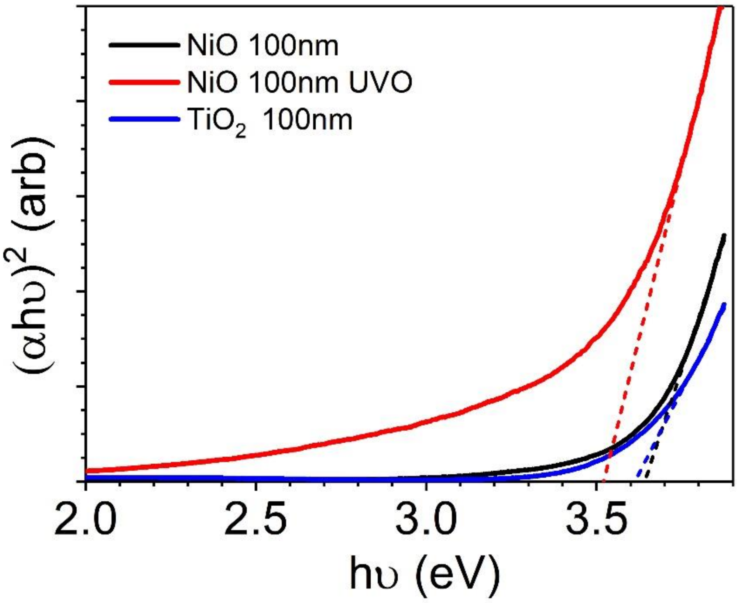

Figure S1: *Tauc plots taken from transmission spectra for 100 nm reactive e-beam deposited NiO (black) and TiO_2 (blue) films, and NiO films after UVO treatment (red).*

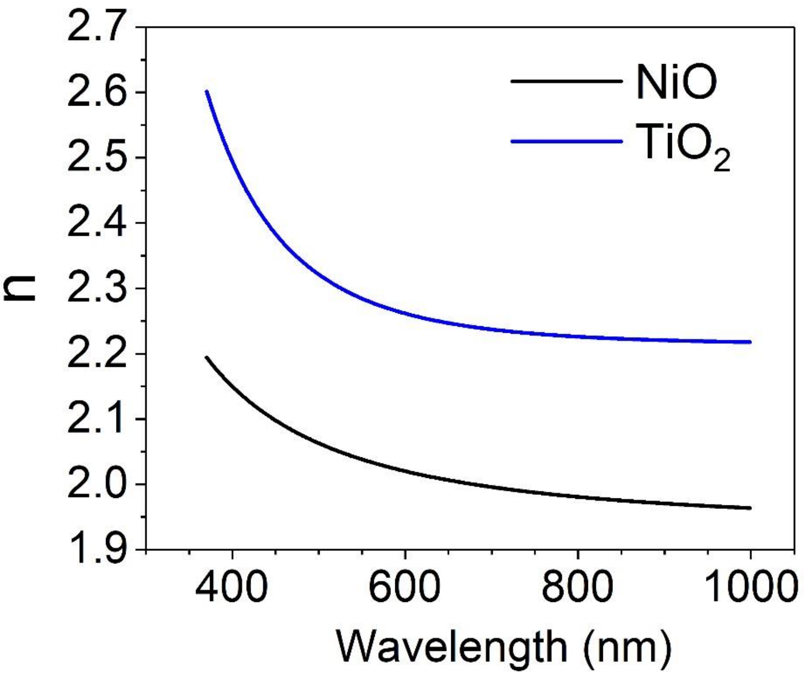

Figure S2: *Refractive index (n) data between 370-1000 nm (1.24-3.35 eV) for 10 nm of reactive e-beam deposited NiO (black) and TiO_2 (blue), both deposited at 1 Å/s under a O_2 partial pressure of $1x10^{-4}$ mbar on top of a silicon oxide/silicon wafer.*

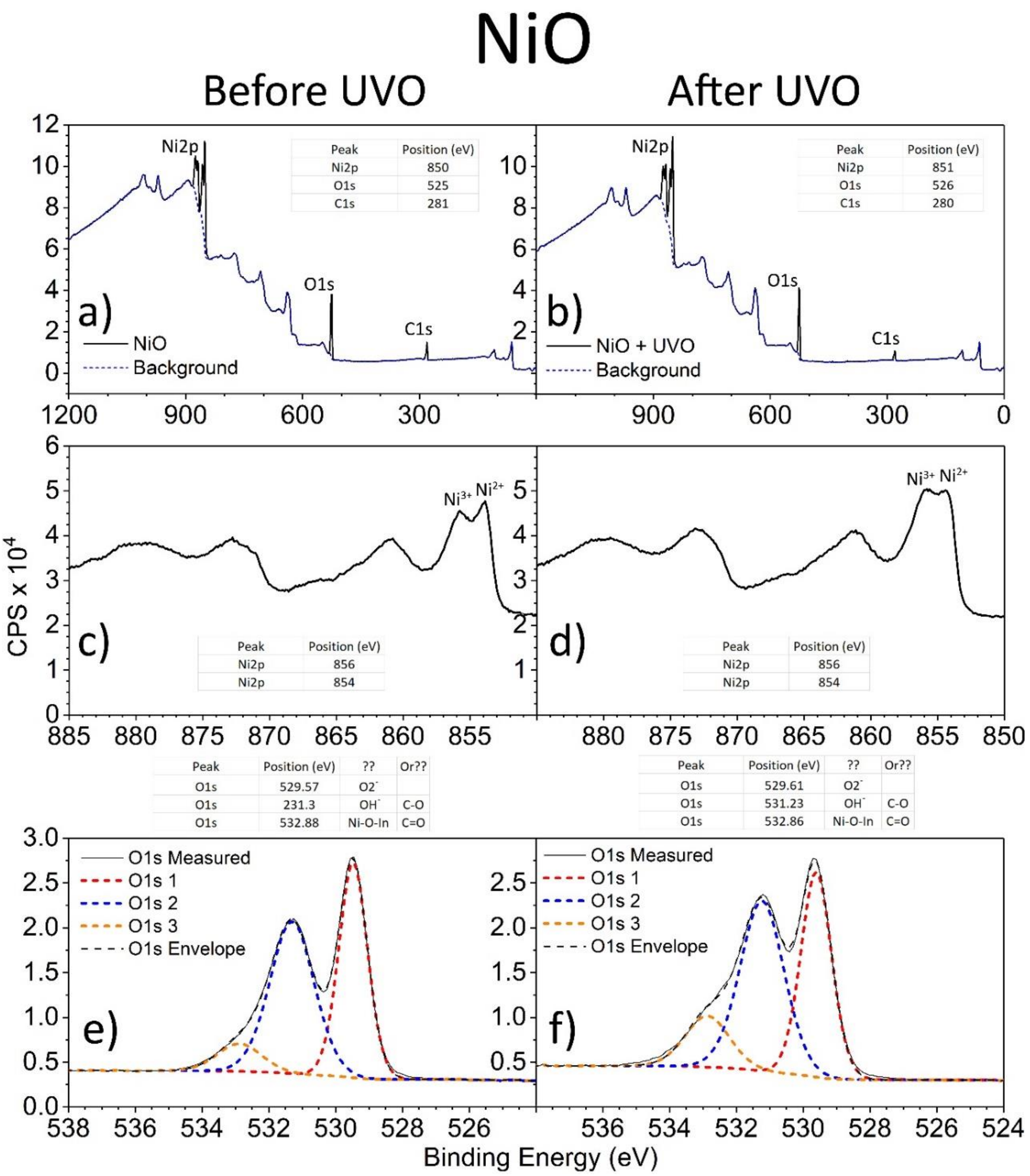

Peak	Position (eV)
Ni2p	850
O1s	525
C1s	281

Peak	Position (eV)
Ni2p	851
O1s	526
C1s	280

Peak	Position (eV)
Ni2p	856
Ni2p	854

Peak	Position (eV)
Ni2p	856
Ni2p	854

Peak	Position (eV)	??	Or??
O1s	529.57	$O2^-$	
O1s	231.3	OH^-	C-O
O1s	532.88	Ni-O-In	C=O

Peak	Position (eV)	??	Or??
O1s	529.61	$O2^-$	
O1s	531.23	OH^-	C-O
O1s	532.86	Ni-O-In	C=O

Figure S3: *XPS of NiO films before and after 15 minutes of UVO treatment. Solid black lines are measured sample. a) and b) are survey scans of NiO with background signal shown as dashed blue line, c) and d) high-resolution spectra of Ni2p peaks, and e) and f) high-resolution spectra of O1s peaks. O1s is characterised by 3 fitted component curves (red, blue, and orange dashed line), which are summed to make an envelope of fitted measured data (dashed black line). Inset tables list the peak positions and any well-known identification of those peaks obtained from literature.*

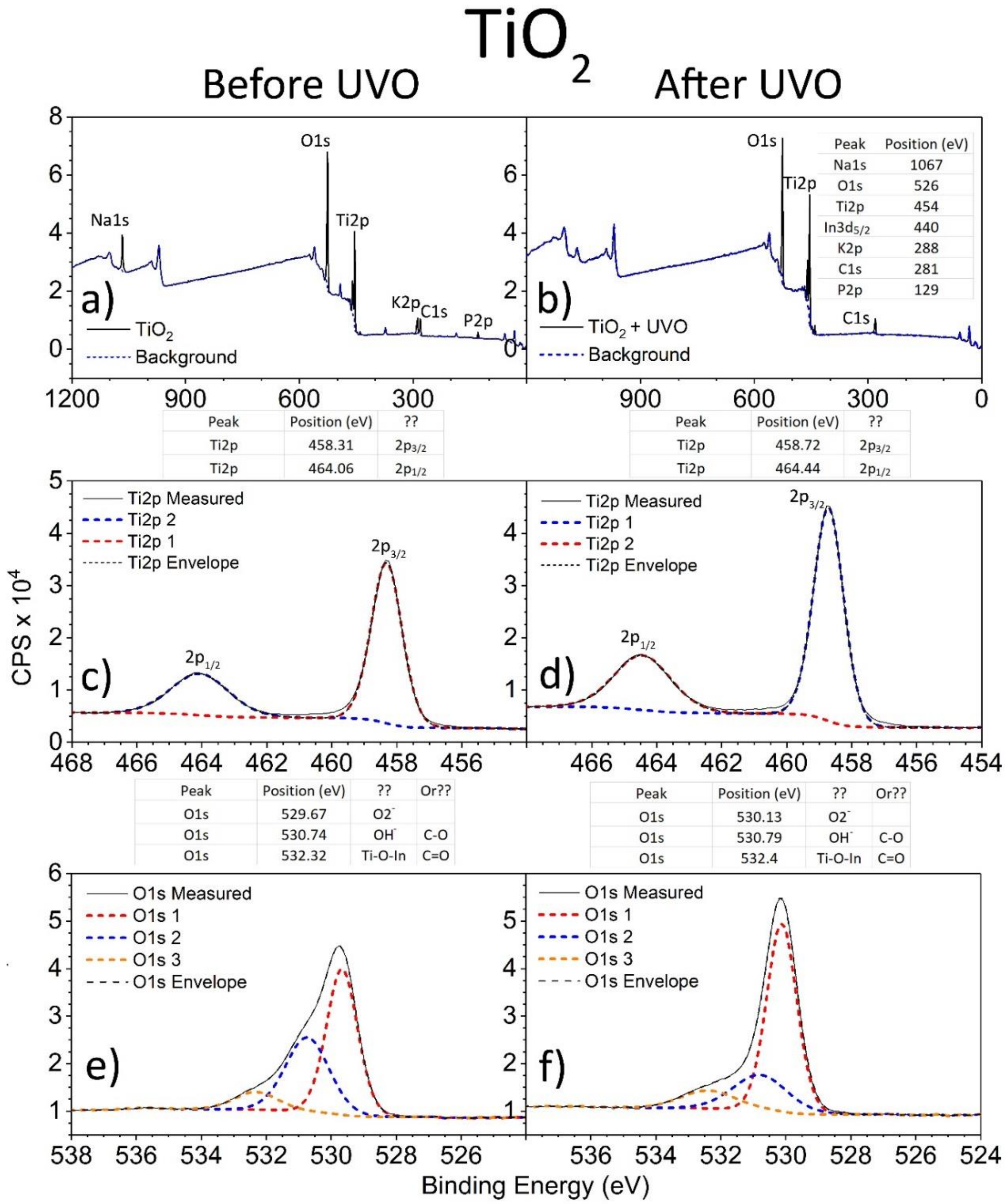

Peak	Position (eV)
Na1s	1067
O1s	526
Ti2p	454
In3d$_{5/2}$	440
K2p	288
C1s	281
P2p	129

Peak	Position (eV)	??
Ti2p	458.31	2p$_{3/2}$
Ti2p	464.06	2p$_{1/2}$

Peak	Position (eV)	??
Ti2p	458.72	2p$_{3/2}$
Ti2p	464.44	2p$_{1/2}$

Peak	Position (eV)	??	Or??
O1s	529.67	O2$^-$	
O1s	530.74	OH$^-$	C-O
O1s	532.32	Ti-O-In	C=O

Peak	Position (eV)	??	Or??
O1s	530.13	O2$^-$	
O1s	530.79	OH$^-$	C-O
O1s	532.4	Ti-O-In	C=O

FigureS4: *XPS of TiO$_2$ films before and after 15 minutes of UVO treatment. Solid black lines are measured sample. a) and b) are survey scans of TiO$_2$ with background signal shown as dashed blue line, c) and d) high-resolution spectra of Ti2p peaks, and e) and f) high-resolution spectra of O1s peaks. Ti2p is characterised by 2 fitted component curves (red, blue corresponding to 2p$_{3/2}$ and 2p$_{1/2}$ respectively), O1s is characterised by 3 fitted component curves (red, blue, and orange dashed line). These components are summed to make an envelope of fitted measured data (dashed black line). Inset tables list the peak positions and any well-known identification of those peaks obtained from literature.*

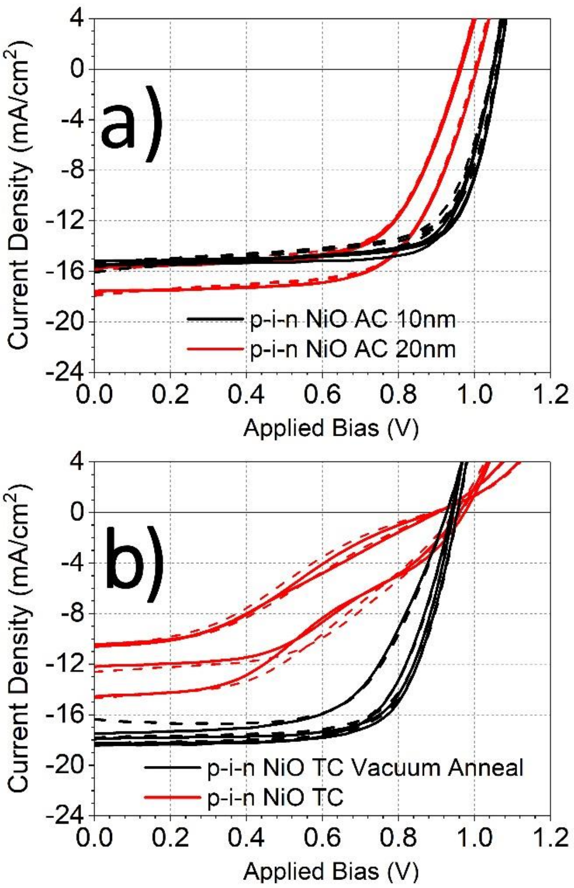

Figure S5: *Current-voltage sweeps for PSCs with reactive e-beam deposited NiO HTM with a) 10 nm (black) and 20 nm (red) of NiO (deposited at 1 Å/s) with an AC* $MAPbI_3$ *active layer. b) 10nm of NiO deposited at a rate of 1 Å/s with a TC active layer, converted using a 100* °C *(red) or alternative 80* °C *vacuum (black) perovskite anneal. Dotted lines represent forward sweeps and solid lines represent reverse sweeps.*

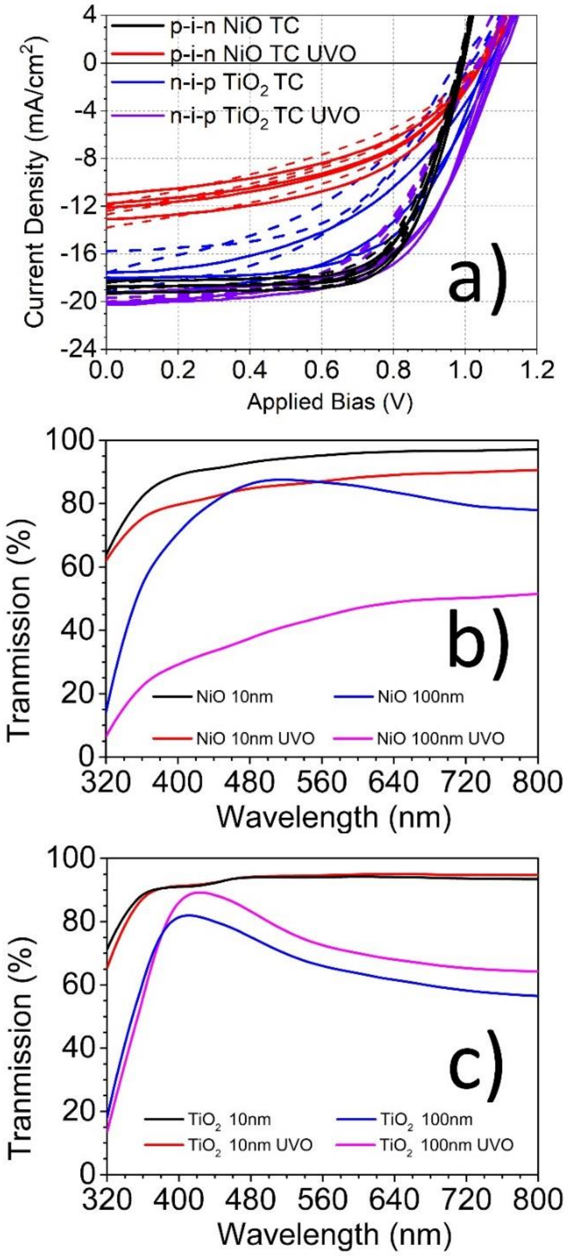

Figure S6: *a) Current-voltage sweeps for p-i-n (black, red) and n-i-p (blue, purple) PSCs with 10 nm of reactive e-beam deposited NiO HTM and TiO_2 ETM respectively, using a TC $CsI_{0.05}((FAPbI_3)_{0.83}(MAPbBr_3)_{0.17})_{0.95}$ active layer. The perovskite precursor is either deposited directly onto the metal oxides (black, blue) or treated with UV-Ozone for 15 minutes (red, purple) prior to deposition of the perovskite. Dotted lines represent forward sweeps and solid lines represent reverse sweeps. b) Transmission spectra of 10 nm (black, red) and 100 nm (blue, purple) of NiO as deposited (black, blue), or with 15 minutes UVO treatment (red, purple). c) Transmission spectra of 10 nm (black, red) and 100 nm (blue, purple) of TiO_2 as deposited (black, blue), or with 15 minutes UVO treatment (red, purple).*

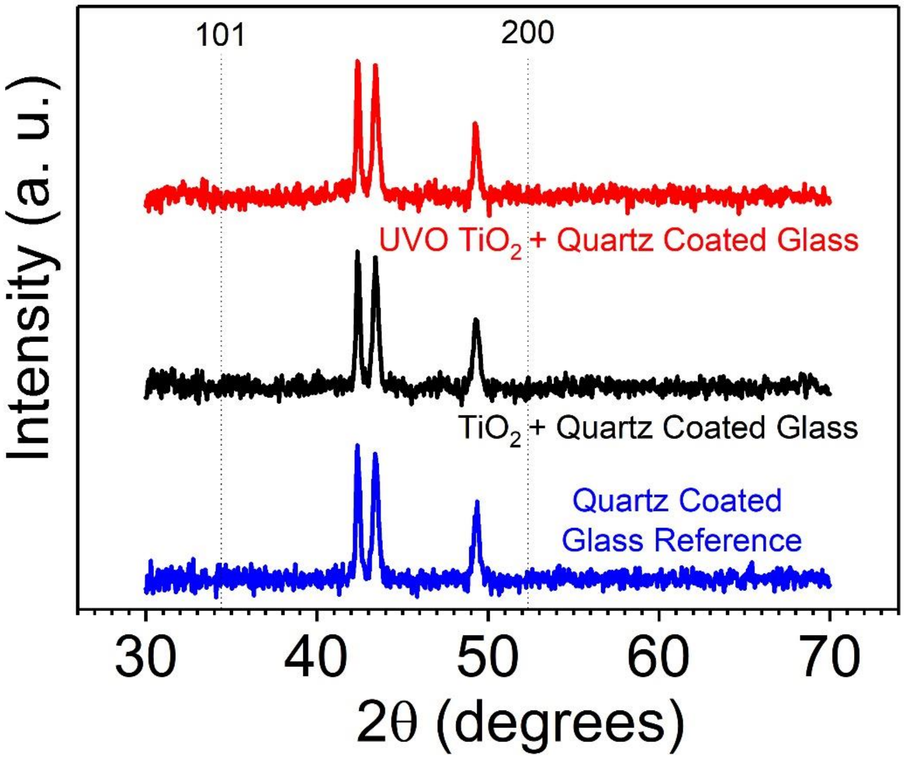

Figure S7: *X-ray diffraction patterns of 100nm thick TiO$_2$ films deposited onto quartz coated glass using the reactive e-beam process, before (black) and after (red) UVO treatment.*

O_2 Pressure [mbar]	Rate of evaporation [Å/s]			O_2 Pressure [mbar]	Rate of evaporation [Å/s]		
NiO							
PCE	**0.5**	**1.5**	**10**	**J_{SC}**	**0.5**	**1.5**	**10**
$1.9x10^{-4}$	12.3 ± 0.5	11.1 ± 0.9	12.9 ± 0.7	**$1.9x10^{-4}$**	18.2 ± 0.2	16.7 ± 1.1	18.9 ± 0.2
$1x10^{-4}$	12.9 ± 1.0	12.3 ± 0.9		**$1x10^{-4}$**	18.6 ± 0.6	18.8 ± 0.4	
$5x10^{-5}$	12.9 ± 0.4	12.1 ± 0.5		**$5x10^{-5}$**	17.9 ± 0.5	17.9 ± 0.4	
FF	**0.5**	**1.5**	**10**	**V_{OC}**	**0.5**	**1.5**	**10**
$1.9x10^{-4}$	67.5 ± 3.0	66.8 ± 3.9	71.8 ± 2.8	**$1.9x10^{-4}$**	1.00 ± 0.01	0.99 ± 0.01	0.95 ± 0.02
$1x10^{-4}$	69.7 ±4.2	66.8 ± 2.6		**$1x10^{-4}$**	0.99 ± 0.02	0.98 ± 0.03	
$5x10^{-5}$	69.3 ± 1.5	68.2 ± 3.9		**$5x10^{-5}$**	1.04 ± 0.01	0.99 ± 0.01	
TiO_2							
PCE	**0.5**	**2**	**10**	**J_{SC}**	**0.5**	**2**	**10**
$1.9x10^{-4}$	12.6 ± 1.1	11.9 ± 0.6	12.1 ± 1.0	**$1.9x10^{-4}$**	19.7 ± 1.06	20.0 ±0.5	19.2 ± 0.9
$1x10^{-4}$	8.9 ± 3.0	11.0 ± 0.7		**$1x10^{-4}$**	18.6 ±1.8	19.5 ± 0.6	
$5x10^{-5}$	12.1 ± 0.2	12.1 ± 0.8		**$5x10^{-5}$**	20.0 ± 0.3	20.0 ± 0.3	
FF	**0.5**	**2**	**10**	**V_{OC}**	**0.5**	**2**	**10**
$1.9x10^{-4}$	62. 5± 2.0	57.9 ± 1.4	60 ± 1.9	**$1.9x10^{-4}$**	1.02 ± 0.03	1.03 ± 0.02	1.04 ± 0.02
$1x10^{-4}$	46.0 ±10.2	54.9 ± 2.1		**$1x10^{-4}$**	1.04 ± 0.02	1.03 ± 0.03	
$5x10^{-5}$	58.2 ± 0.8	59.8 ± 1.7		**$5x10^{-5}$**	1.04 ± 0.01	1.01 ± 0.04	

Table S1: *Matrix of performance metrics (average ± standard deviation) for p-i-n and n-i-p PSCs with reactive e-beam deposited NiO HTM and* TiO_2 *ETM respectively, using an 80 °C vacuum anneal for a TC* $CsI_{0.05}((FAPbI_3)_{0.83}(MAPbBr_3)_{0.17})_{0.95}$ *perovskite active layer. The matrix is comprised of different* O_2 *partial pressures:* $5x10^{-5}$ *mbar,* $1x10^{-4}$ *and 1.9* $x10^{-4}$ *mbar and low (0.5 Å/s) and high (1.5 Å/s for NiO and 2 Å/s for* TiO_2*) evaporation rates for the metal oxides.*

Additional Discussion

To confirm the photocurrent of the champion 15.8 % PCE p-i-n ITO/NiO/$MAPbI_3$/$PC_{60}BM$/BPhen/Ag PSC, an external quantum efficiency (EQE) measurement was also performed. This EQE measurement is presented in Figure S7, where the integrated J_{SC} is found to be 18.5 mA/cm^2. As stated in the main chapter, the J_{SC} is lower for inverted architecture PSCs compared to n-i-p standard architecture PSCs, and only reached values approaching 19 mA/cm^2 by utilising the multilayer encapsulation technique discussed in Chapter 5.

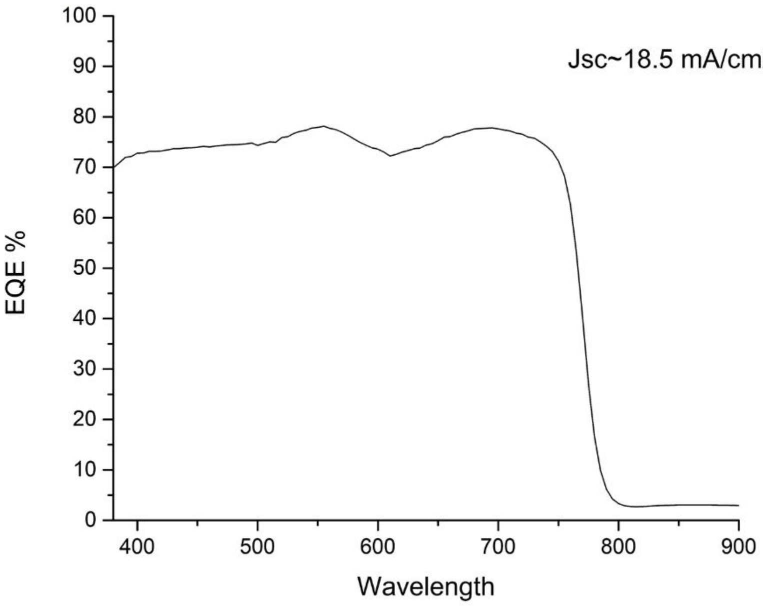

Figure S7: *External quantum efficiency (EQE) champion for p-i-n PSCs with reactive e-beam deposited NiO HTL and AC $MAPbI_3$ layer.*

6.3: Further Context

The process described in this chapter is reproducible, roll-to-roll compatible, and applicable inside and beyond the scientific photovoltaic community. This report is a proof on concept for reactive evaporation deposition of NiO and TiO_2 that could be used in a variety of thin-film electronic devices architectures. This reactive process has also been successfully performed in a commercial roll-to-roll deposition system (Power Roll), however, providing details of this roll-to-roll deposition and the financial cost-model is outside the scope of this thesis.

The rapid and scalable reactive e-beam deposition developed here was also used in the work described in Chapter 7, where NiO was directly deposited onto a flexible polymeric substrate. Electron-beam evaporated TiO_2 also has the potential to be deposited into groove back-contact solar cells using similar techniques.

6.4: References

[1] M. Stolterfoht, C. M. Wolff, Y. Amir, A. Paulke, L. Perdigón-Toro, P. Caprioglio, D. Neher, *Energy Environ. Sci.* **2017**, *10*, 1530.

[2] M. Abdi-Jalebi, Z. Andaji-Garmaroudi, S. Cacovich, C. Stavrakas, B. Philippe, J. M. Richter, M. Alsari, E. P. Booker, E. M. Hutter, A. J. Pearson, S. Lilliu, T. J. Savenije, H. Rensmo, G. Divitini, C. Ducati, R. H. Friend, S. D. Stranks, *Nature* **2018**, *555*, 497.

[3] Z. H. Bakr, Q. Wali, A. Fakharuddin, L. Schmidt-Mende, T. M. Brown, R. Jose, *Nano Energy* **2017**, *34*, 271.

[4] L. Calió, S. Kazim, M. Grätzel, S. Ahmad, *Angew. Chemie Int. Ed.* **2016**, 2.

[5] S. Ameen, M. A. Rub, S. A. Kosa, K. A. Alamry, M. S. Akhtar, H. S. Shin, H. K. Seo, A. M. Asiri, M. K. Nazeeruddin, *ChemSusChem* **2016**, *9*, 10.

[6] M. Wong-Stringer, J. E. Bishop, J. A. Smith, D. K. Mohamad, A. J. Parnell, V. Kumar, C. Rodenburg, D. G. Lidzey, *J. Mater. Chem. A* **2017**, *5*, 15714.

[7] D. Wang, M. Wright, N. K. Elumalai, A. Uddin, *Sol. Energy Mater. Sol. Cells* **2016**, *147*, 255.

[8] J. Sun, J. Lu, B. Li, L. Jiang, A. S. R. Chesman, A. D. Scully, T. R. Gengenbach, Y. B. Cheng, J. J. Jasieniak, *Nano Energy* **2018**, *49*, 163.

[9] W. Chen, Y. Wu, Y. Yue, J. Liu, W. Zhang, X. Yang, H. Chen, E. Bi, I. Ashraful, M. Grätzel, L. Han, *Science.* **2015**, *350*, 944.

[10] S. Sajid, A. M. Elseman, H. Huang, J. Ji, S. Dou, H. Jiang, X. Liu, D. Wei, P. Cui, M. Li, *Nano Energy* **2018**, *51*, 408.

[11] Y. Lv, P. Xu, G. Ren, F. Chen, H. Nan, R. Liu, D. Wang, X. Tan, X. Liu, H. Zhang, Z.-K. Chen, *ACS Appl. Mater. Interfaces*, **2018**, *10, 28,* 23928-23937.

[12] H. Lee, Y. T. Huang, M. W. Horn, S. P. Feng, *Sci. Rep.* **2018**, *8*, 1.

[13] J. You, L. Meng, T. Bin Song, T. F. Guo, W. H. Chang, Z. Hong, H. Chen, H. Zhou, Q. Chen, Y. Liu, N. De Marco, Y. Yang, *Nat. Nanotechnol.* **2016**, *11*, 75.

[14] K. Yao, F. Li, Q. He, X. Wang, Y. Jiang, H. Huang, A. K. Y. Jen, *Nano Energy* **2017**, *40*, 155.

[15] M. Najafi, F. Di Giacomo, D. Zhang, S. Shanmugam, A. Senes, W. Verhees, A. Hadipour, Y. Galagan, T. Aernouts, S. Veenstra, R. Andriessen, *Small* **2018**, *14*, 1.

[16] I. Senain, N. Nayan, H. Saim, *Int. J. Integr. Eng.* **2010**, *2*, 29.

[17] D. Bi, W. Tress, M. I. Dar, P. Gao, J. Luo, C. Renevier, K. Schenk, A. Abate, F. Giordano, J.-P. Correa Baena, J.-D. Decoppet, S. M. Zakeeruddin, M. K. Nazeeruddin, M. Grätzel, A. Hagfeldt, *Sci. Adv.* **2016**, *2*, e1501170.

[18] B. Mustafa, J. Griffin, A. S. Alsulami, D. G. Lidzey, A. R. Buckley, *Appl. Phys. Lett.* **2014**, *104*, 5.

[19] S. Yue, K. Liu, R. Xu, M. Li, M. Azam, K. Ren, J. Liu, Y. Sun, Z. Wang, D. Cao, X. Yan, S. Qu, Y. Lei, Z. Wang, *Energy Environ. Sci.* **2017**, *10*, 2570.

[20] J. W. Jung, C. C. Chueh, A. K. Y. Jen, *Adv. Mater.* **2015**, *27*, 7874.

[21] I. Sta, M. Jlassi, M. Hajji, H. Ezzaouia, *Thin Solid Films* **2014**, *555*, 131.

[22] J. Jeng, K. Chen, T. Chiang, P. Lin, T. Tsai, Y. Chang, T. Guo, P. Chen, T. Wen and Y. Hsu, *Adv. Mater.*, 2014, **26,** 4107–4113.

[23] W. Lai, K. Lin, T. Guo and J. Lee, *IEEE Trans. Electron Devices*, 2015, **62**, 1590–1595.

[24] W. Lai, K. Lin, Y. Wang, T. Chiang, P. Chen and T. Guo, *Adv. Mater.*, 2016, **28,** 3290–3297.

[25] J. H. Park, J. Seo, S. Park, S. S. Shin, Y. C. Kim, N. J. Jeon, H. W. Shin, T. K. Ahn, J. H. Noh, S. C. Yoon, C. S. Hwang, S. Il Seok, *Adv. Mater.* **2015**, *27*, 4013.

[26] H. L. Zhu, J. Cheng, D. Zhang, C. Liang, C. J. Reckmeier, H. Huang, A. L. Rogach, W. C. H. Choy, *ACS Nano* **2016**, *10*, 6808.

[27] U. Kwon, B. G. Kim, D. C. Nguyen, J. H. Park, N. Y. Ha, S. J. Kim, S. H. Ko, S. Lee, D. Lee, H. J. Park, *Sci. Rep.* **2016**, *6*, 1.

[28] G. Li, Y. Jiang, S. Deng, A. Tam, P. Xu, M. Wong, H. S. Kwok, *Adv. Sci.* **2017**, *4*, 1.

[29] K. Wojciechowski, M. Saliba, T. Leijtens, A. Abate, H. J. Snaith, *Energy Environ. Sci.* **2014**, *7*, 1142.

[30] D. Yang, R. Yang, J. Zhang, Z. Yang, S. Liu, C. Li, *Energy Environ. Sci.* **2015**, *8*, 3208.

[31] J. H. Noh, N. J. Jeon, Y. C. Choi, M. K. Nazeeruddin, M. Grätzel, S. Il Seok, *J. Mater. Chem. A* **2013**, *1*, 11842.

[32] K. Mahmood, S. Sarwar, M. T. Mehran, *RSC Adv.* **2017**, *7*, 17044.

[33] S. Weber, T. Rath, J. Mangalam, B. Kunert, A. M. Coclite, M. Bauch, T. Dimopoulos, G. Trimmel, *J. Mater. Sci. Mater. Electron.* **2018**, *29*, 1847.

[34] H. Zhang, J. Cheng, D. Li, F. Lin, J. Mao, C. Liang, A. K. Y. Jen, M. Grätzel, W. C. H. Choy, *Adv. Mater.* **2017**, *29*, 1.

[35] H. Zhou, Q. Chen, G. Li, S. Luo, T. Song, H.-S. Duan, Z. Hong, J. You, Y. Liu, Y. Yang, *Sci. (Washington, DC, U. S.)* **2014**, *345*, 542.

[36] Q. He, K. Yao, X. Wang, X. Xia, S. Leng, F. Li, *ACS Appl. Mater. Interfaces* **2017**, *9*, 41887.

[37] K. Yamamoto, Y. Zhou, T. Kuwabara, K. Takahashi, M. Endo, A. Wakamiya, Y. Ogomi, S. Hayase, T. Taima, in *2014 IEEE 40th Photovolt. Spec. Conf.*, IEEE, **2014**, pp. 1573–1576.

[38] C. Liang, Z. Wu, P. Li, J. Fan, Y. Zhang, G. Shao, *Appl. Surf. Sci.* **2017**, *391*, 337.

[39] W. Qiu, U. W. Paetzold, R. Gehlhaar, V. Smirnov, H. G. Boyen, J. G. Tait, B. Conings, W. Zhang, C. B. Nielsen, I. McCulloch, L. Froyen, P. Heremans, D. Cheyns, *J. Mater. Chem. A* **2015**, *3*, 22824.

[40] S. R. Pae, S. Byun, J. Kim, M. Kim, I. Gereige, B. Shin, *ACS Appl. Mater. Interfaces* ***2018, 10, 1,*** 534-540.

[41] M. F. Hossain, S. Naka, H. Okada, *J. Photochem. Photobiol. A Chem.* **2018**, *360*, 109.

[42] W. Qiu, U. W. Paetzold, R. Gehlhaar, V. Smirnov, H.-G. Boyen, J. G. Tait, B. Conings, W. Zhang, C. Nielsen, I. Mcculloch, L. Froyen, P. Heremans, D. Cheyns, *J. Mater. Chem. A* **2015**, 22824.

[43] C.-H. Wei, C.-M. Chang, *Mater. Trans.* **2011**, *52*, 554.

[44] J. Cui, F. Meng, H. Zhang, K. Cao, H. Yuan, Y. Cheng, F. Huang, M. Wang, *ACS Appl. Mater. Interfaces* **2014**, *6*, 22862.

[45] K. C. Wang, P. S. Shen, M. H. Li, S. Chen, M. W. Lin, P. Chen, T. F. Guo, *ACS Appl. Mater. Interfaces* **2014**, *6*, 11851.

[46] Z. Song, C. L. McElvany, A. B. Phillips, I. Celik, P. W. Krantz, S. C. Watthage, G. K. Liyanage, D. Apul, M. J. Heben, *Energy Environ. Sci.* **2017**, *10*, 1297.

[47] J. Gong, S. B. Darling, F. You, *Energy Environ. Sci.* **2015**, *8*, 1953.

[48] G. Abbas, H. Assender, M. Ibrahim, D. Martin Taylor, *J. Vac. Sci. Technol. B Microelectron. Nanom. Struct.* **2011**, *29*, 052401.

[49] M. Saliba, T. Matsui, J.-Y. Seo, K. Domanski, J.-P. Correa-Baena, N. Mohammad K., S. M. Zakeeruddin, W. Tress, A. Abate, A. Hagfeldt, M. Grätzel, *Energy Environ. Sci.* **2016**, *9*. 1989-1997

[50] N. K. Noel, S. N. Habisreutinger, B. Wenger, M. T. Klug, M. T. Hörantner, M. B. Johnston, R. J. Nicholas, D. T. Moore, H. J. Snaith, Energy Environ. Sci. 2017, 10, 145-152.

[51] A. P. Grosvenor, M. C. Biesinger, R. S. C. Smart, N. S. McIntyre, *Surf. Sci.* **2006**, *600*, 1771.

[52] U. Diebold, T. E. Madey, *Surf. Sci. Spectra* **1996**, *4*, 227.

[53] B. Erdem, R. A. Hunsicker, G. W. Simmons, E. D. Sudol, V. L. Dimonie, M. S. El-Aasser, *Langmuir* **2001**, *17*, 2664.

[54] R. Islam, G. Chen, P. Ramesh, J. Suh, N. Fuchigami, D. Lee, K. A. Littau, K. Weiner, R. T. Collins, K. C. Saraswat, *ACS Appl. Mater. Interfaces* **2017**, *9*, 17201.

[55] Z. Wang, J. Fang, Y. Mi, X. Zhu, H. Ren, X. Liu, Y. Yan, *Appl. Surf. Sci.* **2018**, *436*, 596.

[56] B. Mustafa, J. Griffin, A. S. Alsulami, D. G. Lidzey, A. R. Buckley, *Appl. Phys. Lett.* **2014**, *104*, 4.

[57] M. Wong-stringer, O. S. Game, J. A. Smith, T. J. Routledge, B. A. Alqurashy, B. G. Freestone, A. J. Parnell, N. Vaenas, V. Kumar, M. O. A. Alawad, A. Iraqi, C. Rodenburg, D. G. Lidzey, *Adv. Energy Mater.,* **2018**, *1801234*, 1.

[58] Y. Bai, S. Xiao, C. Hu, T. Zhang, X. Meng, Q. Li, Y. Yang, K. S. Wong, H. Chen, S. Yang, *Nano Energy* **2017**, *34*, 58.

[59] Y. Xie, K. Lu, J. Duan, Y. Jiang, L. Hu, T. Liu, Y. Zhou, B. Hu, *ACS Appl. Mater. Interfaces* **2018**, *10*, 14153.

[60] M. Wong-Stringer, T. J. Routledge, T. McArdle, C. Wood, O. S. Game, J. A. Smith, J. E. Bishop, N. Vaenas, D. M. Coles, A. R. Buckley, and D. G. Lidzey (in press), *Energy Environ. Sci.,* DIO: TBA

Chapter 7

A Flexible Back-Contact Perovskite Solar Mini-Module

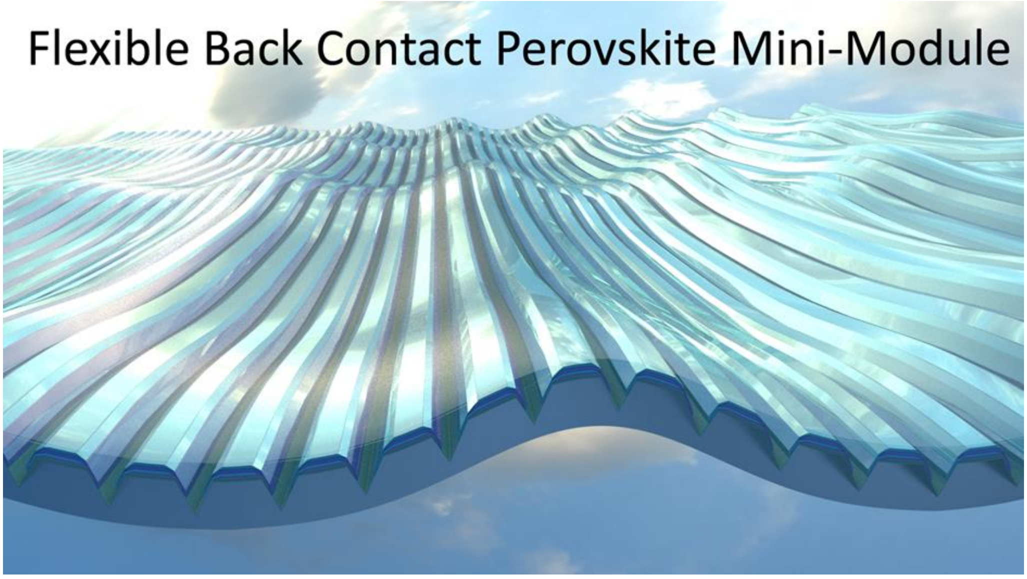

Submitted for peer review

7.0: Publication Forward: A Step Towards Commercialisation?

This chapter is a culmination of many projects; applying the acetonitrile route perovskite first explored in Chapter 5, combined with the prototype reactive electron-beam deposition process demonstrated in Chapter 6, which is then applied to a novel PV technology. Both Chapter 6 and Appendix C contain screening experiments to discover suitable directionally evaporable charge transport materials. Here, such low-temperature deposition processes are used to turn flexible polymeric 'V' shaped grooves into back-contact perovskite solar cells and modules.

7.1: Publication Main Body

A flexible back-contact perovskite solar mini-module

Michael Wong-Stringer[1,α], Thomas J. Routledge[1,α], Trevor McArdle[2], Christopher Wood[2], Onkar S. Game[1], Joel A. Smith[1], James E. Bishop[1], Naoum Vaenas[1], David M. Coles[1,3], Neil Spann[2], Alastair R. Buckley[1,3] and David G. Lidzey[1,3]*

[1]Department of Physics & Astronomy, University of Sheffield, Hicks Building, Hounsfield Road, Sheffield, S3 7RH, United Kingdom

[2]Power Roll Limited, Washington Business Centre, 2 Turbine Way, Sunderland, SR5 3NZ, United Kingdom

[3]Ossila Limited, Windsor Street, Sheffield, S4 7WB, United Kingdom

[α]These authors contributed equally to this work

*Corresponding author, email d.g.lidzey@sheffield.ac.uk

Keywords: perovskite solar module, flexible, back contact, rare-metal free, groove, electron-beam evaporation, scalable, low-temperature.

Abstract

Back-contact perovskite solar cells are fabricated by depositing methylammonium lead iodide perovskite into micron-sized grooves, with opposite walls of each groove being coated with either n- or p-type selective contacts. V-shaped grooves are created by embossing a polymeric substrate, with the different charge-selective electrodes deposited onto the walls of the groove using a directional evaporation technique. We show that individual grooves act as photovoltaic devices, having a power conversion efficiency of up to 7.3 %. By series-connecting multiple grooves, we create integrated mini-modules that build open circuit voltages up to nearly 15 V and power conversion efficiencies over 4 %. The devices created are fully flexible, do not include rare-metals, and are processed using techniques applicable to roll-to-roll processing.

Introduction

Both silicon and emergent thin-film photovoltaic (PV) devices are designed with the primary goal of maximising the amount of incident illumination reaching the absorbing layer and maximising the efficiency by which photogenerated charges are subsequently extracted. In so-called "back-contact" solar cells, the absorbing layer is positioned at the front surface of the device (i.e. closest to the source of illumination), with patterned n- and p-type charge collection electrodes typically positioned behind the active absorber layer.[1–3] This type of architecture has the advantage that it can reduce parasitic absorption losses that otherwise occur in the device substrate or in semi-transparent conductive oxide (TCO) layers that are used to extract photogenerated charges.[2–4] Back-contact designs also enable the use of non-transparent electrodes, including highly conductive metals. This gives back-contact PV devices an inherent advantage, as the loss of photogenerated charges due to the series resistance of the electrodes can be a significant issue in large area solar modules, as the TCOs[2–4] typically used often have a sheet resistance of 10-20 Ω/square. Thus, replacing TCOs with metallic layers whilst using back-contact architecture presents - in principle - a method to both maximise light collection and minimise parasitic resistance losses in PV devices. The open architecture that is inherent to back-contact PV devices is also compatible with surface-sensitive techniques that can be used to study material-properties; for example back-contact

PV devices have previously been studied using kelvin probe force microscopy and grazing-incidence wide-angle x-ray scattering,[5,6] allowing a unique in-situ perspective to be gained of the properties of an active semiconducting layer.

The emergence of metal halide perovskites as efficient semiconductors for photovoltaic applications has transformed the landscape of thin-film solar research. The near-ideal semiconducting properties of perovskites has allowed single junction perovskite PV devices to be created having power conversion efficiencies (PCEs) in excess of 22 %; a result that has pushed such technologies towards commercialization.[7,8] For this reason, there is increasing focus on the development of scalable techniques for perovskite solar cell (PSC) fabrication that can be used to create large solar modules.[9–14] However, few studies have attempted to fabricate back-contact perovskite solar cells, and none have addressed the fabrication of back-contact solar modules. So far, the few attempts to create PSCs with an interdigitated back-contact (IBC) architectures have utilized charge selective electrodes that have been selectively patterned using electrodeposition, laser ablation, mechanical etching, or photoresist templating.[5,6,9–13,15] To date, the best IBC PSCs demonstrated have achieved a PCE of ~4 %, with devices utilising a honeycomb design for charge selection layers.[3]

In this paper, we describe experiments to construct IBC PSCs on polyethylene terephthalate (PET) substrates whose surfaces were embossed with a series of V-shaped micro-grooves. This groove architecture has been developed and patented by Power Roll Ltd. A directional coating process has been developed to selectively deposit electron- and hole-extracting contacts onto the two opposing walls of the grooves. Grooves were then filled with a metal-halide perovskite by spin-coating a precursor material onto the surface of the charge-selective grooves, forming a horizontally spaced PV device. Such an architecture has been previously combined with copper indium diselenide nano-crystals as the active layer, with a champion PCE of 2.2 % achieved, and corrected to 4.4 % PCE after properly characterising the active area.[13] Here we show that such perovskite-based groove devices achieve a maximum PCE of 7.3 %. Furthermore, embossing multiple grooves in series can be used to create integrated mini-modules, having PCEs of up to 4.4 % and open circuit voltages (V_{OC}) of up to nearly 15 V. We characterise the solar grooves with focussed ion beam-scanning electron microscopy (FIB-SEM) and laser-beam-induced current (LBIC). These techniques confirm the successful directional coating of the evaporated layers, and demonstrate photocurrent generation is occurring within each groove; a result that allows the active area of the PSC groove-devices to be verified. Our results indicate that PSCs can be fabricated using an IBC architecture, with the process developed being directly scalable to large-area manufacturing.

V-shaped micro-grooves having widths between 1 and 3 μm were fabricated into an acrylic coated PET substrate using an embossing process, with the angle between groove walls being 55 °. The grooves were then selectively coated with metal electrodes and n-type and p-type transport layers using a directional thermal or electron-beam evaporation process as illustrated schematically in Figure 1a. As the substrate was mounted at an oblique angle α with respect to the directional deposition source, the groove wall nearest to the deposition source is left 'in shadow', with evaporated material being deposited both onto the wall of the groove that faces the source and on to the 'flat' area either side of the grooves (see schematic in Figure 1b). Figure 1c shows a typical cross-section of a single micro-groove obtained from FIB-SEM, where we colour-code charge-selective materials using the same colours used in Figure 1b. We have routinely used FIB-SEM to confirm the thickness and coverage of the electrode materials that were selectively deposited on the groove walls.

Different materials were coated onto opposing walls of the groove by rotating the substrates (relative to the position of the source) by 180 ° between deposition runs (see Figure 1a). By adjusting the angle of incidence between coatings, it is also possible to control the relative depth over which each material was deposited into the groove. As an n-type contact, we utilised a multilayer-combination of C_{60}/Ti (deposited by thermal evaporation and e-beam evaporation respectively), while the p-type contact consisted of NiO/Ni. Here, the NiO was deposited by a reactive electron-beam evaporation process, in which metallic Ni pellets were heated by an electron-beam in a partial pressure of O_2. To minimise the sheet-resistance of the device, the metal contacts deposited had a thickness of around 250 nm. We have previously demonstrated the effectiveness of reactive e-beam to deposit NiO as a p-type material in conventional planar perovskite solar cells – even without the necessity for thermal annealing (see Chapter 6). C_{60} was selected as the n-type selective material based on a series of screening experiments, in which many evaporable electron transporting materials (ETM) were investigated. Here C_{60} was found to produce the most reproducible, lowest hysteresis and, highest performance conventional planar PSCs, without the need for a high-temperature anneal. The stabilised PCE output of an ITO/C_{60}/$MAPbI_3$/spiro-OMeTAD/Au PSC is shown in Figure S1, demonstrating that thermally evaporated C_{60} can act as an effective electron transporting and hole blocking layer below a $MAPbI_3$ perovskite active layer, allowing ~14 % PCE standard architecture PSCs to be created.

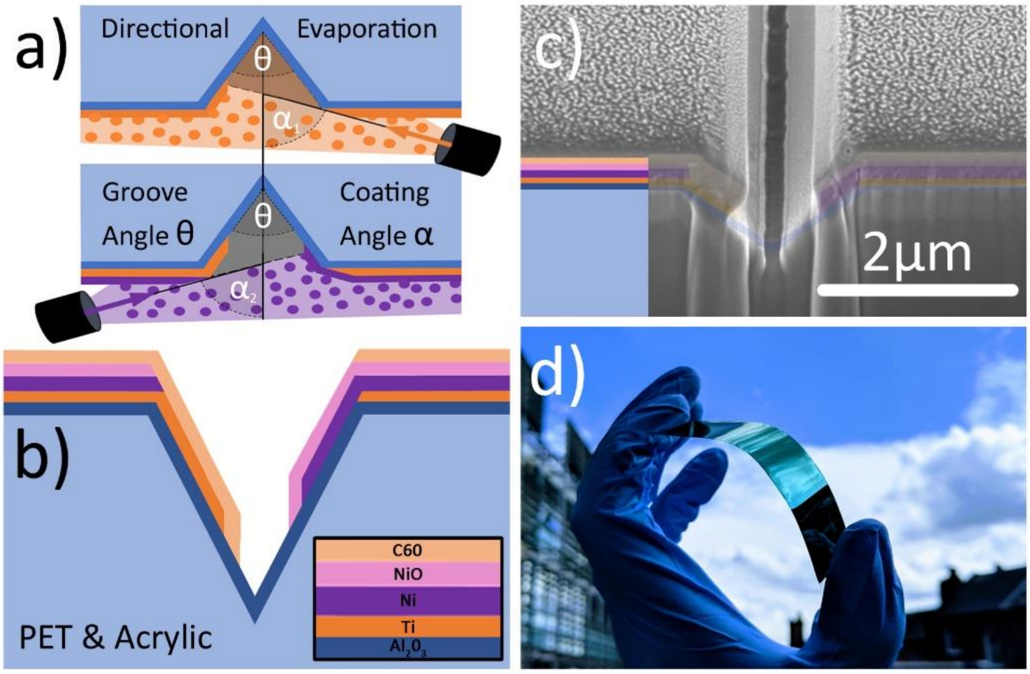

Figure 1: *a) Schematic illustration of directional evaporation onto a grooved substrate creating selective electrodes on opposing groove walls. Consecutive layers can be deposited at different deposition angles to control the filling depth of the groove. b) Schematic of a coated groove after a non-directional coating of* Al_2O_3 *followed by an n-type Titanium &* C_{60} *electrode on one groove wall and a p-type Ni & NiO electrode on the opposite wall. c) A focussed ion beam-scanning electron microscope image of a cross-section through a 2 µm wide single groove after the deposition of all evaporated layers. The inset and translucent shading indicates the location of the selectively deposited metal electrodes and charge-transporting layers. d) An image of a flexible groove substrate after the deposition of all evaporated layers.*

The flexibility of the coated, embossed PET substrate is clearly evident from the image shown in Figure 1d. Here, the grooves run parallel to the long-axis of the flexible strip. We have measured the temperature of the PET substrate during a typical e-beam deposition, and find that it does not exceed 100 °C. To convert the surface-coated charge-selective groove structures into a back-contact perovskite solar cells, the flexible substrates (similar to those shown in Figure 1d) were first cut into (4 x 20) mm pieces. These were then spin-cast at 6000 rotations per minute (rpm) with methylammonium lead halide ($MAPbI_3$) solution, resulting in the formation of a $MAPbI_3$ film. Here, the perovskite material that filled the groove acted as the device active layer, with the device having the multilayer structure $Ti/C_{60}/MAPbI_3/NiO/Ni$. To deposit the perovskite active layer, we have used a precursor ink based on the low viscosity, low boiling point solvent acetonitrile containing $MAPbI_3$ that had been previously bubbled using methylamine gas.[17] This perovskite precursor ink combines the advantages that (i) the acetonitrile solvent does not damage the PET substrate, and (ii) it does not require thermal annealing to generate the final perovskite. Figure 2a shows an SEM image of a focussed-ion beam cross-section through a 2 µm wide groove filled with a $MAPbI_3$ active layer. Interestingly, it can be seen that only very limited amounts of perovskite are found on the flat surfaces either side of the groove.

Results and Discussion

To confirm that the structures created act as a photovoltaic device, it was first determined that a photocurrent could be generated from the perovskite material that filled the V-groove. This was done by a focussing a chopped 635 nm laser to a 2 µm (near diffraction-limited) spot on the substrate surface. This spot was then raster-scanned across the surface in steps of 0.5 µm while the photocurrent was recorded using a lock-in amplifier. Figure 2b plots a typical LBIC image of a 2 µm wide device. Here it can be seen that even though the spot size is approximately coincident with the width of the groove, the majority of the photocurrent appears localised within the groove. As might be expected, the flat regions either side of the groove apparently contribute very little photocurrent, with the peak of the photocurrent being located in the centre of the groove. It is also apparent that there are variations in local photocurrent generated along the length of the groove; a result that most likely indicates that the perovskite does not uniformly fill the groove. We can use such a measurement to make a first estimation of the total active area of each individual groove PSC device from the product of the groove width (as measured using FIB-SEM) and its length. Although this methodology is relatively crude and open to error, we later describe the use of a self-masking technique to demonstrate that such methods provide an accurate measure of the device active area.

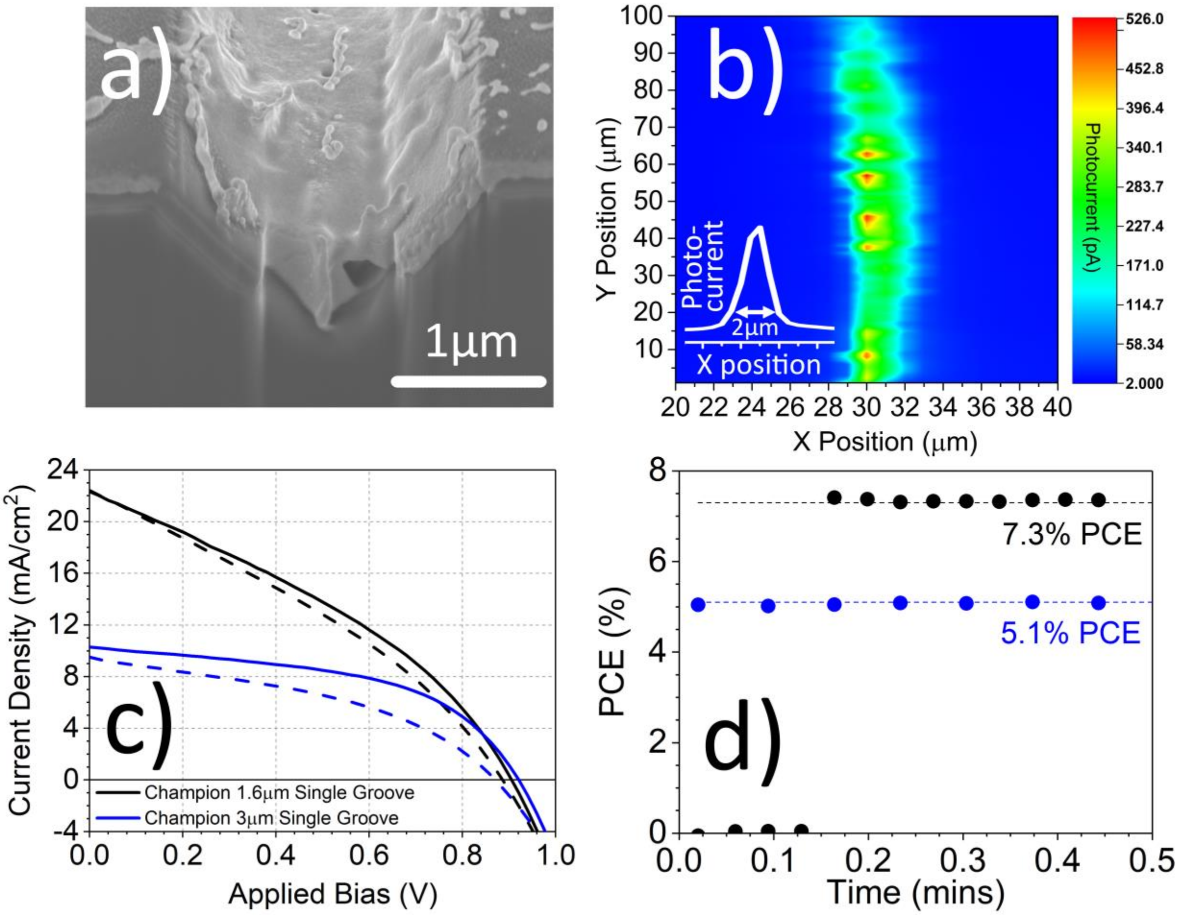

Figure 2: *a) A focussed ion beam-scanning electron microscope cross-section image of a 2 µm wide $MAPbI_3$ coated groove. b) A laser-beam induced current map of a single $MAPbI_3$ filled groove, inset is cross section of the LBIC map. c) Current-voltage curves of champion 1.6 µm (black) and 3 µm (blue) wide single grooves. Solid lines and dotted line represent reverse and forward sweeps respectively. d) Stabilised power conversion efficiency outputs for the same champion grooves. Performance metrics of these devices are given in Table 1.*

Groove Width	PCE [%]	J_{SC} [mA/cm^2]	V_{oc} [V]	FF [%]	Active Area [cm^2]
1.6 µm	7.03 (7.3)	22.33	0.91	34.8	6.4 x 10^{-5}
3 µm	4.83 (5.1)	10.33	0.92	51.0	1.2 x 10^{-4}

Table 1: *Solar cell performance metrics of the single $MAPbI_3$ filled grooves shown in Figure 2. Both grooves were 4 mm in length. Stabilised PCEs are given in parenthesis.*

Having provided a first estimate of device active area, we now proceed to measure device efficiency. Here, current-voltage (*JV*) sweeps were measured for individual PSC grooves when illuminated by simulated AM1.5 radiation calibrated to 100 mW/cm^2. Figure 2c plots *JV* sweeps for 1.6 and 3 µm wide grooves; from this we determine that the 1.6 µm wide groove had a PCE of 7.0 %, while the 3 µm wide groove had a relatively high fill factor (FF) of 51 %. We tabulate the performance metrics and active area of the grooves in Table 1. Here the enhanced higher *FF* and significantly higher shunt resistance of the wider groove suggests a relative reduction in leakage pathways between the opposing wall contacts. Stabilized power outputs of the grooves are plotted in Figure 2d, with the 1.6 and 3 µm wide grooves having a stabilised efficiency of 7.3 % and 5.1 % PCE respectively. Remarkably, a V_{OC} of over 0.9 V is obtained for both groove widths; a value that is equivalent to PSCs using similar contact materials in a conventional planar-cell architecture.

We now discuss the construction of IBC micro-modules that are created through the serial connection of adjacent PSC grooves. Here we study structures in which 3, 4, 6 and 16 grooves were fabricated using the same embossing and directional coating techniques that were used to deposit n- and p-type contacts onto the walls of a single groove. Figure 3a presents a schematic of a groove module, illustrating that the flat sections between the grooves constitute a series connection between n- and p-type contacts on neighbouring walls, creating a PV micro-module built from multiple solar cells (here represented as simple photodiodes). Such a multi-groove mini-module will in principle allow large open-circuit voltages to be built, with the voltage ideally scaling with the number of grooves in the module. Figure S2 indicates how both the spacing between the grooves and the groove widths can be tuned.

Figure 3b presents a FIB-SEM image of a multi-groove module in which it can be seen that the $MAPbI_3$ perovskite fills each groove while leaving the flat sections between the grooves largely uncoated. Additional images of unfilled mini-module groove arrays are provided in Figure S3. We have performed LBIC measurements on a mini-module composed of 16 grooves. The results of this measurement are shown in Figure 3c, with Figure 3d displaying a cross section across the photocurrent map. It can be seen that 15 out of the 16 grooves are clearly resolved, with one of the 16 grooves apparently generating very little photocurrent, indicating that it is likely at short-circuit. This measurement indicates that higher efficiencies from such mini-modules can be expected following further groove embossing and device fabrication optimisation.

We have also tested the performance of the mini-modules by measuring their JV response under illumination with AM1.5 radiation. Since the LBIC measurements indicate that the regions between the grooves do not generate significant photocurrent, we use a geometrical fill factor to adjust module efficiency to account for the inactive regions between the grooves. Geometric fill factors (FF_G) are thus calculated via a ratio of total module area to usable groove active area using Equation 1, where n is number of grooves, W_G groove width, and W_S is the spacing between the grooves.

$$PCE_{Corrected} = PCE \times \frac{FF_G\ (\%)}{100} = PCE \times \frac{[n \times W_G]}{[n \times W_G] + [(n-1) \times W_S]} \qquad (Eq. 1)$$

Figure 3e plots champion current-voltage characteristics of mini-modules consisting of 3, 4, and 6 grooves. Our measurements indicate that the 4-groove mini-module has a PCE of 4.4 % and a V_{OC} of 3.5 V. The stabilised power output of this groove is shown in supplementary Figure S4. In Figure 3f we present the current-voltage response of a larger 2.6 % PCE mini-module consisting of 16 grooves which builds an impressive V_{OC} of 14.6 V. This high V_{OC} groove mini-module also has an FF of 43.5 % and generates an average voltage per groove of 0.91 V; a value that matches the V_{OC} of best performing single grooves. The performance metrics of all these champion multi-groove mini-modules are given in Table 2, which also lists device active areas, geometric fill-factors, geometrically corrected PCEs, and the average voltage per groove built in each module type.

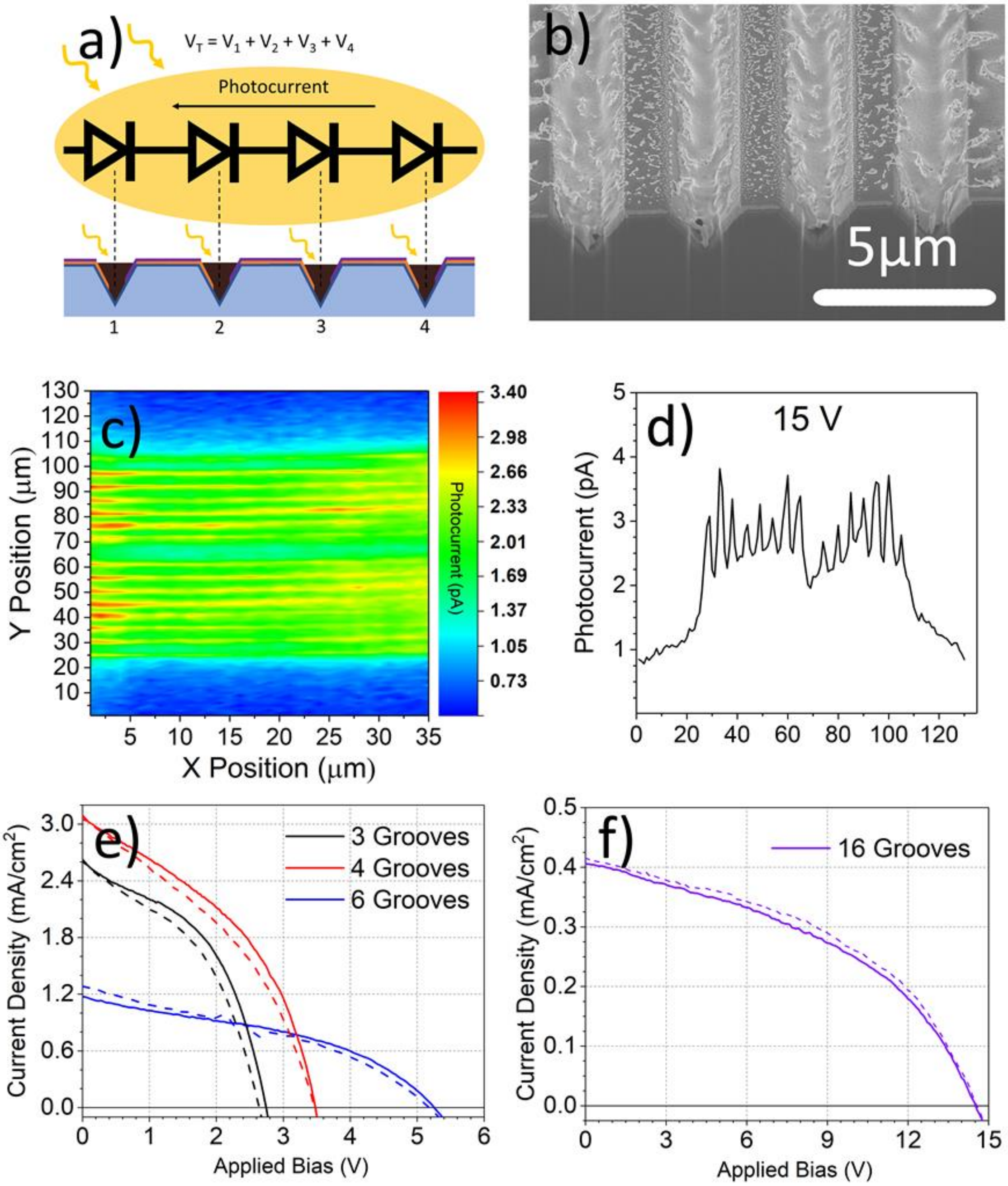

Figure 3: *a) Simple schematic demonstrating how multiple grooves form a mini-module. b) A focussed ion beam-scanning electron microscopy image of a perovskite coated multi-groove. c) Laser-beam induced current map across 16 multi-groove mini-module, recorded at a step size of 1 µm. d) Cross-section of induced photocurrent map shown in part c). e) Current-voltage curves of champion* $MAPbI_3$ *filled 3, 4 and 6 multi-groove mini-modules and, f) current-voltage curves of 16 groove mini-modules. Solid lines and dotted line represent reverse and forward sweeps respectively. PV device performance metrics of mini-modules are shown in Table 2.*

No of Grooves	PCE [%]	J_{SC} [mA/cm^2]	V_{oc} [V]	FF [%]	Active Area [cm^2]	Geometric FF [%]	Corrected PCE [%]	Voltage Per Groove [V]
3	3.27	2.61	2.74	45.7	2.88×10^{-4}	82.9	2.71	0.91
4	4.43	3.05	3.48	41.7	3.1×10^{-4}	72.7	3.22	0.87
6*	2.51	1.18	5.26	40.6	2.4×10^{-4}	44.5	1.12	0.88
16*	2.63	0.42	14.56	43.5	9.6×10^{-4}	41.6	1.09	0.91

Table 2: *Solar cell performance metrics of the $MAPbI_3$ filled multi-groove mini-modules shown in Figure 3. Here the geometrical fill factor is used as a scaling factor to calculate a corrected power conversion efficiency (see text for details). Devices with * did not have an Al_2O_3 layer below the electrodes.*

It is apparent that the efficiency of the solar grooves is critically dependent on the value of the active area that is used in the calculation. This problem is illustrated in Figure 4; by illuminating the top surface of a device, it is in principle possible to generate carriers in the surrounding flat region between the V-grooves that are then able to diffuse to the groove active region (See Figure 4a). Such a diffusion process will clearly result in an over-estimate of device efficiency; a problem frequently encountered when testing PSCs without an illumination mask.[18] Unfortunately, the width of the individual grooves is too small to use an *external* illumination mask. However, the thick metal contacts on the walls can be used as an *internal* illumination mask provided that the device is illuminated through its substrate (see Figure 4b). Using FIB-SEM cross-sections of a groove as shown in Figure 4c, we can measure the width of the aperture subtended by the region at the bottom of the groove that is uncoated with a metal. Note that we have performed control UV-visible absorption measurements on PET/acrylic substrates both with and without electrodes / charge extraction contacts, and find that the optical transmission through electrode coated films is negligible (see Figure S5). Encouragingly, we find that the PCE of the champion 4-groove mini-module is 4 % when illuminated from the front surface, and 4.4 % when illuminated through the underlying substrate (See Table S1). This indicates that the relative error in device efficiency determined on the basis of groove area is likely to be around 10 % at most.

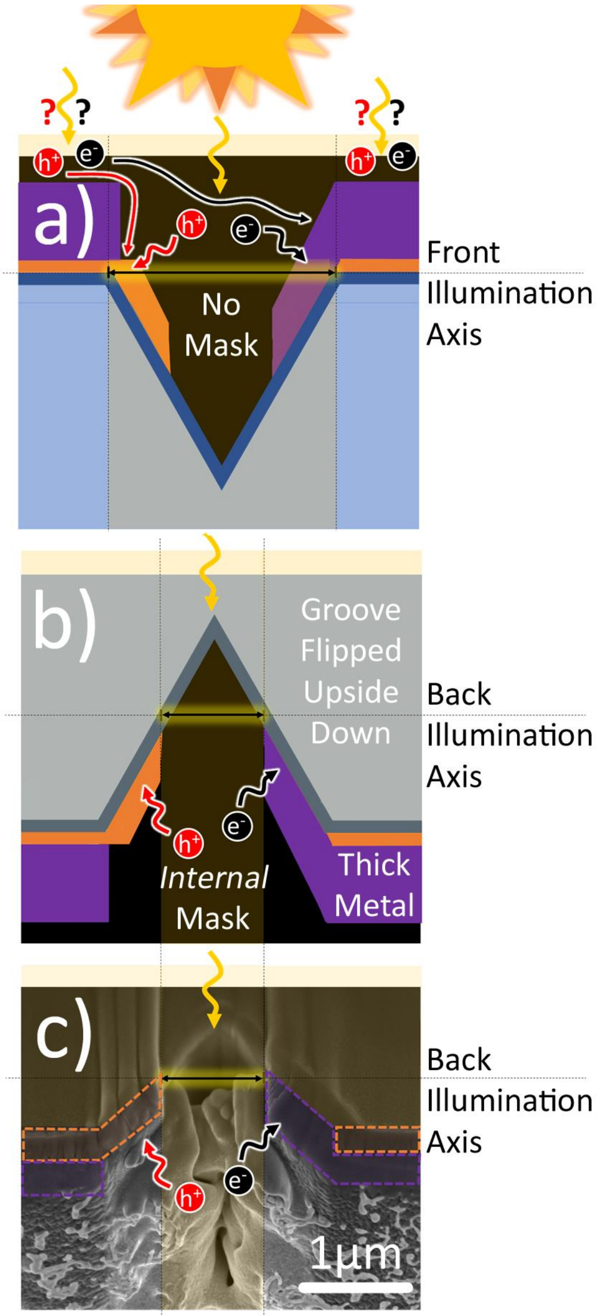

Figure 4: *Schematic indicating two methods used to determine the active area of the grooves. Part a) indicates the use of the physical width of the groove to calculate active area, where the width is defined by the embossing process. It is possible that photogenerated charges could be diffusing to the charge selective groove walls from outside the groove width. In part b) the groove is illuminated through the device substrate. Here, the thick electrodes act as internal illumination mask. The width of the aperture at the bottom of the groove is determined from focussed ion beam-scanning electron microscopy images, presented in part c), where the image of the device is orientated to show how it might look upon illumination from the back. Here, there can be no photogenerated charges diffusing from outside the defined illuminated area.*

We have performed some preliminary device optimisation studies focussing on understanding the effect of the spin-coating velocity used to coat the perovskite precursor ink. Here, we have explored two perovskite deposition conditions in which the perovskite solution was either spin-coated at 2000 rpm or 6000 rpm. We find that the faster spin speeds lead to the creation of semi-filled grooves with very little perovskite material found between grooves. In contrast, the slower spin-speed results in the formation of a fully-filled groove, with the flat surfaces either side of the groove being coated by a layer of perovskite that is 100's of nm thick. This can be seen in supplementary Figure S6 that compares FIB-SEM cross-sections of grooves coated with perovskite deposited using both spin-speed conditions.

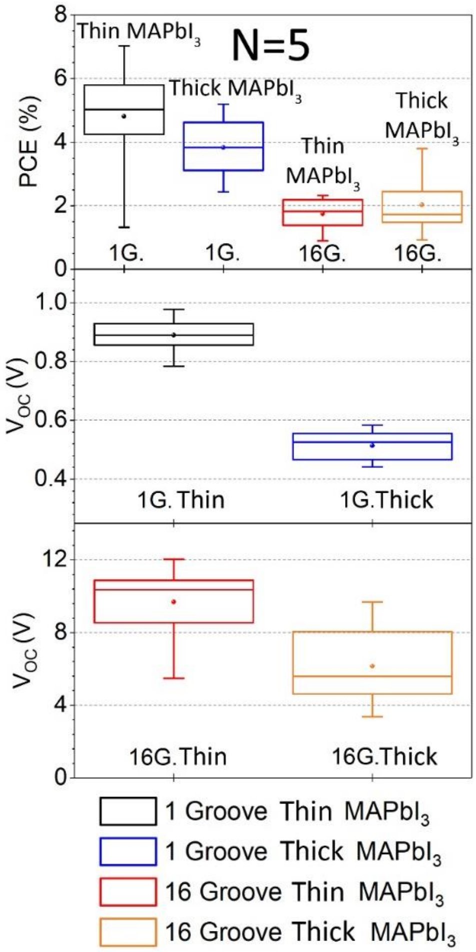

Figure 5: *Boxplots showing distribution of power conversion efficiency and open circuit voltage for a batch of single grooves (black, blue) and 16 groove (red, orange) solar mini-modules. Here, the thickness of the perovskite in the grooves is varied through control of the* $MAPbI_3$ *deposition conditions. Devices based on thick* $MAPbI_3$ *shown using blue and orange lines, while the thinner* $MAPbI_3$ *active later is indicated using black and red lines.*

We have explored the statistical variation in solar groove efficiency as shown in Figure 5. Here, we present boxplots of device performance metrics for (N = 5) single groove devices and 16-groove mini-modules when either coated by a thin (conformally semi filling the groove) or thick (fully filling the groove) $MAPbI_3$ absorbing layer. It can be seen that there is a significant variation in performance metrics within each boxplot; a result that most likely originates from variations in the degree to which the perovskite fills each groove. It is also apparent that device efficiency is dependent on the thickness of the perovskite film. Interestingly, we find that the use of a thicker perovskite film results in single-groove devices that have slightly reduced average efficiency than comparable devices containing a thinner perovskite film, being (3.8 ± 0.5) % and (4.8 ± 0.3) % respectively. This contrasts with multi-groove modules that demonstrate a higher peak PCE of 3.8 % when a thicker perovskite is used relative to 2.2 % for modules incorporating a thinner perovskite. This variation in efficiency results from a loss in average V_{OC}, with this effect apparent in both single-groove devices and multi-groove modules. However, in the case of multi-groove mini-modules, the photocurrent is apparently higher when employing thicker perovskite active layers; an effect that offsets the loss of PCE due to the lower V_{OC}. We believe this loss in V_{OC}. results from the presence of the thick layer of perovskite between grooves that generates short circuit pathways for photogenerated charges between the different grooves. This suggests that for every groove shape, size and pattern, there is likely to be an optimum perovskite coating thickness.

Conclusions

In conclusion, we have fabricated flexible $MAPbI_3$ micro-groove back-contact solar cells reaching a PCE of 7.3 %. Mini-modules are also created through the serial connection of adjacent grooves, with such modules achieving a champion PCE of 4.4%, with other modules building an open-circuit voltage of up to 14.6 V. These back-contact mini-modules are fully functional without the use of electrode patterning techniques such as electrodeposition, laser ablation, mechanical etching, or photoresist templating. The techniques we have developed do not require high temperature substrate conditioning, are free from the complex cocktail of dopants that often used to increase the conductivity of charge-transport materials in PSCs[19] and do not contain rare metals such as gold, silver or indium that are commonly used in PSCs. The process techniques we have developed are conceptually similar to the low-cost metallisation of plastic used in the food packing industry,[20] and thus the use of inexpensive metals, metal oxides, and flexible polymeric substrates make the technology outlined suitable for scalable, high throughput roll-to-roll processes.[21,22] This unique back-contact architecture (patented by Power Roll Ltd) also presents an exciting opportunity to allow surface-sensitive in-situ studies of perovskites to be made during device operation - for example - allowing the optoelectronic and crystal properties of the perovskite active layer to be investigated as it is deposited or during post-deposition treatments.

Methods

Device fabrication

Materials – All solvents used were purchased from Sigma Aldrich and were anhydrous. All solvents and dry powders were stored in a N_2 filled glovebox.

Embossed, Cleaning & Substrate Preparation – V-grooves were patterned into a poly (methyl methacrylate) (acrylic) coated polyethylene terephthalate (PET) by embossing. Here, a diamond turned nickel master was coated using a UV-cured acrylic that was cured and then removed to produce a mother-tool, which is the mirror image of the desired pattern (ridges instead of grooves). The mother tool was then used to emboss individual PET/acrylic sheets. The embossed sheets were rinsed with isopropyl alcohol (IPA) before deposition. Before evaporation a 50 nm film of Al_2O_3 was coated over the entire substrate via electron beam evaporation to help protect the PET/acrylic from the process solvents used to deposit the perovskite.

Substrate Mounting – Embossed substrates were mounted onto a plate so that a groove wall was almost facing the e-beam source (see Figure 1). Deposition was performed at an angle oblique angle α. The groove substrates were then rotated 180° between evaporations to permit n-type (Titanium/C_{60}) and p-type (Ni/NiO) contacts to be deposited onto the opposing groove walls.

Directional Electron Beam Evaporated Titanium, Nickel and Nickel Oxide (Ti, Ni and NiO) – Titanium or Nickel (Kurt Lesker, ¼ by ¼ inch pellets, 99.995 % purity) were either placed inside a carbon crucible or directly inside a copper hearth. The metals were preconditioned by exposure to a high power and wide pattern electron beam to create a pool of molten material. A 250 nm thick film of Ni and Ti were then deposited at a rate varying between 4 and 20 Å/s. Following the deposition of Ni, an O_2 gas stream was fed into the chamber at a pressure of $1x10^{-4}$ mbar, enabling the reactive evaporation of 25 nm NiO on top of the Ni. Typically, the NiO was deposited at an evaporation rate of between 2 and 10 Å/s.

Thermally Evaporated C_{60} (TiO_2) – 100 nm of Fullerene C_{60} (Purity > 99.5 %) was thermally evaporated at a rate between 0.5 and 2.5 Å/s.

Acetonitrile Perovskite (Ac) Spin coating – An acetonitrile perovskite solution containing a 0.5M suspension 1:1.06 Lead (II) Iodide (PbI_2, TCI, Perovskite Precursor) and methylammonium iodide (MAI, Dyesol) was mixed at a ratio of 1:1.06 MAI:PbI_2 to obtain a black powder suspension. As described by Noel et al.[17], the suspension was then bubbled with dry methylamine until a clear (yellow) solution was obtained. This solution was then filtered through a 0.2 μm polytetrafluoroethylene filter, with 40 μl of the resultant solution spin coated onto the groove substrates at a speed between 2000 and 6000 rpm in a N_2 filled glovebox. The resultant substrates were not thermally annealed.

Device and Film Characterisation

Device Characterisation: – Before testing, a NREL certified silicon reference cell was used to adjust light from a Newport 92251A-1000 solar simulator to an intensity of 100 mW/cm^2. Light from the solar simulator was first used to generate a stabilised photocurrent from the groove mini-modules. The photocurrent produced by the groove mini-modules were first characterised at short circuit. This measurement was designed to check that the current produced did not result from electrochemical or capacitive artefacts. A source-measure unit was used to sweep the voltage across devices from 0 to *n* V, where *n* was the number of grooves present in the mini-module. During most characterisation measurements, the top (groove-side) of the substrates were illuminated without the use of an illumination mask.

Champion devices were then illuminated through the substrate (upside down) to effectively mask the illumination area (see text for details). Stabilised power conversion efficiencies were obtained by holding devices at their V_{mpp}. All measurements were performed in air.

Focussed Ion Beam-Scanning Electron Microscopy (FIB-SEM) – Samples were mounted on carbon adhesive discs and sputter coated with 10 nm of gold-palladium using a Cressington 108 auto coating unit. Samples were then examined using an FEI Helios 600 Nanolab SEM. Cross-sections were milled using a 30 kV gallium ion beam at a currents between 2.8 and 6.5 nA. Electron beam imaging of the milled cross-section was performed at 3 kV and 0.17 nA using the in-lens imaging mode.

Laser-Beam-Induced Current (LBIC) – The LBIC mapping system comprised of a mechanically chopped laser that was passed through a spatial filter before being focussed to a spot size of around 2 μm onto the sample via a 100x objective (Mitutoyo, infinity-corrected long working distance). The sample was mounted on a XY-stage and moved in a sawtooth pattern in steps of 0.5 μm. A 4.5 mW, 635 nm diode laser (Thor labs, CPS635) was used to generate the photocurrent which was measured using a lock-in amplifier (Stanford Research Systems, SR830) referenced to the chopped laser.

UV-Vis Transmission – A HR2000+ES spectrometer and Ocean Optics DH-2000-BAL UV-VIS-NIR light source were used to determine the transmission of uncoated PET/acrylic substrates and fully coated PET/acrylic/Al_2O_3/Ti/Ni/NiO/C_{60} substrates.

Supporting Information: Supporting information is available online.

Acknowledgments: Acknowledgments: This work was partly funded by the UK Engineering and Physical Sciences Research Council (EPSRC) via grant EP/M025020/1 'High resolution mapping of performance and degradation mechanisms in printable photovoltaic devices' and EP/M014797/1 'Improved Understanding, Development and Optimization of Perovskite-based Solar Cells'. We also thank the EPSRC for PhD studentships via the University of Sheffield DTG account (T.R. and J.B.) and from the Centre for Doctoral Training in New and Sustainable PV, EP/L01551X/1 (M.S. and J.S.). We would like to thank Budhika

Mendis at Durham University for recording the FIB-SEM images. Power Roll Ltd had co-sponsored this Research.

Conflict of Interest: D.G.L. and A.R.B. are co-directors of the company Ossila Ltd that retails materials used in perovskite photovoltaic research. PowerRoll Ltd hold the following patents relating to the substrates used in this work: Canada 2840327, China, 201180071841.6, 201480006419.6, Europe 2724380, EP 2951866, USA 14/264670, 14/764599, South Africa 2014/00531, Brazil BR1120150175007, Hong Kong 16103709.8, India 2812/KOLNP/2015, Japan 2015-555797, UK GB2487419.

7.2: Additional Discussion and Supplementary Information

Original Supplementary Information

Supplementary Table

Groove Width Used for Active Area	Groove Width [µm]	Illumination Mask?	Stabilised PCE [%]
Groove Width	2	Not Possible	4%
Back Illumination	1	Yes (Self Masking)	4.4%

Table S1: *Stabilised power conversion efficiencies obtained when using: standard front illumination, where the groove width is used to calculate the active area, and back illumination, where the thick metal electrodes are used as an integrated illumination mask. Width of groove and masked width are checked with focussed ion beam-scanning electron microscopy.*

Supplementary Figures

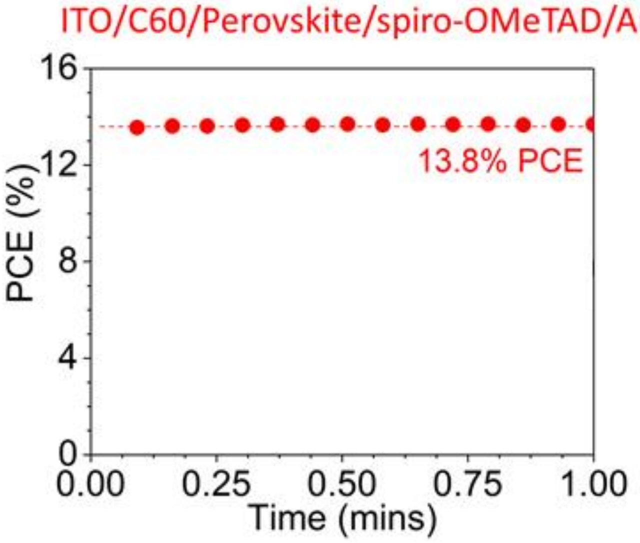

Figure S1: *Stabilised power conversion efficiency output of flat standard architecture ITO/C60/MAPbI*$_3$*/spiro-OMeTAD/Au PSC, showing C60 is an ideal evaporable ETL.*

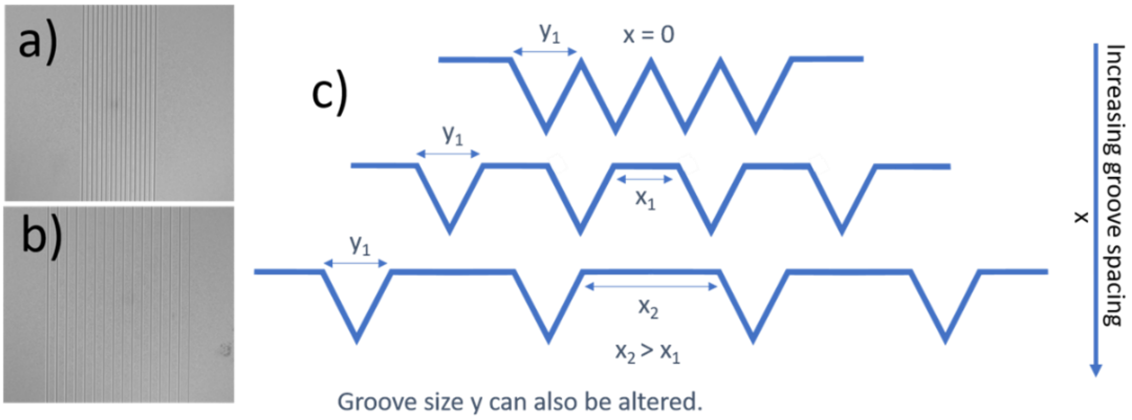

Figure S2: *Top down focussed ion beam-scanning electron microscopy images a) and b) showing a groove spacing of 0.5 µm and 3 µm respectively. c) A simple diagram indicating how the groove size and spacing can be altered.*

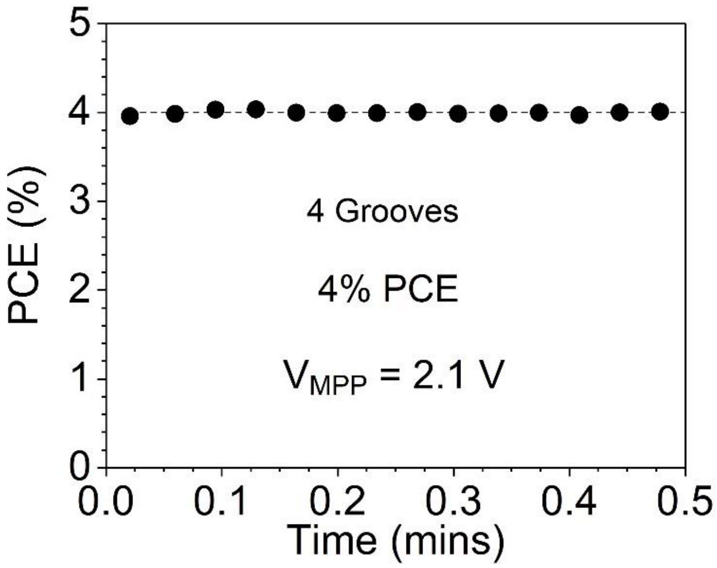

Figure S3: *Stabilised power conversion efficiency output of the champion four groove solar mini-module presented in Figure 3.*

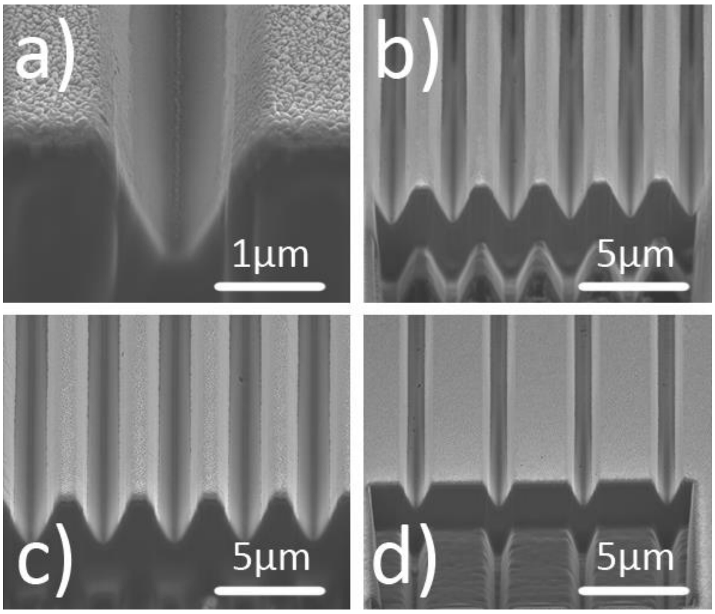

Figure S4: *Focussed ion beam-scanning electron microscopy images of grooves before perovskite deposition. a) A 1.6 µm wide single groove. b) A multi-groove pattern with 2 µm grooves and 0.5 µm spacing. c) A multi-groove pattern with 3 µm grooves and 0.5 µm spacing. d) A multi-groove pattern with 2 µm grooves and 3 µm spacing.*

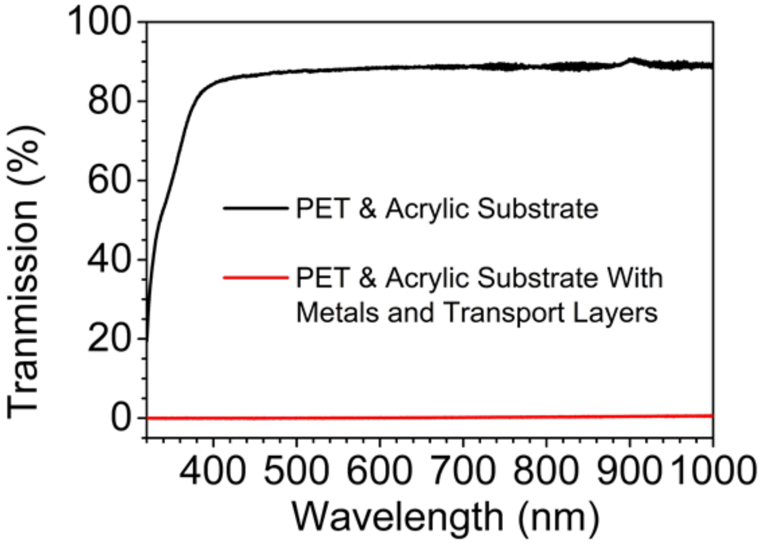

Figure S5: *UV-Visible transmission spectra of the PET and acrylic substrate before (black) and after (red) the deposition of the metal electrodes and transport layers.*

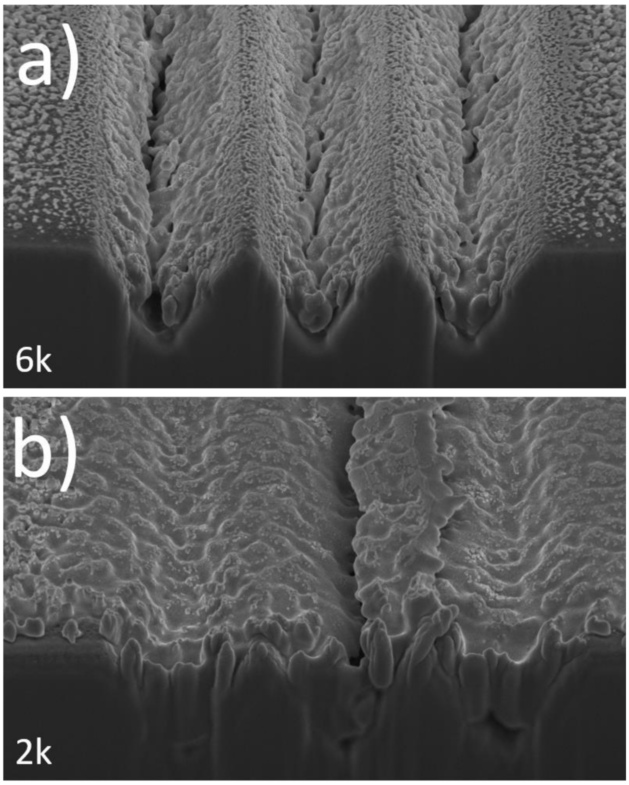

Figure S6: *Focussed ion beam-scanning electron microscopy images of multi-grooves after different* $MAPbI_3$ *spin coating solution depositions. a) Spin speed of 6000 rpm. b) Spin speed of 2000 rpm.*

Additional Discussion

It is important to understand how the LBIC and FIB-SEM measurements can be used to understand solar groove performance and optimize their fabrication. When grooves are embossed and devices are fabricated, there is a possibility that defects in the PET substrate or metal electrodes will cause grooves to short-circuit. Furthermore, the photocurrent generated within a series-connected mini-module is limited by the photocurrent of its worst cell. In the case of serially connected grooves, the groove with the lowest performance will determine the overall mini-module photocurrent. Here, the extent to which the perovskite fills the grooves is critical. Examples of non-ideal perovskite fill include: (i) the perovskite solution dewetting from one of the grooves and leaving it completely empty, leading to a reduction in the whole module photocurrent or a completely open circuit module, or (ii) a large overlayer of perovskite forming a bridge over a groove but not filling it, causing that groove to act as a resistor instead of a photocurrent generator. It is unclear how many grooves are 'active' from a module's *JV* characteristics alone; an issue that complicates our understanding of module functionality (i.e. the equivalent circuit that best describes a micro-groove mini-module). FIB-SEM can be used to identify the morphology of the perovskite film in the grooves, but it is a destructive and time-consuming process. The LBIC image provides additional information regarding the nature of micro-groove mini-module device performance. For example, Figure S7 presents four 16 groove mini-modules, where each are found to have open circuit voltages of 6 V, 10 V, 12 V and 15 V. Upon first inspection of *JV* characteristics, it is difficult to determine why the voltages (and also PCEs) are low for some modules. The LBIC reveals that the V_{OC} of the modules are directly correlated to the number of grooves that generate a photocurrent; a result that indicates that low module V_{OC} has little to do with quality of the perovskite or transport layers, but is most likely due to short-circuited grooves that do not provide V_{OC}. Taken together, *JV* characteristics, FIB-SEM and LBIC can be used to identify the parameters that are important for efficient module operation. It is evident that focussing on reducing defects the embossing and electrode deposition processes will lead to modules with more reproducible and higher open circuit voltage.

To build solar micro-modules of larger area, both serial and parallel connections will be required to build higher voltages and photocurrents respectively. Such parallel connected groove architectures are not fully protected by patents and are outside the scope of this thesis. Micro-modules exceeding 2 % PCE with active areas up to 2 cm^2 that employ over 3000 grooves have been achieved. These large-area micro-modules implement a patterning technique that generates groove cascades connected in parallel without the need of laser ablation or photolithography.

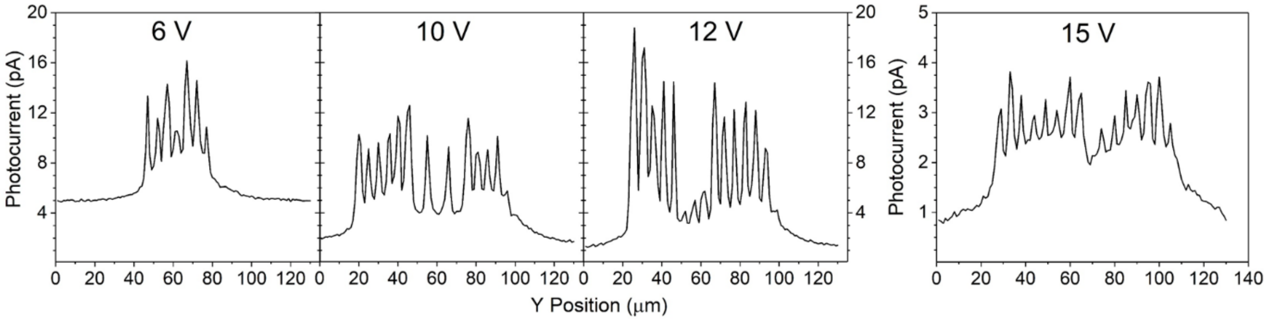

Figure S7: *2D LBIC line scan of similar 16 groove substrates. Solar modules producing 6 V, 10 V, 12 V and 15V open circuit voltage all appear to have photocurrent contribution from the number of grooves that correspond to that voltage.*

7.3: References

[1] G. W. P. Adhyaksa, E. Johlin, E. C. Garnett, *Nano Lett.* **2017**, *17*, 5206.

[2] A. Jumabekov, E. Della Gaspera, Z. Xu, A. Chesman, J. van Embden, S. Bonke, Q. Bao, D. Vak, U. Bach, *J. Mater. Chem. C.* **2016**, *4*, 3125.

[3] Q. Hou, D. Bacal, A. N. Jumabekov, W. Li, Z. Wang, X. Lin, S. H. Ng, B. Tan, Q. Bao, A. S. R. Chesman, Y.-B. Cheng, U. Bach, *Nano Energy* **2018**, *50, 710.*

[4] Z. Hu, G. Kapil, H. Shimazaki, S. S. Pandey, T. Ma, S. Hayase, *J. Phys. Chem. C* **2017**, *121*, 4214.

[5] M. Alsari, O. Bikondoa, J. Bishop, M. Abdi-Jalebi, L. Y. Ozer, M. Hampton, P. Thompson, M. T. Hörantner, S. Mahesh, C. Greenland, J. E. Macdonald, G. Palmisano, H. J. Snaith, D. G. Lidzey, S. D. Stranks, R. H. Friend, S. Lilliu, *Energy Environ. Sci.* **2018**, 18.

[6] S. Weber, I. M. Hermes, S. H. Turren Cruz, C. Gort, V. W. Bergmann, L. Gilson, A. Hagfeldt, M. Grätzel, W. Tress, R. Berger, *Energy Environ. Sci.* **2018**, *11*, 2404-2413.

[7] H. J. Snaith, *Nat. Mater.* **2018**, *17*, 372.

[8] M. A. Green, A. Ho-Baillie, *ACS Energy Lett.* **2017**, *2*, 822.

[9] M. Yang, D. H. Kim, T. R. Klein, Z. Li, M. O. Reese, B. J. Tremolet De Villers, J. J. Berry, M. F. A. M. Van Hest, K. Zhu, *ACS Energy Lett.* **2018**, *3*, 322.

[10] A. L. Palma, F. Matteocci, A. Agresti, S. Pescetelli, E. Calabrò, L. Vesce, S. Christiansen, M. Schmidt, A. Di Carlo, *IEEE J. Photovoltaics* **2017**, *7*, 1674.

[11] J. Dagar, S. Castro-Hermosa, M. Gasbarri, A. L. Palma, L. Cina, F. Matteocci, E. Calabrò, A. Di Carlo, T. M. Brown, *Nano Res.* **2018**, *11*, 2669.

[12] A. Di Carlo, F. Matteocci, S. Razza, M. Mincuzzi, F. Di Giacomo, S. Casaluci, D. Gentilini, T. M. Brown, a. Reale, F. Brunetti, a. D'Epifanio, S. Licoccia, *14th IEEE Int. Conf. Nanotechnol.* **2014**, 70.

[13] S. Razza, F. Di Giacomo, F. Matteocci, L. Cinà, A. L. Palma, S. Casaluci, P. Cameron, A. D'Epifanio, S. Licoccia, A. Reale, T. M. Brown, A. Di Carlo, *J. Power Sources* **2015**, *277*, 286.

[14] H. C. Liao, P. Guo, C. P. Hsu, M. Lin, B. Wang, L. Zeng, W. Huang, C. M. M. Soe, W. F. Su, M. J. Bedzyk, M. R. Wasielewski, A. Facchetti, R. P. H. Chang, M. G. Kanatzidis, T. J. Marks, *Adv. Energy Mater.* **2017**, *7*, 1.

[15] L. Cai, L. Liang, J. Wu, B. Ding, L. Gao, B. Fan, *J. Semicond.* **2017**, *38*, 1.

[16] D. R. Pernik, M. Gutierrez, C. Thomas, V. R. Voggu, Y. Yu, J. van Embden, A. J. Topping, J. J. Jasieniak, D. A. Vanden Bout, R. Lewandowski, B. A. Korgel, *ACS Energy Lett.* **2016**, 1021.

[17] N. K. Noel, S. N. Habisreutinger, B. Wenger, M. T. Klug, M. T. Hörantner, M. B. Johnston, R. J. Nicholas, D. T. Moore, H. J. Snaith, *Energy Environ. Sci.* **2017**, *10*, 145-152.

[18] J. a. Christians, J. S. Manser, P. V. Kamat, *J. Phys. Chem. Lett.* **2015**, *6*, 852.

[19] M. Wong-Stringer, J. E. Bishop, J. A. Smith, D. K. Mohamad, A. J. Parnell, V. Kumar, C. Rodenburg, D. G. Lidzey, *J. Mater. Chem. A* **2017**, *5*, 15714.

[20] G. A. Abbas, Z. Ding, H. E. Assender, J. J. Morrison, S. G. Yeates, E. R. Patchett, D. M. Taylor, *Org. Electron. physics, Mater. Appl.* **2014**, *15*, 1998.

[21] Z. Song, C. L. McElvany, A. B. Phillips, I. Celik, P. W. Krantz, S. C. Watthage, G. K. Liyanage, D. Apul, M. J. Heben, *Energy Environ. Sci.* **2017**, *10*, 1297.

[22] J. Gong, S. B. Darling, F. You, *Energy Environ. Sci.* **2015**, *8*, 1953.

Chapter 8

Conclusions

Each of the experimental chapters in this thesis have their own conclusions. Here, the impact of all these chapters and their relevance to the PV scientific community is discussed further.

In Chapter 4, a family of carbazole and benzothiadiazole polymers were identified as potential hole-transporting materials (HTMs) for perovskite solar cells. This field of research continues to develop; for example, a copolymer with methoxy side-chains on the benzothiadiazole (PCDTBT1) has been used as a hole transport layer in perovskite solar cells.[1] Notably, by processing a smooth perovskite and very thin PCDTBT1 layer, the requirement for organic dopants (that are perceived as a barrier to commercialisation) used to boost conductivity is removed. However, the long-term stability of PSCs using such polymers as HTMs has not yet been extensively explored. Indeed, in Chapter 5 it is identified that PEDOT:PSS (which is both acidic and hydrophilic) is a likely cause of PSC instability. A large sample size, long-term aging study should be performed – utilising PCDTBT1 in perovskite solar cells.

In Chapter 5, a multi-layer encapsulation was used to stabilise perovskite solar cells. Reasonable payback times of solar modules are entirely reliant on the modules remaining stable over many years of constant operation. Here it was shown that $MAPbI_3$ perovskite active layers could be used to create devices with lifetimes exceeding 1000 hours. Perovskites of other compositions that are more stable will only further increase the stability of perovskite solar cells. This encapsulation developed involved rigid epoxy and glass, which are expensive and inflexible materials that are unlikely to be used in encapsulating flexible roll-to-roll compatible perovskite solar cells. However, the ability to encapsulate lab-scale solar cells allows the scientific community to continually improve the stability of perovskite PV. For example, a colleague and collaborating author (Onkar Game) is currently in the process of providing an answer to one of Chapter 5's biggest questions – namely, why do solvent annealed perovskite devices degrade quicker?

It is hypothesised that the lead excess stoichiometry plays a role in this instability, and that solvent-annealing a perovskite active layer often generates a large excess of lead iodide (as organic components are further liberated from the perovskite film). This encapsulation system has also been used to investigate the stability of high-efficiency lead acetate route perovskite devices, where it is found that perovskite materials made from the lead acetate precursor route are intrinsically very unstable.

The inclusion of a protective interlayer is a transferable piece of knowledge that should help other research groups. Such protective interlayers should prove useful in encapsulating the micro-groove mini-modules discussed in Chapter 7. Crucially, the results in Chapter 5 indicate that caution must be taken when encapsulating perovskite solar cells, as the encapsulation being utilised can cause damage to the solar cell itself.

Chapter 6 and 7 directly address the fabrication of cheap, flexible, and roll-to-roll compatible perovskite solar modules. Applying a reactive electron-beam evaporation process to deposit metal oxides into the micro-groove mini-modules is a good example of a working 'proof of concept'. There is still a large parameter space to explore with Power Roll Ltd's novel flexible groove-based back-contact solar module architecture, with many potential development routes. Fundamentally, the next step for further 'proof of concept' must demonstrate that scalable fabrication processes can create solar modules with much larger active areas. Power Roll already have design concepts in place to tackle this next stage of commercial development.

The key results presented in this thesis can be used to help shape future research directions needed to develop commercial perovskite solar cell architectures. Metal oxides appear to be primary candidates for stable transport layers, and many (if not all) layers can be deposited by vacuum-assisted deposition processes. A new commercial PV competitor would likely employ either a tandem 2-junction or a flexible back-contact solar module architecture. Taken together, this work contributes a small step in the direction of perovskite PV commercialisation.

[1] F. Cai, J. Cai, L. Yang, W. Li, R. S. Gurney, H. Yi, A. Iraqi, D. Liu, T. Wang, *Nano Energy* **2018**, *45*, 28.

Chapter 9

Appendices

9.1: Appendix A - Device Fabrication

9.1.1: Substrate Preparation

Firstly, prepatterned ITO or patterned fluorine tin oxide (FTO) and ITO were chosen as the base substrate. 8-pixel and 6-pixel ITO substrates were purchased from Ossila. FTO was purchased from XOP. FTO was patterned by etching each substrate with zinc powder and 4 M hydrochloric acid (HCl). Kapton tape was used to cover the areas that did not need etching. A thin layer of zinc powder was rubbed into the area that was to be etched, and 4 M HCl is dropped onto the zinc powder. After a few minutes the substrates were rubbed clear with a cotton bud and dumped into boiling water.

All substrates were cleaned of large contaminates by sonicating them in dilute 2 % Hellmanex solution, followed by dump rinsing in boiling deionised (DI) water, sonicating in DI water, and then sonicating them in isopropyl alcohol (IPA) for 15 minutes. Substrates were dried with N_2 and then UV-Ozone treated for 15 minutes to remove final organic residues prior to subsequent layer deposition.

9.1.2: Perovskite Deposition

The following perovskite deposition recipes were used interchangeably between standard and inverted architecture devices. Architecture specific transport layers are detailed after these perovskite recipes. Some of the perovskite recipes involve the use of DMSO with an antisolvent quench, and others contain lead acetate route perovskites, both of which were described in Chapter 2.

$(FAPbI_3)_{0.85}(MAPbBr_3)_{0.15}$ -N_2 Glovebox – 'MC'

To prepare the multi-cation perovskite layer, formamidinium iodide FAI (>99.5%, Ossila), lead (II) iodide PbI_2 (99%, Sigma Aldrich), methylammonium bromide MABr (Dyesol) and lead bromide $PbBr_2$ (99.999%, Sigma Aldrich) were dissolved in a 4:1 v/v DMF:DMSO solvent blend at a concentration of 1.31 M, 1.38 M, 0.24 M, 0.24 M for FAI, PbI_2, MABr and $PbBr_2$ respectively. This produced a ~50% wt $(FAPbI_3)_{0.85}(MAPbBr_3)_{0.15}$ perovskite solution, however the 0.95:1 FAI:PbI_2 molar ratio used resulted in a excess of lead in the final film. The resultant ink was not heated and is not stable beyond one week when stored in air.

Firstly, 50 µl of the perovskite solution was dispensed onto the stationary substrate from a pipette. The substrate was then spun at 2000 rpm for 10 s with a ramp-up of 200 $rpms^{-1}$ then at 6000 rpm for 30 s with a ramp-up of 2000 $rpms^{-1}$. A near continuous stream of 100 µl of chlorobenzene was then rapidly deposited onto the spinning substrate after 10 seconds into the second stage of the spin cycle (corresponding to 20 seconds after the perovskite was originally dispensed). Immediately after spin-casting, the substrate was placed on a hotplate at 100 °C and annealed for 90 minutes.

$CsI_{0.05}((FAPbI_3)_{0.83}(MAPbBr_3)_{0.17})_{0.95}$ - N_2 Glovebox – 'TC'

Triple-cation perovskite solution with composition $CsI_{0.05}((FAPbI_3)_{0.83}(MAPbBr_3)_{0.17})_{0.95}$ was prepared using 1 mL of mixed solvent (anhydrous n,n-dimethylformamide: dimethyl sulfoxide (DMF:DMSO) 4:1 volume ratio) containing 1 M FAI (Greatcell), 0.2 M MABr (Greatcell), 1.1 M PbI_2 (TCI) and 0.2 M $PbBr_2$ (TCI), which was heated at 70 °C and intermittently vortex mixed for around 30 minutes before adding 50 µl of caesium iodide (CsI) in DMSO (1.5 M concentration).

This solution was filtered through a 0.2 µm polytetrafluoroethylene (PTFE) filter before being spin coating at 1000 rpm for 10 seconds and then at 6000 rpm for 20 seconds. 100 µl of chlorobenzene (CB) was then rapidly dripped on the film surface 5 seconds before the end of the programme. Films were annealed at 80 °C for 60 minutes inside a vacuum chamber or at 100 °C for 60 minutes in a nitrogen atmosphere.

$MAPbI_3$ Acetonitrile Route - N_2 Glovebox – 'iAc1' or 'AC'

Methylamine bubbled acetonitrile perovskite solutions were prepared using 4 – 10 mL of anhydrous acetonitrile. A 0.5 M suspension was prepared containing PbI_2 and MAI (Greatcell) at a stoichiometric ratio of 1:1.06. As first demonstrated by Noel et al, this black suspension of powder in acetonitrile was then bubbled with dry methylamine gas to create a clear-yellow solution. This solution was then filtered through a 0.2 µm PTFE filter before it was dynamically deposited via spin coating at 4000 rpm for 30 seconds. Films were annealed at 100 °C for 60 minutes in a nitrogen atmosphere. To solvent anneal the PSCs, the $MAPbI_3$ films were held at 100 °C for a further 30 minutes. During the first 15 minutes of this extra anneal, they were sealed under a glass petri dish in a solvent atmosphere created using 20 µl of dimethylformamide (DMF). After 15 minutes, the petri-dish lid was then removed.

$MAPbI_3$ Acetate Route - N_2 Glovebox – 'iace'

MAI and lead acetate ($PbAc_2$) were dissolved in DMF at a molar ratio of 3:1 with a total concentration of 40% wt. This solution was never heated. This solution was spun at 2000 rpm and annealed at 100 °C for 5-15 minutes.

9.1.3: Standard Architecture (n-i-p) Charge Transport Layers

Electron Transport Layer (ETL)

Either TiO_2, C_{60}, or ZnO were deposited as base electron transport layers, using both solution processing and vacuum assisted evaporation.

Solution processing

The c-TiO_2 layer was deposited by spray-pyrolysis. Here, a dilution of 1.72 mL of titanium diisopropoxide bis(acetylacetonate) (75wt % Sigma Aldrich) in 18.3 mL of IPA (Sigma Alrich) was sprayed onto a hotplate at 450 °C and left to sinter for 30 minutes.

In addition to c-TiO_2 layer a meso-porous TiO_2 (mp-TiO_2) layer was sometimes used. This was fabricated from a titanium oxide paste (18-NRT Dyesol) that was first diluted to 15 wt % in ethanol. The resulting solution was spin coated in air (< 35 % RH) at room temperature on top of the c-TiO_2 at 5000 rpm for 15 s. After deposition, the substrates were left at room temperature for 10 minutes before being sintered in air for 1 hour at 450 °C. For some devices, a 19 mg mL^{-1} solution of LiTFSI (Sigma Aldrich) in acetonitrile was spun onto the c-TiO_2/mp-TiO_2 in air (<35% RH) at 3000rpm, with the substrates then re-sintered in air at 450 °C for a further 30 minutes before being transferred into a nitrogen filled glove box.

Thermal Evaporation

For evaporation on flat cells, a mask was used to pattern the electron transport layer onto an area of the substrate that coated the active area but left the edges of the substrate clear. The substrates were rotated during evaporation to obtain a uniform thin-film.

Titanium pellets were purchased from Kurt Lesker (¼ by ¼ inch, 99.995 % purity). For deposition, titanium pellets were placed inside a carbon crucible. The deposition sources were first preconditioned through a long, high power electron-beam exposure using a wide sweep pattern. This created a pool of melted metal that was free from initial oxide impurities. During deposition, O_2 was first fed into the chamber at a partial pressure between from $5x10^{-5}$ mbar to $1.9 x10^{-4}$ mbar. During evaporation the O_2 flow rate was maintained at the chosen constant partial pressure and substrates were rotated at approximately 10 rpm. Evaporation of the metal oxide was performed using a smaller electron-beam pattern, at rates ranging from 0.3 to 10 $Ås^{-1}$, creating a 10 nm (unless otherwise stated) transparent film.

Alternatively, either C_{60} or ZnO were thermally evaporated at various thicknesses and various deposition rates.

<u>Hole Transport Layer (HTL)</u>

Solution processing

After the perovskite film was cooled to room temperature, either a spiro-OMeTAD, PCDTBT, CuPc, or MoO_3 was deposited as a hole transport layer. Solution processing was used for spiro-OMeTAD and PCDTBT, whilst thermal evaporation was used for CuPc, or MoO_3.

Spiro-OMeTAD (Ossila) and PCDTBT (low palladium content with Mw ~ 34,900) were added to CB at 86 mg mL^{-1} and 20mg mL^{-1} respectively unless otherwise stated. These solutions were prepared with each mL containing additional dopants.

The exact formulation of dopants was changed between experiments. As such the doping procedure is reported in more detail in each chapter. In simple terms dopants including: 4-tert-butyl-pyridine (TBP), and lithium bis(trifluoromethanesulfonyl)imide (LiTFSI), were used in combination with either tris(2-(1H-pyrazol-1-yl)-4-tert-butylpyridine)cobalt(II) di[hexafluorophosphate] (FK 209 Co(II) PF6 (FK209-PF6) or FK 209 Co(III) – TFSI. For optimum device performance, HTMs were spun onto a static perovskite coated substrate at 2000 to 4000 rpm for 30s in a N_2 filled glovebox.

Thermal Evaporation

Alternatively, either CuPc or MoO_3 were thermally evaporated at various thicknesses and various deposition rates.

9.1.4: Inverted Architecture (p-i-n) Charge Transport Layers

Hole Transport Layer (HTL)

Either PEDOT:PSS, Poly-TPD, PTAA, NiO, CuPC or MoO_3 were deposited as a base hole transport layer. Solution processing was used for all polymers. NiO, CuPC and MoO_3 were thermally evaporated.

Solution processing

Poly-TPD or PTAA were dissolved in toluene at 1 mg mL^{-1}. These solutions were sometimes prepared containing the dopant F4TCNQ dissolved at 0.2mg mL^{-1} with the polymer. The solution was heated to 80 °C to fully dissolve the solution. The polymer was then spin-coated from a hot solution onto a UVO treated substrate at a speed of 4000 rpm to create a uniform ultra-thin poly-TPD film. This was then annealed at 110 °C for 10 minutes before being transferred to N_2 glovebox.

Alternatively PEDOT:PSS Heraeus Clevios™ AI 4083 was passed through a polyvinylidene fluoride (PVDF) 0.4 μm filter and immediately spin coated at 4000-6000 rpm in air. The resultant film was annealed in air at 120 °C for 20 minutes.

Thermal Evaporation

An evaporation mask was used, and the substrates were rotated.

Nickel pellets were purchased from Kurt Lesker (¼ by ¼ inch, 99.995 % purity). For deposition, nickel pellets were placed directly inside a copper hearth. An electron-beam evaporation deposition was then performed in a similar fashion to that of TiO_2 described above.

Alternatively, either CuPC or MoO_3 were thermally evaporated at various thicknesses and various evaporation rates.

Electron Transport Layer (ETL)

After the perovskite film was cooled to room temperature either $PC_{60}BM$, $PC_{70}BM$, or C_{60} fullerenes were deposited as electron transport layers. Solution processing was used for $PC_{60}BM$ and $PC_{70}BM$. Alternativity, C_{60} was thermally evaporated.

Solution Processing

A $PC_{60}BM$ or $PC_{70}BM$ (Ossila) solution was prepared at 30 mg mL^{-1} in CB and was stirred overnight at 70 °C and then left to cool. This solution was filtered through a 0.2 µm PTFE filter before spin coating at 4000 rpm onto the perovskite film for 20 seconds. The substrates were annealed for 10 minutes at 90 °C in a N_2 filled glovebox.

Thermal Evaporation

Alternatively, C_{60} was thermally evaporated at various thicknesses and various evaporation rates.

Inverted Structure Wide-Band Interlayer

In order to improve the band alignment between the fullerene layer and the metal electrode, a thin layer of wide-band gap material was utilised to cause favourable band bending across the ETL/electrode interface.

After the device stack was coated with a fullerene was cooled to room temperature, a 0.5 mg mL^{-1} Bphen in IPA solution was spin-coated at 6000 rpm onto the substrates for 20 s.

9.1.5: Device Patterning

The completed device stack was patterned such that probes could contact the ITO or FTO. The devices were either brought into a humidity controlled clean room (<35 % RH) and held at 80 °C whilst being swabbed with a DMF coated cotton bud, or patterned using a razor blade to allow contact to the ITO as required.

The patterning of materials and clearing of contact for testing probes are important factors to consider when fabricating PSCs. For example, the position of chemical etch on FTO substrates can be too close to the desired 'active area' meaning there is no FTO to collect charges beneath the perovskite active layer, or it can be too small, making a long strip of FTO that is only isolated from the gold top contact by the active layer and transport layers. This is shown in device schematics in Figure A1a, where the longer the gold and FTO overlap is, the greater the statistical chance of a pin hole causing a catastrophic short circuit.

In a prepatterned 8-pixel design (predominantly used for inverted structure devices) the device stack must be removed from the edges of the device so that the probes can contact the ITO pads. However, if the material is removed from regions that are too close to the central ITO active area, then the top metal electrode will directly touch the base ITO and again create a catastrophic short circuit pathway. The 6-pixel chemically etched FTO substrate layout is more robust as it does not need this detailed patterning, the gold top electrode can go directly to the edge of the substrate. However, the FTO pad still needs to be exposed via removal of the material on that substrate edge (see Figure A1b). Unfortunately, the contact of probes onto this FTO pad can still make a poor connection due to it being difficult to properly remove material from the edges (particularly the ETL layers). This can be resolved in two ways: (i) all materials are patterned as they are deposited such that the edge of the FTO are never covered with any layers, or more simply, (ii) A electrode bus bar can be added onto a less thoroughly (either swabbed or scratched away, or a trench made through the device stack) patterned area (See Figure A1c).

For standard architecture device development, the material was either patterned (for example the c-TiO_2 was sprayed through a mask), scratched away, or swabbed away from the FTO edge. The *FF* of devices was shown to sufficiently increase upon addition of the bus bar and reproducibility of devices performance was greatly improved. This indicated that contact resistance was causing significant variation in observed device performance metrics. As such, a gold bus bars were used for devices with non-prepatterned substrates in this thesis.

9.1.6: Metal Contacts

Thermal evaporation was used to deposit the final metal electrodes. An evaporation mask was used to pattern either 6 or 8 metal pixels, connecting the top of the active area to an ITO or FTO pad that was probed when the devices were tested. The substrates were rotated to obtain a uniform thin-film. Au contacts were used on top of HTLs in standard structure devices. Ag contacts were used on top of ETLs in inverted structure devices. In some cases, Au was also used as the electrode for inverted devices. These were deposited between 80-120 nm thick at evaporation rates between 1-2 $Ås^{-1}$

9.1.7: Device Encapsulation

The PSCs were either left without encapsulation, or coated with 135 ± 5 nm of polyvinylpyrrolidone (Sigma Aldrich) spin-coated at 6000 rpm from a 25 mg mL^{-1} methanol solution, or coated with an 250 nm electron-beam evaporated layer of Al_2O_3. Following this, a drop of UV initiated one-part epoxy was placed on the top of the device stack and covered with a glass encapsulation slide. This epoxy was cured under a UV light for 20 minutes. This encapsulation process is discussed further in Chapter 5. Devices that contain PEDOT:PSS were found to degrade quickly without encapsulation. All other material combinations were air stable enough to characterise before significant degradation occurred.

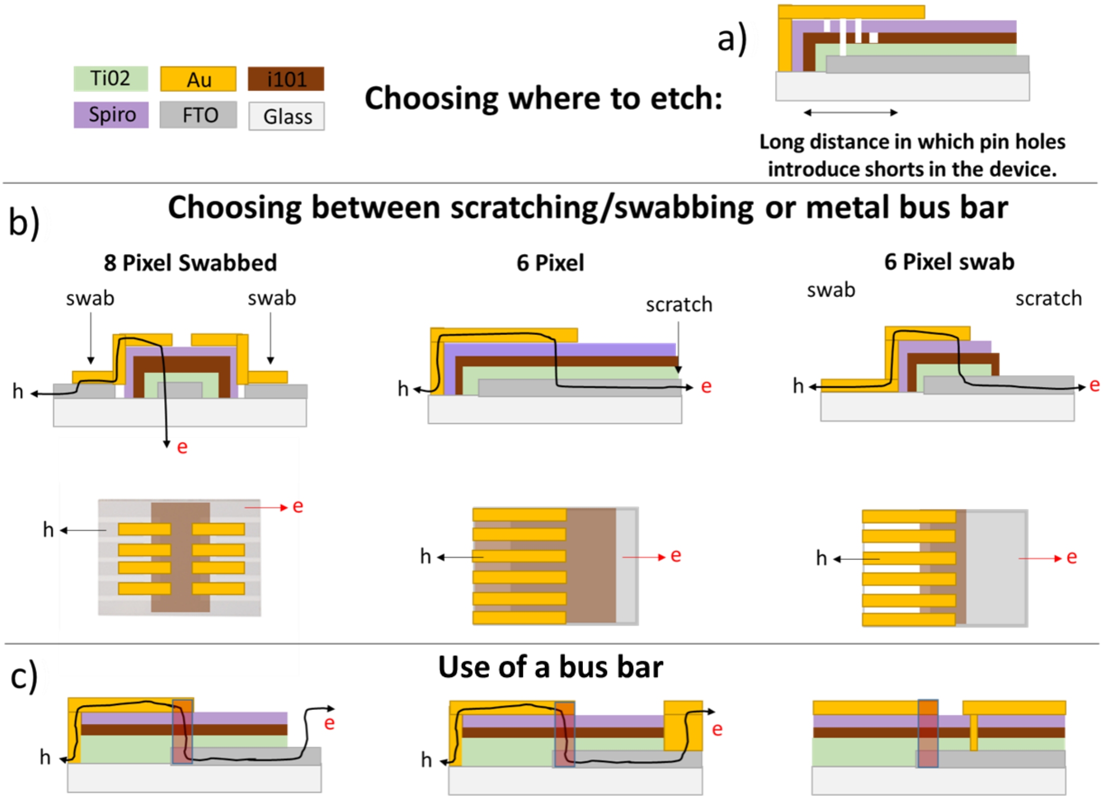

Figure A1: *Etching and patterning substrates. a) A schematic showing how the FTO is etched away from the gold finger. b) Schematics showing 8-pixel and 6-pixel substrate layouts indicating the potential areas that need to be swabbed or scratched in order to make proper contact to the device. c) Schematics indicating position of potential metal bus bars that can be placed on top of a swabbed or scratched.*

9.2: Appendix B - Additional PSC Stability Measurements

9.2.1: Measurement Regime for Aging Perovskite Solar Cells.

Al lifetime measurements involved repeatedly performing current-voltage sweeps, where it was found that sweeping the voltage from -1.2 to 1.2 V induced degradation in the device. This effect is shown in Figure A4. Due to this result, all PSCs stability data presented in this thesis is collected with PSCs scanned only from 0 to 1.2 V.

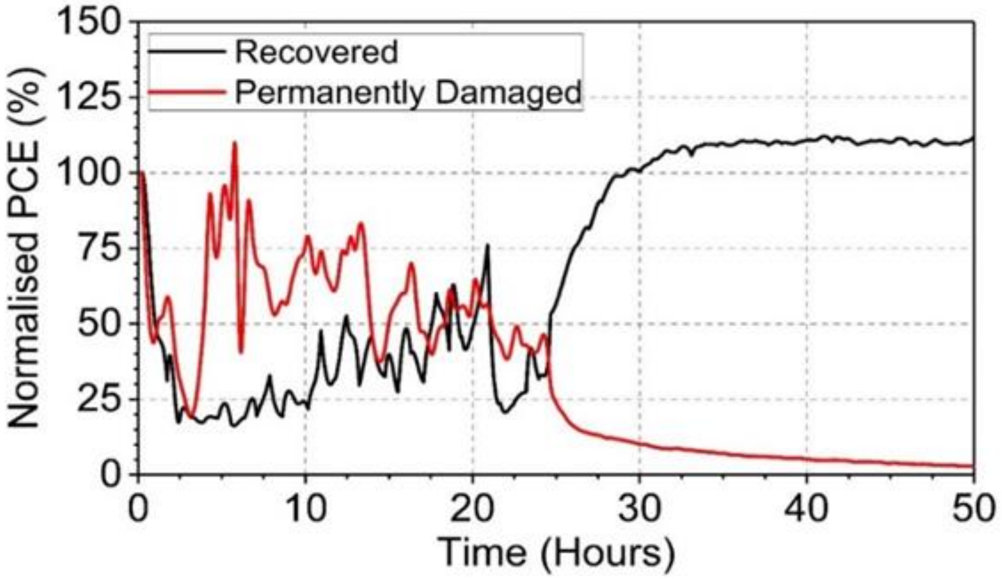

Figure A4: *The effect of aging under illumination and varying voltage conditions on perovskite solar cell device performance. Sweeps were taken from -1.2 to 1.2 V for first 24 hours before switching to a new scanning regime of 0 to 1.2 V. Stability of PSC was poor when being swept into negative voltage. Some were pixels permanently damaged and some recovered to above their initial power conversion efficiency.*

9.2.2: Acetate Route Perovskite Stability

Implementation of acetate route $MAPbI_3$ into p-i-n architecture produced PSCs with up to 18 % PCE. As described in the fabrication routines, an alternative methylamine bubbled acetonitrile $MAPbI_3$ solution was also adapted from literature. This low boiling point highly volatile solution allowed complete and uniform wetting of any HTL, including the poly-TPD. Figure A2 contains box plots of ITO/poly-TPD/$MAPbI_3$/$PC_{60}BM$/Bphen/Ag devices made with either the acetonitrile or acetate route perovskite. Whilst acetate route devices achieve high champion PCEs with V_{OCs} up to 1.16 V, they also possess a larger variation in device performance metrics. The variation was probably due to the inconsistent wetting of acetate route perovskite onto the poly-TPD. When deposited on poly-TPD such perovskites formulations produce extremely specular smooth perovskite films with RMS roughness as low as 5 nm, however, surface coverage was often low.

Unfortunately, the stability of perovskite solar cells with an acetate route perovskite active layer is very poor. Figure A3 shows the stabilised power output (a) and sweep (b) of champion acetate route perovskite solar cells.

Even with a multi-layer encapsulation, these high efficiency acetate devices were found to fully degrade within 10 hours (see Figure A3c). Figure A3d shows that this degradation is entirely due to a loss in photocurrent. The origin of acetate route perovskite leading to perovskite solar cell instability is still unclear. It is possible that the off-stoichiometric route perovskite (3:1 MAAc:PbI_2) is more sensitive to processing conditions, leading to excess MAAc, MA or Ac left in the perovskite film, even after thermal annealing. It is for these reason that Chapter 5 and 6 avoid the use of acetate route perovskite.

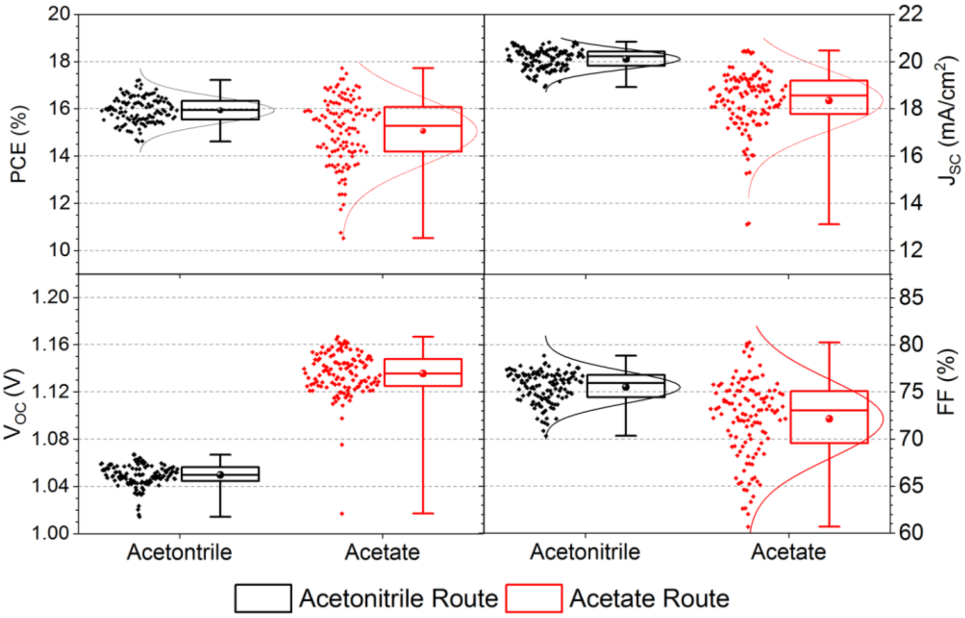

Figure A2: *Boxplots of solar cell performance metrics for ITO/poly-TPD/MAPbI$_3$/PC$_{60}$BM/Bphen/Ag devices from methylamine bubbled acetonitrile route and acetate route.*

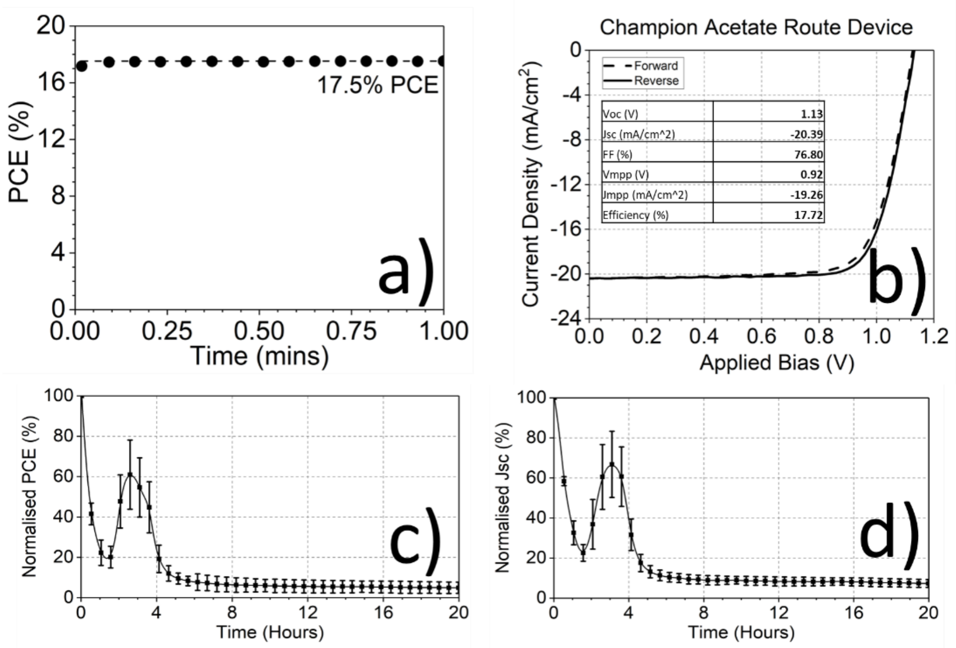

Figure A3: *Champion acetate route ITO/poly-TPD/MAPbI$_3$/PC$_{60}$BM/Bphen/Ag devices, with a) stabilised power output, b) current-voltage sweep, c) and d) PCE and J_{SC} of these unstable acetate devices over 20 hours of lifetime testing. Solid lines and dotted line represent reverse and forward sweeps respectively.*

9.3: Appendix C - Screening Materials for Solar Grooves

Conventional planar PSCs were used to help develop materials for groove mini-modules. Materials are primarily chosen from their band alignment relative to $MAPbI_3$. These materials did not have to be transparent but had to be p-type and n-type selective and must not dissolve or detrimentally chemically react with the perovskite solution. Materials must also be evaporable and demonstrate directionality of evaporation. Thicknesses of evaporated charge transport layers were typically fixed at 20 nm when used below a perovskite active layer and 50nm when used above the perovskite, unless otherwise stated.

9.3:1 Electron-Beam Evaporated c-TiO_2

n-i-p ITO/c-TiO_2/$MAPbI_3$/spiro-OMeTAD/Au PSCs were fabricated with reactive electron-beam evaporated having thicknesses of 10 to 50 nm thick c-TiO_2 (from a Ti_3O_5 source). Unfortunately, no c-TiO_2 film (regardless of inclusion of O_2 partial pressure during the evaporation or thickness of film) enabled PCSs having > 4 % PCE. As can be seen in Figure A5a, the only process that enabled perovskite devices to achieve a stabilised PCE matching that of those with a reference spray pyrolysis c-TiO_2, was a high temperature (450 °C) anneal of the electon-beam deposited TiO_2. This thermal anneal (which was performed in air) likely resulted in crystallisation of anatase phase TiO_2 (increasing the TiO_2 conductivity) and an improvement in the CB alignment of TiO_2 with the perovskite. Unfortunately, this high temperature heating step is not compatible with flexible PET substrates.

9.3:2 Thermally Evaporated C_{60}

n-i-p ITO/C_{60}/$MAPbI_3$/spiro-OMeTAD/Au and p-i-n ITO/poly-TPD/$MAPbI_3$/C_{60}/ Au perovskite solar cells were fabricated to explore wheather C_{60} worked in both inverted and standard architecture devices. Figure A5b details the stabilised PCE outputs of champion devices. Without optimization C_{60} was able to achieve good device performance metrics in both cases. Most importantly, the n-i-p devices were able to achieve a PCE of nearly 14 % with C_{60} below the perovskite without the inclusion of a c-TiO_2 ETL. C_{60} was therefore deemed compatible with flexible PET substrates.

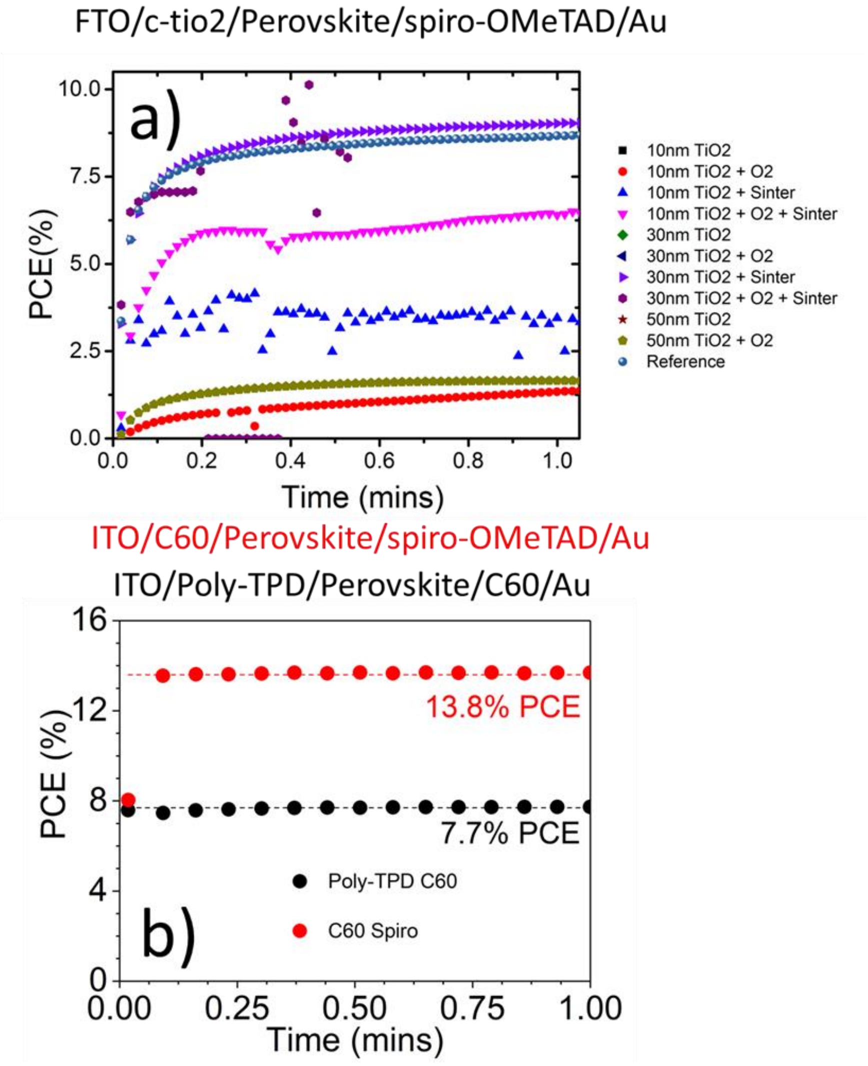

Figure A5: *Evaporated charge transport material screening of* TiO_2 *and* C_{60} *as ETLs for perovskite solar cells. a) Stabilised power output of electron-beam evaporated* TiO_2 *processed from a* Ti_3O_5 *source material, with and without an oxygen partial pressure.* TiO_2 *was deposited at a thickness of 10, 20 and 30 nm. Reference c-*TiO_2 *from a spray pyrolysis process is included (teal). Electron-beam deposited* TiO_2 *has also been sintered at 450 °C (purple, pink). b) Stabilised power output of perovskite solar cells using* C_{60} *as a charge transport layer on the bottom of a standard architecture device or top of an inverted device.*

9.3:3 Thermally Evaporated CuPc and MoO_3

CuPc and MoO_3 were screened as alternative evaporable HTLs. As shown in Figure A6a, CuPc enabled inverted architecture PSCs to be created with champion PCEs exceeding 10 % PCE. Note that CuPc is not a transparent material. Unfortunately, evaporated MoO_3 was found to react and discolour significantly once coated with methylene bubbled acetonitrile perovskite solution. Figure A6b is a photograph with a piece of fresh MoO_3 source material next to another piece that has been submerged in perovskite solution. The picture clearly indicates that the MoO_3 was reduced by the perovskite solution. Therefore, MoO_3 was there not suitable for use in a back-contact solar cell HTL.

9.3:4 Electron-Beam Evaporated ZnO

ZnO was screened as an alternative ETL. Surprisingly, ZnO was also found to react with the perovskite solution upon perovskite deposition. Standard architecture PSCs with a stabilised PCE of 5.6 % were achieved (Figure A7a). This low PCE meant that ZnO was not investigated further for use with flexile PET micro-groove mini-modules

9.3:5 Further Screening

Figure A7a shows the stabilised PCE output from a champion n-i-p ITO/C_{60}/$MAPbI_3$/CuPc/Au devices, demonstrating that C_{60} and CuPc can work interchangeable below and above the perovskite active layer.

To determine if C_{60} and CuPc were materials which could be used in flexible PET micro-groove mini-modules, devices were fabricated comparing reference p-i-n devices ITO/poly-TPD/Perovskite/$PC_{60}BM$/Bphen/Ag, n-i-p devices with C_{60} on the bottom; ITO/C_{60}/$MAPbI_3$/CuPc/Au, and p-i-n devices with CuPc on the bottom ITO/CuPc/$MAPbI_3$/C_{60}/Au. Boxplots in Figure A7b show the device performance metrics of a batch of each of these devices. Unfortunately, p-i-n devices with CuPc below the perovskite device were found to have large variations in V_{OC}, *FF*, and PCE regardless of the evaporation rate.

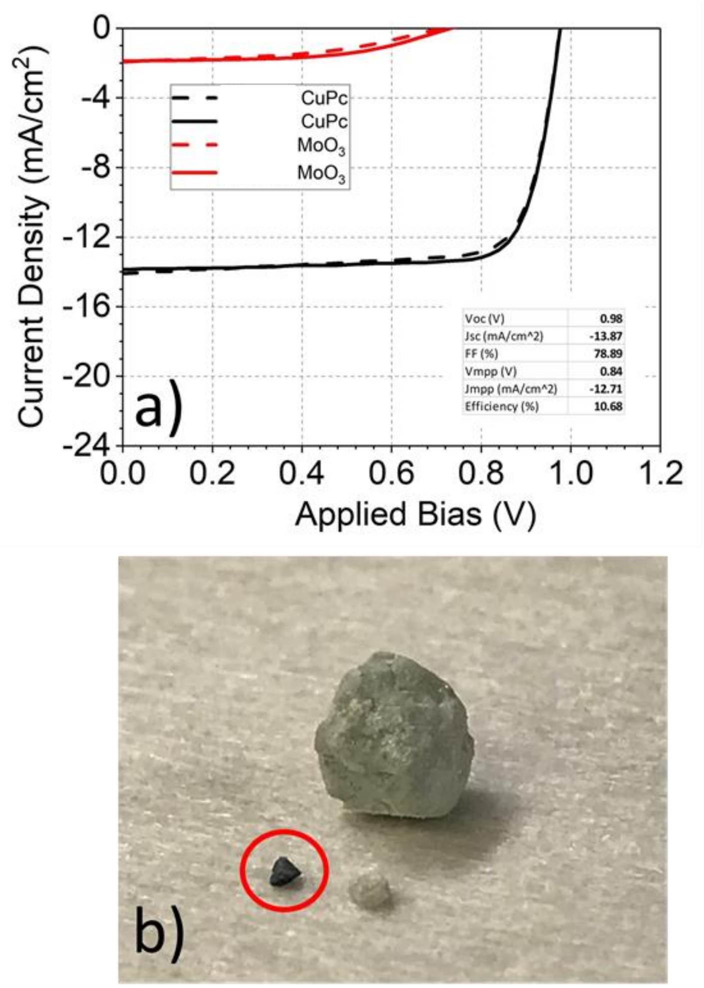

Figure A6: *Evaporated charge transport material screening of MoO_3 and CuPC as HTLs for inverted perovskite solar cells. HTLs are used below the perovskite active layer. a) Current-voltage sweeps of characteristic devices employing electron-beam evaporated CuPc (black) and MoO_3 (red). Solid lines and dotted line represent reverse and forward sweeps respectively. b) Photograph of chunks of MoO_3 before (white) and after (black, red circle) being submerged in a methylamine bubbled acetonitrile solution.*

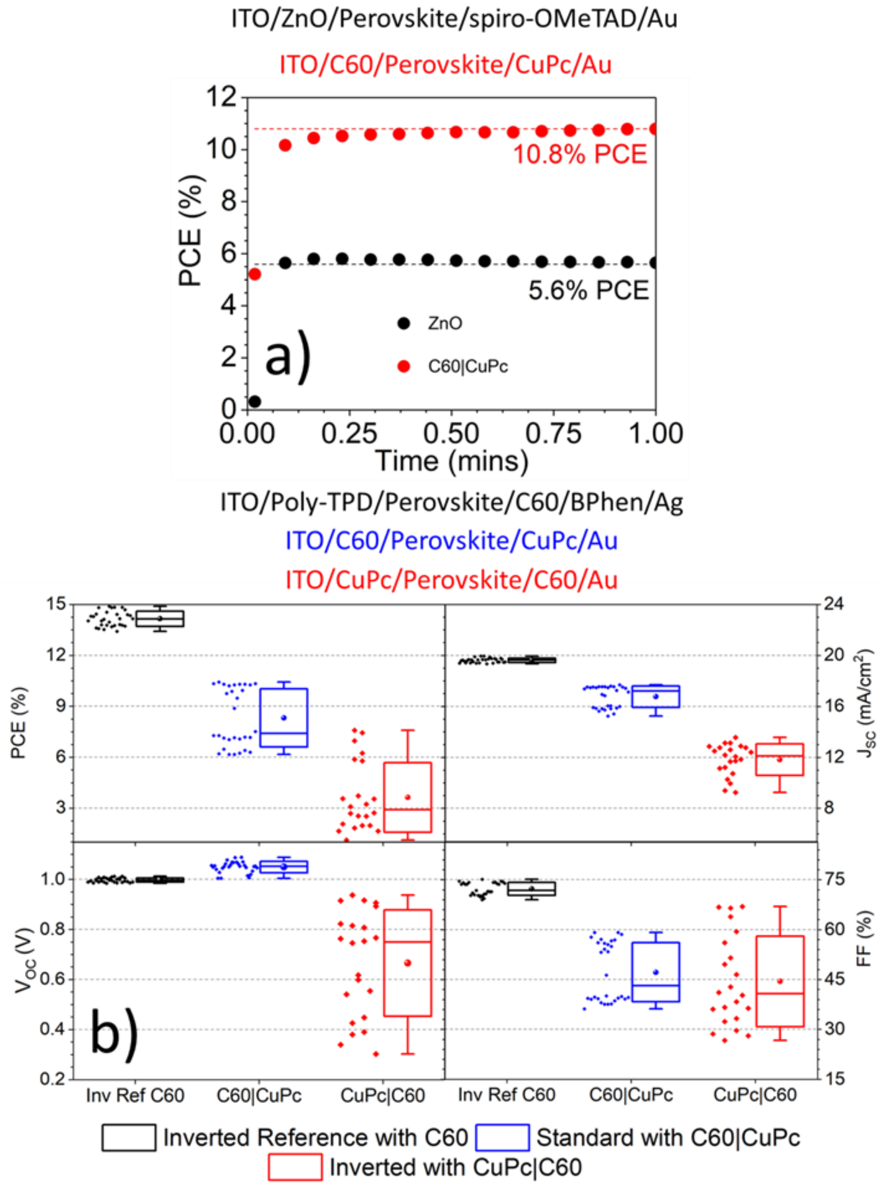

***Figure A7**: Evaporated charge transport material further screening of C_{60}, ZnO and CuPC as transport layers for perovskite solar cells. The materials are used interchangeable above and below the perovskite active layer. a) Characteristic stabilised power output of perovskite solar cells with a ZnO ETL (black) and C_{60} ETL with a CuPc HTL (red). b) Boxplots of performance metrics of perovskite solar cells using a top C_{60} ETL with a poly-TPD HTL (black), using a bottom C_{60} ETL with a top CuPc HTL(blue) , and using a top C_{60} ETL with a bottom CuPC HTL (red).*